Modeling for the SAFRR Tsunami Scenario—Generation, Propagation, Inundation, and Currents in Ports and Harbors

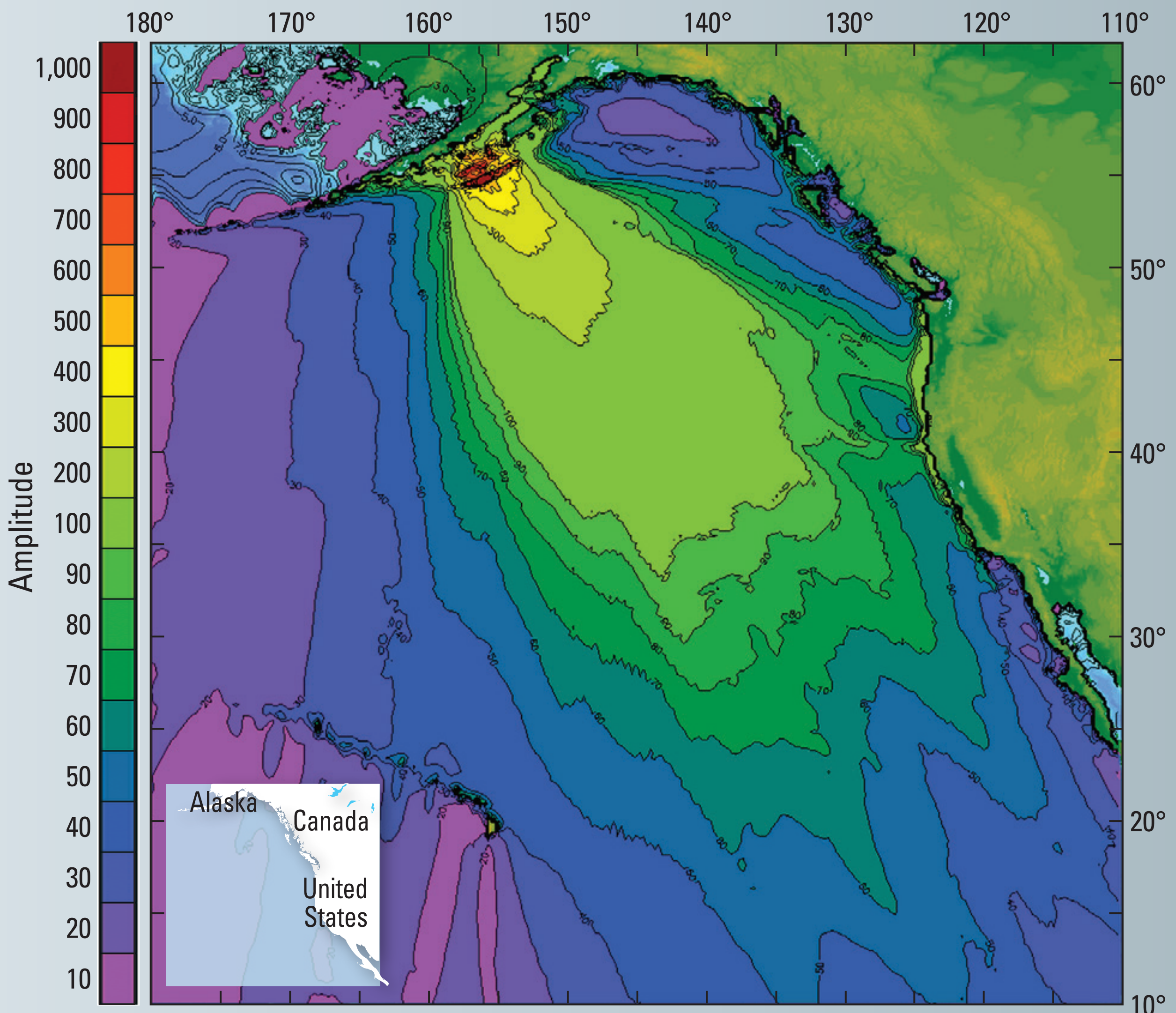

Open-File Report 2013–1170–D
California Geological Survey Special Report 229

U.S. Department of the Interior
U.S. Geological Survey

COVER—Maximum tsunami amplitude of scenario tsunami throughout the northeast Pacific Ocean using the Method of Splitting Tsunami (MOST) model. Image courtesy Vasily Titov, National Oceanic and Atmospheric Administration/Pacific Marine Environmental Laboratory.

The SAFRR (Science Application for Risk Reduction) Tsunami Scenario

Stephanie Ross and Lucile Jones, Editors

Modeling for the SAFRR Tsunami Scenario—Generation, Propagation, Inundation, and Currents in Ports and Harbors

By the SAFRR Tsunami Modeling Working Group

Open-File Report 2013–1170–D

California Geological Survey Special Report 229

U.S. Department of the Interior
U.S. Geological Survey

U.S. Department of the Interior
SALLY JEWELL, Secretary

U.S. Geological Survey
Suzette M. Kimball, Acting Director

U.S. Geological Survey, Reston, Virginia 2013

For product and ordering information:
World Wide Web: http://www.usgs.gov/pubprod
Telephone: 1-888-ASK-USGS

For more information on the USGS—the Federal source for science about the Earth,
its natural and living resources, natural hazards, and the environment:
World Wide Web: http://www.usgs.gov
Telephone: 1-888-ASK-USGS

Suggested citation:
The SAFRR Tsunami Modeling Working Group, 2013, Modeling for the SAFRR Tsunami Scenario—Generation, propagation, inundation, and currents in ports and harbors, chap. D, *in* Ross, S.L., and Jones, L.M., eds., The SAFRR (Science Application for Risk Reduction) Tsunami Scenario: U.S. Geological Survey Open-File Report 2013–1170, 136 p., http://pubs.usgs.gov/of/2013/1170/d/.

STATE OF CALIFORNIA
EDMUND G. BROWNJR.
GOVERNOR

THE NATURAL RESOURCES AGENCY
JOHN LAIRD
SECRETARY FOR RESOURCES

DEPARTMENT OF CONSERVATION
MARK NECHODOM
DIRECTOR

CALIFORNIA GEOLOGICAL SURVEY
JOHN G. PARRISH, Ph.D.
STATE GEOLOGIST

Contents

Figures

Tables

Modeling for the SAFRR Tsunami Scenario—Generation, Propagation, Inundation, and Currents in Ports and Harbors

By the SAFRR Tsunami Modeling Working Group[1]

Preface

By Eric L. Geist

This U.S. Geological Survey (USGS) Open-File report presents a compilation of tsunami modeling studies for the Science Application for Risk Reduction (SAFRR) tsunami scenario. These modeling studies are based on an earthquake source specified by the SAFRR tsunami source working group (Kirby and others, 2013). The modeling studies in this report are organized into three groups. The first group relates to tsunami generation. The effects that source discretization and horizontal displacement have on tsunami initial conditions are examined in section 1 (Whitmore and others). In section 2 (Ryan and others), dynamic earthquake rupture models are explored in modeling tsunami generation. These models calculate slip distribution and vertical displacement of the seafloor as a result of realistic fault friction, physical properties of rocks surrounding the fault, and dynamic stresses resolved on the fault.

The second group of papers relates to tsunami propagation and inundation modeling. Section 3 (Thio) presents a modeling study for the entire California coast that includes runup and inundation modeling where there is significant exposure and estimates of maximum velocity and momentum flux at the shoreline. In section 4 (Borrero and others), modeling of tsunami propagation and high-resolution inundation of critical locations in southern California is performed using the National Oceanic and Atmospheric Administration's (NOAA) Method of Splitting Tsunami (MOST) model and NOAA's Community Model Interface for Tsunamis (ComMIT) modeling tool. Adjustments to the inundation line owing to fine-scale structures such as levees are described in section 5 (Wilson).

The third group of papers relates to modeling of hydrodynamics in ports and harbors. Section 6 (Nicolsky and Suleimani) presents results of the model used at the Alaska Earthquake Information Center for the Ports of Los Angeles and Long Beach, as well as synthetic time series of the modeled tsunami for other selected locales in southern California. Importantly, section 6 provides a comparison of the effect of including horizontal displacements at the source described in section 1 and differences in

---

[1] Members of the working group (in alphabetical order): Bohyun Bahng (National Oceanic and Atmospheric Administration, West Coast and Alaska Tsunami Warning Center), José Borrero (University of Southern California and eCoast Ltd.), Eric L. Geist (U.S. Geological Survey; SAFRR Tsunami Modeling Coordinator), William Knight (National Oceanic and Atmospheric Administration, West Coast and Alaska Tsunami Warning Center), Patrick Lynett (University of Southern California), Dmitry J. Nicolsky (Alaska Earthquake Information Center, Geophysical Institute, University of Alaska), David D. Oglesby (University of California Riverside), Kenny Ryan (University of California Riverside), Sangyoung Son (University of Southern California), Elena N. Suleimani (Alaska Earthquake Information Center, Geophysical Institute, University of Alaska), Costas Synolakis (University of Southern California and Hellenic Centre for Marine Research), Hong Kie Thio (URS Corporation), Vasily Titov (National Oceanic and Atmospheric Administration, Pacific Marine Environmental Laboratory), Paul Whitmore (National Oceanic and Atmospheric Administration, West Coast and Alaska Tsunami Warning Center), and Rick Wilson (California Geological Survey).

bottom friction on wave heights and inundation in the Ports of Los Angeles and Long Beach. Modeling described in section 7 (Lynett and Son) uses a higher order physical model to determine variations of currents during the tsunami and complex flow structures such as jets and eddies. Section 7 also uses sediment transport models to estimate scour and deposition of sediment in ports and harbors—a significant effect that was observed in southern California following the 2011 Tohoku tsunami. Together, all of the sections in this report form the basis for damage, impact, and emergency preparedness aspects of the SAFRR tsunami scenario.

Three sections of this report independently calculate wave height and inundation results using the source specified by Kirby and others (2013). Refer to figure 29 in section 3, figure 52 in section 4, and figure 62 in section 6. All of these results are relative to a mean high water (MHW) vertical datum. Slight differences in the results are observed in East Basin of the Port of Los Angeles, Alamitos Bay, and the Seal Beach National Wildlife Refuge. However, given that these three modeling efforts involved different implementations of the source, different numerical wave propagation and runup models, and slight differences in the digital elevation models (DEMs), the similarity among the results is remarkable.

1. Effects of Subfault Discretization and Horizontal Displacement on Tsunami Generation

By Paul Whitmore, Bohyun Bahng, and William Knight

Vertical Deformation Summation Effect Induced by Abruptly Changing Fault Dip

A common practice in tsunami modeling is to break a fault source up into multiple subfaults and then use the Okada static dislocation formulae to compute the vertical displacement from each subfault and sum these together to determine the total uplift. A potential problem with this approach is noted when the dip angle changes abruptly between subfaults located updip or downdip from each other. The effect is for the trough produced by the updip subfault to decrease the uplift produced by the downdip subfault. An abrupt change in dip likely does not represent the actual situation; a smoothly varying dip would reproduce the event uplift more realistically.

The 2014 Alaska Peninsula tsunami scenario (Kirby and others, 2013) was examined to see whether the abrupt change in dips influenced the resultant uplift. The 64 subfaults as defined by Kirby and others were first used to compute static vertical displacement in the traditional manner. Figure 1 shows this uplift.

The 64 subfaults used in the 2014 scenario are approximately 50 km long by 25 km wide (downdip). They are arranged in 8 rows with 8 subfaults in each row, producing approximately a 400-km-long by 200-km-wide source zone. To test the influence of abrupt dip changes in the downdip direction, each subfault is divided into 5 units approximately 50 km long by 5 km wide (320 subfaults total). A spline fit is used to compute the subfault dips respecting the original dips. That is, each subfault (50 km x 5 km) is assigned a dip that smoothly interfaces with the next downdip subfault. The vertical displacement is computed for each of the 320 subfaults and summed. Figure 2 shows the summation based on the 320 subfaults with smoothly varying dips from farthest updip to farthest downdip subfault.

Figure 3 shows the difference between the traditional approach of summing up 64 subfaults (fig. 1) and the smoothly dipping approach (fig. 2). Note that the uplift in figure 2 has a longer spatial period and that figure 3 shows significant differences between the two approaches.

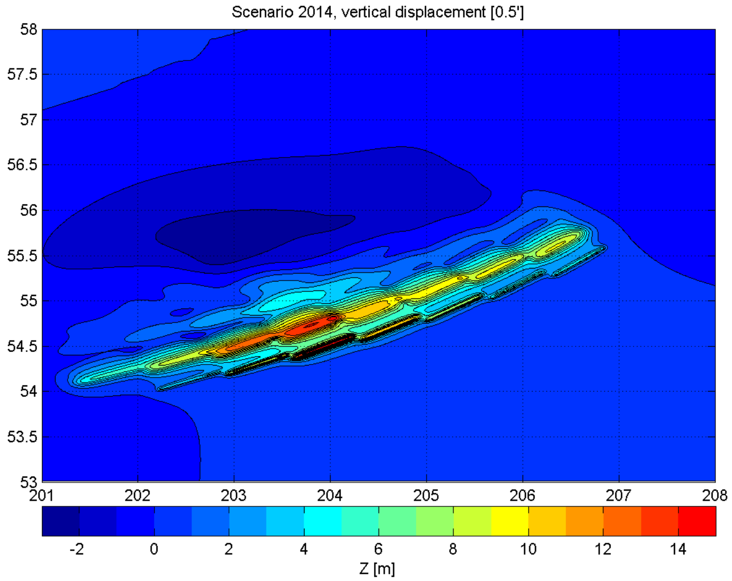

Figure 1. Map-view diagram showing vertical displacement (Z, in meters) in the 2014 tsunami scenario computed at the West Coast and Alaska Tsunami Warning Center (WCATWC) based on 64-subfault summation. Degrees of longitude and latitude indicated for horizontal and vertical axes, respectively.

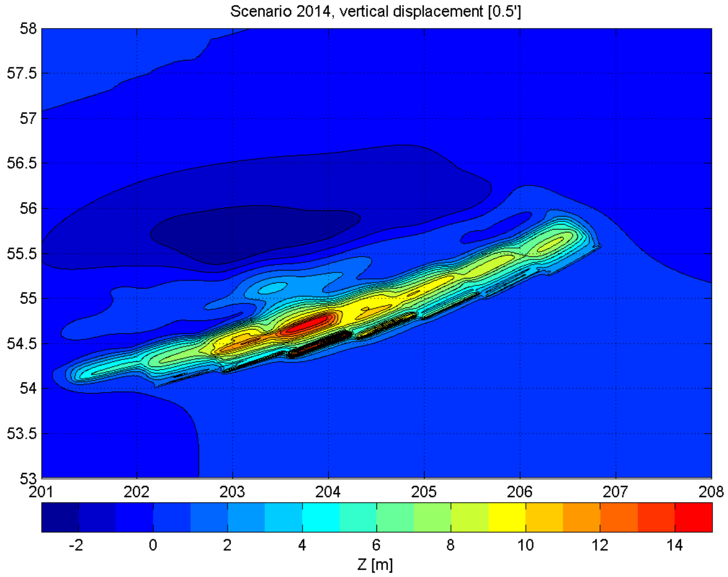

Figure 2. Map-view diagram showing vertical displacement (Z, in meters) in the 2014 tsunami scenario computed at WCATWC based on smoothed subfault dips and a splitting of each subfault into fifths (5 km x 50 km subfaults). Degrees of longitude and latitude indicated for horizontal and vertical axes, respectively.

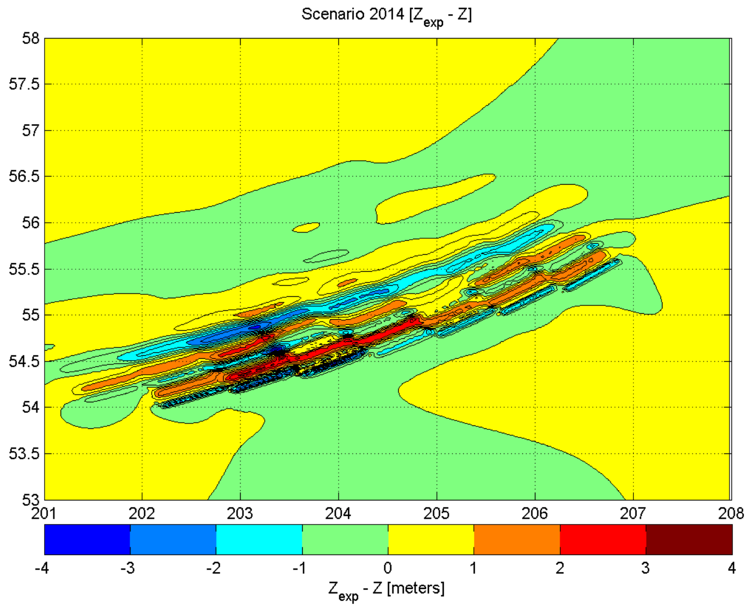

Figure 3. Map-view diagram showing difference in vertical displacement (Z, in meters) between the original 64 subfault source and the 320 subfault source with smoothly varying dip. Degrees of longitude and latitude indicated for horizontal and vertical axes, respectively.

Influence of Initial Sea Level Profile by Horizontal Slip over Sloping Seafloor

Another factor not normally considered in determining sea-floor uplift given earthquake fault parameters is the contribution of the horizontal component of slip over an inclined seafloor. Several studies have shown that this contribution can be significant where the seafloor is inclined. We examine the 2014 tsunami exercise source to determine if the horizontal component of slip is important when determining sea-floor uplift.

Figure 4 shows the sea-floor uplift using the 320 source zones of figure 2 and adding the vertical uplift induced by horizontal slip over inclined sea-floor surfaces. Note that the impact of including this type of motion is significant over the continental slope (which in this case happens to be where most of the horizontal motion occurs). The pixilation of this figure relates to the bathymetric data increment (5 feet, 1.52 m) on which the horizontal slip influence was computed. While this is fairly coarse, the overall level of uplift is significantly greater when including this component. Note the difference in scale between figure 4 and figure 2. Figure 5 shows the difference between figures 2 and 4; that is, the vertical motion induced by horizontal slip. In this case, the induced vertical motion exceeds 8 m in some areas and will likely be an important factor to take into account when numerically generating the tsunami.

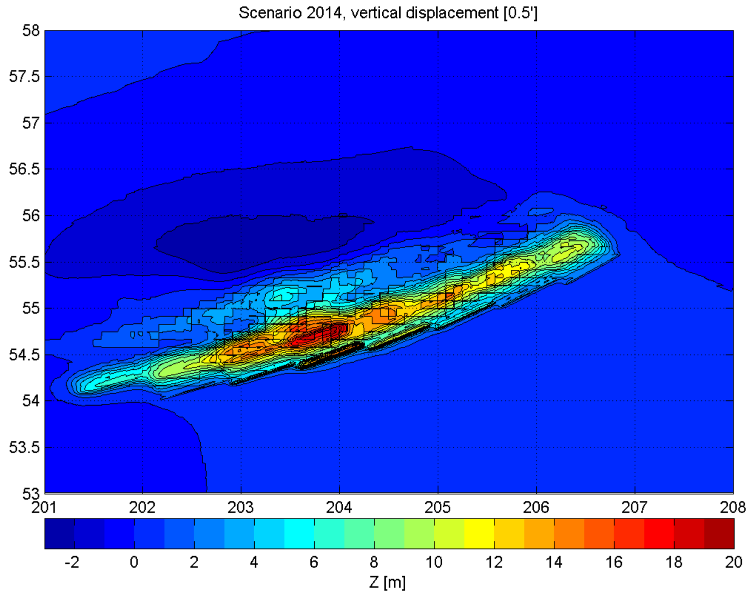

Figure 4. Map-view diagram showing total sea-floor vertical movement (Z, in meters) for the 2014 tsunami exercise computed using a smoothly varying dip on 320 source blocks and including vertical uplift induced by horizontal motion over sloping seafloor. Pixilation caused by grid increment used in the bathymetry data. Degrees of longitude and latitude indicated for horizontal and vertical axes, respectively.

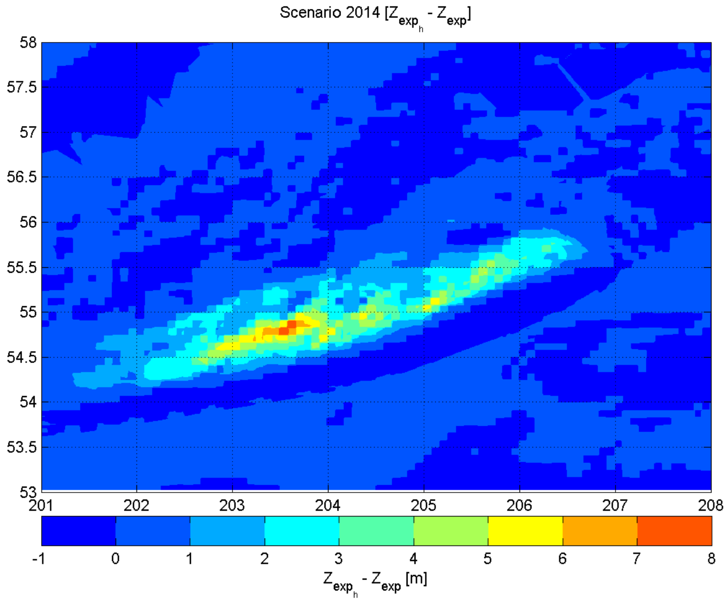

Figure 5. Map-view diagram showing vertical sea-floor motion (Z, in meters) induced by horizontal slip over sloping seafloor. Pixilation caused by grid increment used in the bathymetry data. Degrees of longitude and latitude indicated for horizontal and vertical axes, respectively.

2. Modeling Sea-Floor Deformation and Tsunami Generation using Dynamic Finite Element Analysis

By Kenny Ryan, David D. Oglesby, and Eric L. Geist

Abstract

Motivated by the 2011 *M*9 Tohoku earthquake and potential earthquakes on the Alaskan-Aleutian megathrust, we use computational simulations to investigate the effects of fault-rupture dynamics on slip, free surface deformation, and resulting tsunami formation from scenario *M*9.1 megathrust earthquakes. Unlike static dislocation models, dynamic models account for the force that the entire fault system exerts on each individual element of the model for each time step, so that earthquake rupture takes a path that is consistent with the physics of the model. To isolate the effects of different physical variables, we model four different dynamic rupture scenarios: a spatially homogenous prestress and frictional parameter scenario, two scenarios with rate-strengthening-like friction (for example, Dieterich, 1992), and one scenario with spatially heterogeneous prestress. Given geometric, material, and plate-coupling data along the Alaska-Aleutian megathrust assembled from the Science Application for Risk Reduction team (SAFRR) (Bruns and others, 1987; Johnson and Satake, 1994; Santini and others, 2003; Wells and others, 2003; Wells and others, 2011; Hayes and others, 2012), we are able to dynamically model rupture of an *M*9.1 earthquake. The homogeneous model shows an average fault slip of 18.6 m, with the same seismic moment as the source model used by the SAFRR team to investigate large-scale effects on western U.S. coastlines from a tsunami generated along the Alaskan-Aleutian subduction zone, and a maximum vertical free surface displacement of 5.77 m. However, adding a frictional strengthening zone to an along-strike region of the fault reduces average fault slip to 14.6 m and the maximum vertical free surface displacement to 5.74 m, while significantly reducing the maximum free surface displacement in the area updip from the strengthening zone. Adding a frictional strengthening zone to an updip region of the fault reduces average fault slip to 10.4 m and the maximum vertical free surface displacement to 2.86 m, while significantly reducing the maximum free surface displacement over the entire megathrust. A model with heterogeneous prestress results in a more heterogeneous slip distribution, relative to the homogeneous model; this slip distribution qualitatively matches the slip distribution of the source model used by the SAFRR team. The heterogeneous prestress model has the same average fault slip as the homogeneous model and a maximum vertical free surface displacement of 7.04 m. Corresponding tsunami models, which use a finite difference method to solve linear long-wave equations (Shuto, 1991; Satake, 2002), match temporally evolving seafloor deformation to the free surface deformation from the rupture simulations. Tsunami models show reduced peak amplitudes in the area above the frictional-strengthening zones, relative to the homogeneous case. A tsunami resulting from a heterogeneous fault prestress model results in peak amplitudes immediately above the hanging wall that are spatially more varied than in the homogeneous model, but the overall beaming pattern and maximum amplitudes along the local coasts are similar. All tsunami models also show the resultant gravity wave from the breakout of the earthquake rupture to the seafloor (Oglesby and others, 2000). Tsunamis generated along the Alaska-Aleutian megathrust offshore of the Alaska Peninsula could have large adverse effects on Pacific coasts (Ryan and others, 2012).

Introduction

Megathrust earthquakes in subduction zones are known generators of large, transoceanic tsunamis (for example, Kanamori, 1972). Ryan and others (2012) demonstrated that a tsunami resulting from a large megathrust earthquake on the Alaskan-Aleutian subduction zone (their figure 1) would propagate across the Pacific Ocean and strike the U.S west coast, potentially causing significant damage to ports and other populated areas. Because of its earthquake and tsunami hazards, the Alaskan-Aleutian subduction zone has been well studied seismically and geodetically (for example, Freymueller and others, 2008). Using Global Positioning System (GPS) measurements, Freymueller and Beavan (1999) show that the western Shumagin segment of the Alaskan-Aleutian subduction zone is creeping (figure 1 of Ryan and others, 2012). They further suggest that the entire downdip extent of this section of the megathrust may be unlocked and thus slipping at the local plate-convergence rate. Surface deformation along the Alaskan-Aleutian megathrust is a complex process that results from different mechanisms, including postseismic deformation, spatial variations in plate coupling, and movement of large crustal blocks (Freymueller and others, 2008). Additionally, Freymueller and others (2008) find that both the width of the seismogenic zone and the distribution of locked and creeping zones vary substantially along strike throughout the Alaskan-Aleutian subduction zone.

The distribution of locked and creeping sections along subduction zones is important for tsunami generation and coastline inundation. Kanamori (1972) notes that sediments in the trench could help produce a mechanism for some tsunami earthquakes—earthquakes that cause relatively small ground shaking but larger than expected tsunamis. Specifically, sediments could alter the frictional properties of the fault, making it a locally creeping (stable sliding) section, as well as producing slower rupture propagation during earthquakes. Hyndman and others (1997) point out that stable sliding regions can be caused by unconsolidated sediments in the updip section and by either high temperature or hydrated serpentinite at depth—and that global seismogenic zones typically lie at depths between 10 km and 40 km., For 525 earthquakes around the circum-Pacific, including earthquakes along the Alaskan-Aleutian subduction zone, Bilek and Lay (2002) show longer rupture durations for shallow (<15 km) thrust events than for deeper (>15 km) thrust events. Furthermore, they suggest that conditionally stable and fully stable sliding zones located on the most updip section of a thrust fault can slow rupture velocity and increase duration.

Dynamic rupture models of dip-slip faults are extremely helpful in understanding the free surface deformation that leads to tsunami generation. Specifically, using sea-floor deformation from rupture dynamics as time-dependent boundary conditions for tsunami generation may provide insight into tsunami formation and local propagation. Standard dislocation models use a static slip distribution to model the resulting tsunami (Okada, 1985), whereas for dynamic models the slip distribution is not known beforehand but is rather a calculated result of the model. Dynamic models can validate existing dislocation models by using realistic friction parameterizations and fault geometry to match the slip distribution of the dislocation model and to analyze the resulting tsunami in time. Although dynamic modeling cannot replace the utility of standard dislocation modeling, it can be a useful complement.

Numerical and experimental models show that dip-slip faults exhibit normal stress fluctuations from seismic-wave reflections off the free surface (Brune, 1996; Nielsen, 1998; Oglesby and others, 1998; Oglesby and Archuleta, 2000; Oglesby and others, 2000). For nonvertical dip-slip faults, the free surface allows seismic waves to reflect back and hit the fault again, altering the stress field on the fault near the free surface. Oglesby and others (1998) show that as rupture approaches the free surface along a thrust/reverse fault, there is an increase in normal stress ahead of the crack tip and a decrease in normal stress behind the crack tip; this effect leads to amplified fault motion near the surface (relative to a normal or strike-slip fault rupture). Furthermore, when rupture travels updip along a dip-slip fault and reaches the free surface, it produces a breakout phase (a slip pulse traveling back downdip) and a strong Rayleigh wave traveling along the surface (Burridge and Halliday, 1971; Oglesby and others, 1998), with reverse/thrust faults having stronger breakout phases than normal or strike-slip faults. The particle displacement is also greatly enhanced on the hanging wall relative to the footwall. In agreement with numerical models, Brune's (1996) laboratory foam-block thrust models also produce these effects. Enhanced slip near the trench is capable of generating larger amplitude tsunamis than equivalent slip at depth (Geist, 1999; Geist and Bilek, 2001; Geist, 2002).

In the first part of this work, we use the dynamic finite element code FaultMod (Barall*,* 2008) to show that simple slip-weakening friction (see, for example, Ida, 1972) can serve as a very accurate proxy for rate-strengthening friction as derived from the rate-state framework (Dieterich, 1978, 1979; Ruina, 1980, 1983; Linker and Dieterich, 1992). With this approach to friction thus validated, we then use the dynamic finite element code EQDyna (Duan and Oglesby, 2006) to model 3-D ruptures, using time-weakening friction (Andrews, 2004), along a megathrust approximating a portion of the Alaskan-Aleutian subduction zone. In order to model megathrust faults more realistically, it is important to simulate unstable and stable sliding zones (for example, outer boundaries of seismogenic zones); such models typically use a rate- and state-dependent (RS) friction parameterization (see, for example, Hyndman and others, 1997; Scholz, 1998) to capture the physics of slip under varying degrees of frictional stability. In particular, an increase in the steady-state friction coefficient with slip rate can characterize the stable sliding zones that border the seismogenic zones.

The general form of RS friction is (Dieterich, 1978, 1979; Ruina, 1980, 1983):

$$\tau = \left[\mu_o + a \ln\left(\frac{V}{V_o}\right) + b \ln\left(\frac{\theta}{\theta_o}\right) \right] \sigma^{eff} \tag{1}$$

where μ_0 represents a constant reference value for the coefficient of friction; a and b are constitutive parameters estimated from laboratory experiments; V_0 and θ_0 are reference values for slip rate and the state of the sliding surface, respectively, such that when $V = V_0$ and $\theta = \theta_0$ the friction coefficient is μ_0; θ abstractly represents the average age of contacts at some sliding velocity; and σ^{eff} is the effective normal stress. Within the RS formulation, a positive rate-strengthening parameter (*a*–*b*), where a and b are experimentally determined (Dieterich, 1978, 1979) through observed stress drop, indicates velocity strengthening or stable slip, and a negative parameter indicates velocity weakening or the potential for unstable slip. For reverse/thrust faults it has been suggested that such rate-strengthening zones can simulate weak zones in the inner margin of the trenches, possibly characterized by large amounts of sediment. Sliding experiments on ultrafine-grained quartz (Chester and Higgs, 1992) suggest that rate-weakening behavior occurs between 100 and 300 °C under wet conditions, while higher temperatures lead to a rate-strengthening parameter (*a*–*b*) of 0.03. Experiments on granite (Blanpied and others, 1998) found rate-weakening at lower slip speeds (for example, 1 μm/s) with a rate-strengthening parameter of approximately 0.004 and rate-strengthening at higher slip speeds (for example, 1,000 μm/s) with a rate-strengthening parameter of approximately 0.01.

Real faults likely have heterogeneous stress regimes in addition to distributed frictionally stable and unstable sliding zones; these features can lead to complex stress interactions during rupture. In order to reproduce accurate slip distributions from real earthquakes, dynamic modeling studies incorporate heterogeneous prestress distributions (for example, Olsen and others, 1997; Peyrat and others, 2001; Guatteri and others, 2003; Olsen and others, 2009). However, the resulting total slip distributions typically are much smoother than prestress distributions, as a result of stress interactions from large portions of the fault slipping simultaneously. Beroza and Mikumo (1996) suggest that slip duration for a point on a fault can decrease in cases of high prestress heterogeneity through a self-healing mechanism.

Thus, modeling earthquakes with heterogeneous prestress should result in both heterogeneous rupture propagation (that is, highly variable rupture speed) and heterogeneous slip distributions.

Tsunami generation and propagation are influenced by the slip distribution, geometry, and material properties along the tsunami-generating fault (Geist, 1999; Geist and Dmowska, 1999; Geist and Bilek, 2001; Geist, 2002). These studies indicate that slip distribution near the trench most significantly affects tsunami generation, amplitude, and local runup, versus slip distribution further downdip. Geist and Dmowska (1999) show that dip-directed slip variations affect the maximum amplitude and steepness of the local tsunami, whereas along-strike slip variations result in strike-parallel amplitude changes in the tsunami that are conserved during local propagation, altering the beaming pattern of the tsunami. Geist and Bilek (2001) point out that estimates of initial tsunami size depend on estimates of shear modulus variation with depth. They analyzed 360 circum-Pacific subduction zone earthquakes and found that in order to match observed source time functions, both a relative reduction in shear modulus and an increase in slip near the trench are needed.

Additionally, megathrust earthquakes can incorporate complex slip distributions on multiple fault segments. Thrust events involving rupture of a splay fault can greatly affect the distribution of sea-floor deformation and the resultant tsunami (Cummins and Kaneda, 2000). DeDontney and Rice (2012) suggest that the 2004 Indian Ocean tsunami may have resulted from two major areas of uplift, the main thrust and a splay fault, and further note that splay faults with steeper dip angles require less slip to produce the same vertical sea-floor deformation as the main thrust fault. Whether or not a rupture can propagate onto a splay fault can depend on the dynamics of the earthquake (Wendt and others, 2009). Wendt and others (2009) dynamically modeled the time-dependent earthquake and tsunami generation process on a large thrust fault with a connected, steeper splay fault. They show that if a barrier is introduced on the main thrust fault, rupture can propagate onto the smaller splay fault and produce larger vertical sea-floor deformation and correspondingly larger (local) maximum tsunami wave heights.

Method Part 1

In this study we simulate zones of weak fault coupling for an updip portion and for an along-strike portion of the Alaska-Aleutian megathrust (fig. 7). Although the primary finite element method (FEM) code EQDyna (Duan and Oglesby, 2006) used in this study can model 3-D, shallow dipping, megathrust ruptures, it does not incorporate rate-state friction. Thus, in order to approximate rate-strengthening frictional properties from rate-state friction using a simple slip-weakening-type friction formulation (for example, time-weakening friction, Andrews, 2004), we test three different friction laws using a secondary 2-D FEM code FaultMod (Barall, 2008) that does incorporate rate-state friction in the form of linear slip-weakening (SW) friction and two forms of rate- and state-dependent friction: ageing law (RS-AL), and slip law (RS-SL). We use results from the secondary code FaultMod to model mode II (slip parallel to rupture propagation) dynamic rupture, with a frictional interface, along a planar fault in a whole space (fig. 6, top). Generally, finite element codes divide a given continuum of mass (for example, the Earth's crust) into a number of elements that can then be used to run computations on applied forces, assuming elasticity and a frictional parameterization. FaultMod has been validated in Southern California Earthquake Center/U.S. Geological Survey (SCEC/USGS) rupture benchmark problems (Barall, 2009; Harris and others, 2009, 2011). The code incorporates artificial viscous damping (Dalguer and Day, 2007), as well as algorithmic damping to help damp spurious oscillations and energy-absorbing boundary conditions along the mesh edges to avoid artificial reflections from the model boundaries.

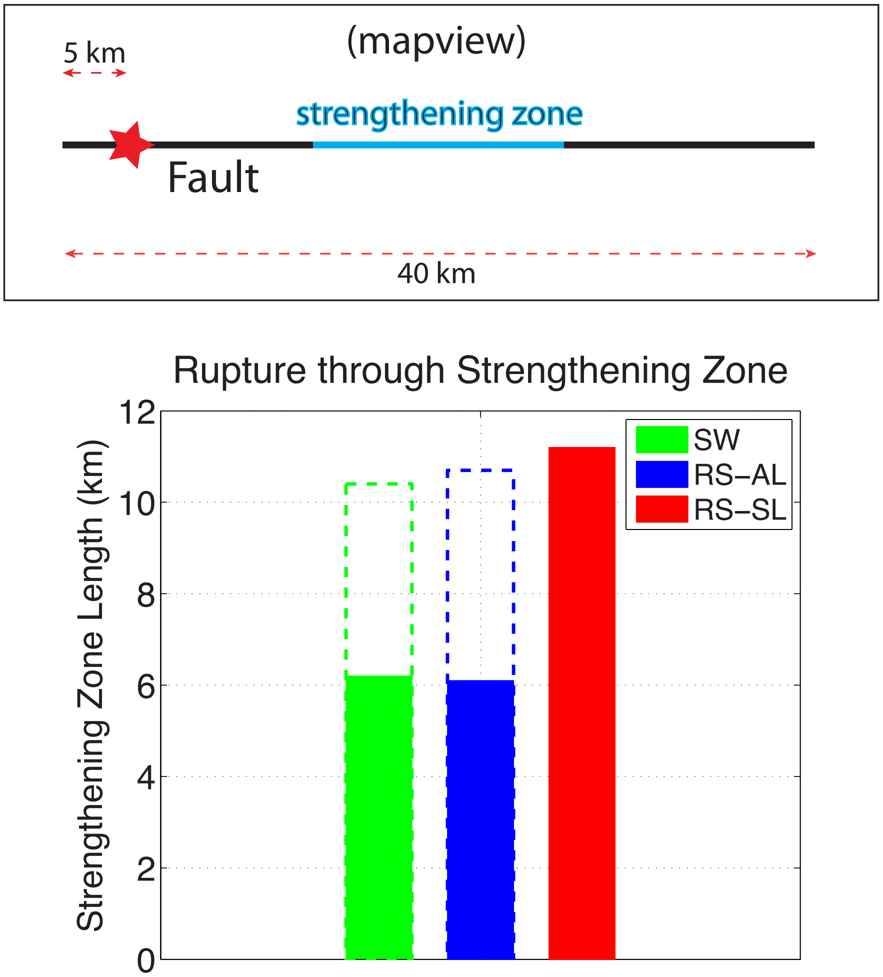

Figure 6. Rupture tunneling through a strengthening zone. Top: Map view of a frictional-strengthening zone modeled in the middle of a homogeneous, planar, 2-D fault in a whole space using slip-weakening (SW), rate-state ageing law (RS-AL), and rate-state slip law (RS-SL) friction parameterizations in finite element code FaultMod. The red star denotes the nucleation zone (1.5 km radius). We increase the size of the strengthening zone, for each friction formulation, until rupture cannot tunnel through the entire strengthening zone. Bottom: Bar graph showing that SW (green) and RS-AL (blue) models tunnel through similar maximum-sized strengthening zones with equivalent slip-weakening distances (solid bars), while SW (green), RS-AL (blue), and RS-SL (red) models tunnel through similar maximum-sized strengthening zones with equivalent fracture energy (dashed bars). For our models, the condition for strengthening using slip-weakening friction is equation 8.

The criterion for linear slip-weakening friction is as follows (Ida, 1972):

$$\mu = \begin{cases} \dfrac{\mu_d - \mu_s}{d_o} d\delta + \mu_s \,, & d\delta < d_o \\ \mu_d \,, & d\delta \geq d_o \end{cases} \tag{2}$$

where the friction coefficient μ drops from a static value to a dynamic value over a slip-weakening distance d_o.

Following Barall (2009), we use a modified form of the bracketed term in equation 1 that does not become singular for very small slip velocities:

$$\mu = \arcsin h\left[\frac{V}{2V_o}\exp\left(\frac{\mu_o+\psi}{a}\right)\right] \approx \mu_o + a\ln\left(\frac{V}{V_o}\right)+\psi \tag{3}$$

This form of the RS law closely approximates equation 1 for slip velocities of seismological interest. Note that the right hand side of equation 3 has the form of the effective friction coefficient in equation 1 with $\psi = b\ln(\theta/\theta_0)$, or conversely, $\theta = \theta_0\exp(\psi/b)$. Conceptually, ψ represents the strength of contacts. For the RS-AL, the state variable evolves according to the equation:

$$\frac{d\theta}{dt} = \frac{-1}{\theta_{ss}}\left(\theta - \theta_{ss}\right) \tag{4}$$

In the RS-SL, the state variable evolves according to the equation:

$$\frac{d\psi}{dt} = \frac{-V}{L}\left(\psi - \psi_{ss}\right) \tag{5}$$

Both the RS-AL (equation 4) and the RS-SL (equation 5) reduce to the standard formula for steady-state sliding:

$$\psi_{ss} = -b\ln\left(\frac{V}{V_o}\right) \tag{6}$$

Rupture is constrained to take place on a 40-km fault (fig. 6, top). We add a frictional-strengthening zone to the center of the fault. For the rate-state simulations this is a rate-strengthening zone governed by the steady state equation:

$$\frac{d\mu_{ss}}{d\ln V} = a - b \tag{7}$$

such that when constitutive parameter b is larger than constitutive parameter a, the steady state friction value decreases as velocity increases, and thus this represents a velocity-weakening zone. However, when constitutive parameter b is smaller than constitutive parameter a, the steady state friction value increases with increasing velocity, and this represents a velocity-strengthening zone. Dieterich (1978, 1979) experimentally determined a and b values to be on the order of 0.01; we use values of 0.008 and 0.012 for parameters a and b, respectively, to simulate rate-weakening. We use values of 0.016 and 0.012 for parameters a and b, respectively, to represent a region of rate-strengthening. The length of strengthening zone is variable and allows us to determine the maximum length of strengthening zone that rupture can tunnel through for each of the three friction laws. We find that the friction coefficients in linear slip-weakening (SW) friction can be tuned to match the rate-state models, so that each friction law tunnels through a similar-sized strengthening zone. Specifically, by analyzing stress-versus-slip weakening curves for the rate-state models within the rate-strengthening zones and within the rate-weakening zones (black segments in figure 6), we tune μs and μd so that the three friction laws have similar weakening curves. For equivalent slip-weakening distances, both SW friction and RS-AL models can tunnel through similar-sized strengthening zone lengths (fig. 6, bottom) and result in similar slip distributions. We note that the relatively nonlinear RS-SL tunnels though larger strengthening zones but that, with equivalent fracture energy (Andrews, 1976; Guatteri and Spudich, 2000), all three models tunnel through similar-sized zones and result in similar slip distributions. The general equation required by SW friction to match RS formulations in the strengthening zone is:

$$\tau_o < \mu_d \sigma_o \tag{8}$$

where τ_0 is the initial shear stress, μ_d is the dynamic friction coefficient, and σ_0 is the initial normal stress. Thus, we have found a useful approximation for rate-strengthening friction using a simpler slip-weakening formulation. Note that this not the same as slip-hardening, which requires the dynamic friction coefficient to be larger than the static friction coefficient. In this study, we simulate rate-strengthening behavior by altering μ_d within the strengthening zones. Under our configuration, shear stress will ultimately increase with slip, assuming no normal stress change. However, dip-slip faults involve dynamic normal stress fluctuations, including reductions that could result in a shear stress drop even in the presence of rate-strengthening.

Method Part 2

In this study we use the 3-D finite element method (FEM) code EQDyna (Duan and Oglesby, 2006) to model mode II dynamic rupture, with a frictional interface along a megathrust intersecting the free surface (fig. 7, top), and the corresponding free surface deformation. Rupture is constrained to take place only on the fault. The megathrust is 358 km along strike, 205.1 km downdip, and 35.6 km in depth, with a constant dip angle of 10° (as determined by the Earthquake Source working group in the SAFRR scenario). EQDyna also has been validated in SCEC/USGS rupture benchmark problems (Harris and others, 2009, 2011). The code incorporates artificial damping (Duan and Day, 2008) to help reduce spurious oscillations. Additionally, we implement a large enough buffer around the fault so that a P-wave cannot travel to the edge of the model and back to the fault within the model duration, 200 seconds. We consider fault ruptures with model and material properties given in tables 1 and 2.

We note that the nucleation zone (shown as a red star in figure 8) used in all models in this study has a radius of 16 km (as indicated by table 1). The nucleation zone is small relative to the size of the modeled megathrust and does not significantly affect the overall slip distribution in our models; for example, there are no obvious asymmetric slip patterns (for example, large amount of slip) near or around the nucleation zone in figure 11. Additionally, we implement a finite element size of approximately 2 km along the modeled fault. Decreasing the element size for our full model is not possible because of computational limitations. However, we have tested smaller fault models (34 km along strike and 20 km downdip)—with the same homogeneous input parameters used in this study—to determine whether our results are grid dependent. We found similar slip distributions, slip rates, and rupture velocities for these smaller earthquake models using 0.5-km, 1-km, 1.5-km, and 2-km element sizes. We therefore believe that a 2-km element size is reasonable and appropriate in this study of a much larger modeled fault, although we cannot directly test this.

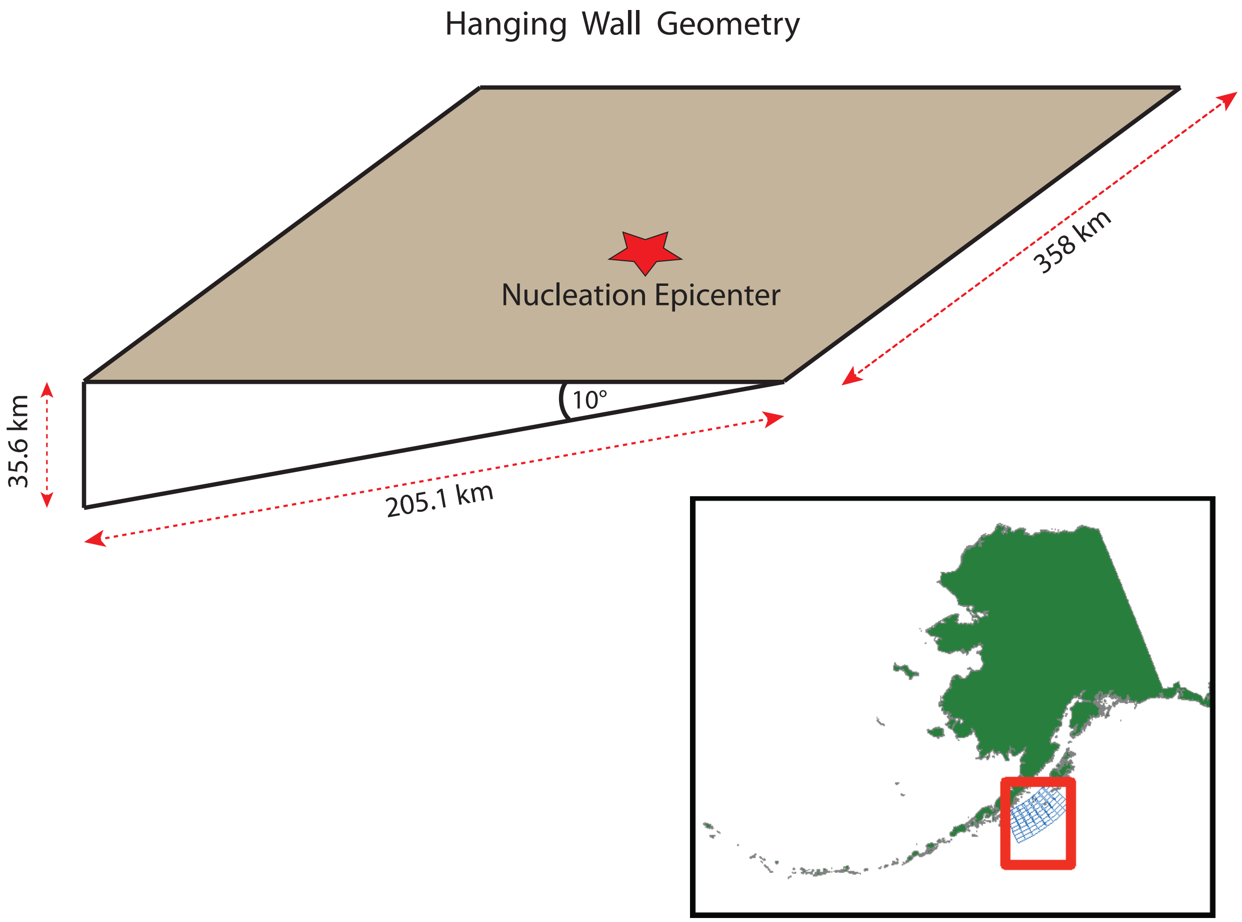

Figure 7. Model approximation to a section of the Alaska-Aleutian megathrust. Top: Cartoon block diagram of fault geometry of the hanging wall using 3-D finite element code EQDyna (Duan and Oglesby, 2006). We use a planar fault geometry with a constant dip of 10o, an along-strike distance of 358 km, a depth of 35.6 km, and a downdip distance of 205.1 km. The fault intersects the free surface. Each element along the fault surface is approximately 2 km along strike and 2 km downdip. Additionally, we implement a buffer zone around the fault to ensure waves do not reflect off the model boundary and return to the fault. Bottom: Map showing geographic region of interest with the section of the Alaska-Aleutian megathrust we are approximating (image from Earthquake Source working group in the SAFRR scenario)

Table 1. Model and material properties for all simulations in this study.

[km, kilometer; m, meter; GPa, gigapascal; s, second]

Density	2670 kg/m^3
Shear Modulus	40.00 GPa
Bulk Modulus	66.67 GPa
S-wave speed	3.871 km/s
P-wave speed	6.704 km/s
Fault Area	73,426 km^2
Nucleation Depth	15.50 km
Nucleation Radius	16.00 km
Nucleation Speed	2.000 km/s
Nucleation Location (along strike)	22.38 km
Nucleation Location (downdip)	-89.26 km
Element Size (along fault)	≈2 km
Time Step	0.01 s
Distance Along-Strike	358.0 km
Distance Downdip	205.1 km
Dip Angle	10°
t_o	2.600 s
Hydrodynamic Grid Size	2 km
Hydrodynamic Time Step	0.1 s

Table 2. Initial shear stress τ_0, initial normal stress σ_0, the static friction coefficient μ_s, the dynamic friction coefficient μ_d, and the strengthening friction coefficient μ_d (strength) (if applicable) for all four models in this study.

[MPA, megapascals]

	τ_0 [MPa]	σ_0 [MPa]	μ_s	μ_d	μ_d (strength)
Homogeneous Prestress/Friction	3.172	11.06	0.5630	0.1333	
West Frictional-strengthening	3.172	11.06	0.5630	0.1333	0.3218
Updip Frictional-strengthening	3.172	11.06	0.5630	0.1333	0.3218
Heterogeneous Prestress	0 – 24.26	1.090 – 84.60	0.5630	0.1333	

For simplicity we use a homogeneous material structure with average midcrustal material properties (see, for example, Harris and others, 2009), although future models may incorporate 3-D material structure heterogeneity. We use a time-weakening friction law (Andrews, 2004; Duan and Day, 2008), in which the stress at a point drops from its static to sliding frictional level over a characteristic time. This friction law produces behavior similar to that of slip-weakening friction, with an effective slip-weakening distance d_0 that is proportional to the square root of rupture velocity multiplied by the distance rupture has propagated:

$$d_o \propto \frac{\Delta\tau}{G}\sqrt{\frac{V_{rupt}t_oL}{k}} \qquad (9)$$

where $\Delta\tau$ is the stress drop, G is the shear modulus, V_{rupt} is the rupture velocity, t_o is the time over which the friction coefficient drops from its static value to its dynamic value, L is the distance rupture has propagated, and the value of *k* depends on the shape of the stress-slip weakening curve. As recommended by Andrews (2004), we use a time-weakening value t_o that is the amount of time it would take for an S-wave to traverse more than three elements (we use five elements) along the fault interface. This parameterization allows us to achieve accuracy and smoothness of the breakdown zone as the rupture front increases in speed and amplitude away from the nucleation zone. As noted above, the computer code EQDyna does not incorporate rate- and state-dependent friction, so we use time-weakening friction with equation 8 as a proxy for rate-strengthening-like zones.

In this study we use four different rupture models: a spatially constant prestress and frictional coefficient model (hereinafter referred to as the homogeneous model), two models with frictional-strengthening zones, and a spatially heterogeneous prestress model. For frictional-strengthening zone models, we use equation 8 with time-weakening friction to simulate rate-strengthening-like zones on updip and along-strike portions of the megathrust (fig. 8; see table 2 for friction coefficients). Specifically, we implement frictional-strengthening zones in either the westernmost portion of the fault (100 km to 179 km along strike) or the most updip portion of the fault (0 km to −50 km downdip). As an example of how time-weakening in these models corresponds to either rate-weakening or rate-strengthening, figure 9 shows stress-slip weakening curves for a point in a frictional-weakening zone and a point in a frictional-strengthening zone for the western frictional-strengthening zone model (locations marked in figure 13). There is a clear stress drop from the initial stress in the weakening zone and a stress increase in the strengthening zone. However, we note that a stress increase is not required for all points in our frictional-strengthening zone, because large dynamic reductions in normal stress can still result in a shear stress drop during sliding. For the heterogeneous prestress model, we divide the fault into 64 subfault sections, each section with a different prestress. The objective of this model is to qualitatively match the slip distribution used by the Earthquake Source working group within the SAFRR Tsunami Scenario team (Kirby and others, 2013). Previous studies show that scaling the prestress distribution in dynamic earthquake models is one way to match observed slip distributions (for example, Olsen and others, 1997; Olsen and others, 2009).

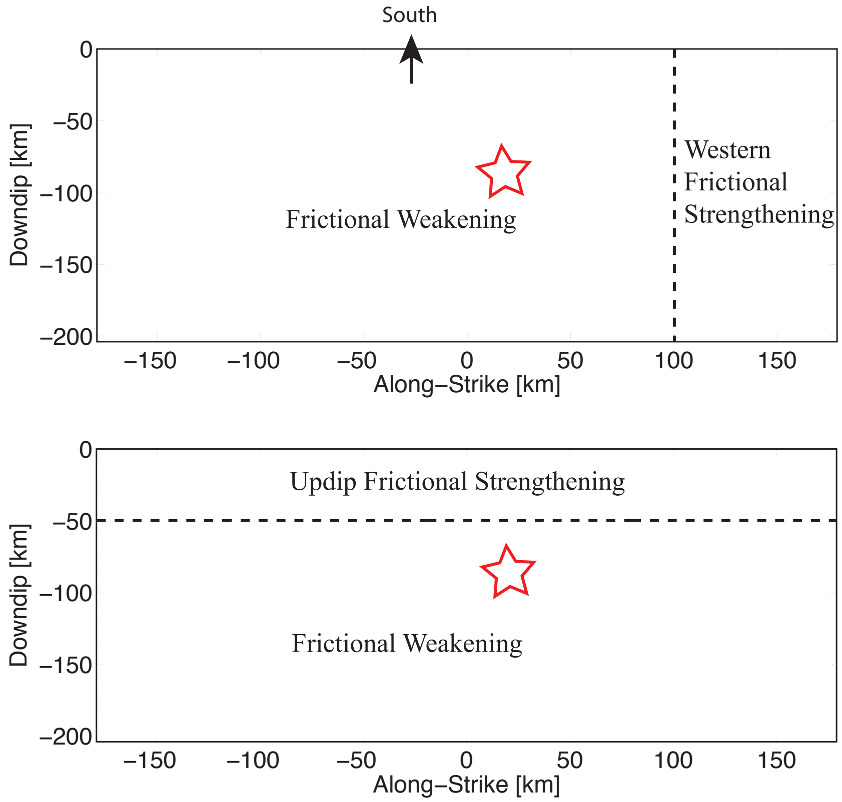

Figure 8. Cross-sectional diagrams illustrating two models with frictional-strengthening zones in (top) the westernmost portion and (bottom) the most up-dip portion of the fault. Note that the point of view is from above the hanging wall, perpendicular to the fault surface. Stars indicate the nucleation zone, which is at the same location for all models. The strengthening areas are 16,203 km2 and 17,900 km2 for the top and bottom models, respectively. See table 2 for frictional coefficients.

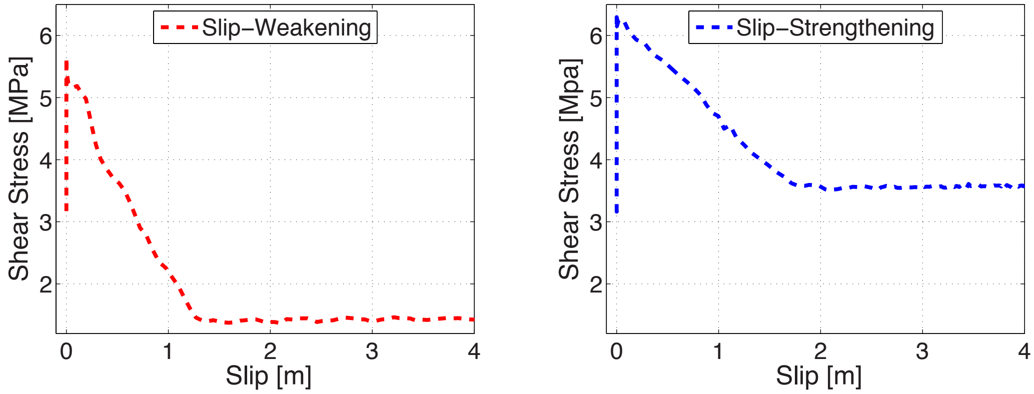

Figure 9. Graphs of shear stress versus slip for a point in the weakening zone (red, left) and a point in the strengthening zone (blue, right), using time-weakening friction to model a 3-D megathrust earthquake within the Alaskan-Aleutian subduction zone. Point locations are marked by red and blue stars in figure 13 (3rd panel down). Results show a decrease in shear stress within the frictional-weakening zone, and an increase in shear stress in the frictional-strengthening zone. Note that shear stress depends on both friction coefficient and normal stress during sliding.

A dynamic finite element code does not just produce a rupture pattern on a fault; it also produces the full wave field and surface deformation. After dynamically modeling earthquake rupture, we feed the resulting time-dependent free surface (that is, seafloor) displacements into a hydrodynamic code using a 2-D finite difference method to solve linear long wave equations (Shuto, 1991; Satake, 2002). In this way, we can model the generation of a tsunami from our dynamic earthquake models. Specifically, time dependent 3-D sea-floor deformation from our earthquake models are used as a time-dependent boundary condition for our hydrodynamic models, assuming that the water surface is displaced by the combined effects from vertical and horizontal sea-floor displacement (Tanioka and Satake, 1996). The leap-frog, finite-difference method of computing of tsunami propagation, described by Satake (2007), is used with the ETOPO1 digital elevation model (http://www.ngdc.noaa.gov/mgg/global/global.html). Incorporation of both dynamic codes allows us to simulate tsunami formation and local propagation in time. Hydrodynamic model parameters are given in table 1.

Results

In this study we focus on rupture dynamics, fault slip distribution, free surface deformation, and the resulting tsunami for four different models: a homogeneous set of prestress and frictional conditions, a western frictional-strengthening zone, an updip frictional-strengthening zone, and a heterogeneous prestress condition (figs. 8 through 22). Both the homogeneous and heterogeneous prestress models match the seismic moment of the dislocation model determined by the Earthquake Source working group within the SAFRR Tsunami Scenario team. For each model, differences in the rupture dynamics ultimately result in different tsunami formations, local maximum water wave amplitudes, and tsunami beaming patterns. We note two key parameters for each model: the maximum vertical free surface displacement $Z_{\max}$ and the average fault slip $\langle S \rangle$ (table 3), which affect maximum tsunami height and the initial tsunami height distribution.

Table 3. Maximum vertical free-surface displacements $Z_{\max}$ and average fault slip $\langle S \rangle$ for all four models in this study.

Model	$Z_{\max}$ [m]	$\langle S \rangle$ [m]
Homogeneous Prestress/Friction	5.77	18.6
West Frictional-strengthening	5.74	14.6
Updip Frictional-strengthening	2.86	10.4
Heterogeneous Prestress	7.04	18.6

Homogeneous Stress and Friction

Figure 10 shows slip-rate snapshots of the homogeneous earthquake rupture at 27 s, 52 s, and 70 s into the simulation. The fault experiences large slip rate pulses near the free surface due to dynamic unclamping of the fault and geometric asymmetry of the hanging wall/footwall (Brune, 1996; Nielsen, 1998; Oglesby and others, 1998; Oglesby and Archuleta, 2000; Oglesby and others, 2000), resulting in a strong breakout phase and the generation of an oceanic Rayleigh wave. Rupture proceeds over the entire fault zone. Fault slip and total vertical free surface deformation for the homogeneous model are shown in figure 11. The largest amount of slip is near the surface, corresponding to large vertical displacement on the surface near the fault trace. Average fault slip is 18.6 m, and maximum vertical surface displacement is 5.77 m. Figure 12 displays local peak tsunami amplitude, resulting from the homogeneous earthquake rupture model, in the geographic region of interest. Water height corresponds well with free surface deformation, and the largest tsunami amplitudes are located closest to the trench. In the model, the Shumagin Islands, Alaska Peninsula, and Kodiak Island are hit with particularly large wave heights from the local tsunami. The tsunami amplitude has a strong southward beaming effect, indicating potential damage to coastlines in Hawaii and the western United States as well as other coastlines around the Pacific rim in the simulation.

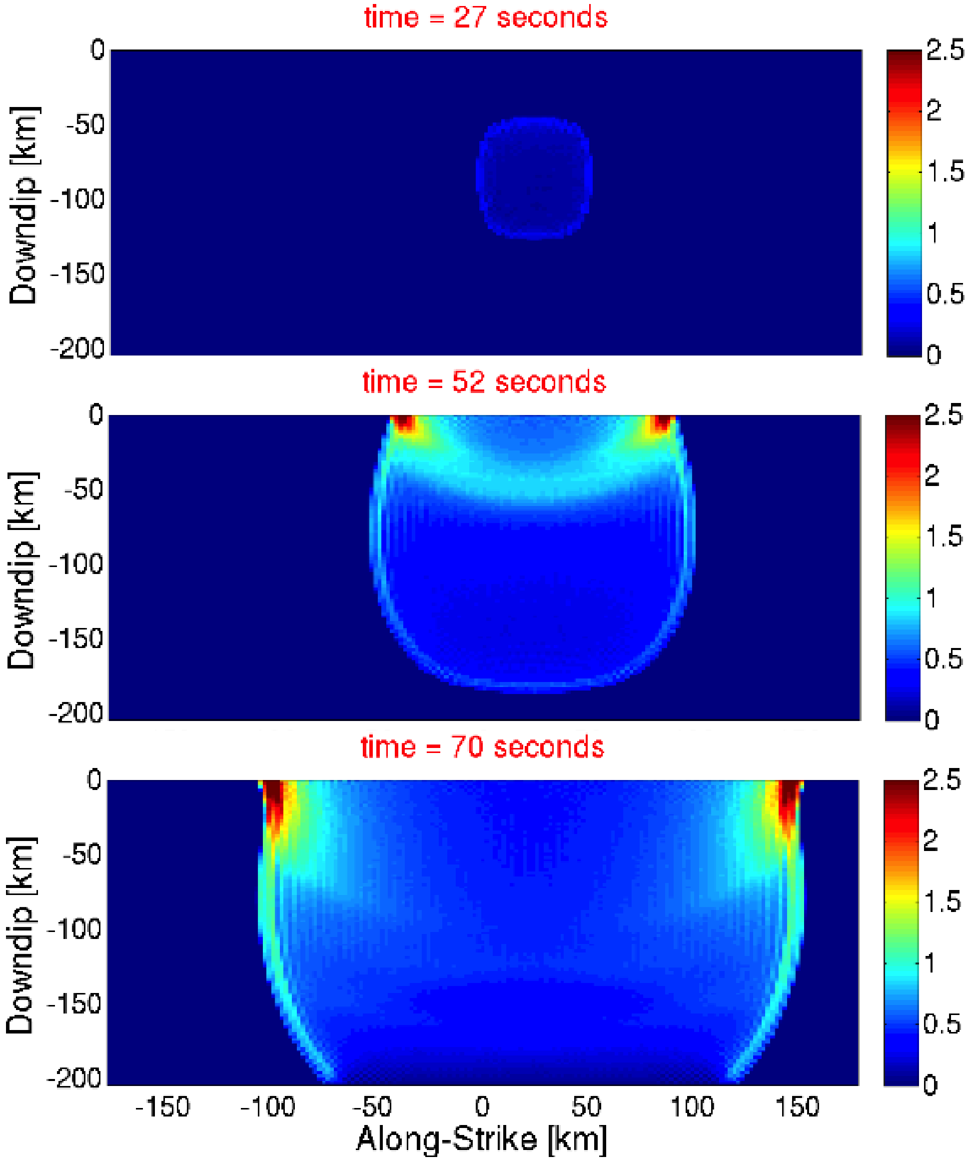

Figure 10. Diagrammatic views of the fault surface showing snapshots of rupture propagation at 27, 512, and 70 s for a homogeneous model (spatially constant prestress, dip angle, and frictional coefficients). Colors represent slip rate in m/s. Rupture shows large slip rate pulses nearest the free surface. Rupture proceeds over the entire fault zone (entire region shown), beginning at the nucleation zone (indicated in figure 8).

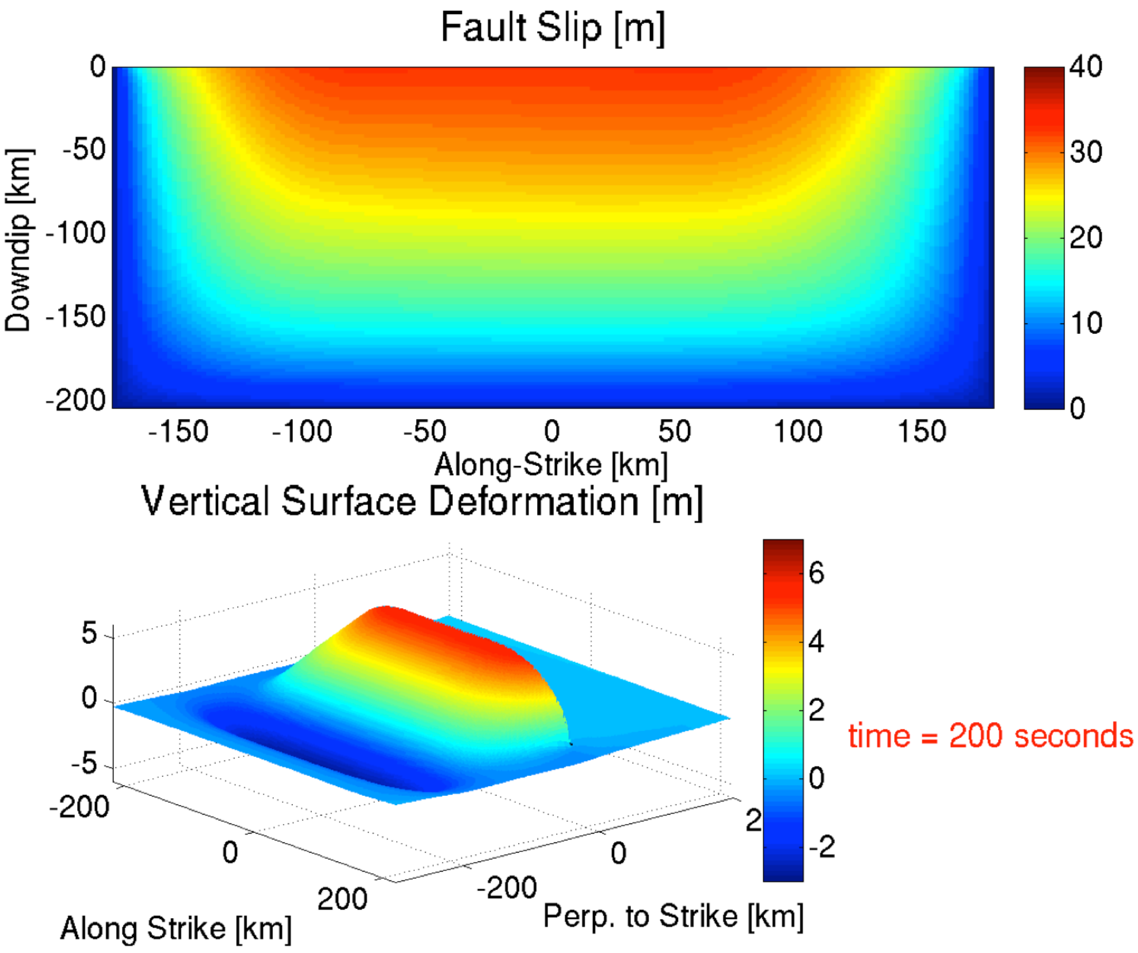

time = 200 seconds

Figure 11. Diagrams showing fault slip (top) and total vertical free surface deformation (bottom) for the homogeneous model. The largest amount of slip is near the surface, corresponding to large vertical displacement on the surface near the fault trace. Average fault slip is 18.6 m, and maximum vertical surface displacement is 5.77 m.

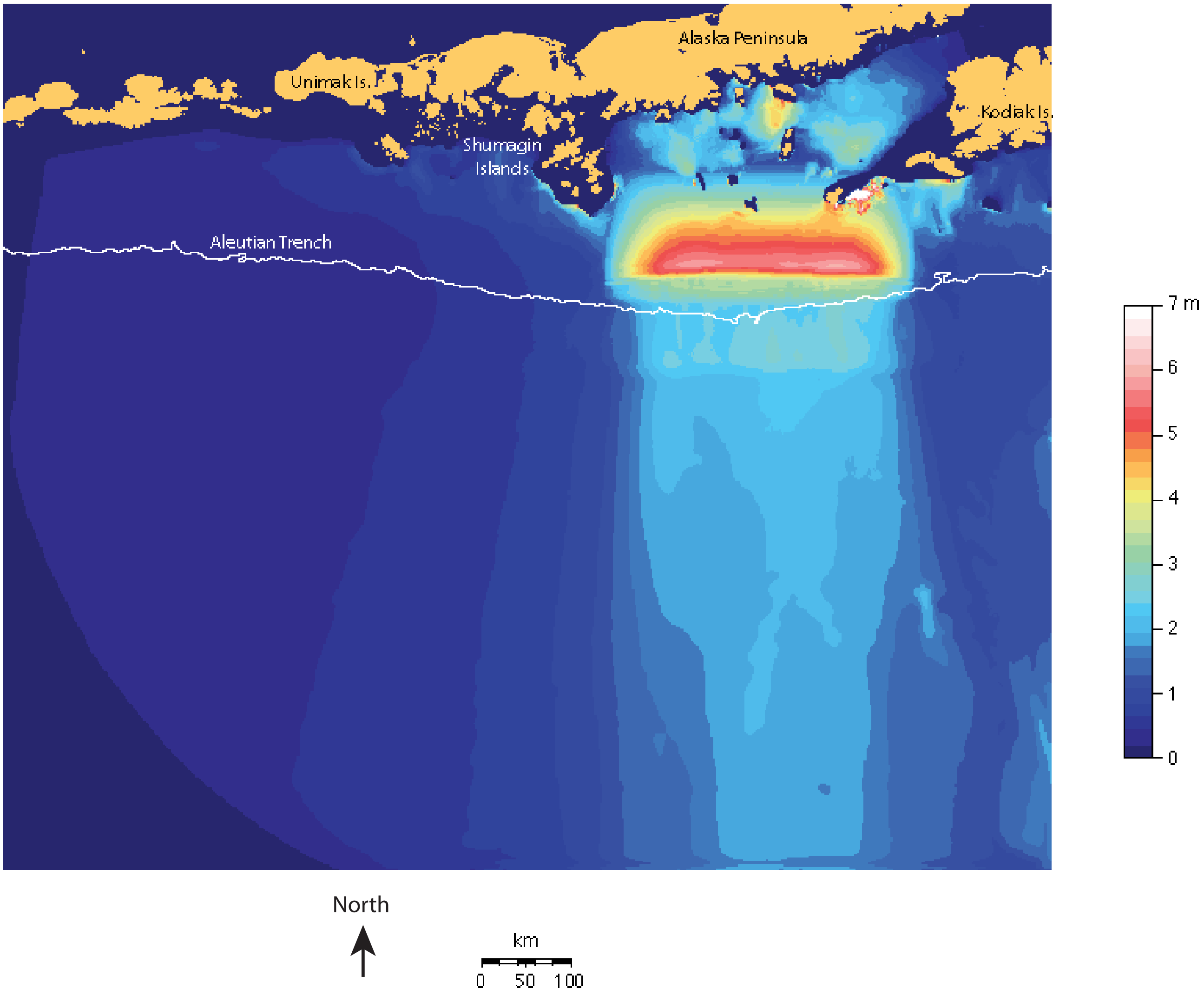

Figure 12. Map showing peak tsunami amplitudes (color scale in m) resulting from the homogeneous earthquake rupture model in the geographic region of interest. The white line represents the Aleutian Trench. Water height corresponds well with free surface deformation (fig. 11, bottom). The Shumagin Islands, Alaska Peninsula, and Kodiak Island are struck with particularly large water height from the local tsunami. Additionally, the tsunami amplitude has a strong southward beaming effect.

Western Frictional-Strengthening Zone Rupture

The homogeneous model discussed above assumes homogeneous frictional conditions along the entire extent of the fault. Realistically, however, faults are likely heterogeneous in frictional properties as well as in their initial stress conditions. GPS data show an unlocked section of the fault bordering our study area to the west (Freymueller and Beavan, 1999; Freymueller and others, 2008). In an effort to incorporate a more realistic frictional regime, we implement a frictional-strengthening zone in the westernmost 79 km of the megathrust (fig. 8, top). Figure 13 shows slip-rate snapshots of rupture propagation for a model with such a western frictional-strengthening zone. This model shows large slip rate pulses nearest the free surface as in the homogeneous model; however, the strengthening zone diminishes the slip rate pulse significantly relative to the homogeneous model. Note the difference in slip rates in the two models at 70 seconds. Rupture proceeds over the entire fault, including through the strengthening zone. The largest slip in the strengthening zone occurs near the free surface, most likely because of dynamic unclamping and the geometric asymmetry near the free surface. We note that the extent that rupture can penetrate a frictional-strengthening zone depends on fault geometry, friction coefficients, initial stress regimes, and location of the nucleation zone. While a strengthening zone in principle releases no seismic energy, slip can still occur, and is driven by seismic energy released on other (weakening) parts of the fault. Figure 14 illustrates fault slip and total vertical free surface deformation for the western frictional-strengthening zone model. Average fault slip is decreased by 4 m (18.6 to 14.6 m), relative to the homogeneous model. Surface deformation is substantially decreased in the region above the strengthening zone, relative to the homogeneous model; however, the maximum vertical surface displacement is decreased only marginally (from 5.77 to 5.74 m). The local peak modeled tsunami amplitudes resulting from the western frictional-strengthening zone model are shown in figure 15. Water height corresponds well with vertical free surface deformation, with the largest tsunami amplitude distributed above the frictional-weakening zone. Converting a western portion of the fault to a frictional-strengthening zone greatly reduces tsunami amplitude locally north of the strengthening zone in the Shumagin Islands region of the heterogeneous model, and it redirects the beaming pattern of the basin-propagating (far-field) tsunami slightly in a counterclockwise direction, but with similar maximum amplitude, relative to the homogeneous model.

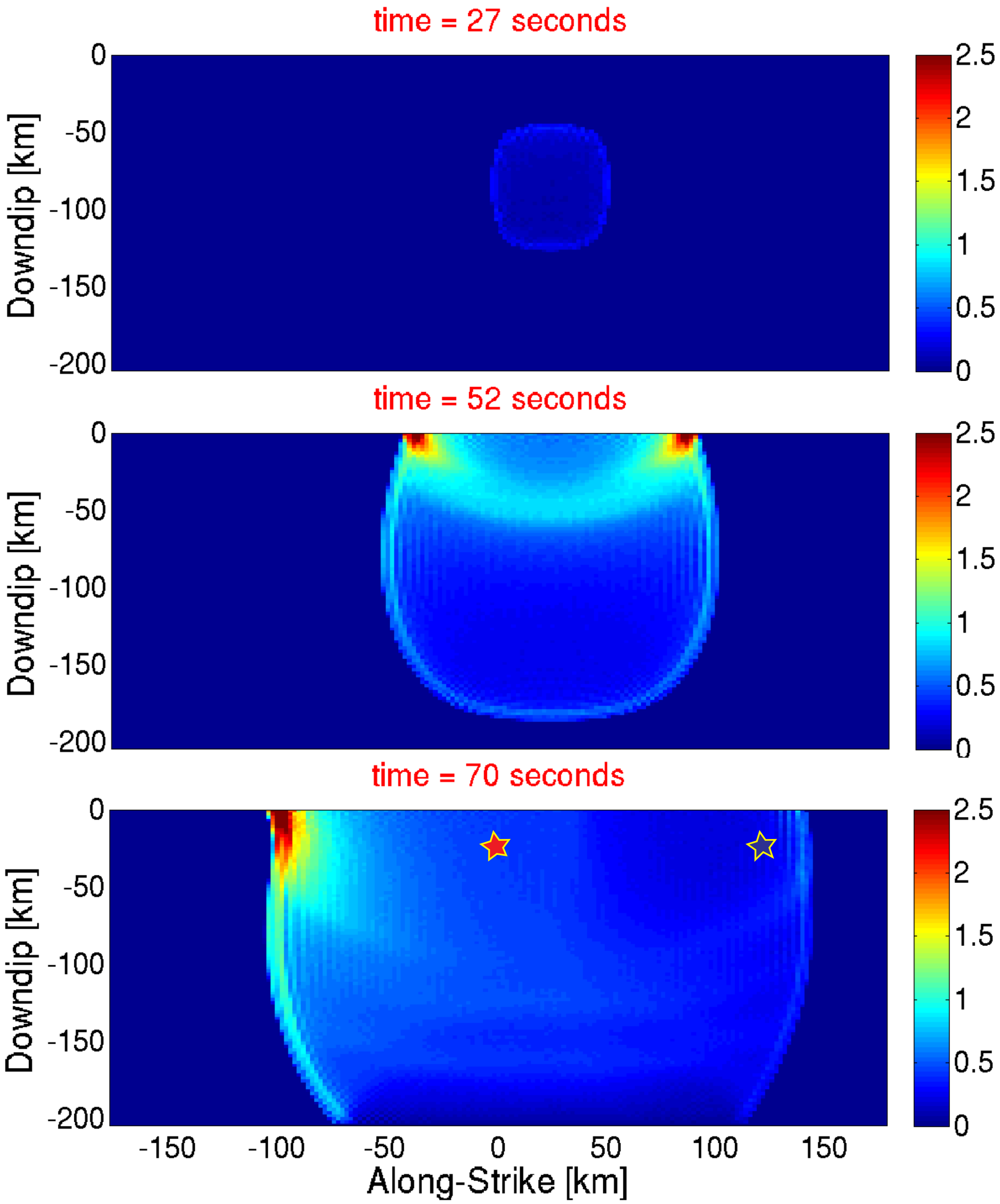

Figure 13. Diagrammatic views of the fault surface showing snapshots of rupture propagation at 27, 52, and 70 s for a model with a frictional-strengthening zone from 100 to 179 km along-strike and over the entire downdip extent of the model (see fig. 8, top), motivated by GPS data showing an unlocked section of the fault that borders our study area to the west (Freymueller and Beavan, 1999). Colors represent slip rate in m/s. Rupture shows large slip rate pulses nearest the free surface; however, the strengthening zone diminishes the slip rate pulse substantially, relative to the homogeneous model. Note the difference in slip rate between this model and the homogeneous model at 70 seconds. Rupture proceeds over the entire strengthening zone. The red and blue stars correspond to the sampling points for the stress weakening plots in figure 9.

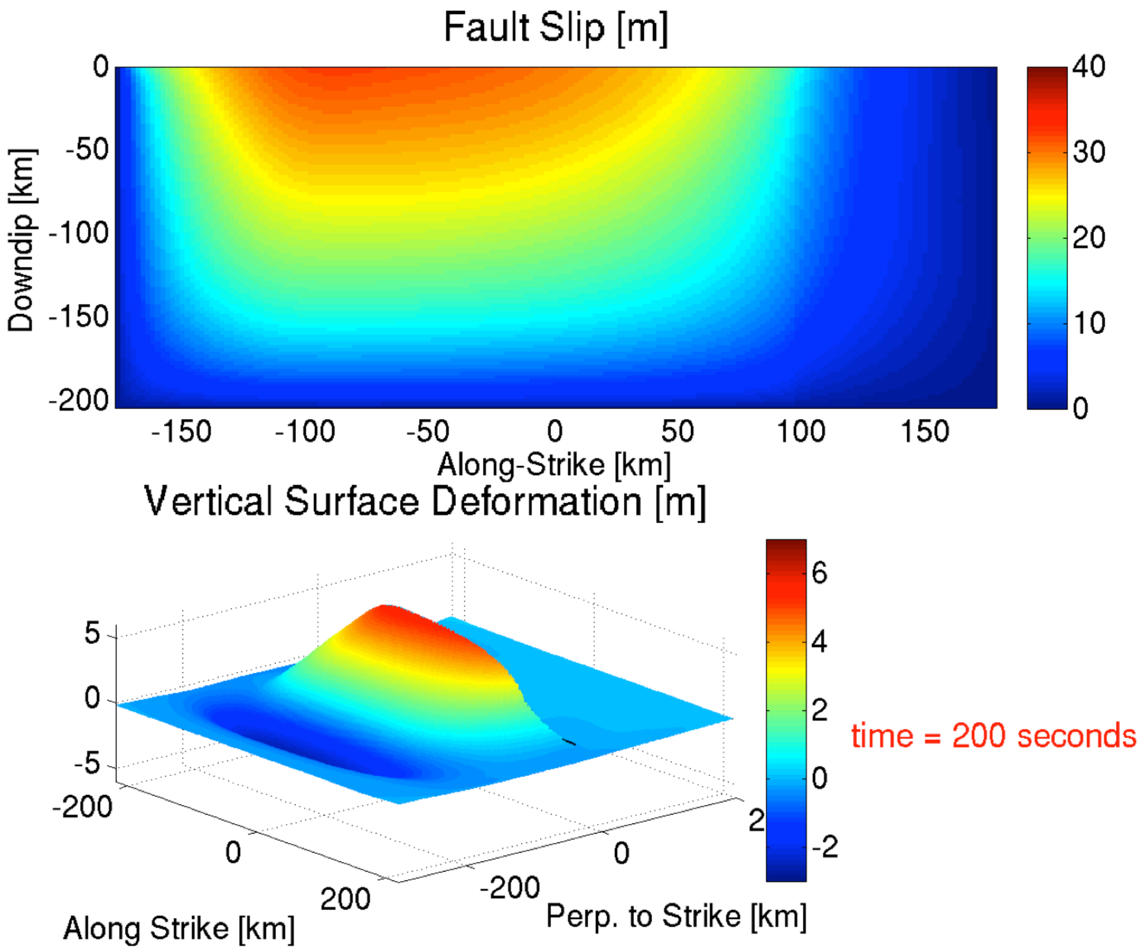

time = 200 seconds

Figure 14. Diagrams showing fault slip (top) and total vertical free surface deformation (bottom) for the western frictional-strengthening zone model. Average fault slip is decreased by 4 m (18.6 to 14.6 m) in the strengthening model, relative to the homogeneous model. Surface deformation is substantially decreased in the region above the strengthening zone, relative to the homogeneous model; however, the maximum vertical surface displacement is decreased marginally (5.77 to 5.74 m).

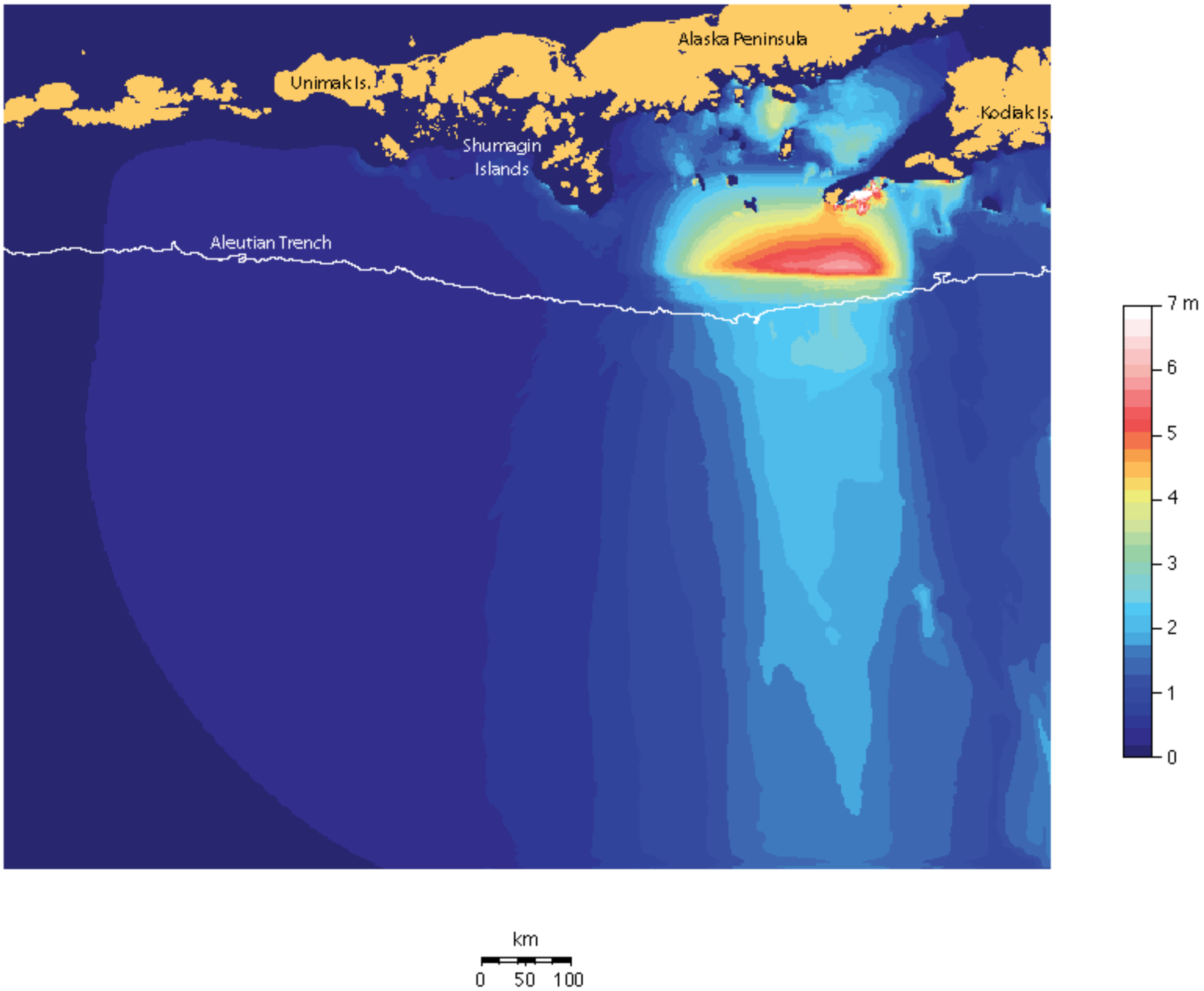

Figure 15. Map showing peak tsunami amplitudes (color scale in m) resulting from the western frictional-strengthening zone model. Water height corresponds well with free surface deformation (fig. 14, bottom). Converting a western portion of the fault to a frictional strengthening zone greatly reduces tsunami amplitudes locally above the strengthening zone in the Shumagin Islands region and alters the beaming pattern of the basin-propagating (far-field) tsunami to a more counterclockwise direction, relative to the homogeneous model. Also, peak amplitudes are reduced near the coasts of the Shumagin Islands.

Updip Frictional-Strengthening Zone Rupture

It has been suggested that subduction zones can have frictional-strengthening regimes close to the trench due to material and frictional properties (for example, Kanamori, 1972; Hyndman and others, 1997). As a first-order effort to model such a frictional regime, we implement a frictional-strengthening zone in the most updip 50 km of the megathrust (fig. 8, bottom). Figure 16 shows slip-rate snapshots for this model. In contrast to the models discussed above, the fault experiences its largest slip rate pulses ~100 km downdip from the free surface, and the slip rate pulse is dramatically reduced over the entire fault relative to the homogeneous model. Note the difference in slip rate between the homogeneous and updip frictional-strengthening models at 52 and 70 seconds. Rupture proceeds over the entire fault, including through the strengthening zone. Within the strengthening zone, the largest slip rates occur along the free surface. Figure 17 displays fault slip and total vertical free surface deformation for the updip frictional-strengthening zone model. Average fault slip is decreased by 8.2 m (18.6 to 10.4 m) in the updip strengthening model, relative to the homogeneous model. Surface deformation is decreased broadly along the free surface, relative to the homogeneous model, and the maximum vertical surface displacement is decreased (5.77 to 2.86 m). Adding an updip frictional-strengthening zone reduces slip across the entire fault more than a western strengthening zone with similar area and the same frictional coefficients. Local peak tsunami amplitudes resulting from the updip frictional-strengthening zone model are shown in figure 18. Water height corresponds well with vertical free surface deformation, showing a broad decrease in the local maximum tsunami height compared to the homogeneous model. Adding a strengthening zone to the updip portion of the fault greatly reduces tsunami amplitudes locally above the strengthening zone near the trench, and it reduces the maximum amplitude of the southward beam but does not change the beam direction of the far-field tsunami, relative to the homogeneous rupture.

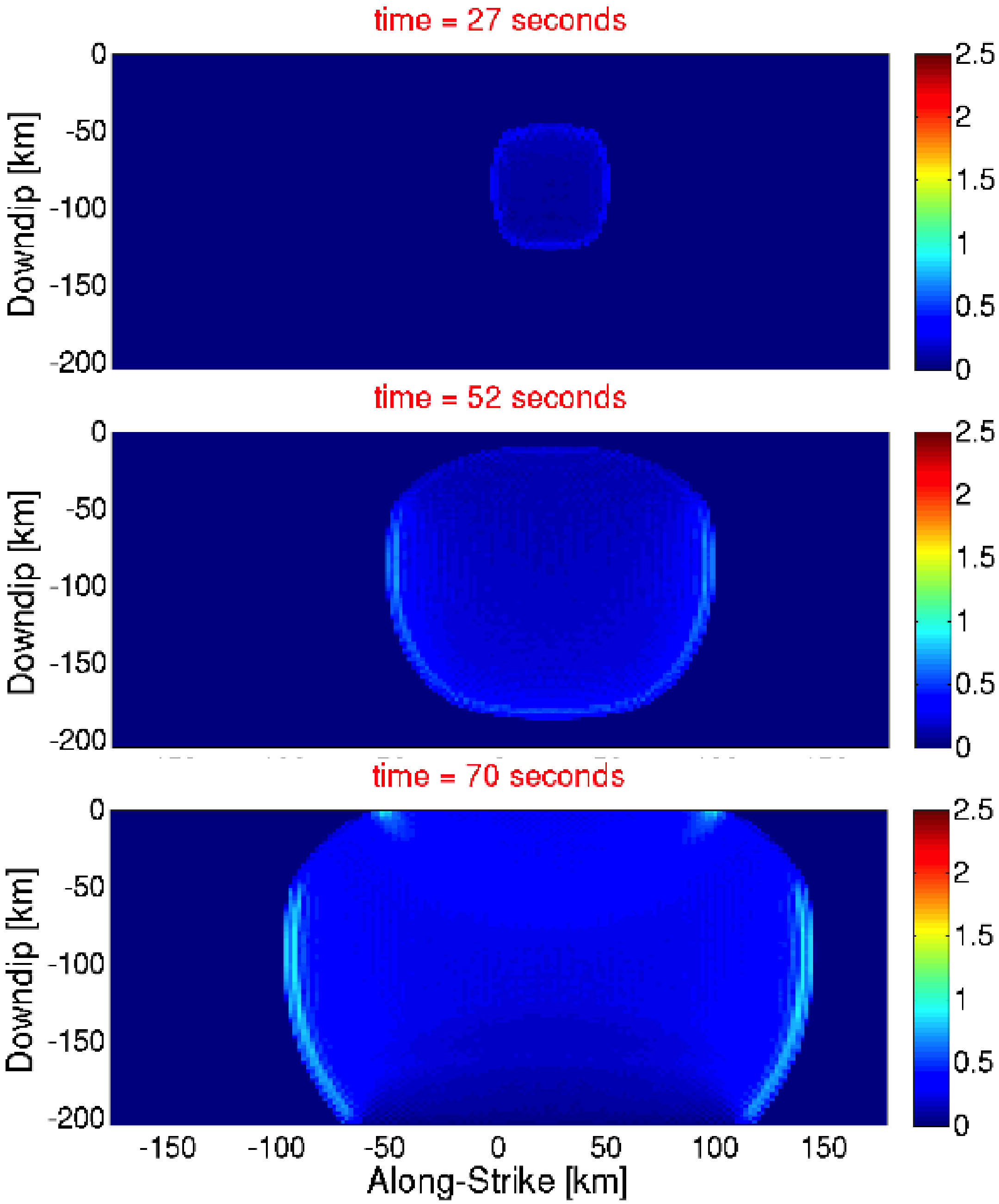

Figure 16. Diagrammatic views of the fault surface showing snapshots of rupture propagation at 27, 52, and 70 s for a model with a frictional-strengthening zone from 0 to –50 km downdip and across the entire along-strike extent of the model (see fig. 8, bottom). Colors represent slip rate in m/s. Rupture shows largest slip rate pulses ~100 km downdip from the surface, and the slip rate pulse is dramatically reduced over the entire fault, relative to the homogeneous model. Note the difference in slip rate between this and the homogeneous models at 52 and 70 seconds. Rupture proceeds through the entire strengthening zone.

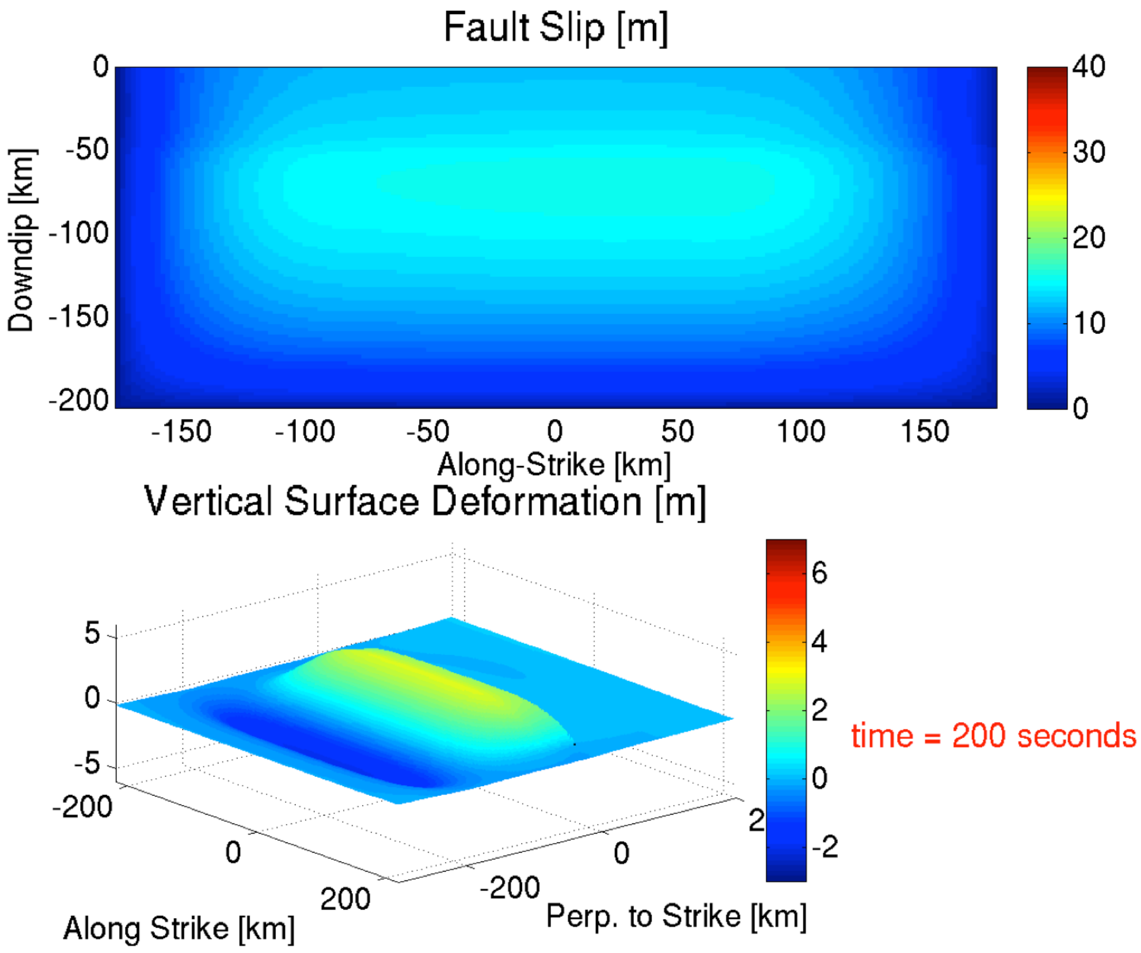

Figure 17. Diagrams showing fault slip (top) and total vertical free surface deformation (bottom) for the updip frictional-strengthening zone model. Average fault slip is decreased by 8.2 m (18.6 to 10.4 m) in the strengthening model, relative to the homogeneous model. Surface deformation is decreased broadly along the free surface, relative to the homogeneous model, and the maximum vertical surface displacement is significantly decreased (5.77 to 2.86 m). Note that adding an updip strengthening zone reduces slip across the entire fault—much more so than a western strengthening zone with similar area.

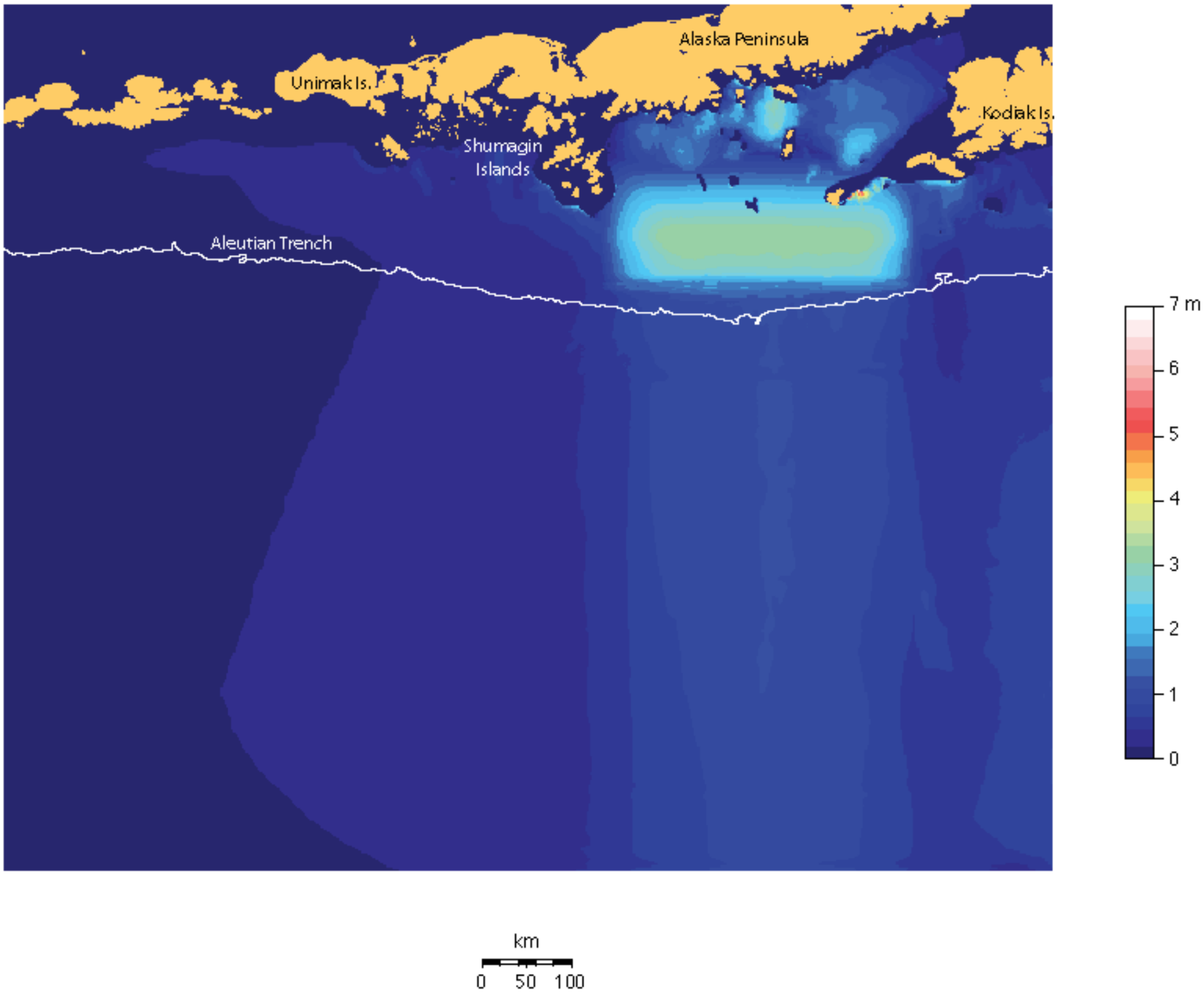

Figure 18. Map showing peak tsunami amplitude (color scale in m) resulting from the updip frictional-strengthening zone model. Water height corresponds well with free surface deformation (fig. 17, bottom). Adding a strengthening zone to the updip portion of the fault greatly reduces tsunami amplitude locally above the strengthening zone as well as broadly above the free surface, relative to the homogeneous model, and it reduces the amplitude of the far-field beaming pattern. In addition, peak amplitudes are substantially reduced near the coasts of the Shumagin Islands, the Alaska Peninsula, and Kodiak Island.

Heterogeneous Prestress Rupture

The three models discussed above assume homogeneous prestress conditions along the entire extent of the fault. However, observational data imply that earthquakes typically have strongly heterogeneous slip distributions that further imply heterogeneous prestress (for example, Olsen and others, 1997). Indeed, the SAFRR tsunami models use a heterogeneous slip model stimulated by the 2011 Tohoku-Oki event and supported by seismic, geodetic, and geologic data along the Alaskan-Aleutian subduction zone (Kirby and others, 2013). Figure 19 shows slip-rate snapshots of rupture propagation for a heterogeneous prestress model designed to qualitatively match the SAFRR dislocation model. As in the case of the homogeneous stress distribution, the fault experiences large slip-rate pulses nearest the free surface. However, because of some high-stress areas downdip, it also experiences high slip rates in other locations. Additionally, the main slip pulse is spatially heterogeneous; it does not have rough elliptical symmetry, reflecting a rupture speed that varies across the fault. Note the difference in slip rate between the homogeneous model and heterogeneous prestress model for each snapshot. Rupture proceeds over the entire fault zone for the heterogeneous prestress model. Figure 20 shows shear prestress and normal prestress distributions. The limiting values are shown in table 2. Figure 21 displays the slip distribution used in the SAFRR Tsunami Scenario (Kirby and others, 2013), as well as fault slip and total vertical free surface deformation for the dynamic heterogeneous prestress model. Average fault slip is the same as in the homogeneous model (18.6 m), and the maximum vertical surface displacement is increased (5.77 to 7.04 m), relative to the homogeneous model. The heterogeneous prestress leads to a more heterogeneous slip distribution and vertical free surface deformation, compared with the homogeneous model. The slip distribution model from the Earthquake Source working group within the SAFRR Tsunami Scenario (Kirby and others, 2013) and the slip distribution from the dynamic model are qualitatively similar, indicating that the slip distribution used by Kirby and others (2013) is self-consistent from a physical standpoint: it is possible to obtain such a slip distribution using relatively rigorous physics from a heterogeneous prestress pattern. The total slip distribution is spatially much smoother (fig. 21, middle) than our initial stress configurations. We note that tuning initial prestress to get a certain slip distribution is an iterative process, and that further tuning would likely result in a slip distribution more closely matched to the top panel in figure 21, but with gradually diminishing returns. Figure 22 shows local peak tsunami amplitudes resulting from the heterogeneous prestress model. Water height corresponds well with vertical free surface deformation, showing peak tsunami amplitudes above regions of the fault nearest the trench with maximum slip. Although the peak amplitudes immediately above the hanging wall are spatially more varied than in the homogeneous model, the overall beaming patterns and maximum amplitudes along the local coasts are similar.

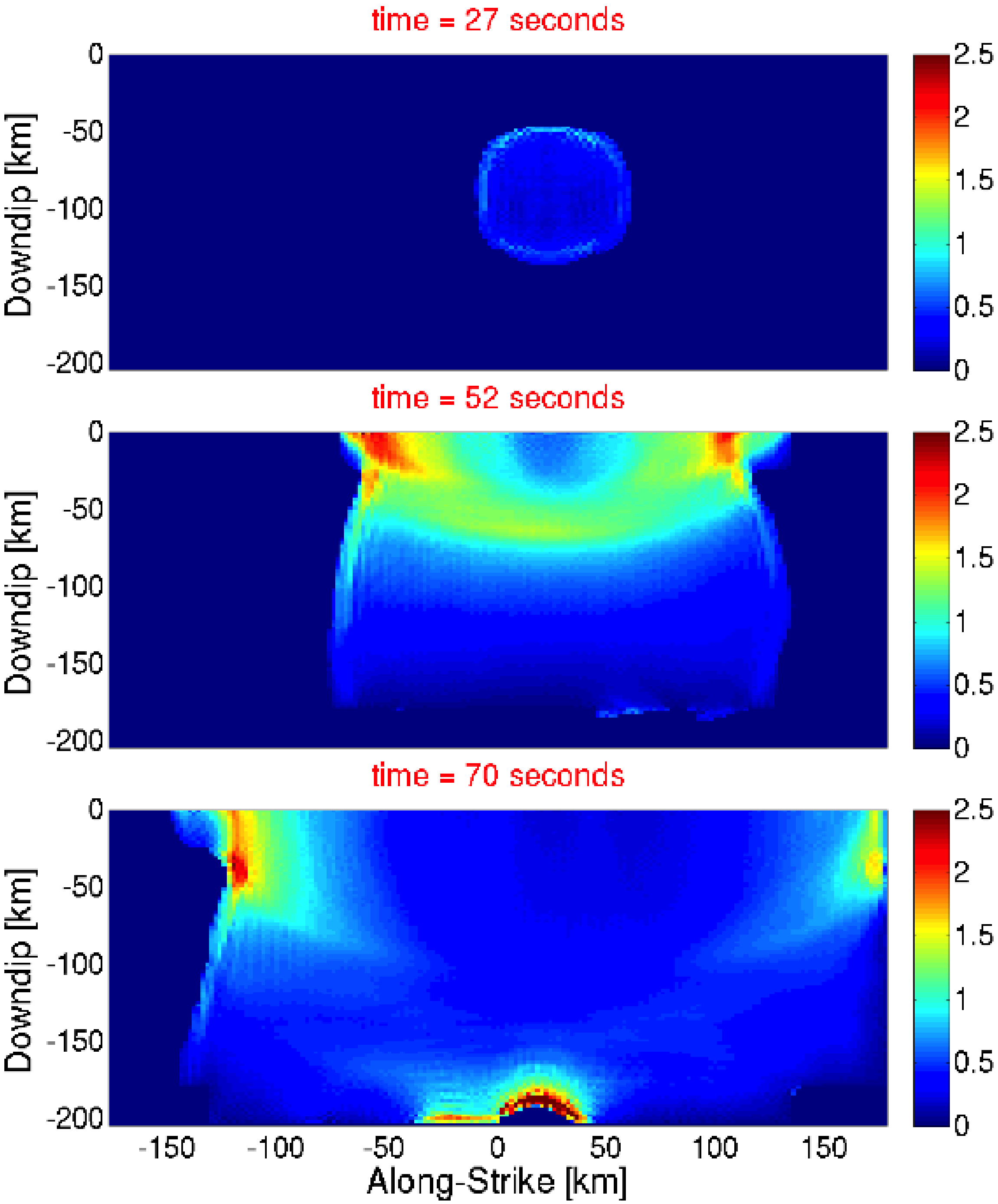

Figure 19. Diagrammatic views of the fault surface showing snapshots of rupture propagation at 27, 52, and 70 s for a heterogeneous prestress model. Colors represent slip rate in m/s. The fault experiences large slip rate pulses nearest the free surface and for some areas downdip (in contrast to the homogeneous model). Note the difference in slip rate between the homogeneous model and heterogeneous prestress model for each snapshot. Rupture proceeds over the entire fault zone.

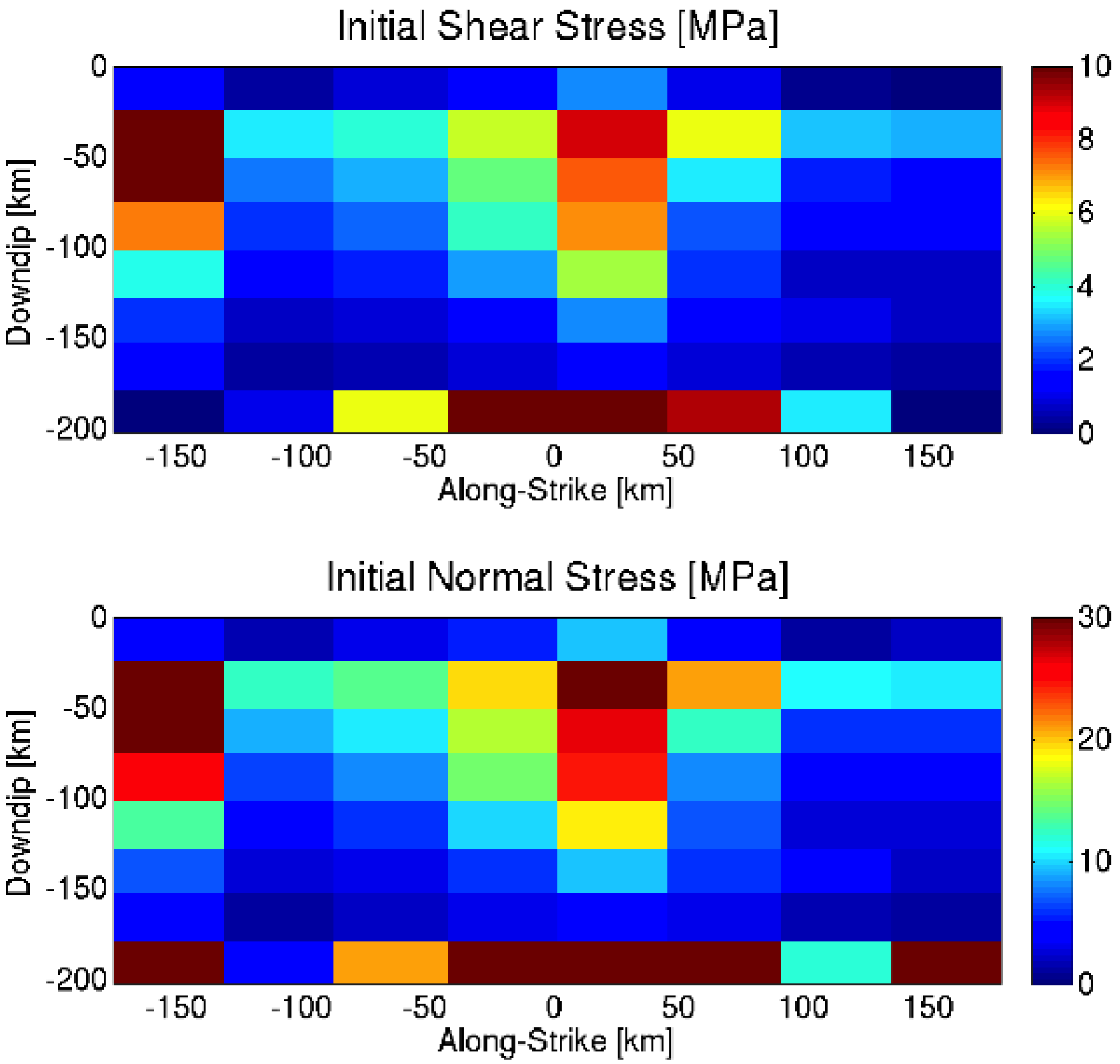

Figure 20. Diagrammatic views of the fault plane showing initial shear stress (top) and normal stress (bottom) for the heterogeneous prestress model. The limiting values of stress are shown in table 2. The total slip distribution is spatially much smoother (fig. 21, middle) than our initial stress configuration.

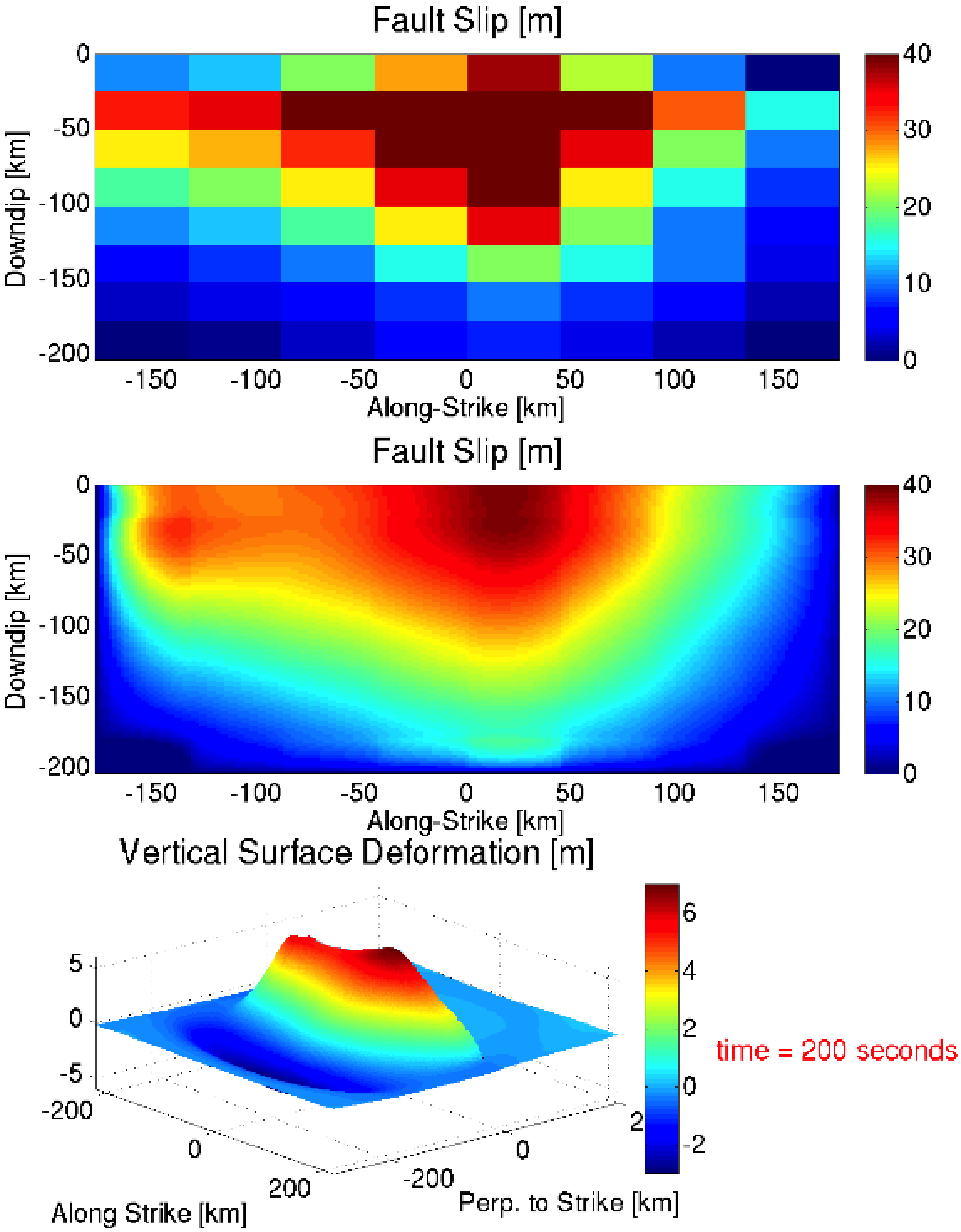

time = 200 seconds

Figure 21. Diagrams showing the slip distribution used in the SAFRR Tsunami Scenario (top), as well as the fault slip (middle) and total vertical free surface deformation (bottom) for the dynamic heterogeneous prestress model. Average fault slip is the same as in the homogeneous model (18.6 m), and the maximum vertical surface displacement is increased (5.77 to 7.04 m) relative to the homogeneous model. The heterogeneous prestress leads to a more heterogeneous slip distribution and vertical free surface deformation, compared with the homogeneous model. The dynamic slip distribution (middle panel) qualitatively resembles the top panel.

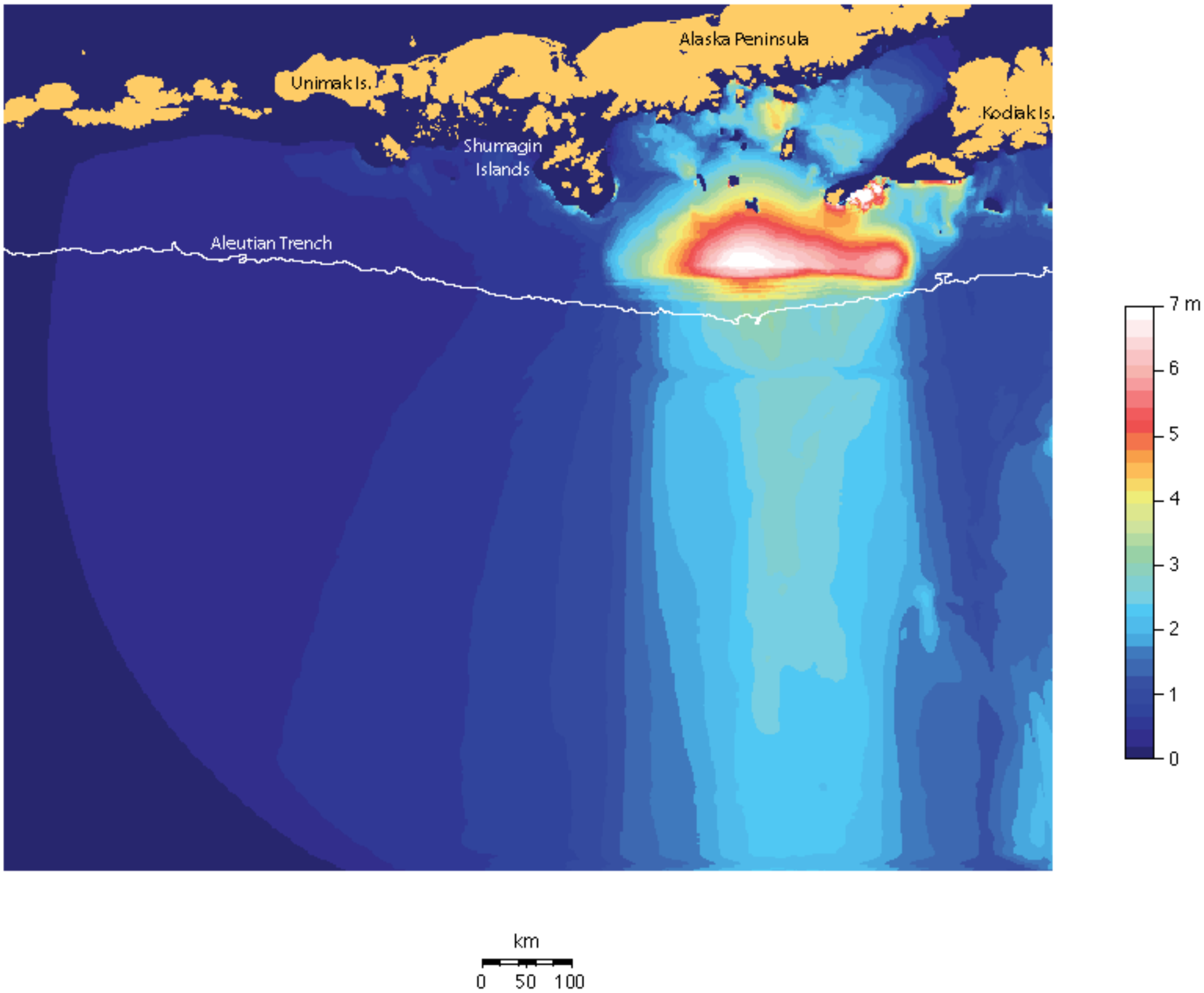

Figure 22. Map showing peak tsunami amplitudes (color scale in m) resulting from the heterogeneous prestress model. Although the peak amplitudes immediately above the hanging wall are spatially more variable than in the homogeneous model, the overall beaming patterns and amplitudes along the local coasts are similar.

Discussion

The four earthquake rupture models in this study generate four different tsunami models along a portion of the Alaskan-Aleutian subduction zone. How a tsunami is locally generated in this region affects inundation and runup on local coasts (that is, Alaska Peninsula) and could affect propagation across the Pacific Ocean onto coastlines along the Pacific rim. For the homogeneous model, there are large slip pulses near the free surface (fig. 10) that result from the dynamic unclamping of the fault and the geometric asymmetry of the hanging wall/footwall. In turn, this effect results in large slip near the free surface and therefore large vertical free surface deformation near the trench (fig. 11). The consequent modeled tsunami most significantly propagates northward and southward into and from the Alaska Peninsula (fig. 12). A completely homogeneous prestress and frictional parameter earthquake rupture model that produces the largest slip near the trench has important implications for the resulting tsunami, because sea-floor displacement is most sensitive to fault slip near the trench (Okada, 1985). Large-amplitude tsunamis can be generated by slip distributions localized near the trench.

Including a frictional-strengthening segment (emulating rate-strengthening behavior) along the Shumagin sector in the model significantly affects the slip distribution and initial tsunami wavefield. The rupture propagates through the entire strengthening zone, but with greatly reduced slip rate, and this effect reduces the overall average slip on the fault commensurately (figs. 13 and 14). The surface deformation is consequently scaled downward in this zone of lower slip. Importantly, the beaming pattern of the far-field tsunami is shifted for the western strengthening rupture, relative to the homogeneous rupture (fig. 15). Therefore, far-field tsunami propagation can shift, potentially changing inundation and runup on coastlines along the Pacific rim. It is interesting to note that the computationally simulated rupture can penetrate a strengthening zone that is as large as 80 km wide along strike. The dynamic reduction of normal stress due to the dip-slip geometry may facilitate this rupture propagation near the free surface. In other words, in our models time-dependent normal stress induced by the free surface allows thrust rupture to more easily penetrate a rate-strengthening region near the surface. This result raises the prospect that rupture might be able to propagate through such a zone into another frictional weakening zone in future earthquakes, generating a larger earthquake and tsunami.

Including a frictional-strengthening segment updip near the trench also significantly affects the slip distribution and initial tsunami wavefield (figs. 16 through 18). Adding a strengthening zone updip affects average fault slip to a greater degree than does adding a strengthening zone along strike. Without a frictional-strengthening zone updip (for example, the homogeneous model), rupture propagates energetically updip, sending radiation to the entire fault, promoting slip. Because it prevents the strong seismic radiation from the most updip section of a thrust fault during rupture, a frictional-strengthening zone updip broadly effects the slip and slip rate for the rest of the fault. As a result, we see a broad decrease in maximum tsunami amplitude, but with a similar beaming pattern when compared to the homogeneous rupture. Slip distributions near the trench are known to be important for tsunami generation (Geist, 1999; Geist and Dmowska, 1999; Geist and Bilek, 2001; Geist, 2002). Our results show slowed rupture propagation in frictional-strengthening zones with a lower peak slip rate, but these zones still have significant slip in those regions. This result hints at a possible mechanism for tsunami earthquakes (Kanamori, 1972).

We note that adding a frictional-strengthening zone along strike or updip does not preclude the ruptures from having static stress drops, particularly in the case of thrust earthquakes (Oglesby and others, 1998). Static stress drop depends on the dynamics of the rupture. It is possible to obtain a stress drop in a frictional-strengthening zone because of a large free-surface-induced reduction in normal stress (Kozdon and Dunham, in press), since the sliding frictional resistance is equal to the friction coefficient multiplied by the normal stress.

A heterogeneous prestress model significantly affects the slip distribution and initial tsunami wavefield, with the largest peak tsunami amplitudes above portions of the fault with the largest slip (fig. 21). Although average slip is the same in the homogeneous rupture and the heterogeneous prestress rupture, the latter has a larger maximum vertical free surface displacement because slip is more localized. Nonetheless, the beaming pattern of the far-field tsunami is similar for both models (figs. 12 and 22). We match the seismic moment in the heterogeneous prestress model to the source model used by Kirby and others (2013) through a trial and error process. We also qualitatively match the slip distribution of the dynamic model to the source model (fig. 21). The total slip distribution is spatially much smoother than the initial stress configurations (figs. 20 and 21), in agreement with previous studies (Olsen and others, 1997; Olsen and others, 2009). Considering all four rupture models in this study, as well as previously studied and observed megathrust events in other parts of the world (for example, Ammon and others, 2011), the SAFRR Tsunami Scenario dislocation model appears to be self-consistent as a tsunami source, even when modeled as a complex rupture that involves frictional-strengthening updip and (or) along strike as well as a heterogeneous prestress. Adding more precise source parameters in 3-D (for example, complex fault geometry, material properties, and stochastic stress fields) would further this study and help produce more realistic modeled sea-floor deformation.

We use a simple planar fault geometry in this study; however, previous work by Oglesby and Archuleta (2003) suggests that fault slip and low-frequency ground motion are relatively unchanged for a nonplanar thrust fault with an abrupt change in dip when compared to a planar fault with an equivalent dip near the free surface. This result suggests that the shallow dipping rupture process is most important in producing ground motion. Combining this with the strong dependence of tsunami generation on slip near the trench (an area that generally has the shallowest dip for a subduction zone), we feel comfortable (at least to first order) using a planar fault with a small dip in this study to study effects on local tsunami generation. However, to better model the dynamics of the rupture process as well as the resultant tsunami, more accurate fault geometry should be used in future modeling efforts.

Using dynamic earthquake rupture models coupled, in time, with hydrodynamic models can be a very useful tool. We show that rupture dynamics on a megathrust can play an important role in tsunami generation and local propagation. It is true that tsunami formation is relatively insensitive to the temporal evolution of rupture. In other words, taking the final sea-floor deformation as an initial condition for tsunami generation would produce a tsunami not tremendously different from one produced by the time-dependent sea-floor deformation. However, this does not mean that the tsunami generation is insensitive to the spatiotemporal details of the rupture process. Indeed, the rupture path and overall slip distribution (which are first-order determinants of the tsunami) crucially depend on dynamic stress interactions (see, for example, Harris and Day, 1993), and thus on these spatiotemporal effects. For thrust faults in particular, it is very instructive to analyze results from dynamic models, because time-dependent normal stress fluctuations that arise from the free surface affect slip rates and slip distribution. Additionally, rupture propagation through stable-sliding zones can be accurately modeled dynamically, and may be used to simulate tsunami earthquakes. Thus, dynamic modeling may be an important complement to standard dislocation models for tsunami hazard analysis in the future.

3. Modeling of Tsunami Wave Excitation, Propagation, and Inundation

By Hong Kie Thio

Introduction

This section presents the results of a numerical modeling analysis of tsunami propagation and inundation along the coast of California from the SAFRR Alaska scenario source model (Kirby and others, 2013) (fig. 23) as well as the dynamic rupture models (Ryan and others, section 2, above). Detailed runup and inundation modeling for areas along the California coast is performed where there is significant exposure. For all areas, I not only provide the maximum wave heights and inundation throughout the region but also the maximum velocity and momentum flux at the shoreline, which may be more appropriate parameters to estimate the impact of tsunami on engineered structures. An overview of my modeling effort and some examples of some of the high-resolution modeling is presented. For more detailed information, refer to the actual data files that have been produced and made available for this project.

Detailed runup and inundation modeling was performed for areas along the California coast where there is significant exposure. For all areas, the results not only provide the maximum wave heights and inundation throughout the region but also the maximum velocity and momentum flux at the shoreline, which may be more appropriate parameters to estimate the impact of tsunami on engineered structures. The section presents an overview of our modeling effort and some examples of some of the high-resolution modeling. For more detailed information, please refer to the actual data files that have been produced and made available for this project.

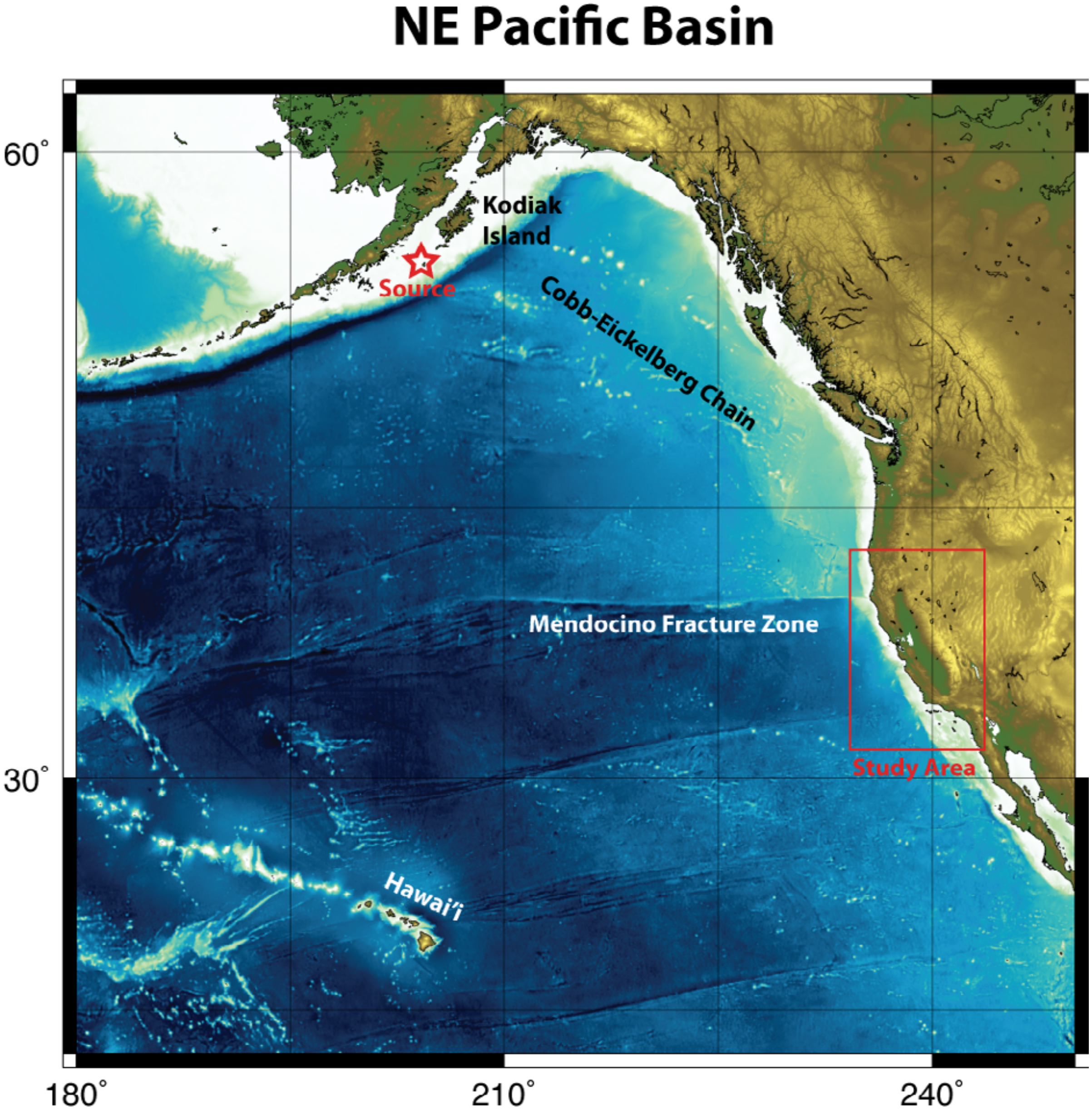

Figure 23. Map of the northeastern Pacific Basin. The scenario source location is indicated with a star; the area of high-resolution modeling (California) is indicated with the red box.

Tsunami Modeling

The simulation of tsunami waves consists of two steps. First, the sea-floor deformation resulting from slip on a fault plane is computed using elastic theory. Then, this static deformation field is used as the starting condition for the actual tsunami propagation and inundation calculations. Our particular implementation of the tsunami propagation and inundation model was developed by Satake (1995) and has been widely used since by many researchers (for example, Baba and others, 2004; Fujii and Satake, 2006; Ichinose and others, 2007; Thio and others, 2007; Burbridge and others, 2008; Baba and others, 2009).

Tsunami Excitation

The tsunami excitation by earthquake sources is modeled by translating the vertical deformation field of the earthquake source (surface faulting) into a vertical displacement of the ocean surface. This method is commonly used in tsunami studies (for example, Satake, 1995; Titov and Synolakis, 1996) and has been shown to be valid for long-wavelength deformation (rupture extent >> water depth). The static displacement fields were computed from the slip distribution provided by Kirby and others (2013) using a frequency-wave-number integration technique (FK) with a simple layered crustal model (Wang and others, 2003, 2006). This method allows for an efficient computation of the static displacement field of a buried rupture using elastic theory. The ground deformation field is shown in figure 24. The pattern shown is typical for a shallow subduction thrust, with a very pronounced region of uplift (with a maximum of 14 m) near the trench and a broader area of subsidence in the back-arc region.

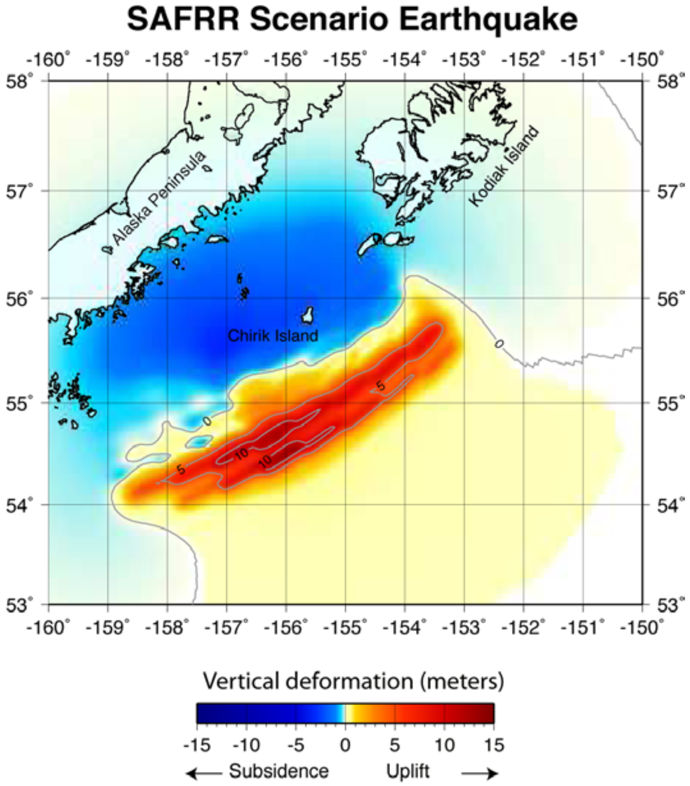

Figure 24. Map showing vertical deformation field of the earthquake source region, which is used as initial condition for the tsunami wave modeling.

Tsunami Propagation

An Eulerian approach is used to describe the particle motion of the fluid. This describes only the velocity changes of the fluid at some point and at some instant of time rather than describing its absolute displacement. Consider a wave that is a propagating disturbance from an equilibrium state. Gravity waves occur when the only restoring force is gravity. When the horizontal scale of motion is much larger than the water depth, then the vertical acceleration of water is much smaller than the gravity acceleration and thus negligible. This means that the whole water mass from the bottom to the surface is assumed to move uniformly in a horizontal direction. This kind of gravity wave is also known as a "long wave." Long-wave approximations are appropriate when the water depth of lakes and oceans (< 5 km) is much smaller than the length of the disturbance (fault lengths ~ 10–1,000 km). This approximation gives an accurate description of tsunami wave propagation in the open ocean. In order to also model the propagation of tsunami waves in coastal areas, an approximation to the wave equation is used in which the low-amplitude linear long-wave requirements are relaxed, as shown below.

General Linear Gravity Wave

The following is a derivation of the general case of gravity waves for two dimensions, where *x* is the horizontal direction and *z* is vertical direction (fig. 25).

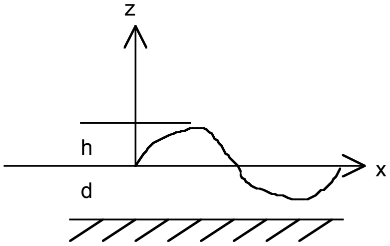

Figure 25. Diagrammatic sketch showing the coordinate system for tsunami model.

We start from the Euler's equation of motion that considers the conservation of momentum on a volume of water. The Newton equations can be simplified as

$$\frac{d}{dt}V = g - \frac{1}{\rho}\nabla p$$

where *d/dt* is the total derivative (∂/∂*t* is the partial derivative) with respect to time, *g* is the gravitational acceleration, $V = (u,w)$ are the depth averaged velocities in the *x* and *z* directions, ρ is the density, and *p* is the fluid pressure. Figure 25 shows that *h* is the tsunami wave height and *d* is the water depth. Next consider the conservation of mass to derive the equation of continuity,

$$\frac{\partial \rho}{\partial t} + \nabla \cdot (\rho V) = 0$$

which for incompressible fluid becomes

$$\nabla \cdot V = 0 .$$

From the Euler equation of motion the horizontal and vertical acceleration components are

$$\frac{du}{dt} = -\frac{1}{\rho}\frac{\partial p}{\partial x}$$
$$\frac{dw}{dt} = -g - \frac{1}{\rho}\frac{\partial p}{\partial z}$$

The relation between h and p is seen through the hydrostatic pressure equation,

$$p = -\rho g(h - z) + p_0$$

where h is the wave height, z is the water depth, and p_0 is the pressure of one atmosphere at $z = 0$ and $h = 0$. The horizontal and vertical pressure gradients given from the slope of the water surface,

$$\frac{\partial}{\partial x} p = pg\frac{\partial h}{\partial x}$$
$$\frac{d}{dz} p = -\rho g$$

are combined with the Euler equation to give the horizontal and vertical components,

$$\frac{du}{dt} = -g\frac{\partial h}{\partial x}$$
$$\frac{dw}{dt} = 0$$

For ocean tsunamis, the nonlinear advective term is small and can be ignored; therefore the equation of motion is,

$$\frac{du}{dt} = \frac{\partial u}{\partial t} + u\frac{\partial u}{\partial x} \approx \frac{\partial u}{\partial t}$$
$$\frac{\partial u}{\partial t} = -g\frac{\partial h}{\partial x}$$

Next consider the conservation of mass for a region with a small length dx. Because the volume change per unit time must be equal to the flow rate of water going out of this region, we can therefore write

$$\frac{\partial}{\partial t}\{(h + d)dx\} = -\frac{\partial}{\partial x}\{u(h + d)\}dx$$
$$\frac{\partial h}{\partial t} = -\frac{\partial}{\partial x}\{u(h + d)\}$$
$$\frac{\partial h}{\partial t} = -\frac{\partial}{\partial x}(du)$$

which is the simplified equation of continuity when the amplitude of the wave is small compared to the water depth. The so-called small-amplitude, linear, long-wave assumption is valid for most of tsunami propagation paths except near coasts.

Nonlinear Gravity Waves and Shallow Water Waves

Linear theory is often sufficient to model the propagation of tsunami in open oceans. However, in the nearshore environment, and in particular for inundation, nonlinear effects become very important and need to be included as well.

Without a viscous force to dissipate wave energy, the equations would have water motion continue forever. In order to include the viscous effect, we can add a term for viscous stress to the equation of motion. We only consider a shear stress at the water bottom, and the normal stress is already included and equal to the pressure. The shear stress in two dimensions is experimentally estimated as

$$\tau_x^{\ b} \approx C_f v_x \sqrt{v_x^{\ 2} + v_y^{\ 2}}$$

and the frictional force is

$$F_x^{\ b} = C_f \frac{v_x \sqrt{v_x^{\ 2} + v_y^{\ 2}}}{d+h} ,$$

where v_x and v_y are now the horizontal components of velocity.

Satake (1995) adopted two types of frictional coefficients from engineering hydrodynamics for including bottom friction for tsunamis. These are the De Chezy (*C*) and Mannings's roughness (*n*) coefficients. These have different dimensions; therefore a nondimensional frictional coefficient C_f is related to these two coefficients by

$$C_f^{\ 2} = \frac{g}{C_c^{\ 2}}$$

and

$$C_f = \frac{gn^2}{(d+h)^{1/3}} .$$

Manning's roughness coefficient *n* is used for a uniform turbulent flow on a rough surface. It indicates that the bottom friction varies with water depth. We use an *n* of 0.03 $\mathrm{m}^{-1/3}$ s, typical for coastal waters. If *n* is translated to C_f, then *n* becomes 2.3×10^{-3} for a total depth of 50 m and 1×10^{-2} for a total depth of 0.6 m, which agree well with observational values of tidal flow and runup of solitary waves (see Satake, 1995).

Because the Earth is rotating, there is a force apparently acting on a body of water. In an inertial reference frame (fixed on the rotating Earth), this force is called the Coriolis force. The derivation of this term is beyond the scope of this report and we refer the reader to textbooks on analytical mechanics. The vertical component of the Coriolis force is much smaller than gravity (3 $\mathrm{cm/s^2}$ compared to 980 $\mathrm{cm/s^2}$ at 4,000-m depth). In a local Cartesian coordinate system, the horizontal components are given by

$$F_x^{\ cor} = -fv_y$$
$$F_y^{\ cor} = fv_x$$

where *f* is the Coriolis parameter, and this force always acts to the right hand side of the motion in the northern hemisphere.

The equations for general gravity waves are derived without making the small-amplitude, linear long-wave approximation appropriate when the wave height is much smaller than the water depth ($h<<d$). If we expand the hyperbolic tangent function using the Taylor series expansion and include the first and second order terms, then the corresponding equation of motion becomes

$$\frac{\partial u}{\partial t} = -g\frac{\partial h}{\partial x} + \frac{1}{3}d^2\frac{\partial^3 u}{\partial x^2 \partial t}$$

which is also known as the Boussinesq equation. After relaxing the small amplitude assumption, the equation of motion and continuity are given as

$$\begin{aligned} &\frac{du}{dt} + u\frac{\partial u}{\partial x} = -g\frac{\partial h}{\partial x} \\ &\frac{\partial h}{\partial t} = -\frac{\partial}{\partial x}\{u(h+d)\} \end{aligned} .$$

These equations are for the finite-amplitude shallow water waves. For the linear case, the phase velocity is given by the following Taylor series expansion of the hyperbolic tangent function,

$$c = \sqrt{gd}\left\{1 - \frac{2\pi^2}{3}\left(\frac{d}{\lambda}\right)^2\right\},$$

where *l* is the wavelength. In the nonlinear case the *d*-term in the phase velocity is replaced by the total height of the water column ($d+h$) which gives us a phase velocity of the form

$$c \sim \sqrt{g(d+h)} .$$

Note that in the nonlinear case there appears a phenomenon of amplitude dispersion—the larger the amplitude, the faster the wave speed. As a consequence, peaks of a wave catch up with troughs in front of them, and the forward-facing portion of the wave continues to get steeper. This wave will eventually break.

Including the bottom friction and Coriolis force, the equation of motion for shallow water waves can be written for a two-dimensional case as follows:

$$\begin{aligned} &\frac{\partial U}{\partial t} + U\frac{\partial U}{\partial x} + V\frac{\partial U}{\partial y} = -fV - g\frac{\partial h}{\partial x} - C_f\frac{U\sqrt{U^2+V^2}}{d+h} \\ &\frac{\partial V}{\partial t} + U\frac{\partial V}{\partial x} + V\frac{\partial V}{\partial y} = -fU - g\frac{\partial h}{\partial y} - C_f\frac{V\sqrt{U^2+V^2}}{d+h} \end{aligned}$$

and the equation of continuity is

$$\frac{\partial h}{\partial t} + \frac{\partial}{\partial x}\{U(h+d)\} + \frac{\partial}{\partial y}\{V(h+d)\} = 0$$

where the coordinate system is x=east y=south, f is the Coriolis parameter, C_f is a nondimensional frictional coefficient, and U and V are the depth-averaged velocities in the x and y directions, respectively. In the equation of motion, the first term on the left side is the local acceleration term, the second and third terms on the left are the advection terms, the first term on the right side is the Coriolis force, the second term on the right is the restoring force from gravitation acceleration, and the third term on the right is the bottom friction force.

Tsunami Model

The tsunami propagation has been modeled using a staggered grid finite-difference algorithm in the so-called shallow water approximation, where the wavelength of the tsunami is assumed to be much larger than the water depth. In these circumstances the only restoring force, when the water level is out of equilibrium, is gravity so that the whole water mass from the bottom to the surface is assumed to move uniformly in a horizontal direction. Shallow water (or “long wave”) approximations are appropriate when the water depth of lakes and oceans (0–10 km) is much smaller than the length of the disturbance (fault lengths ~ 50–1,000 km).

The equations of motion and equation of continuity described above are solved in a spherical coordinate system by finite-difference method using the staggered leapfrog method (see, for example, Satake, 1995). For the advection terms, an upwind difference scheme is used (for example, Press and others, 2007). The land-sea boundary condition in the linear computation is total reflection, and in the nonlinear case there is a moving boundary condition and runup is considered. The time step of computation is determined to satisfy the stability condition (Courant condition) in the linear case and by trial and error for the nonlinear finite-difference computations.

The nested grid setup consists of a master grid with a coarse grid spacing and a number of nested finer grids with decreasing grid sizes around areas of interest. The relations between the coarser and finer grids are referred to as parent (coarse) and child (fine), and every child grid can be a parent grid of an even higher resolution grid. Our finite difference scheme allows for more than one child for every parent, with the only condition that same-level child-grids do not overlap (or are separated by only a few grid points in the parent grid, and that the reduction in grid spacing from parent to child is an odd factor. In practice, the reduction is either 3 or 5, because larger reduction factors would introduce large numerical errors.

In the current model, the deep ocean part is sampled at 120 arc seconds (~ 3.6 km). Because of the very long wavelength of the tsunami waves in the deep ocean, such a sampling is sufficient for accurate results and reduces the computation time and memory requirements considerably. Closer to shore, several nested grids step down to 0.96 arc sec (~ 30 m) at the sites of interest. The timestep for these runs is 0.2 s. Currently, the code uses a fixed timestep, which generally is controlled by the finest grid size.

Bathymetry

The bathymetry used for the open ocean propagation was derived from the SRTM30+ model by Becker and others (2009). This model (fig. 23) is based on a variety of data, but along the coast of North America, a significant source is the National Geophysical Data Center (NGDC) coastal relief model. The higher resolution grids used for the inundation modeling were all provided through the NGDC Tsunami Inundation Gridding program. Most of these data are available in a resolution of 1/3 arc sec, or approximately 10 m. These data were resampled to a resolution of 1 arc sec (~30 m) for the final inundation grids, as well as even lower resolutions for the intermediate nested grids (fig. 26).

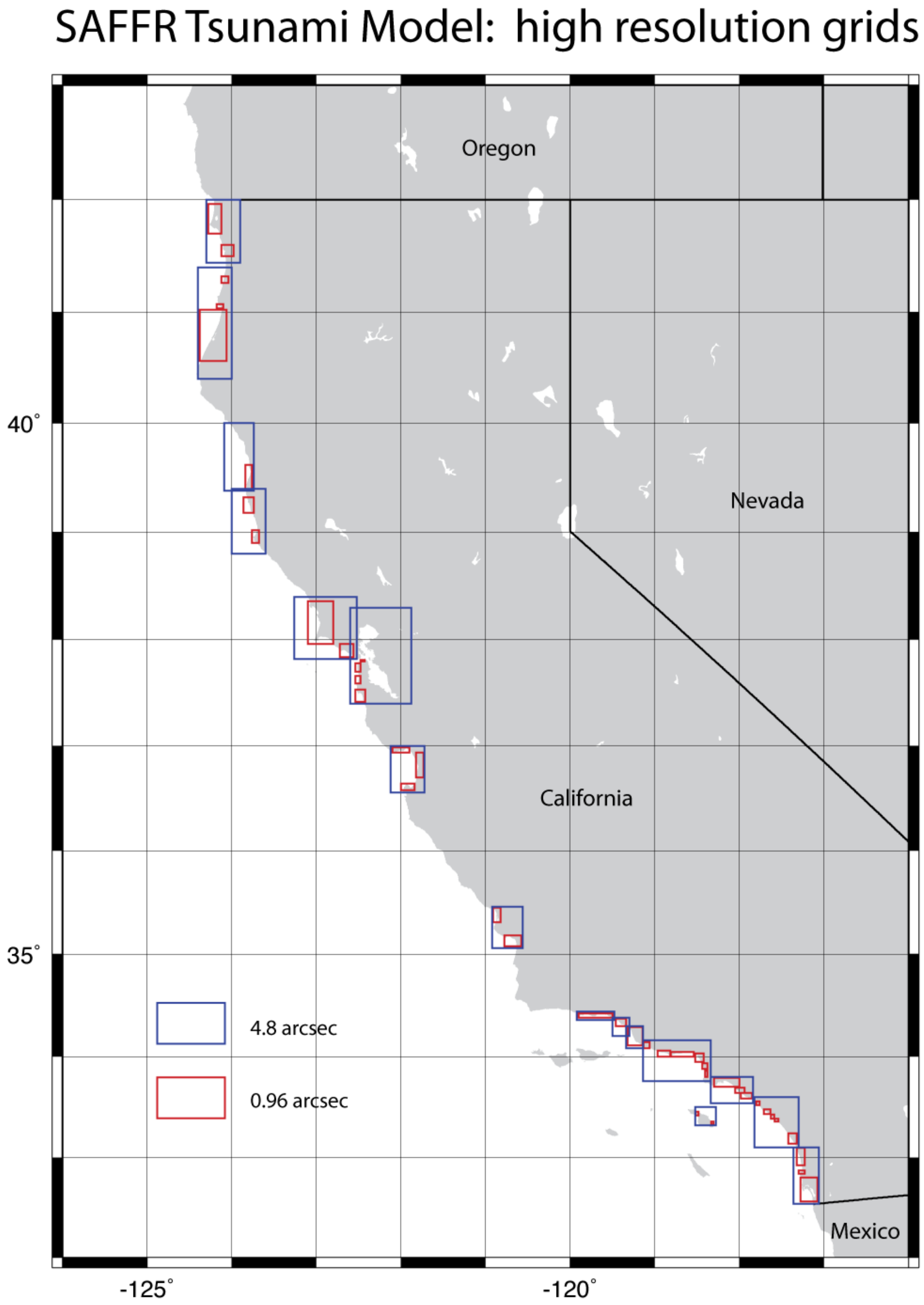

Figure 26. Map showing locations of the high-resolution grids (0.96 arc sec, ~ 30 m) along the California coast. Also shown are the parent grids with a resolution of 4.8 arc sec (~150 m).

Coordinates for the grids used are given in Tables 4 through 6.

Table 4. Longitude and latitude of the boundaries of coarse and 1st nested grid

Area	West	East	South	North
Pacific (120 arc sec)	120	250 (-110)	12	62
California (24 arc sec)	-125	-116	31	43

Table 5. Longitude and latitude of the boundaries of the 2nd order grid (4.8 arcsec)

Area	West	East	South	North
Crescent City	-124.300	-123.900	41.440	42.000
Humboldt Bay	-124.400	-124.000	40.400	41.400
Fort Bragg	-124.920	-123.740	39.380	40.000
Arena Cove	-124.000	-123.600	38.800	39.400
Marin County	-123.260	-122.520	37.820	38.400
San Francisco	-122.600	-121.880	37.400	38.300
Monterey Bay	-122.120	-121.720	36.560	37.000
Port San Luis	-120.920	-120.560	35.060	35.460
Santa Barbara	-119.920	-119.480	34.360	34.440
Ventura	-119.340	-119.140	34.080	34.300
Rincon	-119.500	-119.300	34.200	34.380
Santa Monica Bay	-119.140	-118.340	33.760	34.160
South Bay	-118.340	-117.840	33.540	33.800
Catalina	-118.520	-118.280	33.320	33.500
Oceanside	-117.820	-117.300	33.100	33.600
San Diego	-117.360	-117.060	32.540	33.100

Table 6. Longitude and latitude of the boundaries of the highest resolution grids (.96 arcsec)

Area	West	East	South	North
Crescent City	-124.280	-124.120	41.700	41.960
Klamath	-124.120	-123.980	41.500	41.600
Orick	-124.120	-124.040	41.260	41.320
Trinidad	-124.180	-124.100	41.032	41.072
Humboldt Bay	-124.380	-124.060	40.560	41.020
Fort Bragg	-123.840	-123.760	39.400	39.620
Mendocino	-123.860	-123.740	39.180	39.320
Arena Cove	-123.760	-123.680	38.900	39.020
Stinson Beach	-122.720	-122.560	37.840	37.960
Point Reyes	-123.100	-122.800	37.960	38.360
Marin County	-122.650	-122.500	37.700	38.200
San Francisco	-122.540	-121.920	37.360	38.200
Golden Gate	-122.480	-122.428	37.800	37.812
West Frisco	-122.540	-122.480	37.700	37.780
Pacifica	-122.540	-122.480	37.592	37.660
Half Moon Bay	-122.540	-122.420	37.420	37.532
Santa Cruz	-122.100	-121.900	36.940	36.988
Monterey Bay	-121.824	-121.732	36.700	36.940
Monterey	-122.000	-121.840	36.580	36.644
Morro Bay	-120.912	-120.820	35.312	35.452
Avila Beach	-120.780	-120.580	35.080	35.184
Santa Barbara	-119.900	-119.500	34.380	34.424
Ventura	-119.324	-119.144	34.108	34.288
Rincon	-119.460	-119.340	34.300	34.372
Point Mugu	-119.136	-119.060	34.084	34.140
Malibu	-118.968	-118.816	34.000	34.060
Malibu	-118.812	-118.540	34.000	34.044

Santa Monica	-118.520	-118.420	33.948	34.032
Manhattan Beach	-118.440	-118.380	33.880	33.932
Redondo Beach	-118.408	-118.380	33.800	33.860
POLA/POLB	-118.300	-118.000	33.700	33.788
Huntington Beach	-118.048	-117.940	33.640	33.692
Newport Beach	-117.984	-117.852	33.584	33.640
Avalon	-118.336	-118.304	33.332	33.360
Isthmus	-118.516	-118.484	33.420	33.456
Laguna Beach	-117.800	-117.760	33.520	33.560
Dana Point	-117.712	-117.632	33.432	33.480
San Clemente	-117.628	-117.588	33.384	33.428
San Onofre	-117.584	-117.540	33.356	33.384
Oceanside	-117.420	-117.320	33.140	33.240
Encinitas	-117.320	-117.228	32.924	33.096
San Diego	-117.280	-117.080	32.560	32.800
La Jolla	-117.300	-117.228	32.840	32.872

The original high-resolution grids were defined relative to mean high water (MHW). The expected highest tide on the day of the scenario is 20 cm above MHW, and we lowered the elevation models by this amount to simulate the tsunami waves arriving during high tide.

Even though we used high quality elevation models that were specifically developed for tsunami inundation studies, there are still limitations to these data that can result in inaccurate inundation models. Different elevation datasets have been used to provide dense coverage for these areas, and these may have different uncertainties associated with them. Also, at a resampling to 30-m horizontal resolution it is possible that certain narrow features such as levees disappear or develop holes that can allow inundation to take place where in reality the levees would be sufficient to keep the water out.

Results

The simulations were run on a computing cluster at the URS Corporation office in Los Angeles. We ran simultaneous runs for the different subregions, each of which consisted of several levels of child grids. The entire set of simulations typically would take a day and a half to complete.

The results that are presented here come in different forms, such as maps of maximum amplitude, velocity, and momentum, as well as time series of wave height and velocity. The maxima are taken over the entire duration of the simulations (15 hours). The maps of maximum wave amplitudes show the maximum amplitude and extent of the inundation over the timespan of the computations. We also computed flow depth, which is the height of the water column at any place. The maps of nearshore and onshore maximum amplitudes are all taken from the 0.96 arc sec (~30 m) grids. In some cases, permeable structures such as jetties and breakwaters are represented as solid walls in the original models. The holes created by the resampling in these cases may (inadvertently) result in a more realistic modeling environment in those cases.

Ocean Propagation

In figure 27, we show the maximum wave amplitudes across the northeastern Pacific, from the source in Alaska to the target areas along the California coast. Several characteristics of tsunami wave propagation are discernible on this map (with the annotations corresponding to the list below):

- Source directivity—the amplitude patterns show a clear directional dependence, with the maxima in direction perpendicular to the strike of the fault plane (A). This is because the wavefront in that direction is linear in shape, which reduces the attenuation due to geometrical spreading.

- Focusing due to ocean bathymetry—an example is the effect of the Cobb-Eickelberg seamount chain (B), which has a shallower bathymetry and thus lower propagation velocity, than the surrounding ocean and therefore acts as a waveguide, which can lead to areas of elevated tsunami amplitudes along the coast.
- The Mendocino Fracture Zone—this feature (C) often acts as a waveguide, especially for tsunami arriving from sources farther to the west, such as the Kurile subduction zone and Japan. In the scenario case, we still see some effect as well, because it defines a significant contrast in bathymetry.
- Shoaling—as the bathymetry becomes shallower, the amplitude of the tsunami waves increases, an effect called shoaling, and this is clearly visible along most of the coastline (D). This effect is even more pronounced when we look at the higher resolution inundation maps.
- Coastline geometry—the shape of the California coast, bending east near Lompoc, causes the impact of tsunami from the north to be significantly reduced there compared to central California. The Continental Borderlands are in a kind of shadow zone (E) and in general the tsunami hazard there is smaller than elsewhere along the California coast.

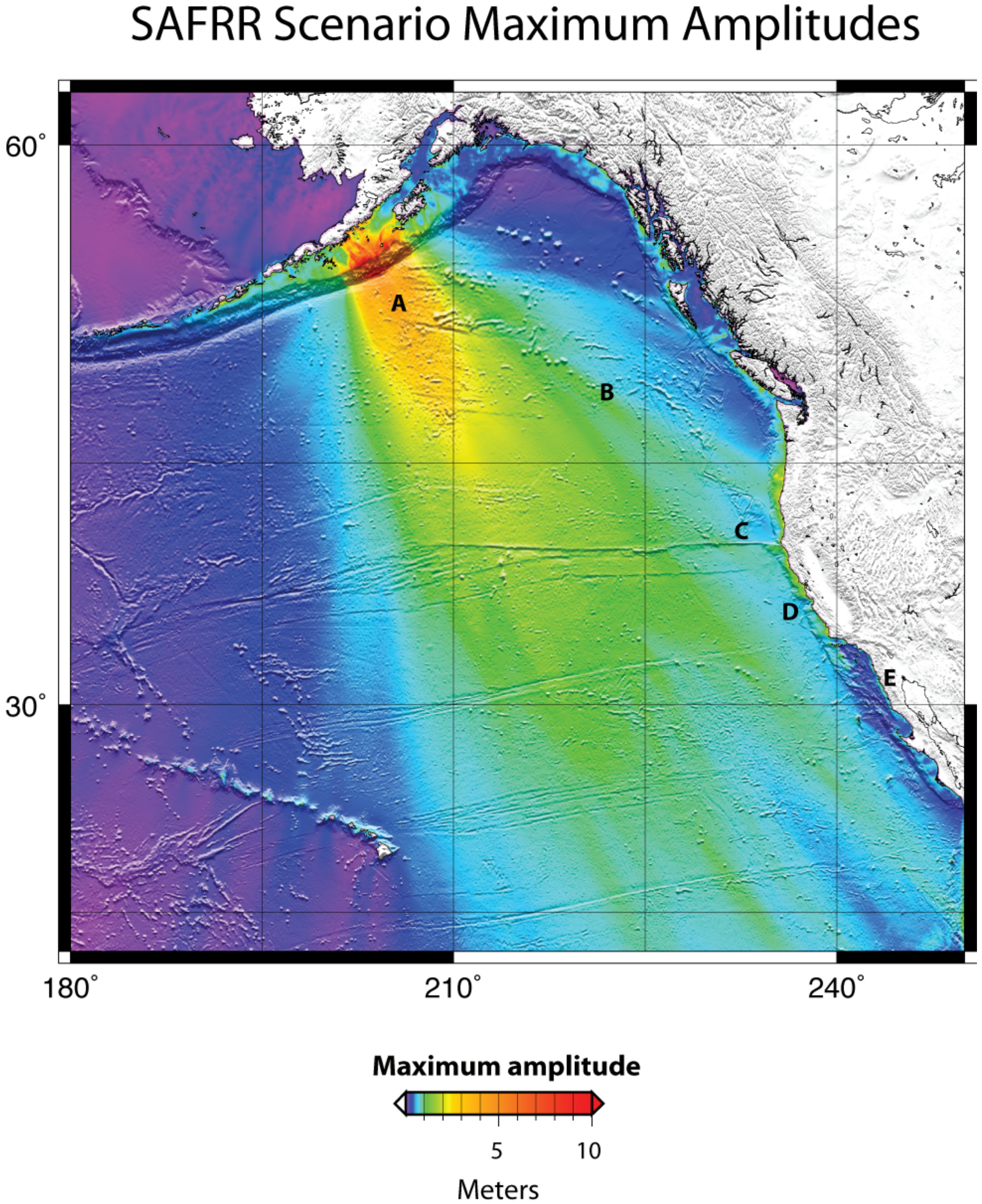

Figure 27. Map of maximum tsunami amplitudes. The letters mark locations referred to in the text.

Figure 28 shows the water-level time series (marigrams) for selected points ordered from south at the top to north at the bottom. The move-out due to longer distances from north to south is very clear. Travel times to California range from 4 hours to Crescent City to almost 6 hours to San Diego. The waveforms are quite different in character. Although all the initial waves are up, only rarely is the first arrival the largest arrival (for example, Monterey Bay, Morro Bay). In most cases the largest waves arrive several hours, and sometimes more than 7 hours, after the initial arrival. Especially in southern California, the tsunami waves attenuate only slowly in time, which may be partly a result of trapped energy in the Continental Borderlands.

Nearshore and Onshore Results

As mentioned before, as waves move closer to shore their amplitudes increase because of the shoaling effect. This is clearly visible in the high-resolution maps, such as the one for the Ports of Los Angeles and Long Beach, shown in figure 29. Whereas the amplitudes in deep water are on the order of 1 m, they increase to more than 2 and even up to 4 m at the shoreline and inland. Our model predicts some significant inundation along the waterfront in Long Beach and Seal Beach, as well as in some of the inner harbor areas. The inundation flow depths, which are also shown in figure 29 (only for areas with elevation higher than MHW) reach up to 2 m in a few locations. As mentioned before, we should be careful to interpret these results directly without evaluating the detailed local topography, but it is clear that this scenario produces significant tsunami amplitudes in this area. The complete 3-component time series (east and north velocity and wave height) at a location within the harbor area (fig. 30) shows significant wave activity for more than 8 hours after the first onset of the tsunami. Here, depth-averaged peak velocities are on the order of 0.5 m/s, with the maximum amplitude at around 1 m.

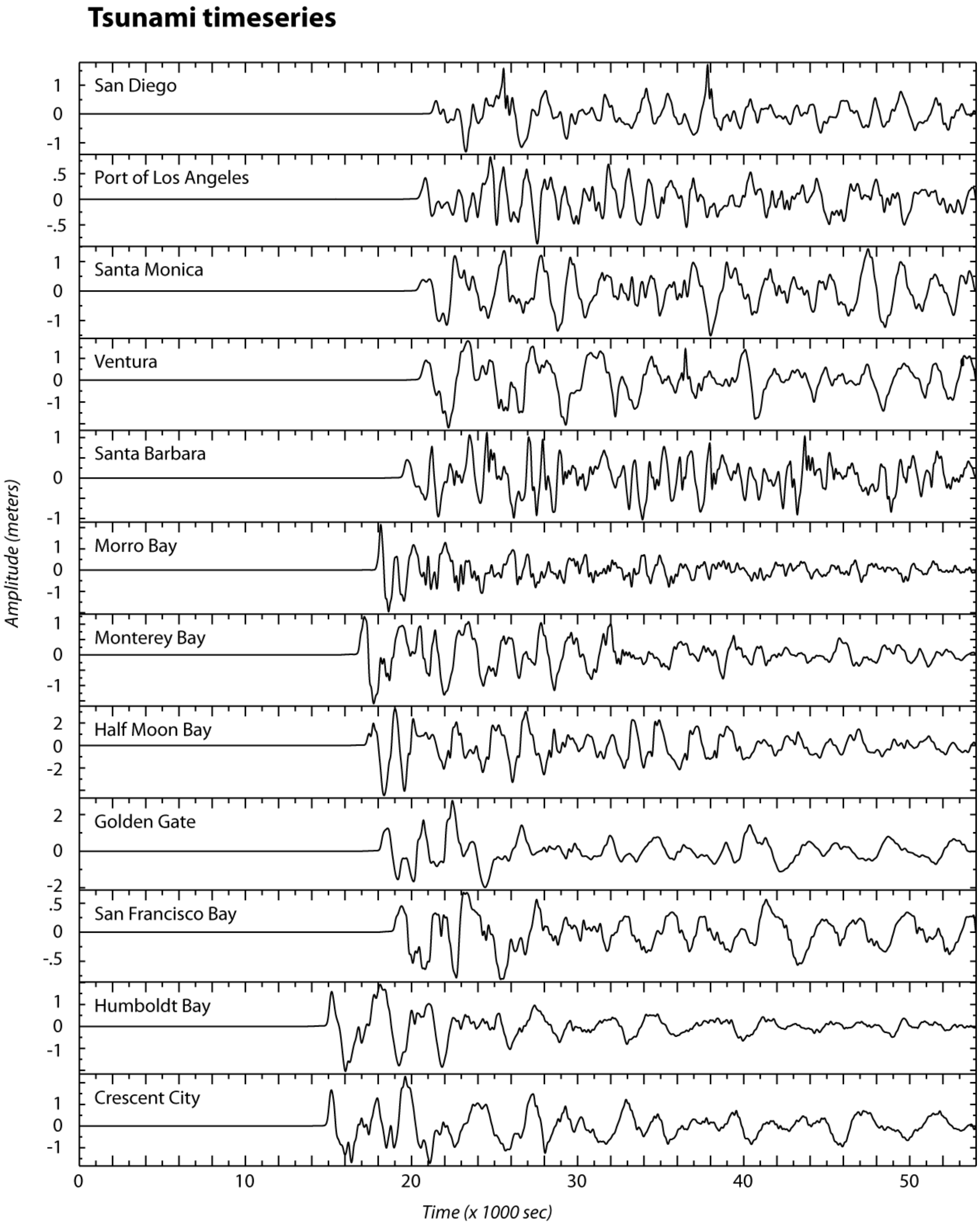

Figure 28. Tsunami wave-height time series (marigrams) from the scenario tsunami for various locations along the California coast.

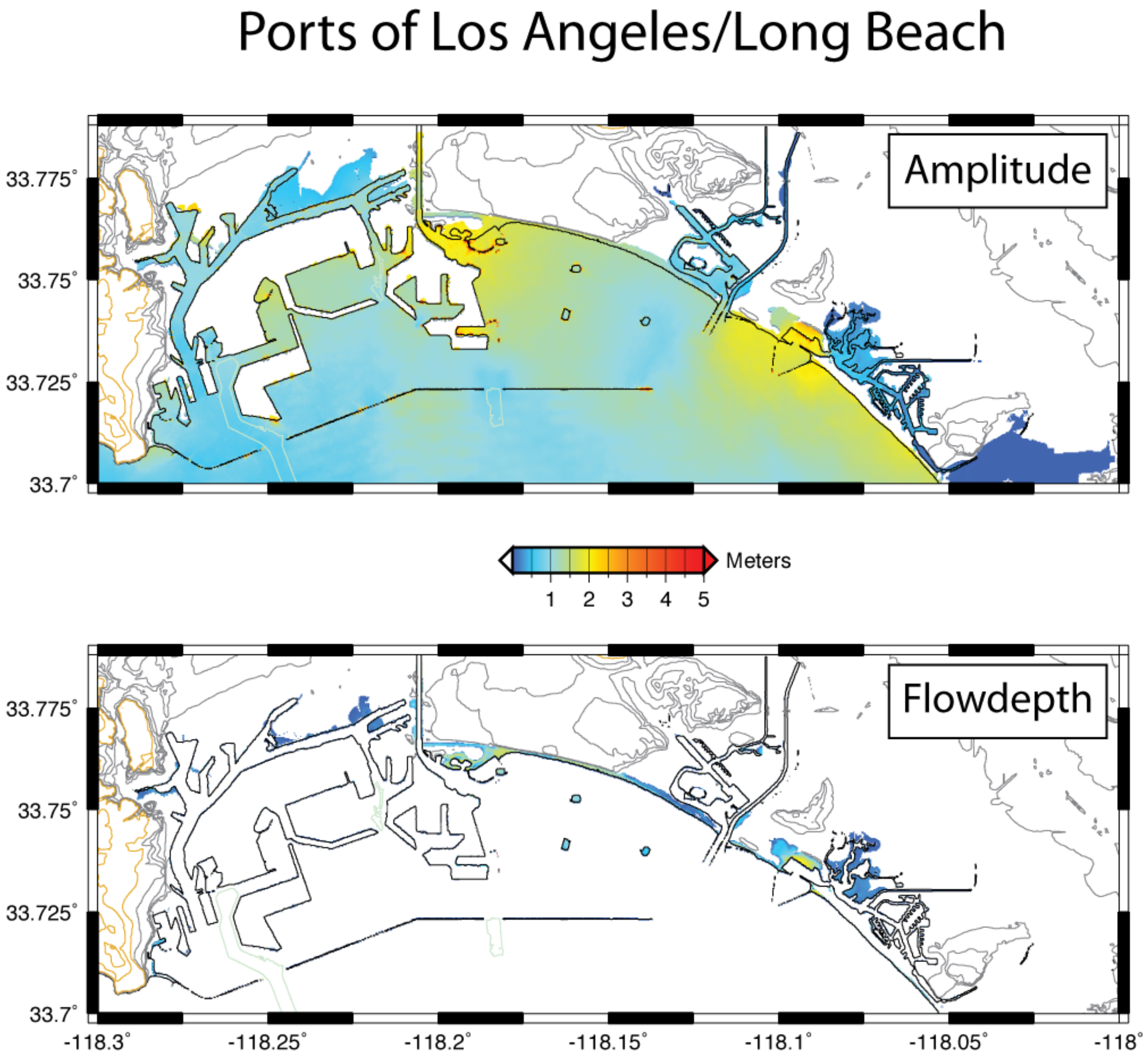
Ports of Los Angeles/Long Beach

Figure 29. Maps showing maximum amplitude (top) and maximum flow depth (bottom) in and around the Ports of Los Angeles and Long Beach. The flow depths are only shown for areas where the elevations are above mean high water. Color bar refers to both amplitude and flow depth.

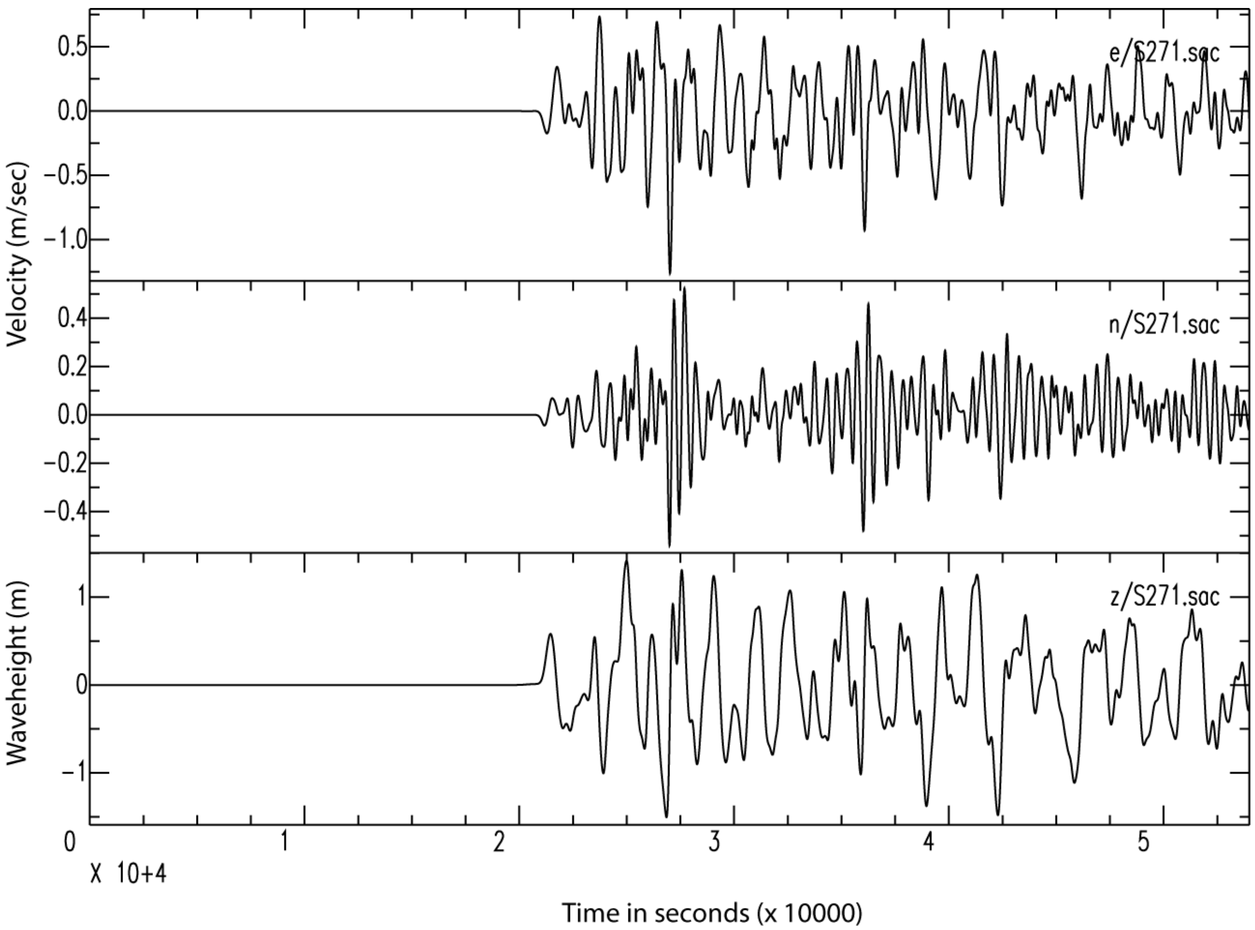

Figure 30. Time series of velocity (east, top; north, center) and wave height (bottom) for the scenario tsunami waves in the Port of Los Angeles.

In figures 31 through 38, we present similar maps for a few selected high-resolution areas along the coast. Crescent City (fig. 31) shows significant flooding of the harbor and downtown area, which is not unexpected given the severe damage that the city experienced after the 1964 Alaska earthquake. Judging from the large-scale tsunami pattern in figure 27, it appears that in addition to local resonance effects (Horrillo and others, 2008; Kowalik and others, 2008; Dengler and Uslu, 2011), the focusing due to the Cobb-Eickelberg seamount chain may contribute to the severity of the tsunami in this region.

Tsunamis increase in height as they approach the shore. In southern California, the tsunami amplitudes would range from 1 to 3 meters near shore. In central California, from Lompoc through Marin County, they would range from 2 to 7 meters in amplitude. And in northern California, the range would be from 3 to 7 meters. Project modelers assumed high tide conditions, increasing the total tsunami height by about a meter. Note that the color scale in the figures saturates at 5 m, so the figures do not fully show the highest tsunami amplitudes.

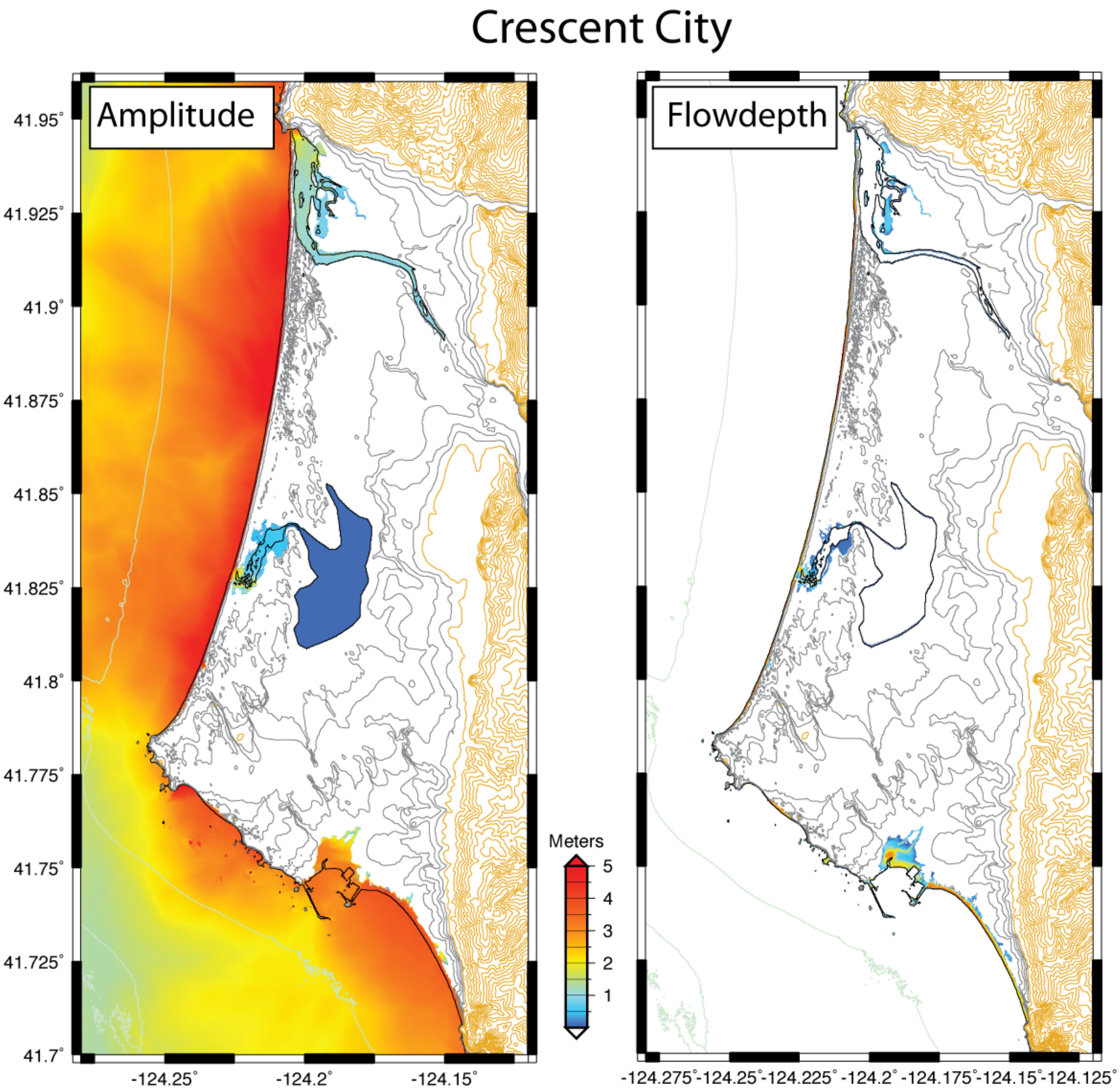

Figure 31. Maps showing maximum amplitude and flow depth of the scenario tsunami around Crescent City, California.

Farther south, we find significant tsunami wave heights and some inundation all along the central California coast, such as at the Golden Gate entrance to San Francisco Bay (fig. 32), Half Moon Bay (fig. 33), Monterey Bay (fig. 34), Morro Bay (fig. 35), and Port San Luis (fig. 36). Entering the Continental Borderlands area in Southern California, the tsunami amplitudes decrease, as was already visible in figure 4 and can also be seen, for instance, on the maps of Ventura (fig. 37), the Los Angeles/Long Beach Ports (fig. 29), and the San Diego area (fig. 38).

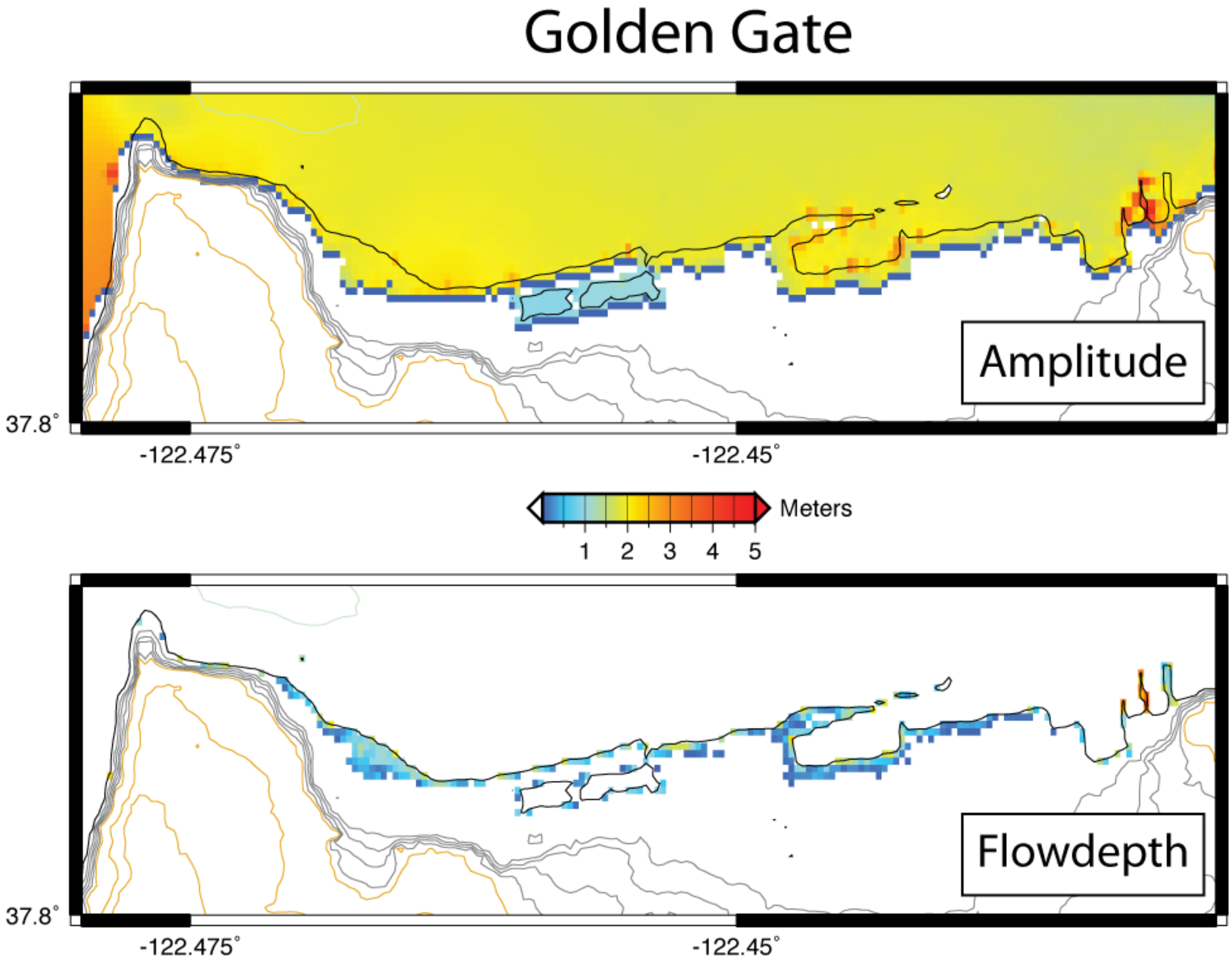

Figure 32. Maps showing maximum amplitude and flow depth of the scenario tsunami around the San Francisco shoreline just inside the Golden Gate.

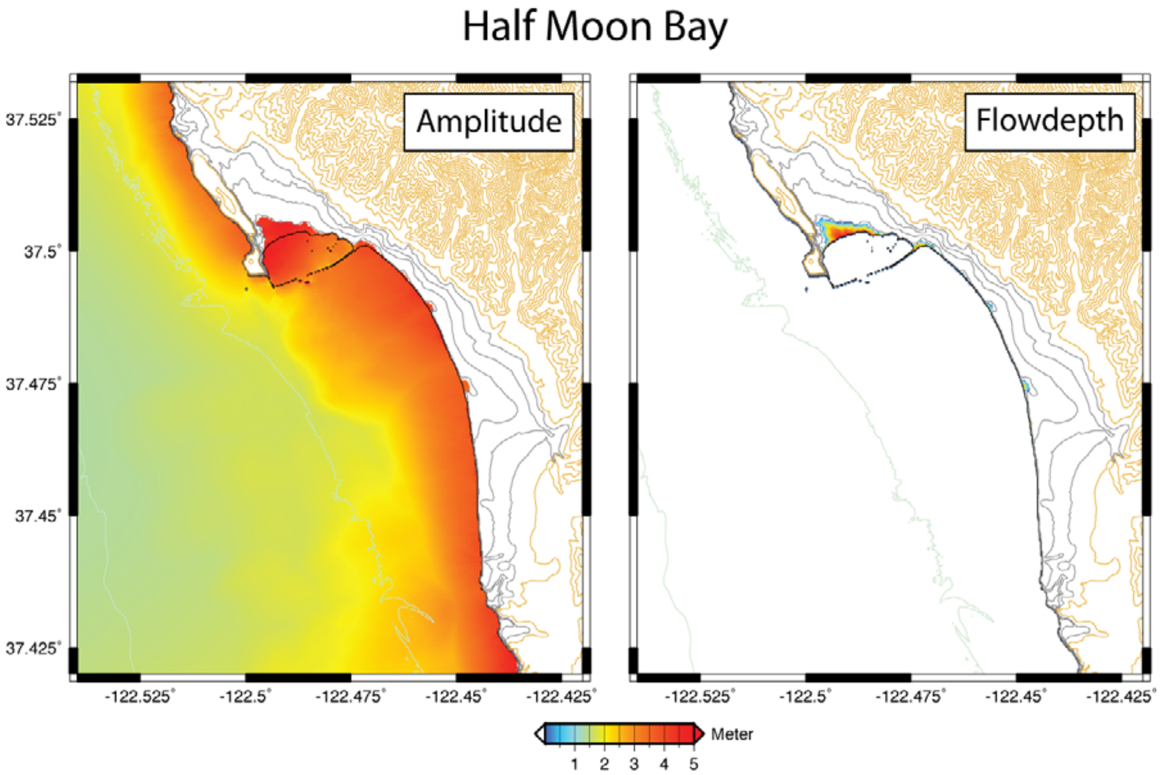

Figure 33. Maps showing maximum amplitude and flow depth of the scenario tsunami in Half Moon Bay, California.

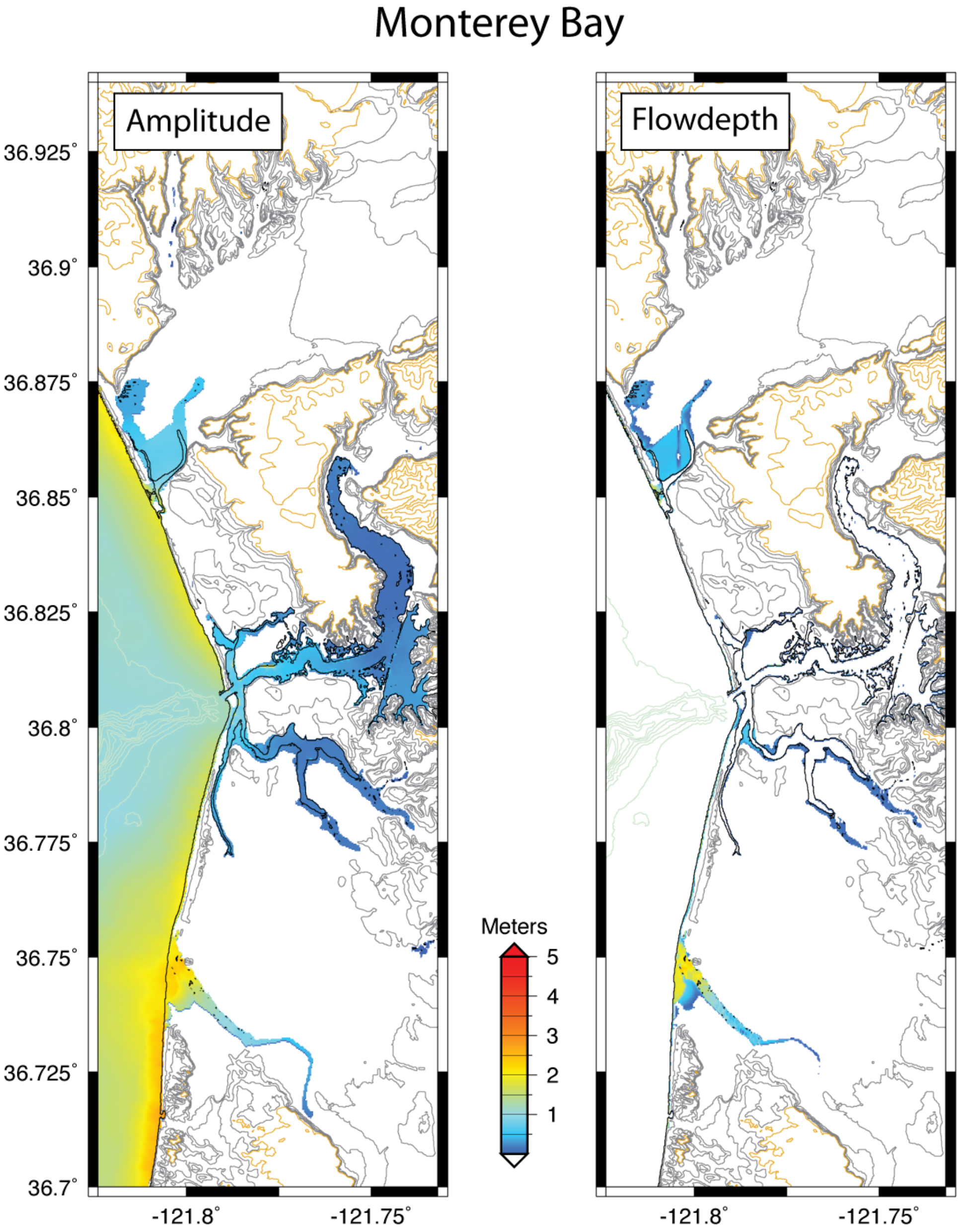

Figure 34. Maps showing maximum amplitude and flow depth of the scenario tsunami along the eastern shore of Monterey Bay, California.

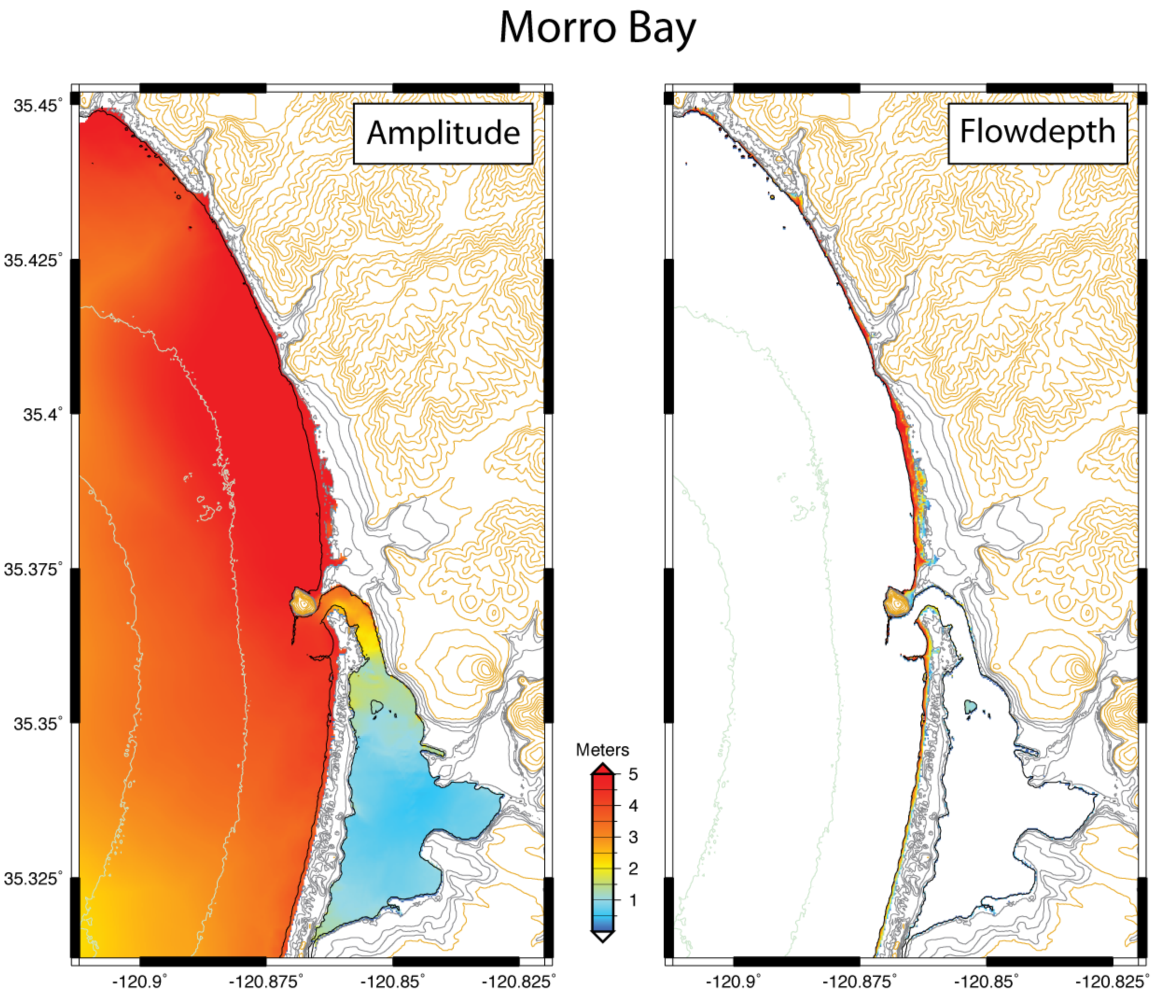

Figure 35. Maps showing maximum amplitude and flow depth of the scenario tsunami around Morro Bay, California.

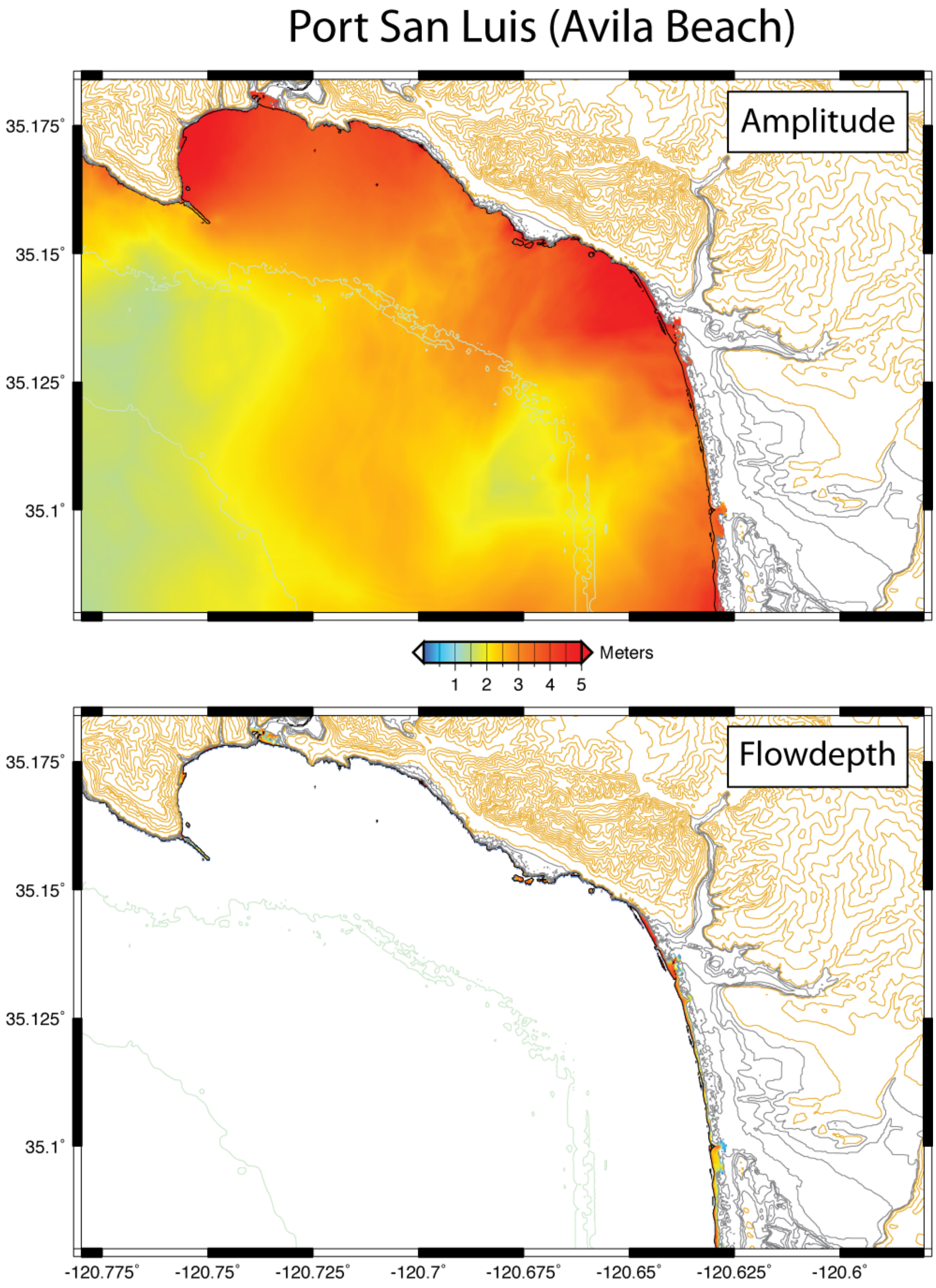

Figure 36. Maps showing maximum amplitude and flow depth of the scenario tsunami around Avila Beach, California.

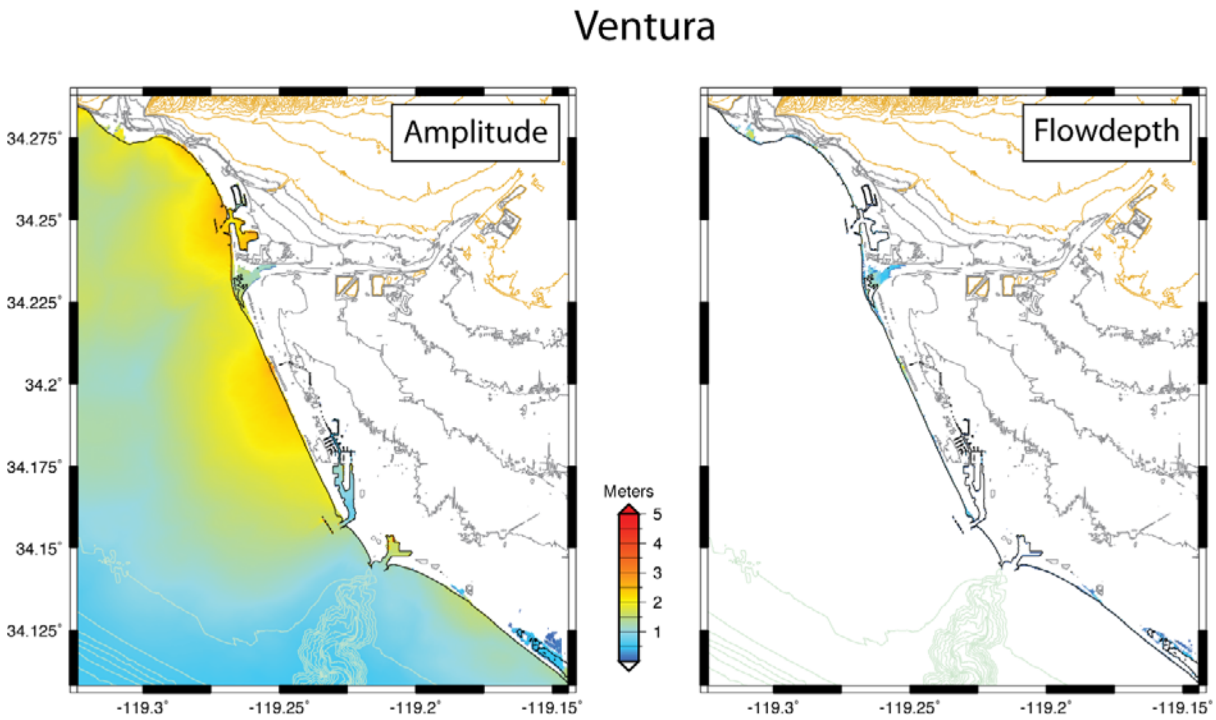

Figure 37. Maps showing maximum amplitude and flow depth of the scenario tsunami at Ventura, California.

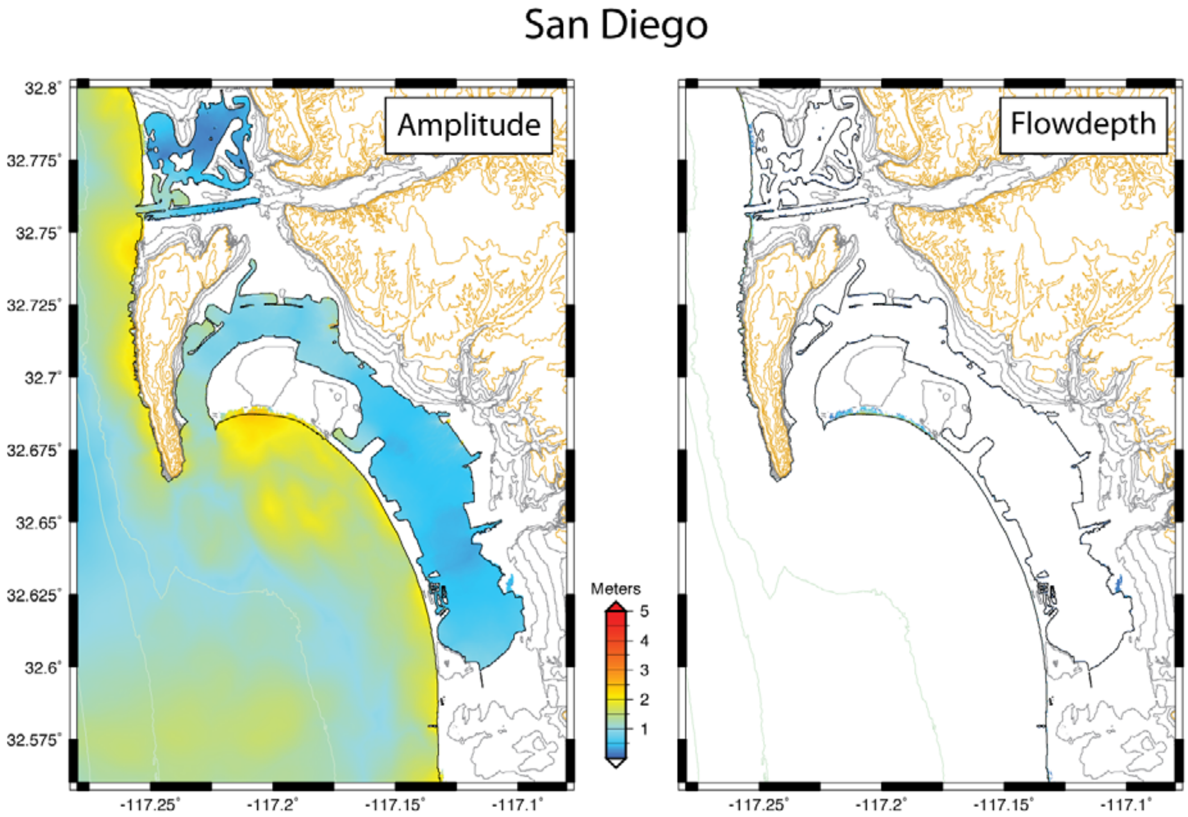

Figure 38. Maps showing maximum amplitude and flow depth of the scenario tsunami at San Diego, California.

The locations of all these detailed maps are shown in figure 26, but they can also be found tabulated and referenced in tables 4 through 6. All the high-resolution maps have been made available in ASCII format as well as in the form of kmz files for viewing in Google Earth. The contents of the data files (both primary wave height/drawdown and velocity data, as well as derived products such as momentum flux, are explained below.

Explanation of Data Files

The maps and other products derived using software of the URS Corporation show the results of the modeling of the scenario tsunami along different parts of the California coast. All maps are at a resolution of approximately 30 m and were derived from the database provided by the National Geophysical Data Center‘s Tsunami Gridding Project (http://www.ngdc.noaa.gov/mgg/inundation/). The kmz files contain the following types of data (using the Oceanside grid as example):

- Inundation-Oceanside.kmz—map of maximum tsunami amplitude. Units are meters, relative to reference level, which is high tide + 0.2 m (maximum tide level for that particular day).
- Flowdepth-Oceanside.kmz—map of maximum height of the water level above the ground surface at any location. Derived from maximum tsunami amplitude minus the topography.
- Velocity-Oceanside.kmz—map of maximum flow speed (m/s) in any direction. Note that the velocity is recorded for any flow depth, and large velocities beyond the shorelines may reflect movement of very thin layers of water during inundation.
- Drawdown-Oceanside.kmz—lowest tsunami amplitude relative to the reference level (high tide + 0.2 m).
- Mindepth-Oceanside.kmz—map of minimum height of the water level relative to the solid ground (including seafloor). These maps are primarily useful to study the possibility of vessels running aground during drawdown.

4. Numerical Modeling of Tsunami Effects in Southern California from a Hypothetical *M*9.1 Earthquake near the Alaska Peninsula

By José Borrero, Costas Synolakis, and Vasily Titov

Introduction

The work presented here describes the hydrodynamic numerical modeling of tsunami-induced effects at several sites along the southern California coast. This modeling study is conducted in support of the U.S. Geological Survey's (USGS) SAFRR: Science Application for Risk Reduction project. The objective of this study is to describe in detail, using the best available science, the effects on the coast and infrastructure of southern California of a hypothetical, but possible, large tsunami generated by a magnitude 9.1 earthquake offshore of the Alaska Peninsula. The results will enable researchers to better understand and prepare for natural disasters and can also be disseminated as educational material for the public.

The model earthquake is defined to occur at 11:50 a.m. PDT (10:50 a.m. Alaska time) on Thursday March 27th, 2014, the 50th anniversary of the great 1964 Alaska earthquake, which generated California's most destructive tsunami in recorded history. The simulations presented here should enable emergency responders, as well as port officials and engineers, to better understand the potential impact of this type of event.

The numerical modeling presented here was carried out using the Community Model Interface for Tsunamis (ComMIT) numerical modeling tool. The ComMIT model interface was developed by the National Oceanic and Atmospheric Administration's (NOAA) Center for Tsunami Research (NCTR) following the disastrous December 26, 2004, Indian Ocean tsunami as a way to efficiently distribute assessment capabilities amongst tsunami prone countries.

The backbone of the ComMIT system is a database of precomputed deep water propagation results for tsunamis generated by unit (for example, 1 m) displacements on fault plane segments (100 x 50 km) positioned along the world's subduction zones. Currently, there are 1,691 precomputed unit-source propagation model runs covering the world's oceans included in the propagation database (fig. 39). Using linear superposition, the deep ocean tsunami propagation results from more complex faulting scenarios can be created by scaling and (or) combining the precomputed propagation results from a number of unit sources (Titov and others, 2011). The resulting transoceanic tsunami propagation results are then used as boundary inputs for a series of nested nearshore grids covering a coastline of interest. The nested model propagates the tsunami to shore, computing wave height, velocity, and overland inundation. The hydrodynamic calculations contained within ComMIT are based on the MOST (Method Of Splitting Tsunami) algorithm developed by Titov and Synolakis (1995, 1998).

During a real tsunami event, the ComMIT system can also be used in conjunction with real-time recordings of tsunami waveforms on one or more of the deep ocean tsunameter (DART) stations deployed throughout the oceans to fine-tune details of an earthquake source mechanism in real time. An iterative algorithm that selects and scales the unit source segments is used until an acceptable fit to the observed DART data is met. Because there are currently several DART stations in operation along the Aleutian trench, a tsunami emanating from this region would be recorded by the system and updated source models would be made available, allowing for an assessment of the potential tsunami impact before its arrival on the affected shores. This approach was used successfully to assess the impacts of the Tohoku tsunami in New Zealand (Borrero and others, 2012).

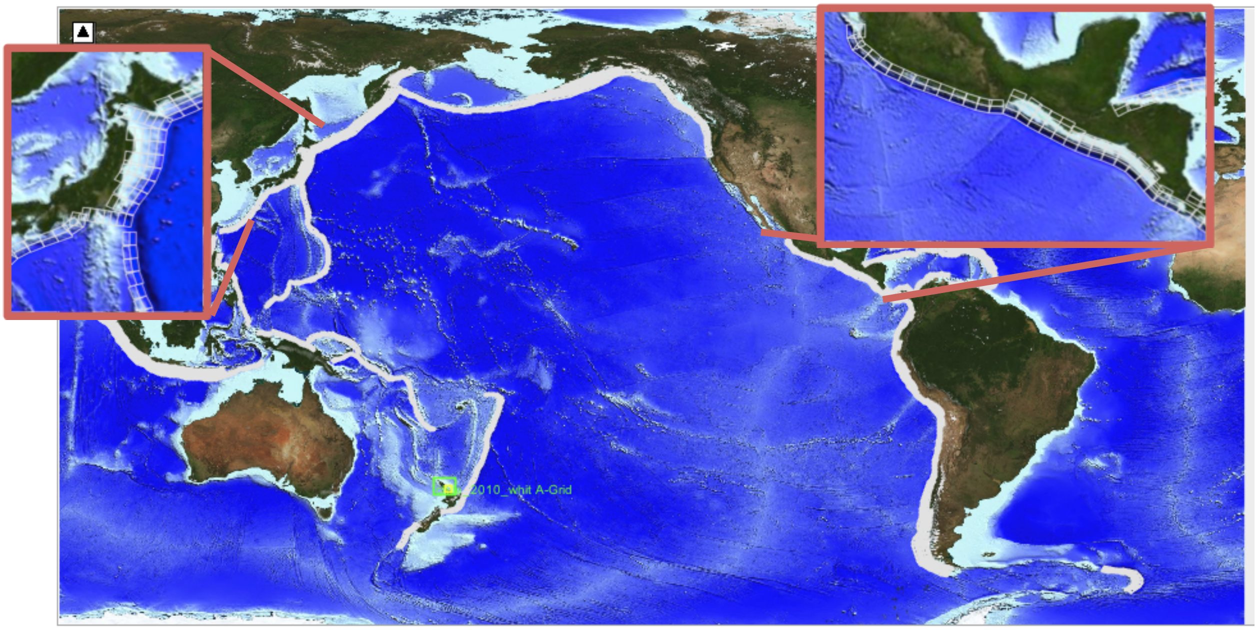

Figure 39. Map showing the source regions and potentially affected coasts in the ComMIT propagation model database for tsunamis in the world's oceans. Inset maps show the details of the source zone discretization into rectangular subfaults.

Earthquake Source Model

The earthquake source model for this scenario was defined by the U.S. Geological Survey (USGS) (fig. 40). The source was defined by 64 subfaults, each approximately 25 x 50 km, for a total fault plane area of 400 x 200 km. The sources featured variable slip amounts and dip angles. Rake was assumed to be pure dip-slip, while strike angle varied across the segments to maintain alignment with the trench bathymetry. The rock rigidity values also varied with harder material at depth (50 GPa) and softer material near the surface (30 GPa).

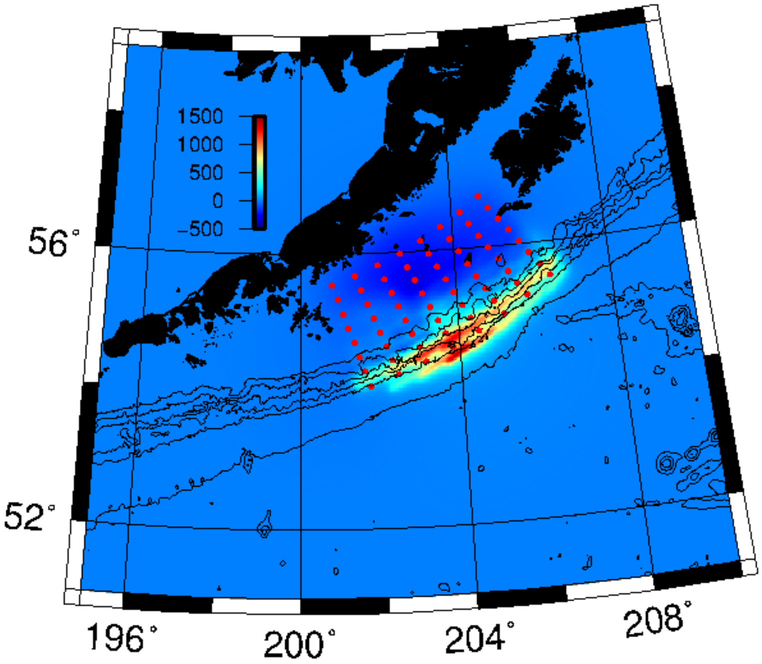

Figure 40. Map showing deformation data for the scenario tsunami provided by the USGS. Subfault epicenters are indicated by the red dots.

To calibrate the initial condition for implementation into the ComMIT model, we used the subfault information provided by USGS to initialize a version of the Okada (1985) elastic dislocation model. Figure 41 shows the output from that exercise and suggests that this particular version of the elastic deformation model gives similar result to the defined source scenario.

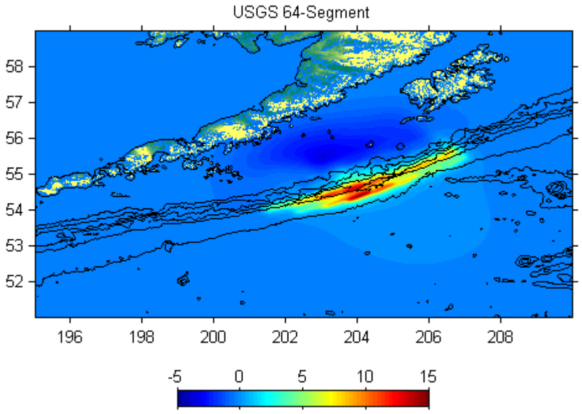

Figure 41. Map showing surface displacement computed by the MOST version of Okada's (1985) elastic dislocation model. Color scale in meters.

Because the subfault size used in the ComMIT framework is larger than the subfaults used in the USGS source model, we adapted the 64-segment model into a 16-segment model compatible with the subfault geometry available via the ComMIT model interface as shown in figure 42.

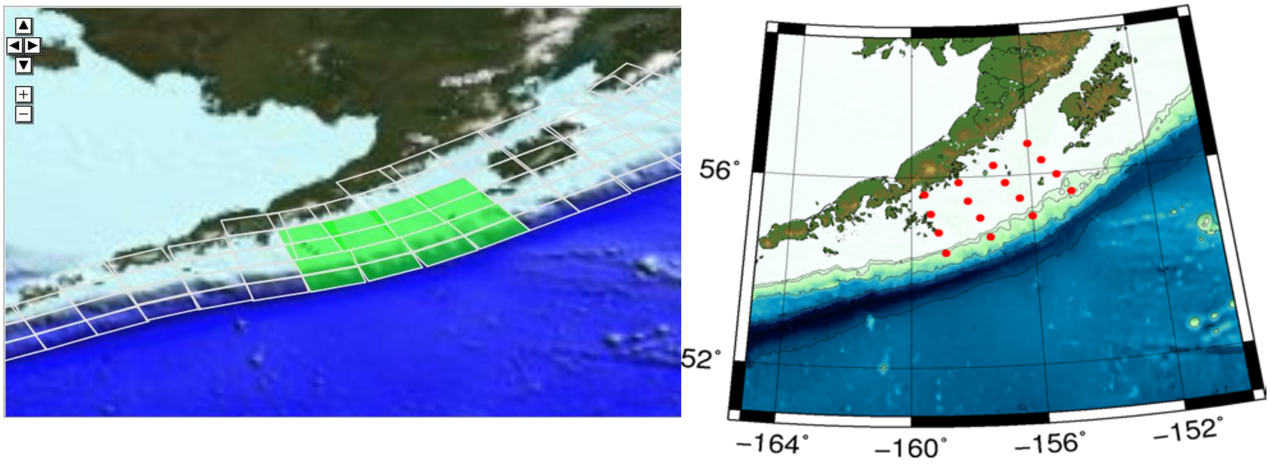

Figure 42. Maps showing the ComMIT subfault segments (left) that most closely match the source region defined for this study (right).

To implement the source model into the ComMIT model, the 64-segment source model (average slip = 18.63 m) was compiled into four-segment clusters as indicated in table 7. The average of each four-segment cluster was then used as the slip over each of the 100 km x 50 km subfaults available to the ComMIT model. Slip amounts are indicated in table 8. The elastic deformation model was then used to compute the corresponding sea-floor deformation (fig. 43).

Table 7. Slip amount (in meters) on each subfault segment of the original source model. Average slip is 18.6 m. The average slip over the four segments highlighted in red is 53 m.

	West						**East**	
North	0	2	4	7	5	3	1	0
	2	5	8	10	8	6	4	3
	4	10	15	20	15	10	8	6
	5	10	20	35	25	18	13	11
	8	15	25	47	35	25	20	18
	10	20	35	55	42	32	27	25
	15	30	50	65	50	40	35	33
South	0	10	22	38	28	20	13	11

Table 8. A 16-segment subfault comprising 4-segment average slip amounts from the 64-segment model. Average slip = 18.5 m.

	W			E
N	2.3	7.3	5.5	2.0
	7.3	22.5	17.0	9.5
	13.3	40.5	33.5	22.5
S	13.8	43.8	34.5	21.6

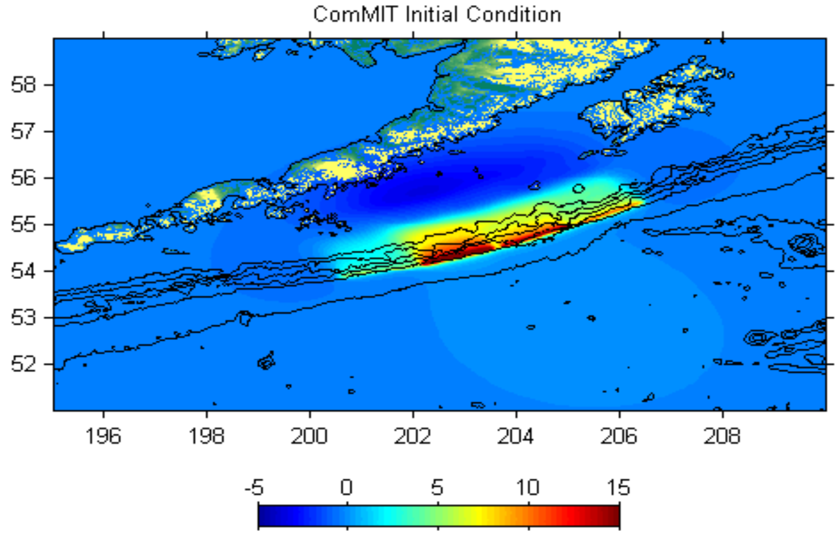

Figure 43. Maps showing surface deformation caused by a 16-segment fault model derived from 4-segment averages of the 64-segment fault model. Color scale in meters.

It is apparent that the deformation predicted by this representation of the slip distribution is somewhat different from that in the 64-segment model. However, the magnitude and areal extent of uplift and subsidence are comparable. In an effort to fine-tune the source to fit the deformation pattern produced by the 64-segment model, we used an ad hoc, trial and error approach to distribute slip across the segments with the goal of maintaining the overall average slip. In this process we noted that choosing the four segments highlighted with the red outline in table 7 yields an average slip of 53 m, which is larger than the average of any other grouping of four segments. We used this number simply as guidance as to what the highest allowable slip amount would be on one segment of the 16-fault model.

While there are virtually an infinite number of possible slip distributions, we eventually chose one that somewhat approximates the deformation pattern indicated in the original 64-segment approach. The primary difference between the 16-segment and 64-segment fault models is the location of the maximum displacement relative to the trench axis. The more detailed 64-segment approach is able to push the deformation towards the southeast and into deeper water than is possible with the constraints imposed by the unit-source geometry used in the ComMIT modeling approach. For this study, we present model results based on the revised deformation model (tables 9 and 10, fig. 44).

Table 9. An ad-hoc, trial and error, modified version of the 16-segment fault model used for the simulations. Average slip = 18.6 m.

	W			**E**
N	5	7	7	3
	10	23	25	12
	15	30	48	15
S	10	32	40	15

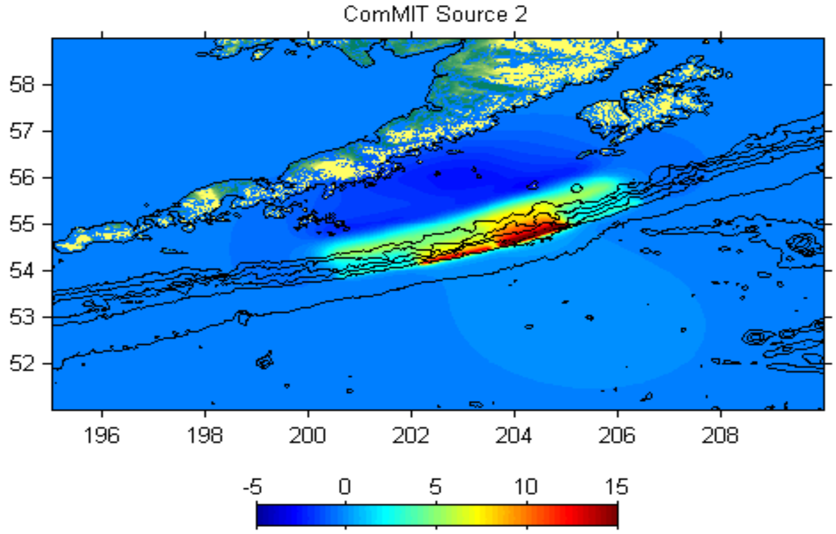

Figure 44. Map showing computed surface deformation created by an alternate version of the 16-segment fault model for the tsunami source region. Color scale in meters.

Table 10. Fault parameters for the 16-segment source based on the NOAA-ComMIT propagation database.

Segment Name	Longitude (deg W)	Latitude (deg E)	Strike (deg)	Dip (deg)	Depth (km)	Slip 1 (m)	Slip 2 (m)
acsz–28a	200.882	54.830	253.0	15	17.94	13.3	15.0
acsz–28b	201.108	54.400	253.0	15	5.00	13.8	10.0
acsz–28y	200.417	55.641	252.7	15	43.82	2.3	5.0
acsz–28z	200.636	55.225	252.9	15	30.88	7.3	10.0
acsz–29a	202.261	55.133	247.0	15	17.94	40.5	30.0
acsz–29b	202.565	54.720	247.0	15	5.00	43.8	32.0
acsz–29y	201.573	55.889	246.0	15	43.82	7.3	7.0
acsz–29z	201.880	55.491	246.2	15	30.88	22.5	23.0
acsz–30a	203.604	55.509	240.0	15	17.94	33.5	48.0
acsz–30b	203.997	55.120	240.0	15	5.00	34.5	40.0
acsz–30y	202.772	56.232	240.2	15	43.82	5.5	7.0
acsz–30z	203.152	55.853	240.5	15	30.88	17.0	25.0
acsz–31a	204.895	55.970	236.0	15	17.94	22.5	15.0
acsz–31b	205.340	55.598	236.0	15	5.00	23.0	15.0
acsz–31y	203.990	56.661	235.3	15	43.82	2.0	3.0
acsz–31z	204.432	56.302	235.7	15	30.88	9.5	12.0
					Average	**18.6**	**18.6**

Bathymetry Grids

The ComMIT model uses a system of three nested numerical grids for the nearshore inundation part of the modeling process. Model grid bathymetry was obtained from the National Geophysical Data Center's (NGDC) Tsunami Inundation Digital Elevation Models (DEM's) (NGDC: *http://www.ngdc.noaa.gov/mgg/inundation/*). The data are freely available for download, and for this project we worked from the Santa Monica and San Diego datasets. Each of these datasets is provided at a resolution of 1/3 arc sec, or approximately 10 m. Coarser model bathymetry grids of 9 arc sec and 2 arc sec covering regional areas were constructed by downsampling the higher resolution source bathymetry. An example of the grid extents for sites in San Pedro Bay is shown in figure 45. Grid systems for a total of eight sites were produced for this study; these included Marina Del Rey in Santa Monica Bay, Long Beach, Seal Beach, Anaheim Bay, Newport Bay, Del Mar, La Jolla, and Mission Bay (Figure 46). The model datum is set to mean high water (MHW).

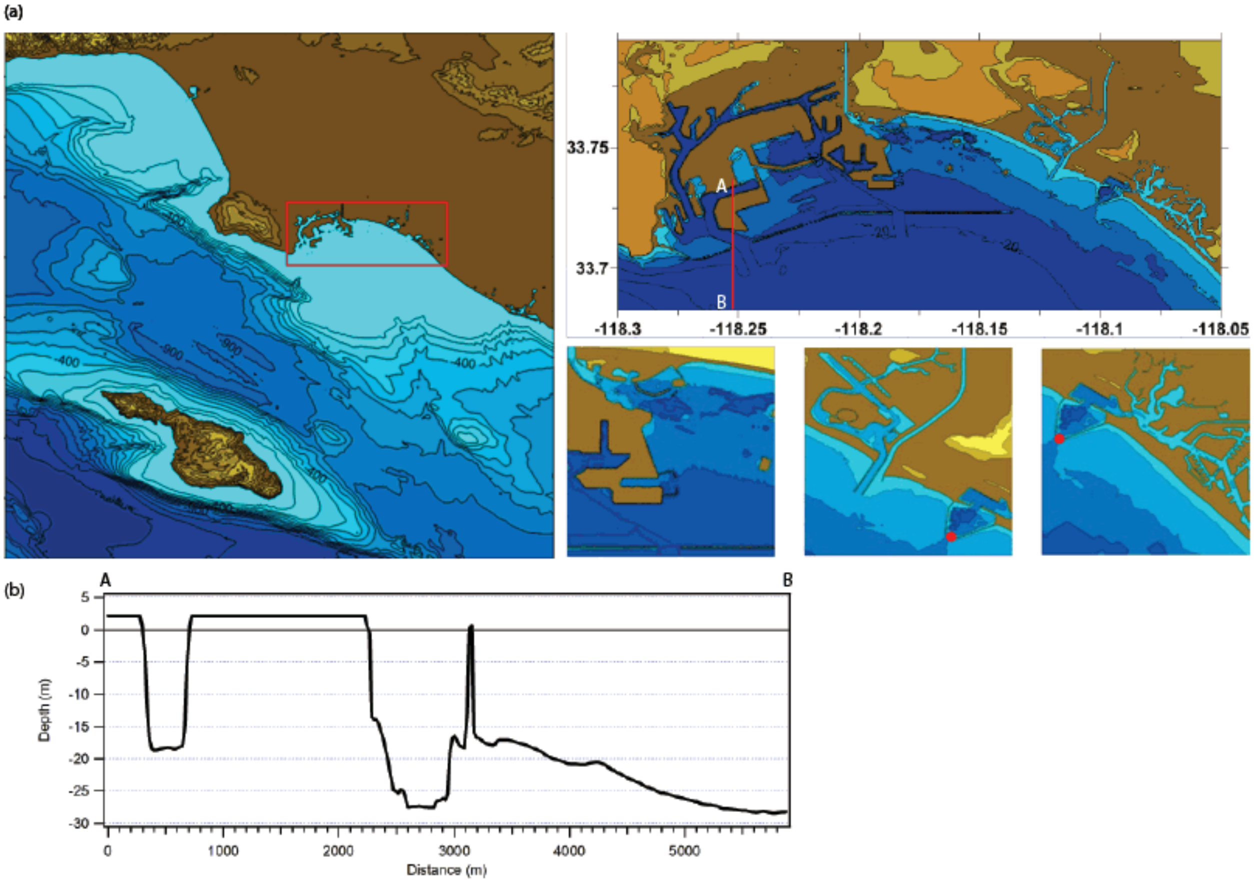

Figure 45. Maps and graph showing model results for San Pedro Bay, California. (a) Examples of the grid coverage for sites in San Pedro Bay. Grid resolutions are 9 arc sec (upper left), 2 arc sec (upper right), and 1/3 arc sec (three small maps). The location of the bathymetry transect (A-B) plotted in panel (b) is indicated with the red line. Red dots indicate location of time-series plots shown in Figures 47 and 48. (b) Bathymetry transect (A-B) across Terminal Island, the entrance channel, and the western breakwater segment.

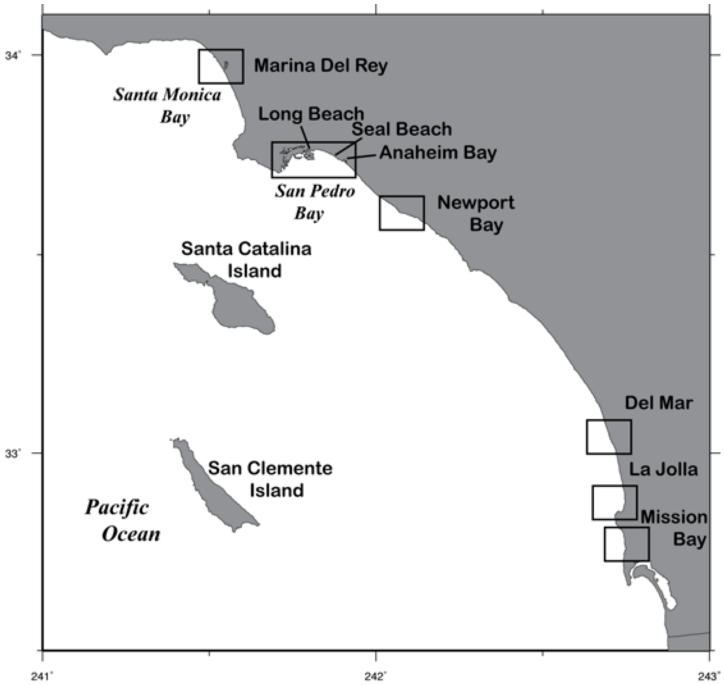

Figure 46. Map showing the sites of modeled tsunami effects in southern California covered by this study.

Model Results

A sensitivity test was first performed to compare the model results between the two earthquake source models described above. This test was conducted only on the Marina del Rey bathymetry. The results presented in figure 47 show that the model output is relatively insensitive to differences in the slip distribution at the source. We also investigated the consistency of the model results over different model grid configurations. For this test, the same tsunami source was used and model output was compared from a point corresponding to the same location in two model grids with overlapping areas. This test compared the model output at the entrance to Anaheim bay, a location covered by both the Seal Beach and Anaheim Bay grids (see the location of the red dot in figure 45. The results shown in figure 48 show that the model results are consistent for each of those two grids, providing a first-order reality check on the model results.

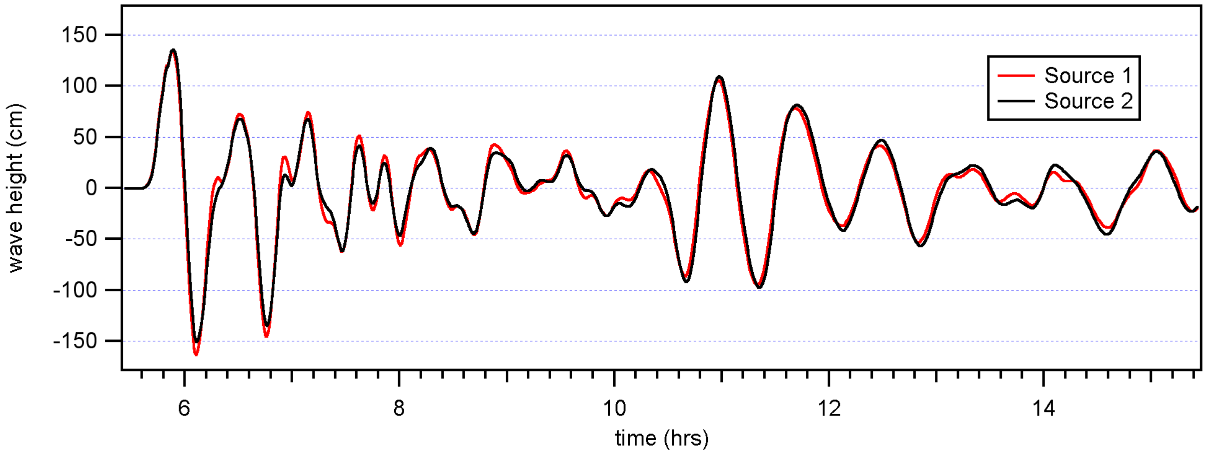

Figure 47. Plot of modeled wave height at Marina del Rey, comparing the effects from tsunami source 1 and tsunami source 2.

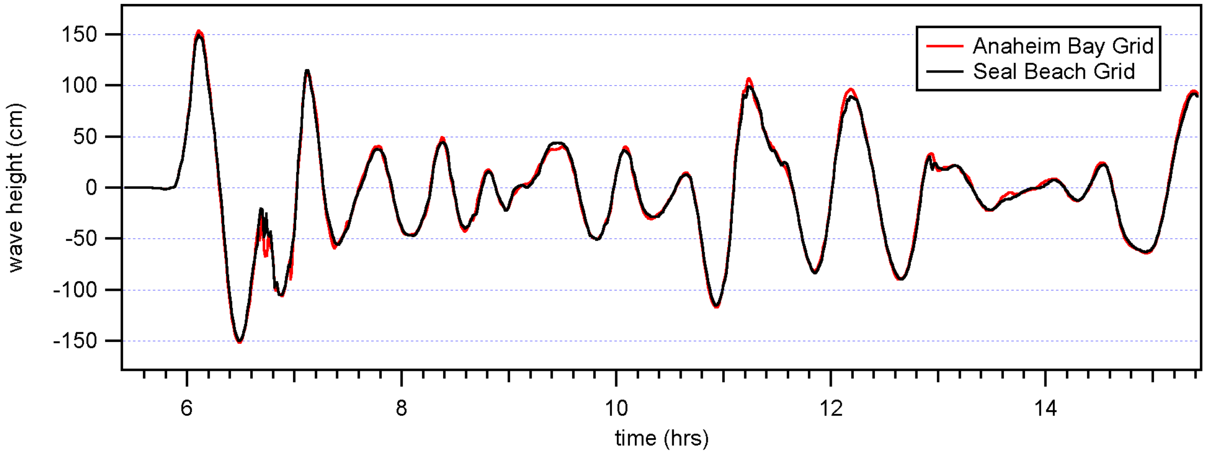

Figure 48. Plot of modeled wave height at the entrance to Anaheim Bay from separate model runs with overlapping model grids. Note that the model returns from the two grids are virtually identical.

The model was then run for the remainder of the nearshore grid regions using tsunami source 2. Model outputs in the form of maximum computed wave height and maximum current speed are presented in figures 49–54. Time-series outputs of wave height from a nearshore point (approximately 5-m depth) in each of the model grids are presented in figure 49. These plots show that the tsunami arrival times along the southern California coast would be just under 6 hours after the earthquake, with the wave reaching the northern sites (such as Marina del Rey) before the southern sites (such as Mission Bay). There is some discrepancy in this general rule, as indicated by the timing of the peak wave heights at the San Pedro Bay sites (Long Beach, Seal Beach, and Anaheim Bay). The shallow waters around these areas slow the tsunami arrival such that peak wave heights occur several minutes after peak wave heights at sites further south (that is, Newport through Mission Bay). Note also that the sites located in Santa Monica and San Pedro Bays have a very noticeable resurgence in tsunami wave heights occurring 10.5 to 13 hours after the earthquake (4.5 to 7 hours after arrival). While this feature is evident at the other sites, it is not as large or long lasting as at Santa Monica or San Pedro Bay. This feature is an indication of the susceptibility of these areas to long-wave resonance, enhanced tsunami wave heights, and extended tsunami duration.

Figure 50 presents the maximum computed water level over the coarsest (A-level) nearshore grids. These two plots show the maximum tsunami wave heights on a regional scale. The effect of seiching in Santa Monica Bay is evident, as well as the elevated wave heights in San Pedro Bay. Figure 51 presents the maximum computed wave height and current velocity in the region around Marina del Rey. Although the wave heights predicted by the model are not extremely large, the currents induced by the tsunami are significant, particularly on the entrance channel to the marina basin and at the ends of each of the marina slipways.

Figure 52 plots the model results for the scenario tsunami at the marine facilities located in San Pedro Bay, south of Los Angeles. This area is home to the ports of Los Angeles and Long Beach, the recreational and residential marinas of Alamitos Bay and Huntington Harbor, and the military installation of Anaheim Bay and the Naval Weapons Station. This area is also one of the most strongly affected by a far field tsunami originating from Alaska. The model results predict maximum water levels of up to 2.5 m, with some significant overland flooding and coastal inundation. Inundation is predicted around the area of downtown Long Beach, as well as over the barrier beach at Belmont Shores and into the grounds around the Naval Weapons Station. Tsunami current speeds are also significant, particularly where the flows are constrained by coastal structures such as harbor training walls or jetties.

The effects at Newport Bay (fig. 53) are not as significant. The predicted wave heights are small and the current speeds are slower. This is probably due to the generally southward-facing orientation of the shoreline here, which does not receive the full, head-on brunt of tsunami coming from the west and northwest. There is however evidence of some small-scale inundation on properties inside the Harbor.

Farther south, the open coast sites of Del Mar (fig. 54) and La Jolla (fig. 55) do not show a strong tsunami signal. The maximum tsunami wave height is on the order of 1.25 m and does not induce any substantial inundation. A small amount of coastal inundation is evident at the entrance to the Del Mar lagoon (see fig. 54); however, it is not significant.

Finally, at Mission Bay, more substantial tsunami effects are seen (fig. 56). Even though the tsunami wave heights are similar to the heights modeled at Del Mar and La Jolla, the lower topography along Mission Beach leads to some on-land inundation. There are also strong currents modeled to occur in the entrance channel to Mission Bay.

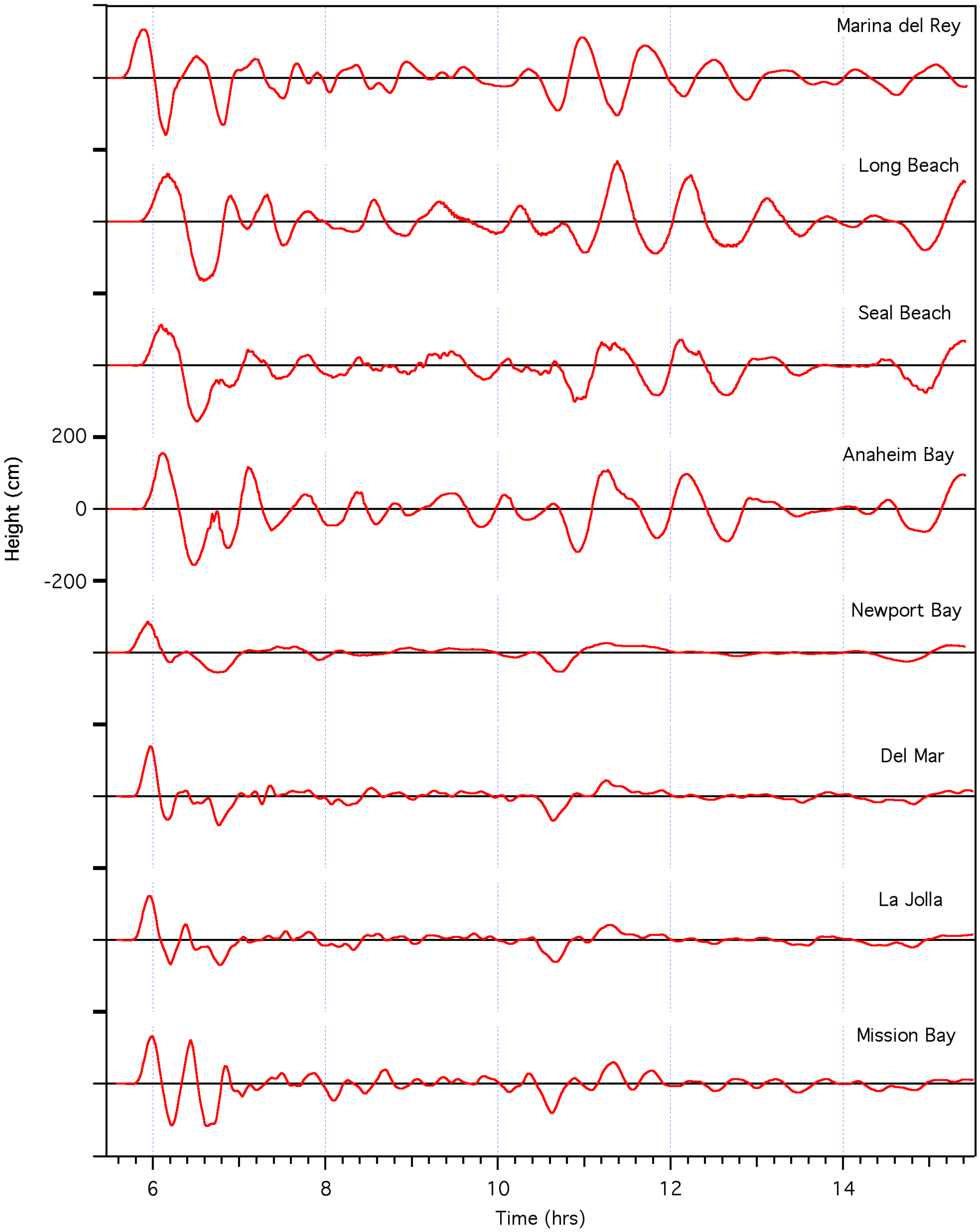

Figure 49. Time series outputs showing tsunami wave heights in each of the nearshore regions.

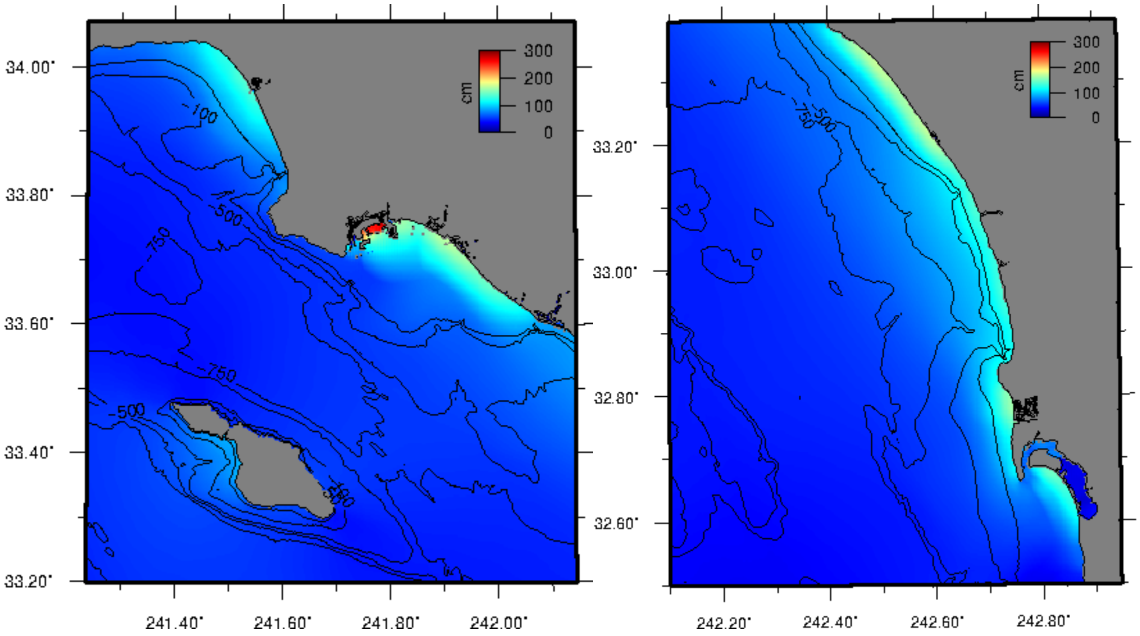

Figure 50. Maps showing maximum computed tsunami wave heights in the A-level (coarsest) grids along the southern California coast. Grid resolution is 9 arc sec.

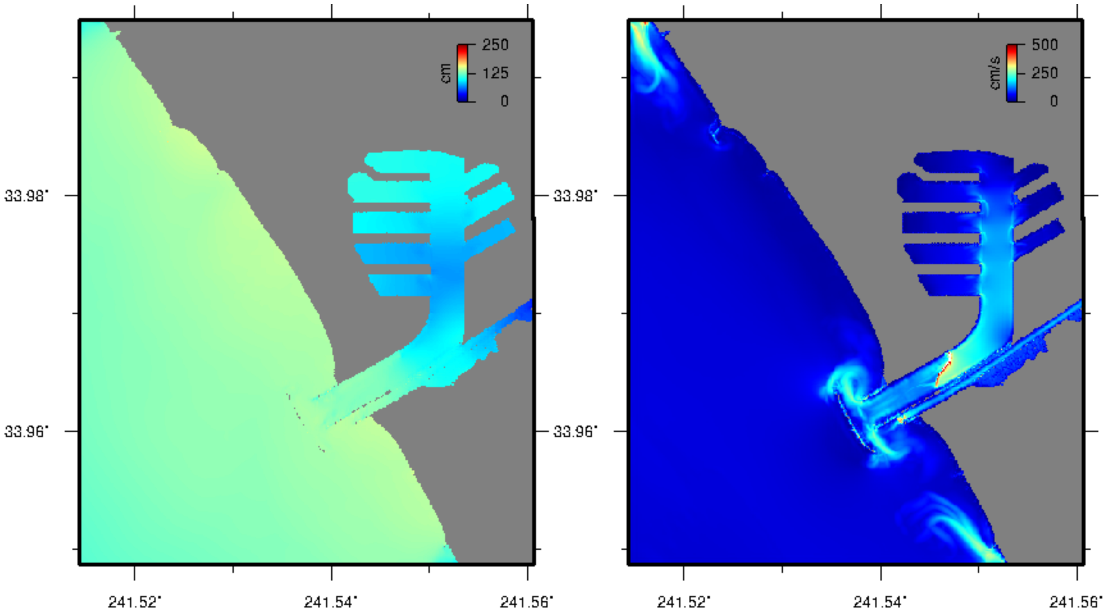

Figure 51. Maps showing maximum computed tsunami wave heights (left) and current speeds (right) at Marina del Rey, California.

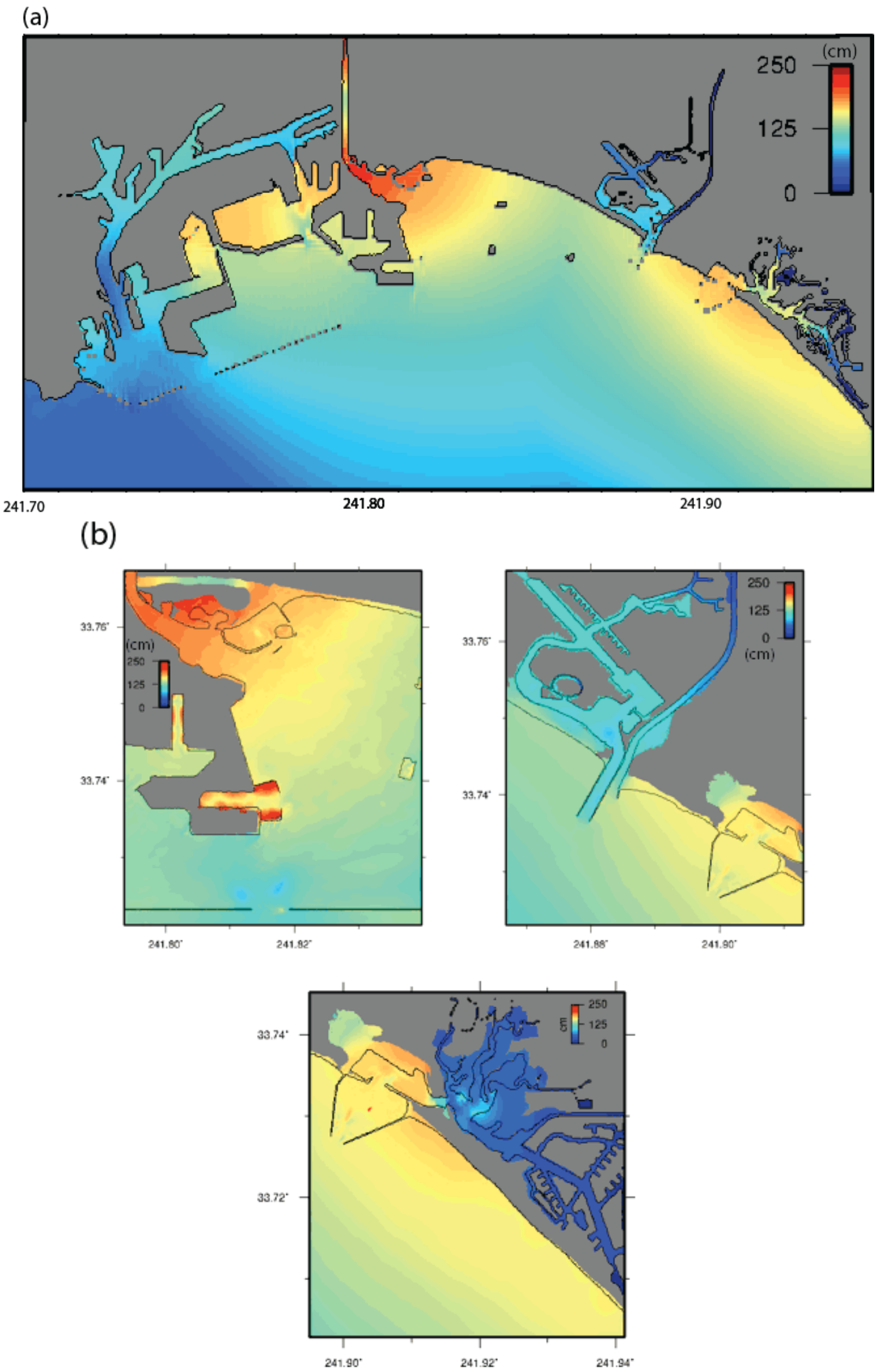
(a)
250
125
0
(cm)
241.70
241.80
241.90
(b)
33.76°
33.74°
(cm)
250
125
0
241.80°
241.82°
33.76°
33.74°
250
125
0
(cm)
241.88°
241.90°
33.74°
33.72°
cm
250
125
0
241.90°
241.92°
241.94°

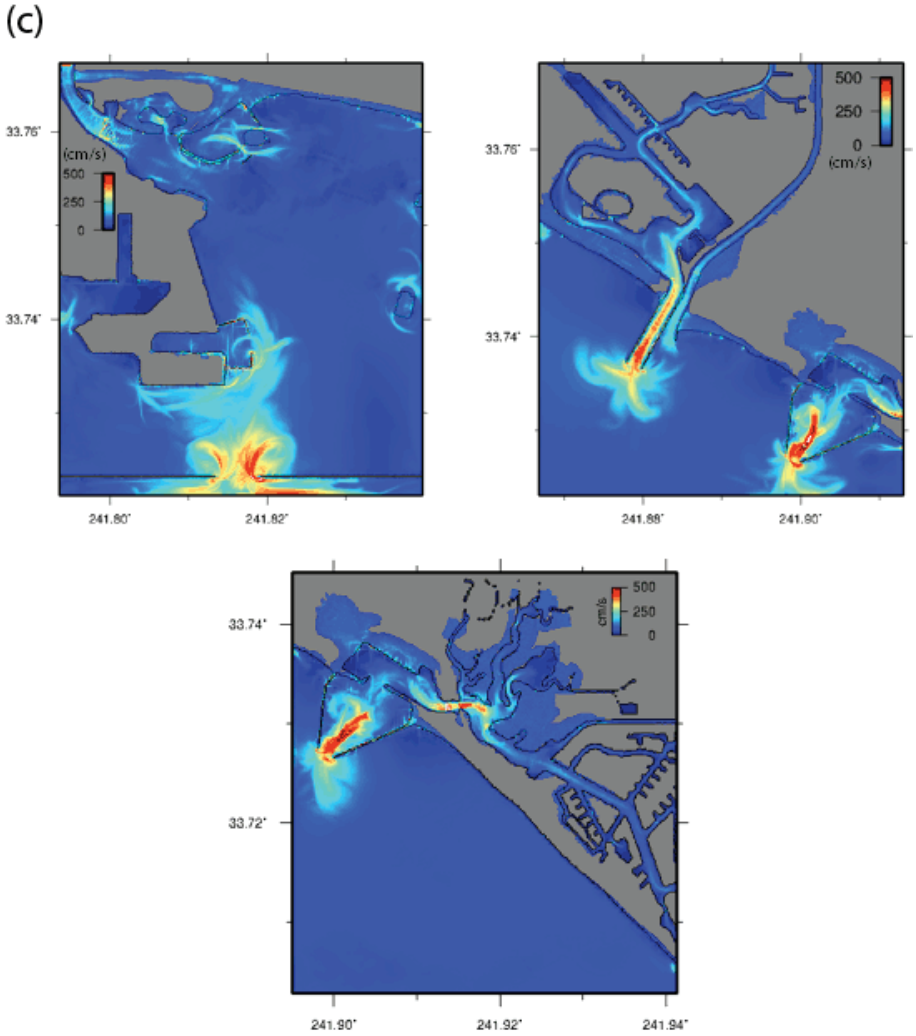

Figure 52. Maps showing modeled maximum tsunami wave heights and current speeds in San Pedro Bay and sites within the bay at different grid levels. Wave heights are in centimeters and current speeds are in cm/sec. (a) Modeled maximum tsunami wave heights in the B-level (2 arc sec) grid covering the marine facilities in San Pedro Bay. (b) Modeled maximum tsunami wave heights in the C-level (1/3 arcsec) grids covering three important maritime installations—Port of Long Beach (left), Seal Beach and Alamitos Bay (middle), and Anaheim Bay, Naval Weapon Station (right). (c) Modeled maximum tsunami current speeds in the C-Level (1/3 arcsec) grids covering the same regions as above.

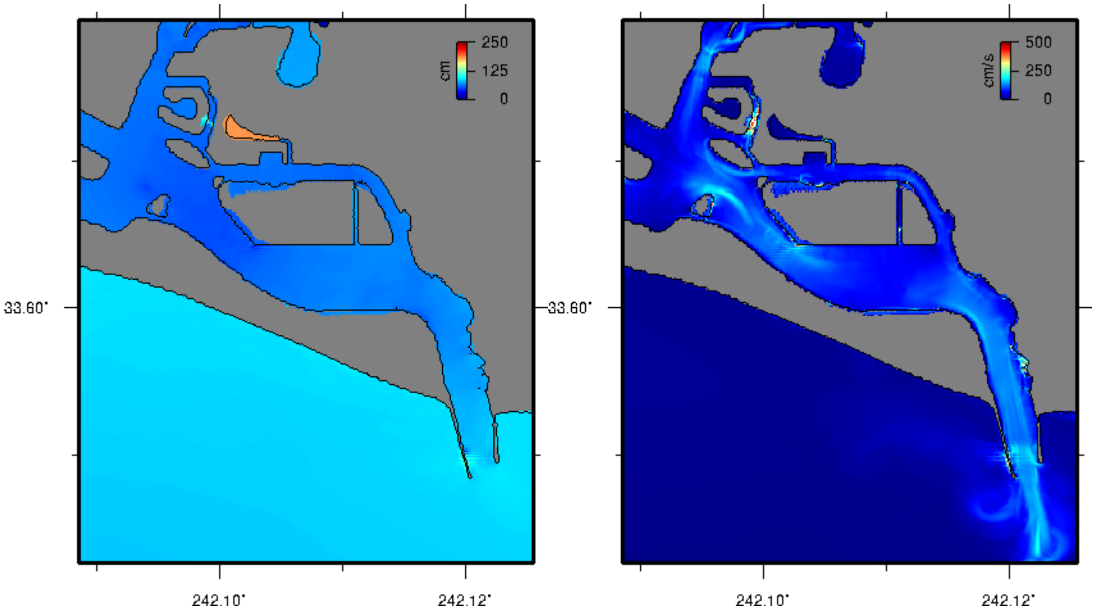

Figure 53. Maps showing modeled maximum tsunami height (left) and current speed (right) in Newport Bay.

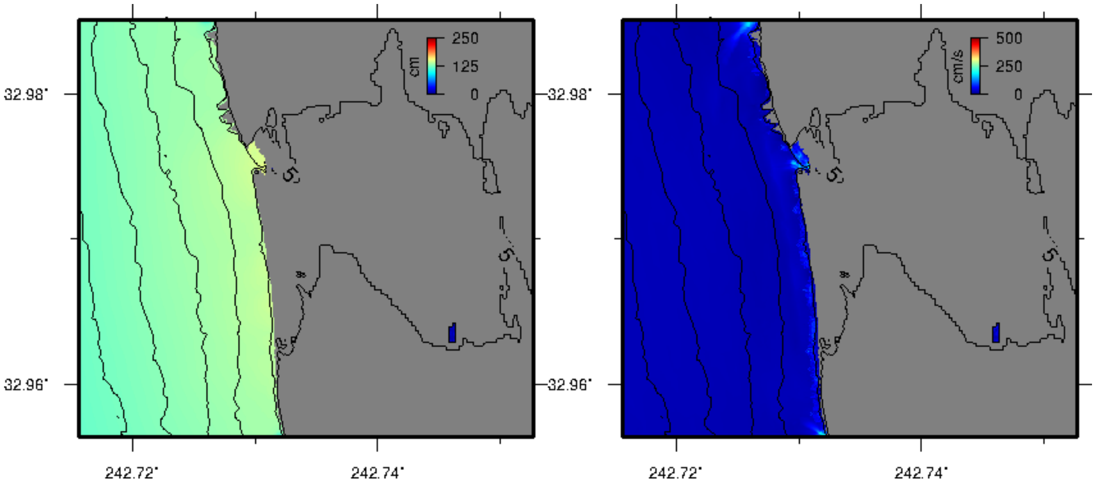

Figure 54. Maps showing modeled maximum tsunami height (left) and current speed (right) at Del Mar. The black line on land is the 5-meter topographic contour.

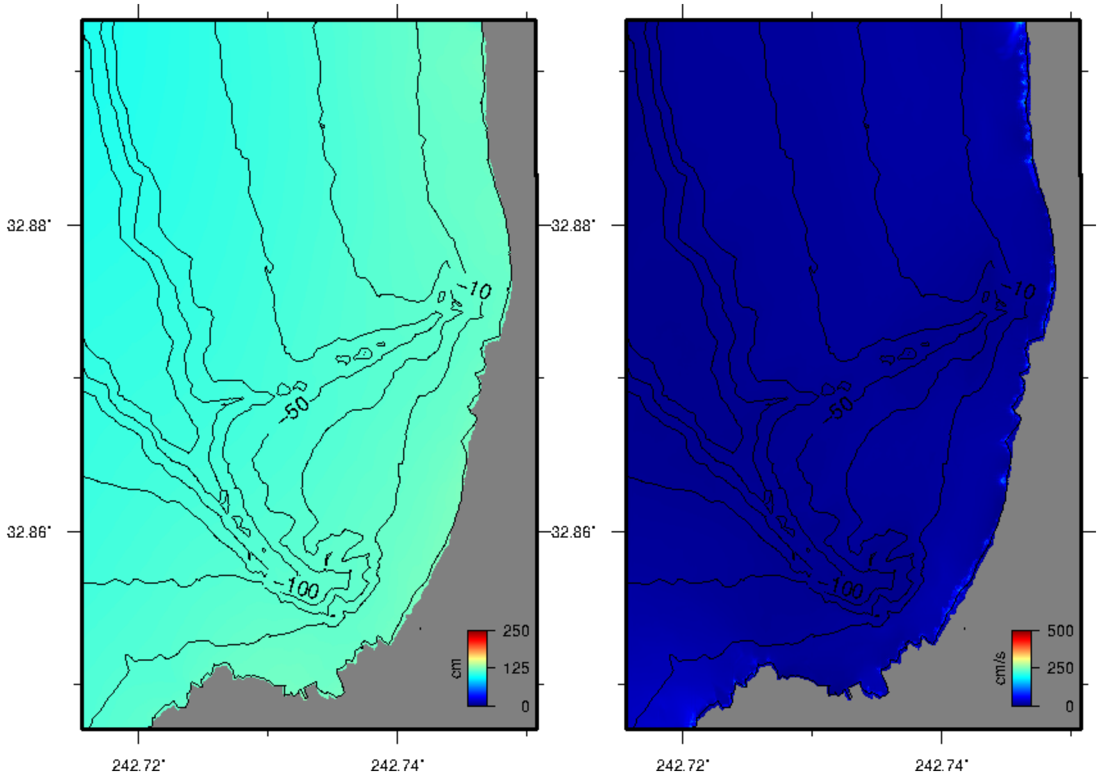

Figure 55. Maps showing modeled maximum tsunami height (left) and current speed (right) at La Jolla.

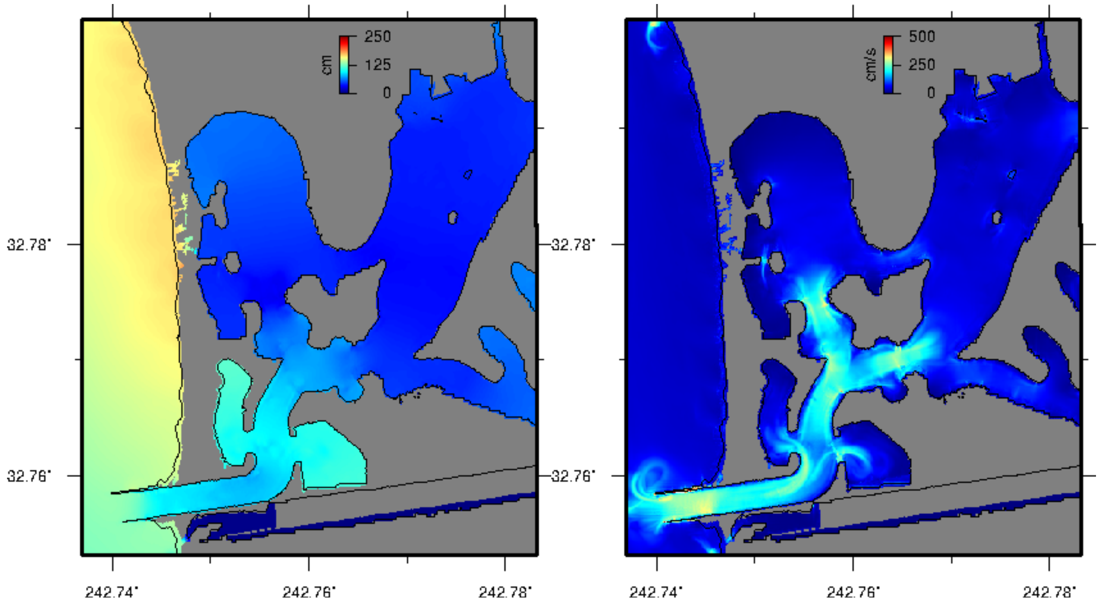

Figure 56. Maps showing modeled maximum tsunami height (left) and current speed (right) in Mission Bay.

Summary and Conclusion

This modeling study has explored the effects on the coast of Southern California of a tsunami from a distant source. It investigated the effect of a very large (*M*9.1) event offshore of the Alaska Peninsula on several sites in Southern California. Study sites include Marina del Rey, the ports area of San Pedro Bay (Long Beach, Seal Beach, Alamitos Bay, and Anaheim Bay), Newport Bay, Del Mar, La Jolla, and Mission Bay.

Tsunami waves from the Aleutian source region begin to affect the Southern California coast in approximately 6 hours, with the largest wave occurring within the first hour of the tsunami event. At sites in Santa Monica and San Pedro Bays, there is a resurgence in the tsunami energy that occurs approximately 4.5 to 7 hours after the tsunami first arrival. This resurgence is evident at the other sites; however, it is not as big nor as long lasting as in Santa Monica and San Pedro Bays.

Overall, the strongest tsunami effects occur in the San Pedro Bay area, an area that coincides with some of the most significant infrastructure developments. Thus the strongest tsunami effects affect an area most vital to commerce and economy in southern California. The effects in this area include strong currents in the vicinity of coastal structures, as well as overland inundation and flooding. Open coast sites such as Newport, Del Mar, and La Jolla do not experience this and only see maximum tsunami wave heights of approximately 1.25 m, a wave height that is less than a typical tidal range for the area. Although only small-scale inundation is predicted for the Del Mar and La Jolla areas, Mission Beach and Mission Bay are shown to be susceptible to possibly more inundation on the heavily populated beach front, as well as being affected by strong currents in the bay entrance and some inundation on the land inside the bay.

5. Production of Inundation Line for SAFRR Tsunami Scenario

By Rick Wilson

Abstract

To help evaluate the impacts from the SAFRR scenario tsunami event, a line of potential tsunami inundation was produced that represents the flood limits to numerical modeling results. Numerical modeling was completed using digital elevation models (DEMs) with grid resolutions of 10 m in select locations in southern California (see Borrero and others, section 4) and 30 m for most other parts of the California coast selected for modeling (see Thio, section 3). The DEMs were produced by the National Geophysical Data Center, which combined bathymetric and topographic data in a seamless dataset for tsunami modeling. Although models using these data are good for identifying general tsunami amplitudes, the DEMs and model results, because of resolution limitations, do not always accurately depict flooding where sudden topographic changes and manmade flood control structures exist. These types of problematic conditions include steep wave-cut beaches, port docks, and river levees. For this reason, recently collected (2009–2011), 1-m resolution lidar (light detection and ranging) DEMs were used to digitize an inundation line to identify where modeled flood limits would likely extend or be contained. In some locations, inundation maps were verified in the field or by use of orthoimagery and stereophotography, with an understanding of the limitations of the DEMs and imagery used. Because of the importance of the Ports of Los Angeles and Long Beach to the SAFRR project, a detailed review of landfill plans was performed to check the inundation line in that area. A similar process of inundation-line production was used by the California Geological Survey (CGS) and the California Governor's Office of Emergency Services (Cal OES) during the completion of the State inundation line for emergency response planning.

Introduction

Numerical tsunami modeling is a computationally complex method to demonstrate how tsunamis that are generated and propagated across the ocean inundate coastal regions of dry land. Most numerical model platforms have gone through validation exercises to demonstrate that the mathematical computations are verified (National Tsunami Hazard Mitigation Program, 2012). For this reason, the accuracy of the numerical models is less likely to be questioned. In most cases, the accuracy of the modeled inundation is more dependent on the accuracy and resolution of the digital elevations models (DEMs) used.

In 2009, a set of tsunami inundation maps were produced for emergency response statewide (Wilson and others, 2008; Barberopoulou and others, 2009). Numerical modeling was performed for a suite of large local- and distant-source tsunami scenarios, the results of which were combined into a single data layer that represented all potential areas that could potentially be flooded. This conservative approach was needed to make sure that during any large tsunami event, local evacuation plans would consider all areas of potential tsunami flooding.

During the production of the inundation maps, errors in the numerical model results were discovered that could have impacted the accuracy of the resulting map. A thorough investigation of the results determined that the errors were a product of either errors in the 30-m and 90-m DEMs used or limitations of these DEMs to resolve higher resolution features, such as (1) steep wave-cut beaches, (2) rock-covered slopes along waterfront areas, (3) port docks and seawalls, and (4) river and flood control levees. Where these issues existed, a geographic information system (GIS) platform was used to incorporate 3-m and 5-m radar-interferometric DEMs and 10-m U.S. Geological Survey (USGS) National Elevation Dataset (NED) DEMs to more accurately project where flooding could travel onshore. All DEMs were adjusted to mean high water tidal datums to accommodate potential worst-case inundation conditions. A preliminary line of potential inundation was generated, verified in the field with county emergency managers and other local map experts, and then finalized and released to the public. This method conformed to the National Tsunami Hazard Mitigation Program's guidelines and best practices for tsunami inundation modeling for evacuation planning (National Tsunami Hazard Mitigation Program, 2009).

Participants in the modeling and mapping aspect of the USGS SAFRR scenario project were cognizant of potential similar limitations to the modeling. Field investigations of the initial 10-m and 30-m modeling results were performed to verify the accuracy of the modeling. Although the resolution and accuracy of this modeling were considerably higher than in the previous statewide inundation mapping project, errors were discovered. The following discussion addresses these errors and the methods that were used to create a more accurate tsunami inundation product.

Verification of Model Results

Once the initial tsunami modeling results were produced, field teams consisting of USGS, CGS, and Cal OES personnel were formed to review the tsunami model products. In southern California, field team members visited a dozen coastal locations between Redondo Beach (Los Angeles County) and Newport Beach (Orange County). Although modeling results accurately portrayed the waterfront tsunami amplitudes in some areas, the modeled inundation areas were not always reflective of the topography and man-made structures inland. For example, figure 57 demonstrates how the 1-m tsunami runup flood level appears to overtop a river levee near the mouth of the Santa Ana River that was measured to be at least 3 m high. Because the levee is only 5 m wide, this manmade feature was not captured on the 10-m or 30-m DEMs used for tsunami modeling and, therefore, areas behind the levees showed erroneous flooding. Other areas where tsunami flooding was not accurately portrayed included steep, wave-cut beach fronts in Huntington Beach and underground parking garages in downtown Long Beach.

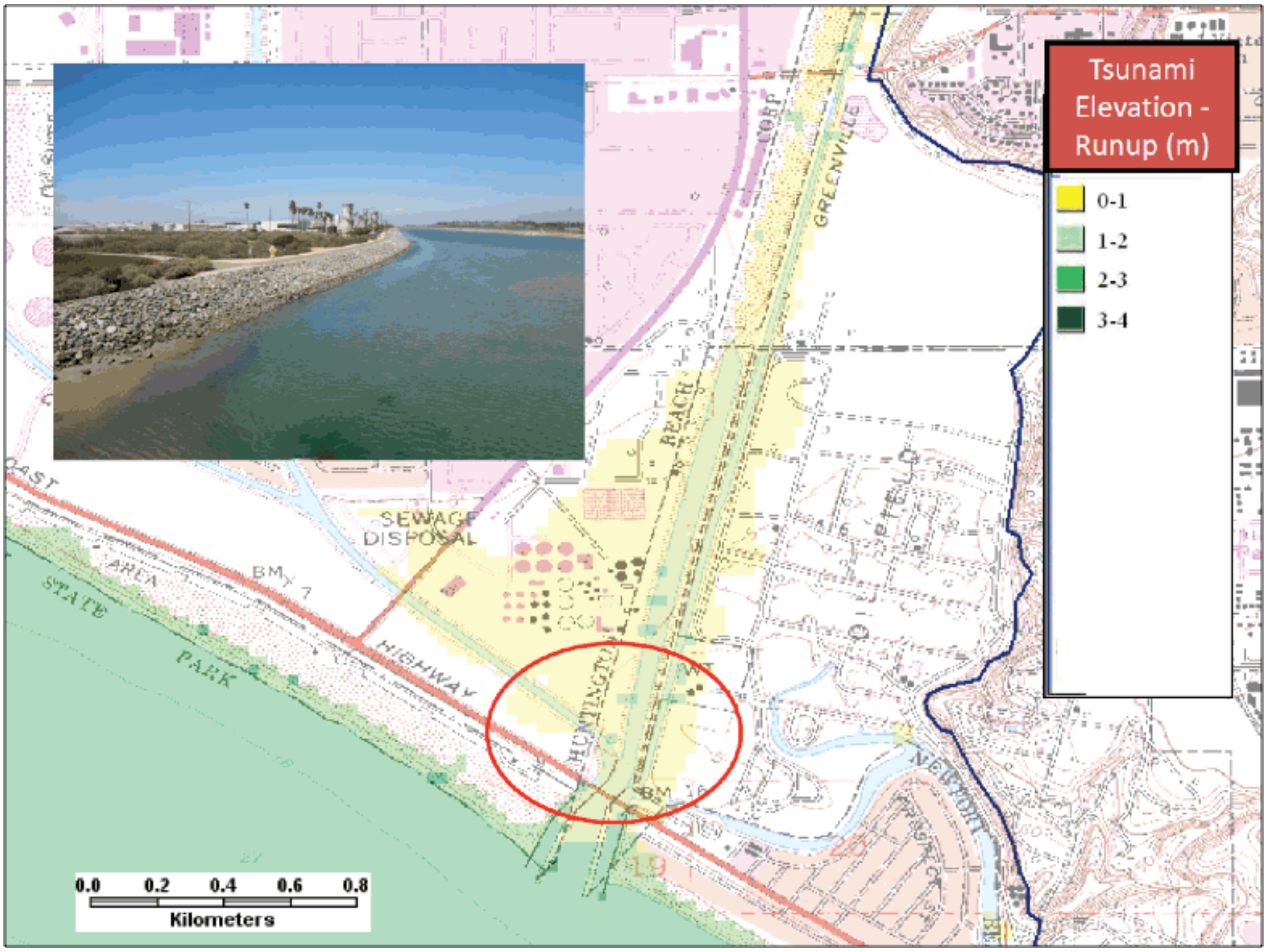

Figure 57. Map showing SAFRR modeled tsunami amplitude results near the outflow for the Santa Ana River in Orange County. The red oval identifies the area of the photo showing the +3-m high levees. These levees (shown in the inset photo) should not be overtopped by the 1-m high tsunami flow. The blue line is the location of the 2009 state tsunami inundation line. Topographic map used as a base map for this figure.

In the Ports of Los Angeles and Long Beach, similar issues were found with the accuracy of model results. Several areas of recent artificially filled land were not included in the DEM used in modeling. In other cases, where tsunami modeling amplitudes overtopped waterfront piers by 1 to 2 m, modeled flooding appeared to stop at the piers despite areas behind the piers being at a lower elevation. Additional information helping to address some of these issues was requested from Moffett and Nichol, the engineering consultants for the Ports.

Fieldwork was also initiated in northern California, specifically in the southwestern part of San Francisco Bay. Preliminary modeling results indicated that large sections of residential areas in Redwood City and Foster City could be inundated by a 1-m-amplitude tsunami. After looking closely at the levees bordering the edges of San Francisco Bay, the field team determined that tsunami inundation would not be anticipated to travel beyond these levees. Therefore, the residential areas in these cities should not be included in the inundation area for the project.

SAFRR Inundation Line Production

Based on the recommendations from the field teams, it was determined that an inundation line should be produced to correctly define where tsunami flooding could inundate. CGS employed a method similar to the work performed on the 2009 State inundation maps. A GIS platform was used to digitize the inundation line, employing 1-m resolution DEMs to determine the extent of potential flooding (DEMs from California Coastal Conservancy: *http://www.opc.ca.gov/2012/03/coastal-mapping-lidar-data-available/*). These DEMs, which are based on lidar data collected between 2009 and 2011 using an airborne system, represent the most comprehensive and accurate coastal topographic data available.

The initial fieldwork helped guide where problem areas needed to be addressed. For several locations in southern California, the inundation line extended inland where it was clear that beach and waterfront areas would not contain the modeled wave heights of the scenario tsunami. In northern California, inundation was confined by levees along the edge of San Francisco Bay. River levees throughout the State were also analyzed to determine if they would confine the flow of the tsunami.

In the Ports of Los Angeles and Long Beach, careful evaluation of the model results led to the production of a more consistent and accurate tsunami inundation line. Low-lying regions were incorporated into the inundation area beyond where tsunami flooding was projected to overtop the piers (fig. 58). Design plans for artificial land fill within the Ports were cross referenced with recent USGS orthophotographic imagery (circa 2011) to determine where tsunami inundation would occur. CGS coordinated closely with Moffatt and Nichol, the engineering consultant for the Ports, to adjust the limits for inundation where appropriate. Although significant work went into the production of the inundation line in the Ports, further detailed evaluation in the field would be needed to determine if more subtle manmade structures, such as small berms and retaining walls, would change the areas of inundation from the tsunami. Appendix A includes examples of inundation for selected areas of the California coast.

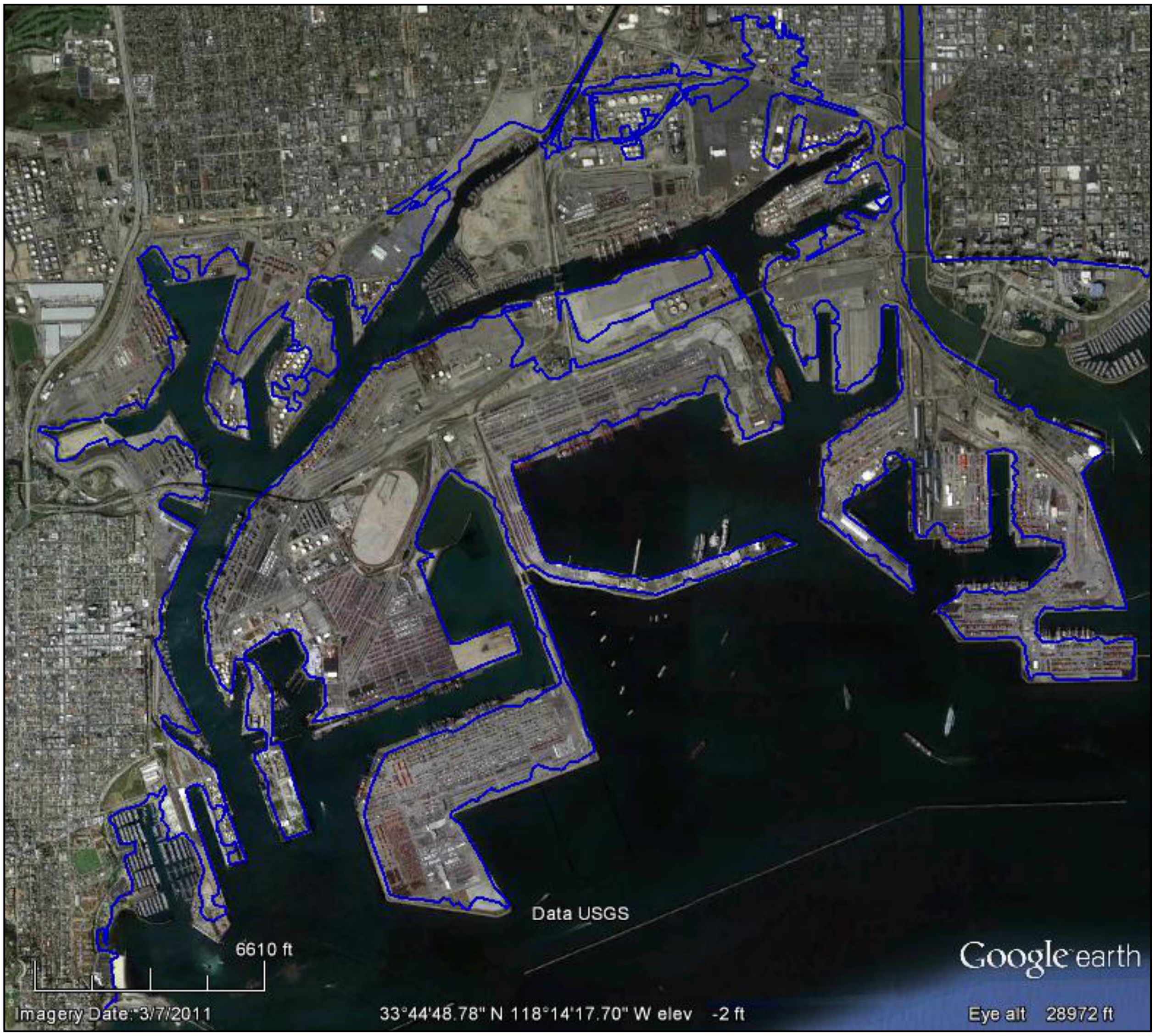

Figure 58. Map showing the SAFRR tsunami inundation line (blue) in the Port of Los Angeles (left part of image) and the adjacent Port of Long Beach. A number of the waterfront areas around the ports show overtopping by the modeled tsunami surge.

Comparison of SAFRR Inundation Line to State Inundation Line

To determine if evacuation plans for coastal communities should be updated, CGS compared the inundation line from the SAFRR scenario to that from the 2009 statewide product. The SAFRR scenario tsunami is considered a very large distant-source event for the California's coast, comparable to some of the "worst-case" sources used during production of the 2009 statewide inundation maps. The modeling results produced for the SAFRR scenario are of higher resolution than those produced for the state inundation maps. The topographic lidar DEM used for the SAFRR line production is a higher resolution, more accurate DEM than what was available when the state inundation line was produced. This evaluation found that the state inundation line was equal to or more conservative (further inland) in almost all areas and under most conditions, with two exceptions:

1. The higher resolution modeling results for SAFRR demonstrated that tsunamis could travel farther up large rivers feeding into the ocean. In some cases, modeled tsunami surges and bores traveled as far as 4 to 5 miles upriver.
2. Higher resolution SAFRR models indicated that amplification of tsunami surges occurred in small inlets and harbors within San Diego and San Francisco Bays, producing tsunami wave heights approximately 0.5 m to 1 m higher than modeling for the 2009 state inundation maps.

For these areas, CGS and Cal OES contacted the relevant emergency management agencies in the coastal jurisdictions to inform them of the situation, and evacuation plans were updated where it was appropriate.

6. Modeling Tsunami Dynamics in the Port of Los Angeles, California

By Dmitry J. Nicolsky and Elena N. Suleimani

Abstract

We have numerically modeled the extent of inundation in the Port of Los Angeles from a tsunami generated by a hypothetical M_w 9.1 earthquake in a segment of the Aleutian megathrust near the Alaska Peninsula. The result of this tsunami scenario is intended to provide assistance in tsunami hazard assessment, evacuation planning, and public education for reducing future casualties and damage from tsunamis.

Introduction

Subduction of the Pacific Plate under the North American Plate along the Alaska-Aleutian subduction zone has resulted in numerous great earthquakes and still has a large potential to generate tsunamis threatening Alaska and other States and territories of the United States. The Aleutian megathrust, where the Pacific Plate is being subducted, is the most seismically active tsunamigenic fault zone in the United States. Several historical tsunamis generated by earthquakes along the Alaska-Aleutian subduction zone traveled across the Pacific Ocean and struck exposed locations around the ocean, resulting in widespread damage and loss of life.

Given the many similarities in tectonic and geologic settings between the Semidi Sector of the Alaska-Aleutian subduction zone and the Tohoku segment of the Kamchatka-Kuril-Japan subduction zone, the U.S. Geological Survey (USGS) Tsunami Source Working Group proposed modeling a hypothetical earthquake similar in its slip distribution to the 2011 Tohoku event. The rupture zone of the hypothetical earthquake lies in the Semidi Sector, between Kodiak Island and the Shumagin Islands off the Pacific coast of the Alaska Peninsula (fig. 22; see fig. 12 for locations). Contours of the sea-floor deformation due to this hypothetical earthquake are displayed in figure 59. The proposed slip distribution was parameterized by multiple subfaults (Kirby and others, 2013), and the vertical and horizontal displacements at the seafloor are computed by the Okada (1985) formulae. The left plot in figure 59 shows the sea-floor deformation due only to the vertical displacements, while the right plot displays the vertical deformation that takes into the account both the vertical and horizontal displacements. At some parts of the ocean bottom with steep bathymetric gradients, the contribution to the sea-floor deformation by the horizontal displacements can be as much as 6 m.

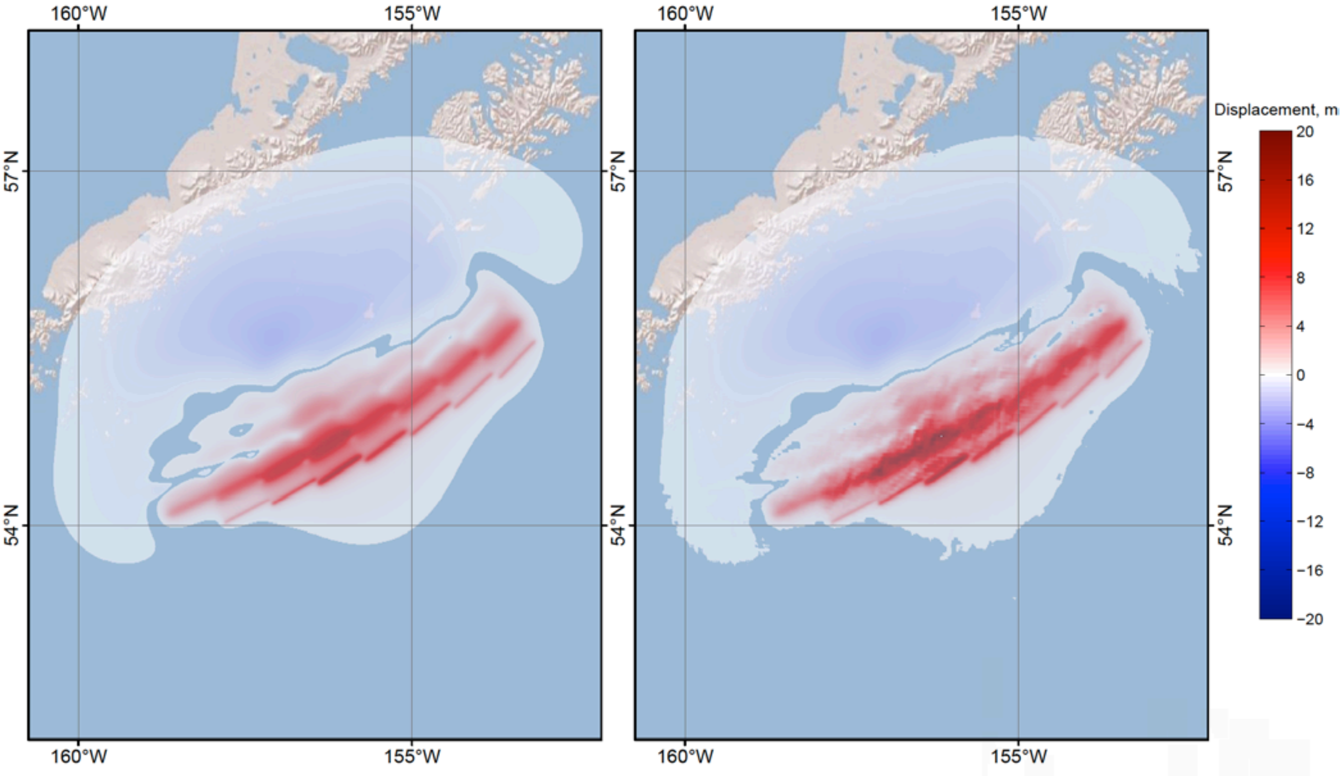

Figure 59. Maps showing the vertical deformation of the ocean floor resulting from the hypothetical earthquake in the Semidi Sector of the Aleutian megathrust. Left: the deformation is assumed to be equal to the vertical displacements. Right: the deformation is computed according to both the vertical and horizontal displacements.

Methodology and Data

Grid Development

To simulate inundation in the Port of Los Angeles by a potential tsunami that can be triggered by the M_w 9.1 earthquake near the Alaska Peninsula, we employ a series of nested computational grids. A nested grid allows for higher resolution in areas where it is needed, without expending computer resources in areas where it is not. The extent of each grid used for modeling tsunami waves in the Port of Los Angeles is shown in figures 60 and 61 and listed in table 11. The coarsest grid, whose resolution is 2 arc minutes, spans the central and northern Pacific Ocean, while the highest resolution grid covers the Port of Los Angeles, including Anaheim Bay and a part of Bolsa Bay. The spatial resolution of the high-resolution grid satisfies National Oceanic and Atmospheric Administration (NOAA) minimum recommended requirements for computation of tsunami inundation (National Tsunami Hazard Mitigation Program, 2010). We briefly summarize some of these requirements as follows. Modeling of inundation should be performed using numerical grids with cell sizes less than 3 arc seconds (~90 m), because cell sizes coarser than this tend to degrade inundation modeling results. The source elevation data in the grids should be thoroughly documented (see figs. 60 and 61). To resolve significant features that affect inundation, the computational grid should be fine enough that the feature covers more than three cells. We note that passages in the Port, between jetties and narrow channels in the wildlife refuge, are resolved with more than three grid cells.

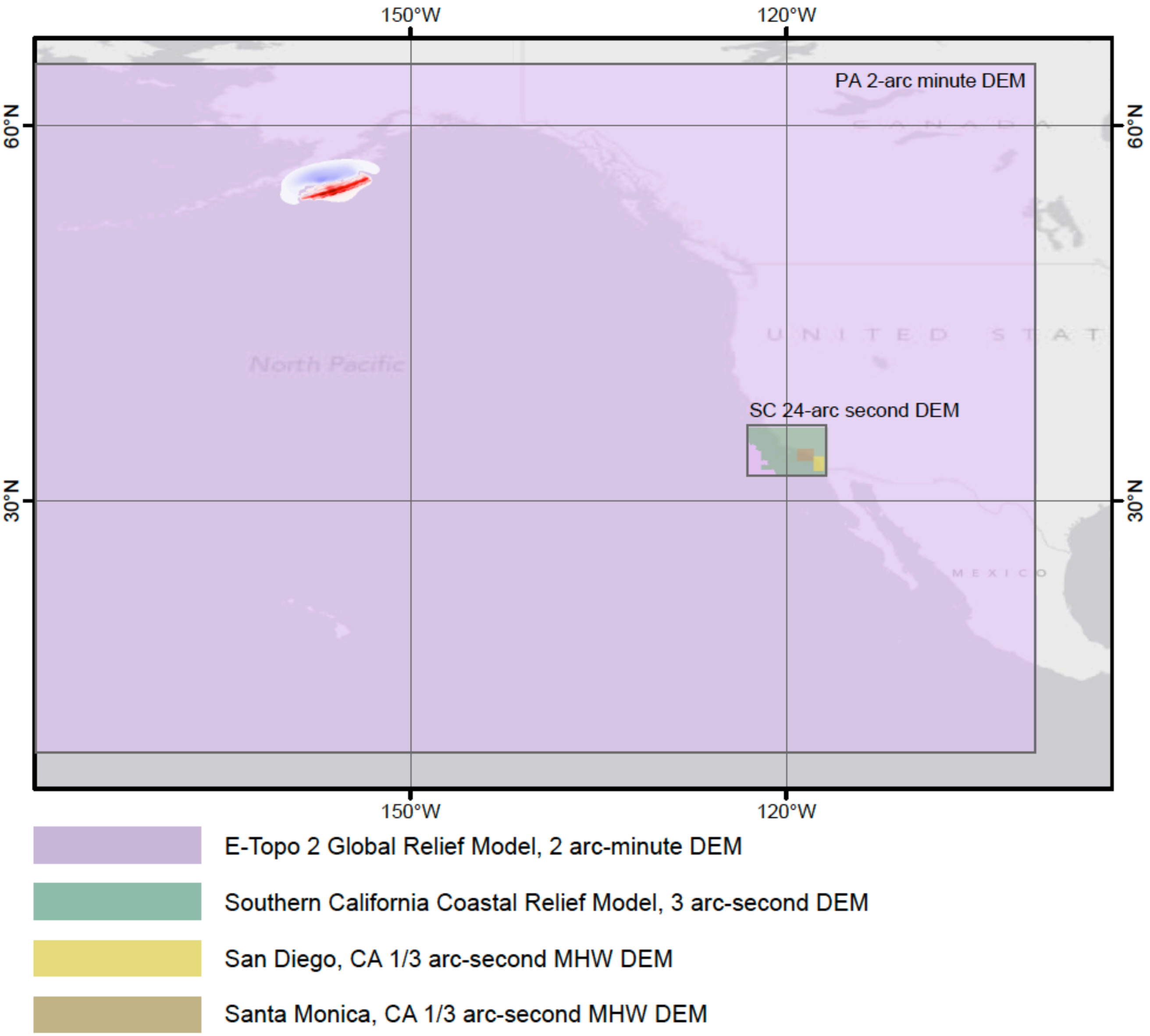

Figure 60. Map showing the coarsest grid (PA02) which covers the central and northern Pacific Ocean, and the 24-arc-second grid (SC24), which is centered at the Port of Los Angeles. The data used to construct the embedded grids near the Port of Los Angeles are provided by the National Geophysical Data Center (NGDC), and their data extents are marked by different colors.

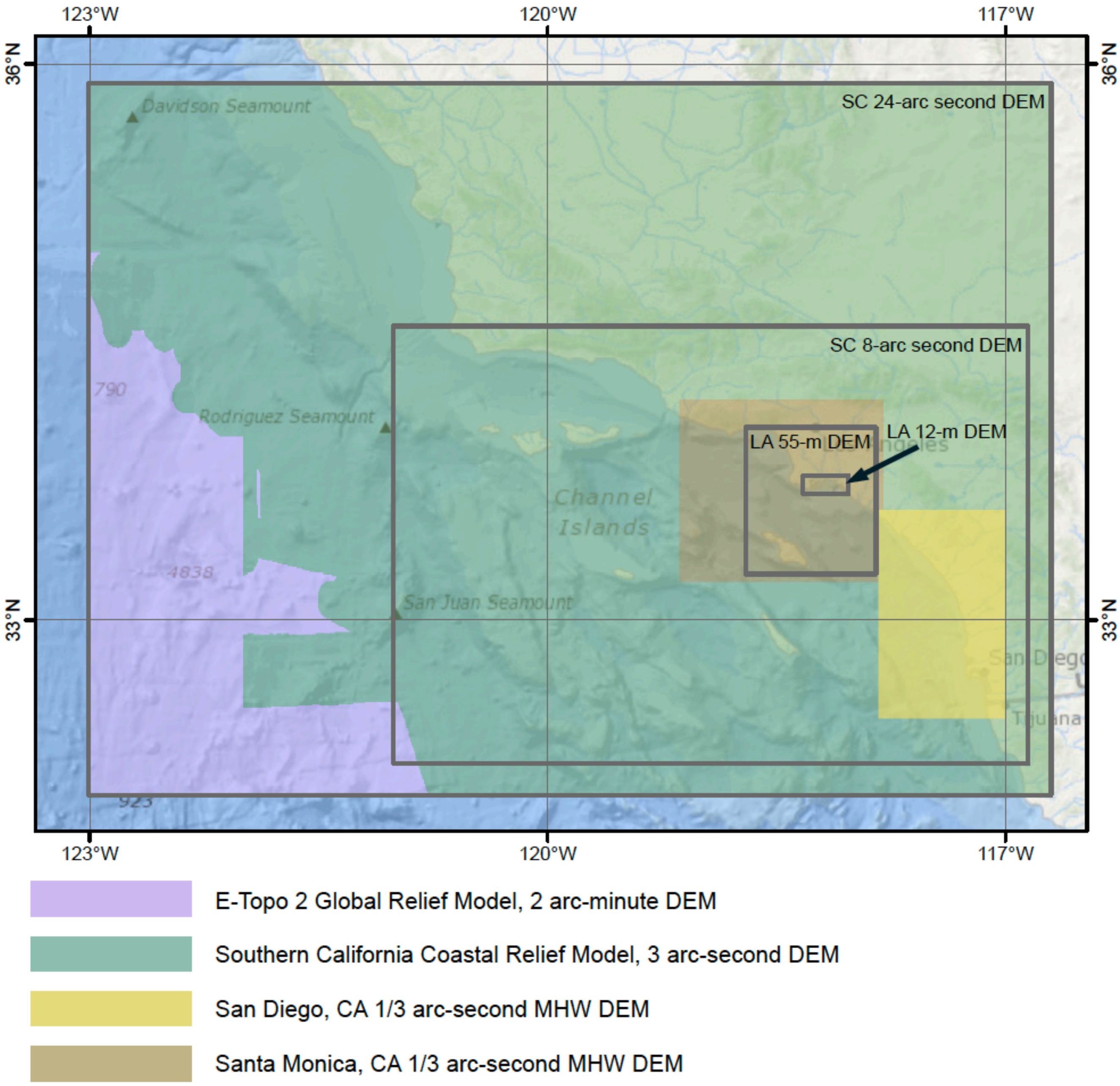

Figure 61. Map showing telescoping embedded bathymetry/topography grids (SC24, SC08, LA55, and LA12) for numerical modeling of tsunami propagation and runup along the southern California coast. Extent of each embedded grid is marked by a gray rectangle. The data used to construct the embedded grids are provided by the National Geophysical Data Center (NGDC), and their data extents are marked by different colors. One-third arc second is approximately 10.3 m.

Table 11. Nested grids used to compute propagation of tsunamis generated along the Alaska Peninsula to the Port of Los Angeles.

[The high-resolution grid is used to compute the inundation. Note that the grid resolution in meters is not uniform and is used to illustrate grid fineness. The first dimension is the longitudinal grid resolution, while the second is the latitudinal grid resolution.]

Grid name	Resolution		East–West boundaries	South-North boundaries
	arc-seconds	meters		
PA02	120 × 120	3,100 × 3,700	120.00E – 100.00W	10.00N – 65.00N
SC24	24" × 24"	614 × 740	116.70W – 123.00W	32.00N – 35.90N
SC08	8" × 8"	206 × 247	116.85W – 121.00W	32.20N – 34.60N
LA55	8/3" × 8/5"	68.4 × 49.3	117.85W – 118.70W	33.25N – 34.05N
LA12 (high-resolution)	8/15" × 2/5"	13.7 × 12.3	118.03W – 118.33W	33.69N – 33.79N

The bathymetry data for the 2-arc-minute resolution grid, whose partial extent is shown in figure 60, is extracted from the ETOPO2 data set (NOAA, National Geophysical Data Center). Telescoping embedded bathymetry/topography grids (SC24, SC08, LA55, and LA12) are used for numerical modeling of tsunami propagation and runup. The extent of each embedded grid is marked by a gray rectangle (figs. 60 and 61). The data used to construct the embedded grids are provided by NGDC, and their data extents are marked by different colors.

Numerical Model of Tsunami Propagation and Runup

NOAA recently published a technical memorandum that outlines major requirements for numerical models used in inundation mapping and tsunami forecasting and describes a procedure for model evaluation (Synolakis and others, 2007). There are two major components to this process. The first is model validation, which ensures that the model correctly solves appropriate equations of motion by comparing model results with known solutions. This is achieved through analytical and laboratory benchmarking. The second component is model verification, or testing the model, using observations of real events through field data benchmarking.

The numerical model that is currently used by the Alaska Earthquake Information Center (AEIC) to model the hypothetical tsunami in the Port of Los Angeles has been validated through a set of analytical benchmarks and tested against laboratory and field data (Nicolsky and others, 2011; Nicolsky, 2012). The model solves nonlinear shallow-water equations using a finite-difference method on a staggered grid. For any coarse–fine pair of computational grids, we apply a time explicit numerical scheme as follows. First, we compute the water flux within a coarse-resolution grid. These calculated flux values are used to define the water flux on a boundary of the fine-resolution grid. Next, the water level and then the water flux are calculated over the fine-resolution grid. Finally, the water level computed in the fine-resolution grid is used to define the water level within the area of the coarse-resolution grid that coincides with the fine grid. Despite the fact that nested grids decrease the total number of grid cells needed to preserve computational accuracy within certain regions of interest, actual simulations are still time demanding if parallel computing is not implemented. Here, we use the Portable Extensible Toolkit for Scientific computation (PETSc), which provides sets of tools for the parallel numerical solution of shallow-water equations (Balay and others, 2004). In particular, each computational grid listed in table 11 can be subdivided among an arbitrary number of processors. The above-mentioned passing of information between the water flux and level is implemented efficiently using PETSc subroutines.

To simulate tsunami dynamics caused by a sea-floor deformation due to an earthquake, we assume some simplifications. First, an initial displacement of the ocean surface is equal to the vertical displacement of the ocean floor induced by the earthquake rupture process. Second, the finite speed of the rupture propagation along the fault is not taken into account—we consider the ocean bottom displacement to be instantaneous. Third, the initial topography is modified to account for coseismic deformation of land due to the earthquake.

At the end of a tsunami simulation, each of the grid points has either a value of 0 if no inundation occurs or 1 if seawater reaches the grid point at any time. The inundation line approximately follows the 0.5 contour between these 0- and 1-point values. Although the developed algorithm has passed through the rigorous benchmarking procedures (Nicolsky and others, 2011; Nicolsky, 2012), there is still an uncertainty in the placement of the inundation line. However, this uncertainty is to a great degree unknown because the inundation line is the result of a complex modeling process. Affecting the accuracy of the inundation line are many factors on which the model depends, including suitability of the earthquake source model, accuracy of the bathymetric and topographic data, and adequacy of the numerical model in representing the generation, propagation, and runup of tsunamis. In this study, we do not attempt to adjust the modeled inundation limits to account for these uncertain factors.

We note that there are several limitations of the model. One of the important shortcomings is that it does not take into account the periodic change of sea level due to tides. We conducted all model runs using bathymetric data that correspond to the MHW tide level in the Port of Los Angeles.

Modeling Results

We model propagation of the tsunami generated by the hypothetical earthquake in the area of Alaska Peninsula using the Alaska Tsunami Online Modeling (ATOM) interface (*http://atom.giseis.alaska.edu)*. The tsunami dynamics were modeled for 12 hours, with the time step in the coarsest grid equal to 1 second. To preserve stability of the computations, the time step in the high-resolution grid was set equal to 0.012 seconds. The initial water displacement is assumed to be equal to the vertical displacements by the Okada's formulae (the left plot in fig. 59), and the Manning roughness in all nested grids is set to be μ=0.01. The modeling results show that the first wave arrives at the Port of Los Angeles about 5 hours after the earthquake, and that the significant wave action starts approximately 6 hours after the earthquake. The maximum calculated wave height with respect to the MHW level is plotted in the top plot in figure 62. The bottom plot in the same figure illustrates the hypothetical flow depth above the dry land.

In addition to the simulated maximum water level and flow depth, we display the computed water level and velocity at selected points along the coast of Los Angeles and inside the Los Angeles harbor. Locations of these points are marked by numbers and red triangles in figures 62 and 63. We plot the computed sea level and water velocity at all selected locations in figure 64. The geographic coordinates of the selected locations are listed in table 12.

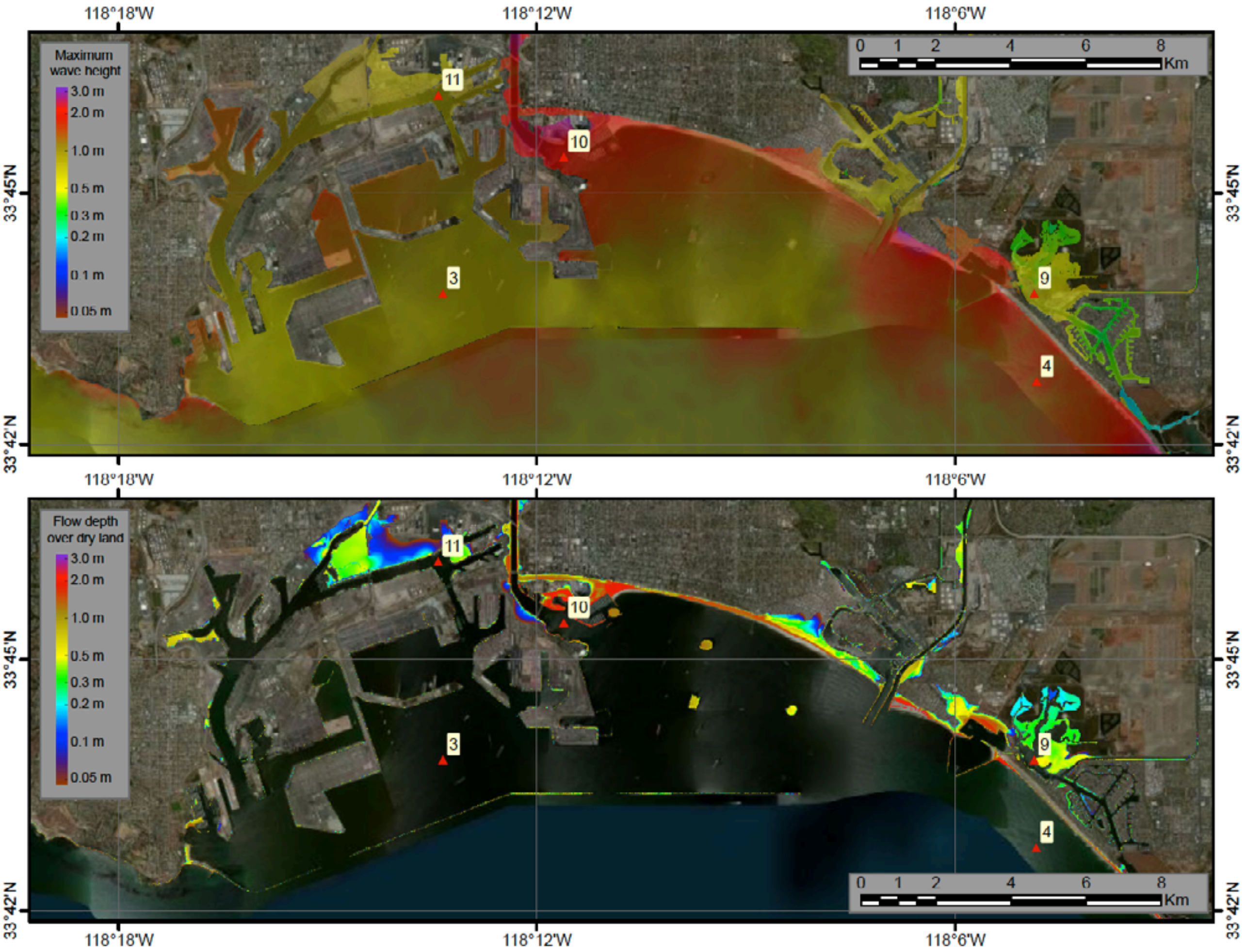

Figure 62. Maps showing modeled wave heights and water flow depths in the Ports of Los Angeles and Long Beach. Numbers mark locations for which data are given in figure 64 and table 12. Top: the maximum potential wave height above the mean high water (MHW) level. Bottom: the simulated water flow depth above the dry land. The DEM corresponds to the present-day MHW datum.

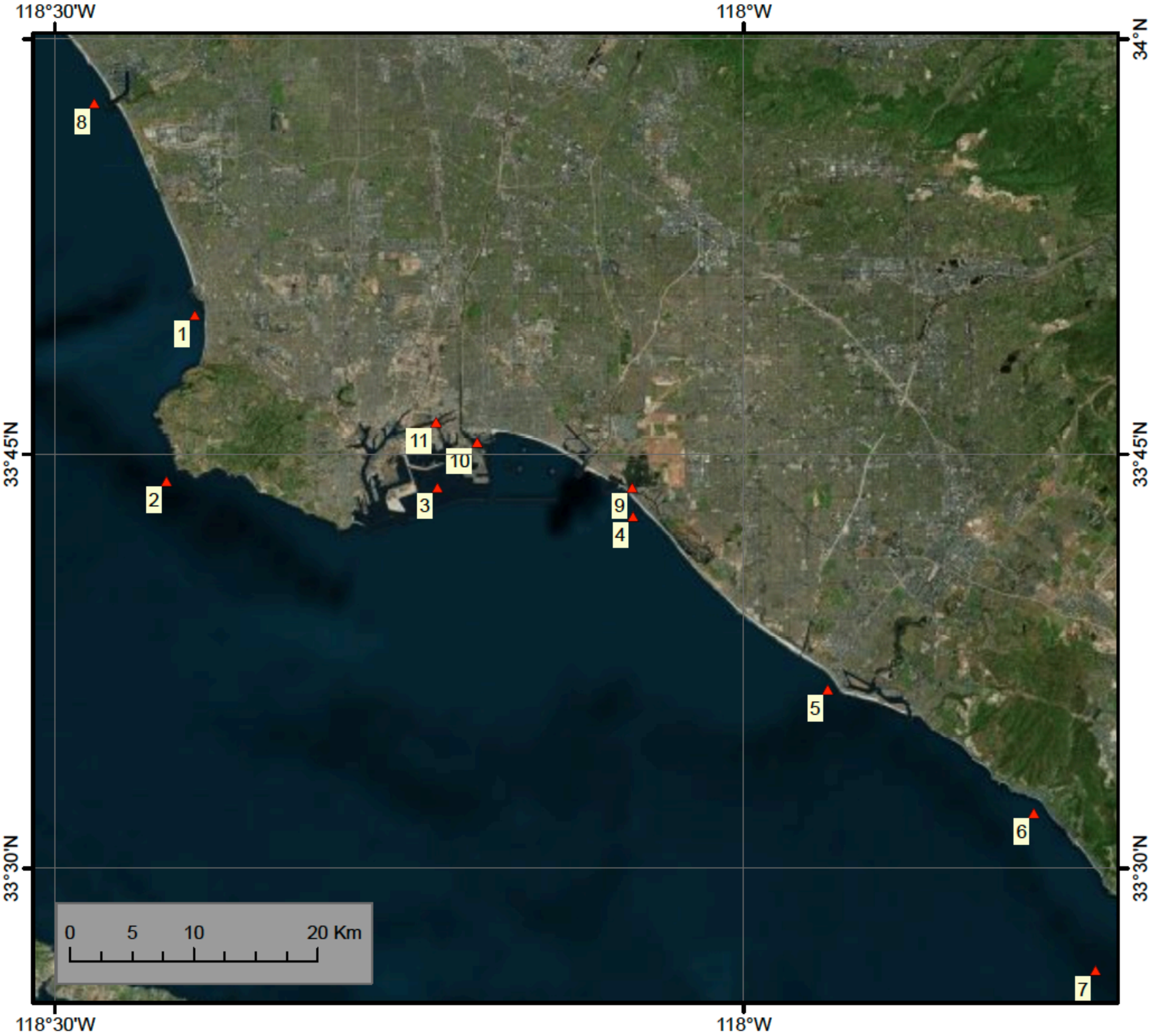

Figure 63. Map showing locations of time-series points (numbered red triangles) on the California coast near the Port of Los Angeles. Locations of the points are given in table 12, and data obtained there appear in figure 64.

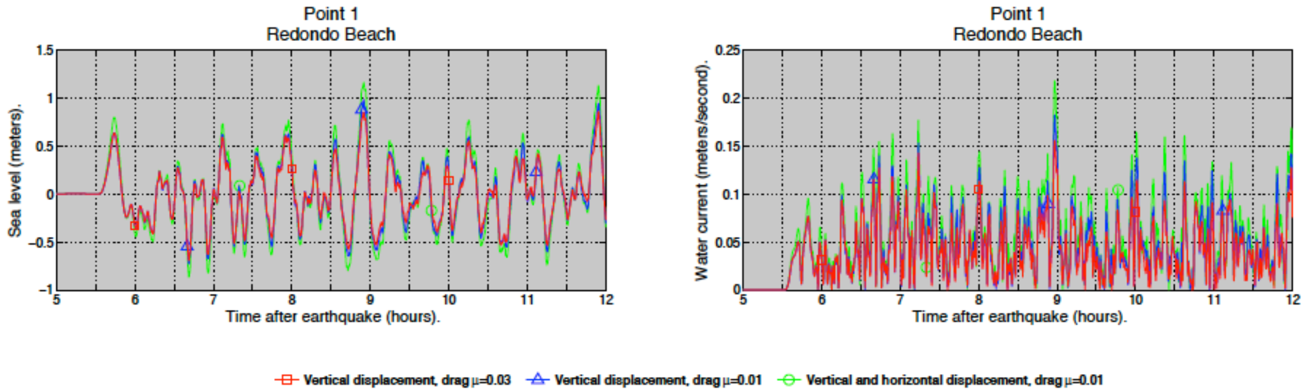
Point 1
Redondo Beach
Sea level (meters).
Time after earthquake (hours).
Point 1
Redondo Beach
Water current (meters/second).
Time after earthquake (hours).
Vertical displacement, drag μ=0.03
Vertical displacement, drag μ=0.01
Vertical and horizontal displacement, drag μ=0.01

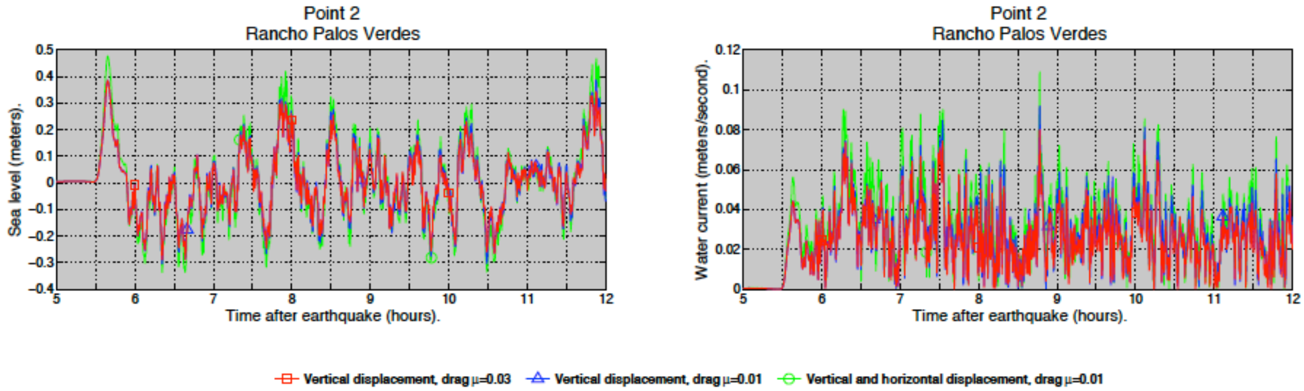
Point 2
Rancho Palos Verdes
Sea level (meters).
Time after earthquake (hours).
Point 2
Rancho Palos Verdes
Water current (meters/second).
Time after earthquake (hours).
Vertical displacement, drag μ=0.03
Vertical displacement, drag μ=0.01
Vertical and horizontal displacement, drag μ=0.01

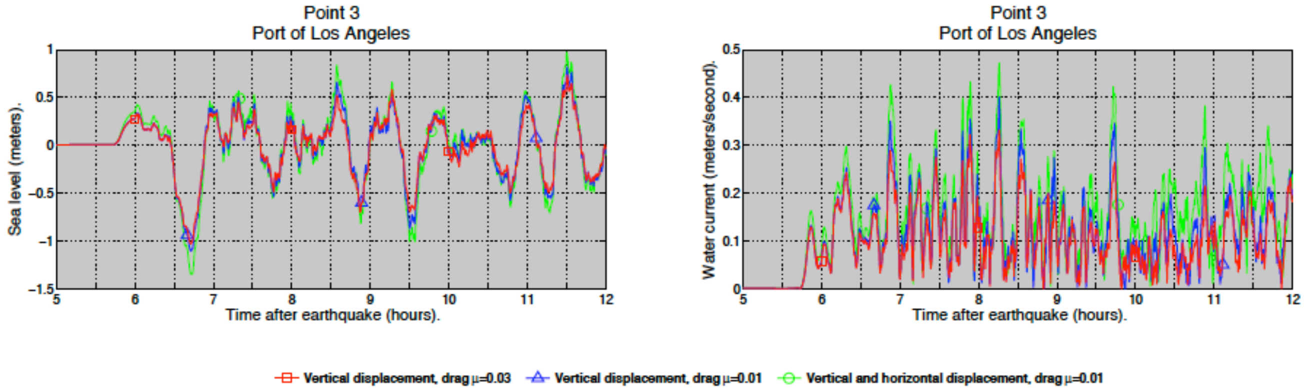
Point 3
Port of Los Angeles
Sea level (meters).
Time after earthquake (hours).
Point 3
Port of Los Angeles
Water current (meters/second).
Time after earthquake (hours).
Vertical displacement, drag μ=0.03
Vertical displacement, drag μ=0.01
Vertical and horizontal displacement, drag μ=0.01

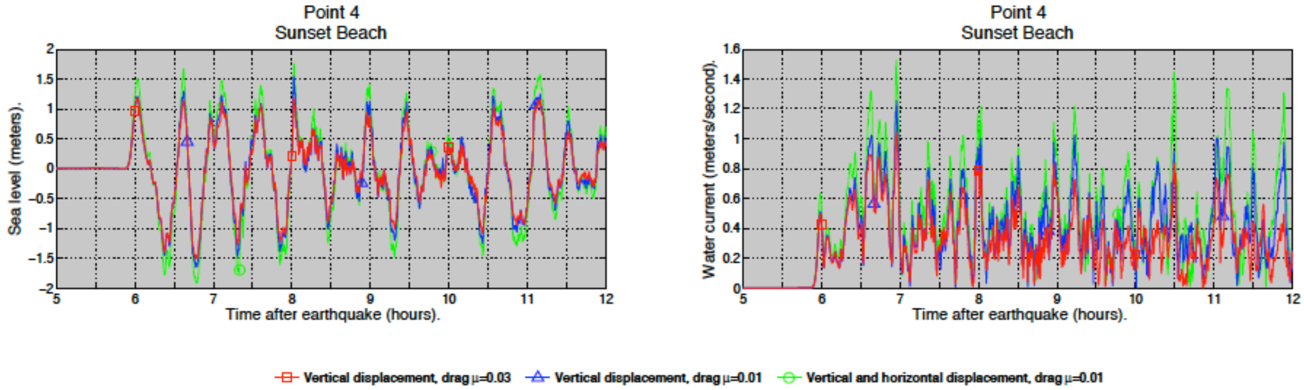
Point 4
Sunset Beach
Sea level (meters).
Time after earthquake (hours).
Point 4
Sunset Beach
Water current (meters/second).
Time after earthquake (hours).
Vertical displacement, drag μ=0.03
Vertical displacement, drag μ=0.01
Vertical and horizontal displacement, drag μ=0.01

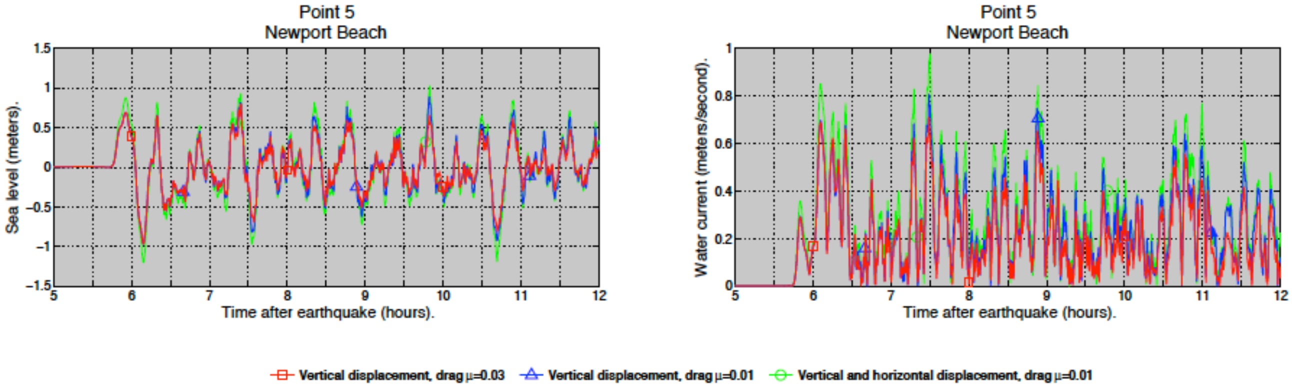
Point 5
Newport Beach
Sea level (meters).
1.5
1
0.5
0
−0.5
−1
−1.5
5
6
7
8
9
10
11
12
Time after earthquake (hours).
Point 5
Newport Beach
Water current (meters/second).
1
0.8
0.6
0.4
0.2
0
Time after earthquake (hours).
Vertical displacement, drag μ=0.03
Vertical displacement, drag μ=0.01
Vertical and horizontal displacement, drag μ=0.01

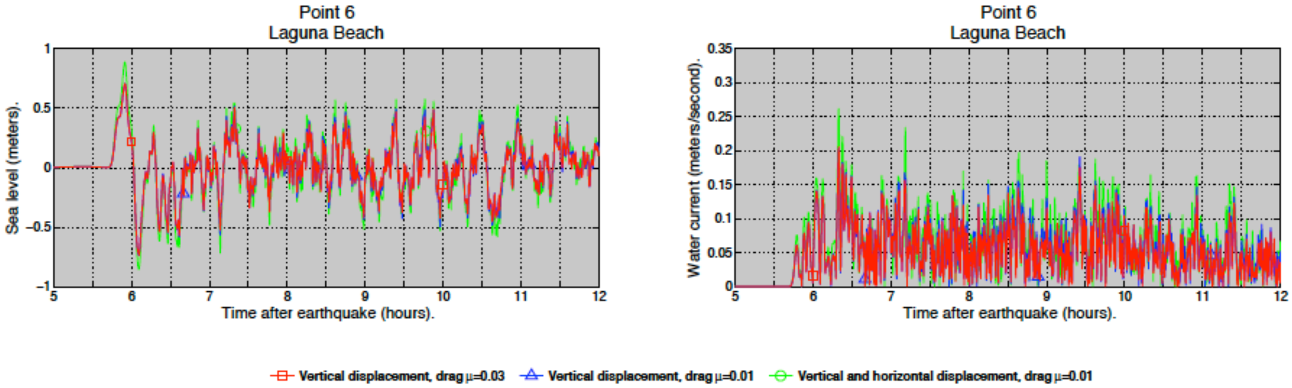
Point 6
Laguna Beach
Sea level (meters).
1
0.5
0
−0.5
−1
5
6
7
8
9
10
11
12
Time after earthquake (hours).
Point 6
Laguna Beach
Water current (meters/second).
0.35
0.3
0.25
0.2
0.15
0.1
0.05
0
Time after earthquake (hours).
Vertical displacement, drag μ=0.03
Vertical displacement, drag μ=0.01
Vertical and horizontal displacement, drag μ=0.01

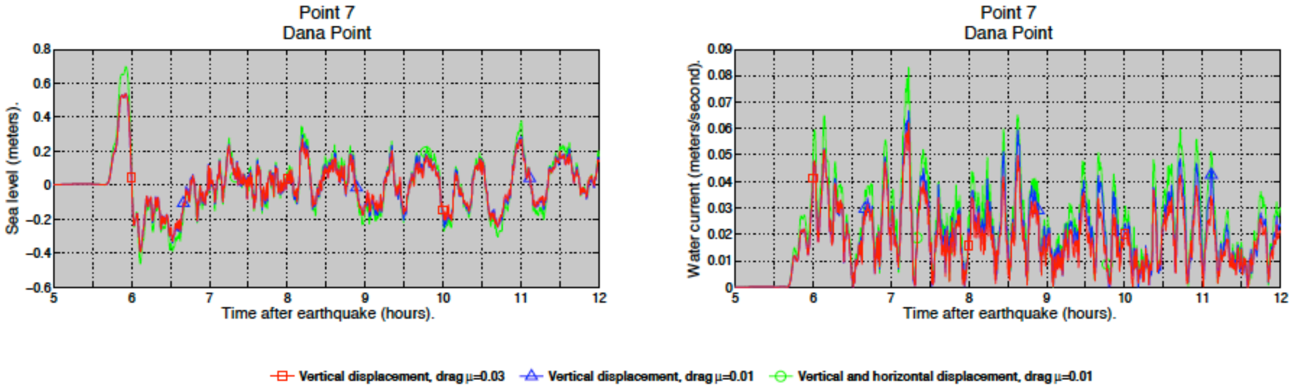
Point 7
Dana Point
Sea level (meters).
0.8
0.6
0.4
0.2
0
−0.2
−0.4
−0.6
5
6
7
8
9
10
11
12
Time after earthquake (hours).
Point 7
Dana Point
Water current (meters/second).
0.09
0.08
0.07
0.06
0.05
0.04
0.03
0.02
0.01
0
Time after earthquake (hours).
Vertical displacement, drag μ=0.03
Vertical displacement, drag μ=0.01
Vertical and horizontal displacement, drag μ=0.01

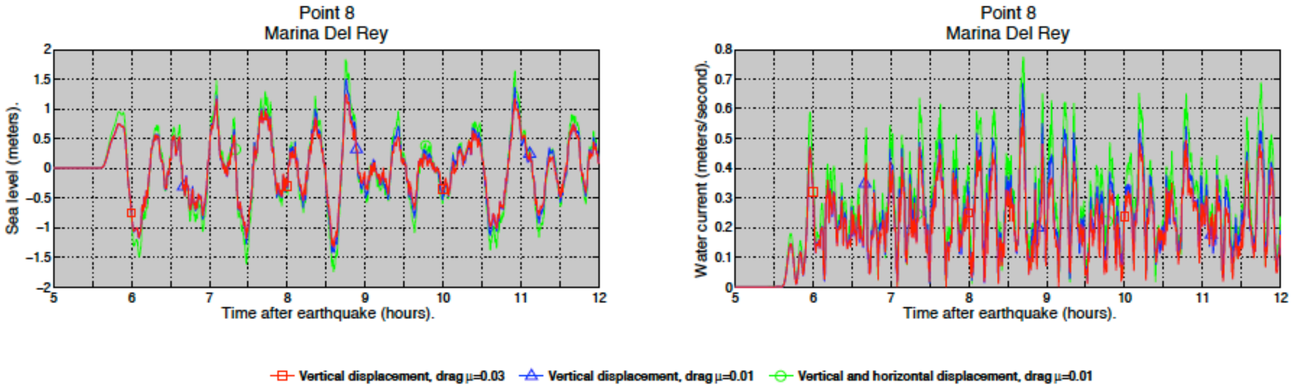
Point 8
Marina Del Rey
Sea level (meters).
2
1.5
1
0.5
0
−0.5
−1
−1.5
−2
5
6
7
8
9
10
11
12
Time after earthquake (hours).
Point 8
Marina Del Rey
Water current (meters/second).
0.8
0.7
0.6
0.5
0.4
0.3
0.2
0.1
0
Time after earthquake (hours).
Vertical displacement, drag μ=0.03
Vertical displacement, drag μ=0.01
Vertical and horizontal displacement, drag μ=0.01

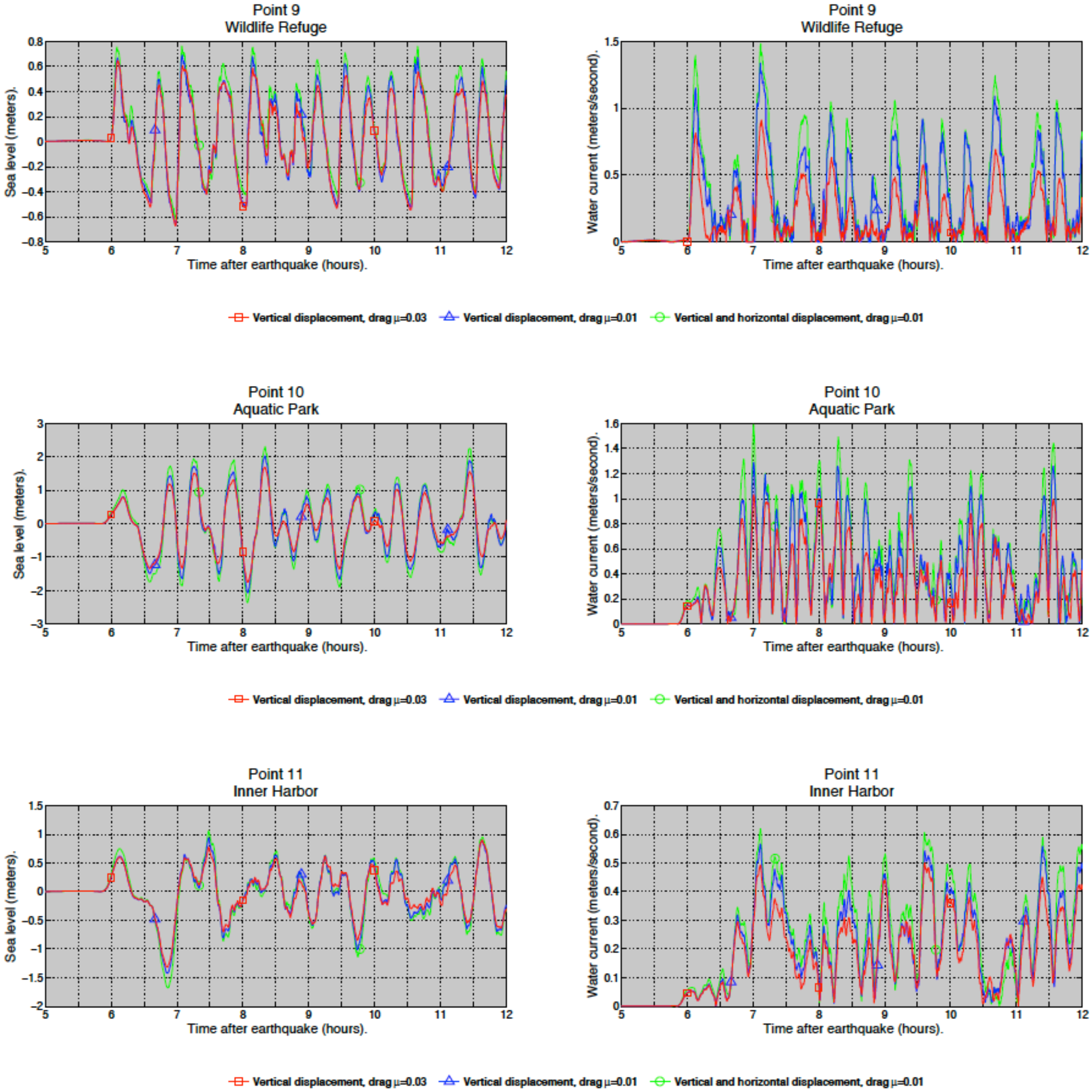

Figure 64. Time-series plots of modeled water level and velocity at the selected locations on the California coast near Los Angeles. The modeled water height is given with respect to the mean high water (MHW) tide level. Red line: vertical displacement only at the source and μ=0.03. Blue line: vertical displacement only at the source and μ=0.01. Green line: vertical and horizontal displacement at the source and μ=0.01.

Table 12. Locations where the simulated water level and velocity in the scenario tsunami are recorded.

[Locations shown on figures 62 and 63; data from the locations presented in figure 64]

ID	Lon	Lat	Label
1	-118.39889	33.83389	Redondo Beach
2	-118.41944	33.73389	Rancho Palos Verdes
3	-118.22250	33.73000	Port of LA
4	-118.08056	33.71250	Sunset Beach
5	-117.93889	33.60806	Newport Beach
6	-117.78917	33.53333	Laguna Beach
7	-117.74444	33.43806	Dana Point
8	-118.47167	33.96139	Marina Del Rey
9	-118.08111	33.73000	Wildlife Refuge
10	-118.19361	33.75722	Aquatic Park
11	-118.22361	33.76944	Inner Harbor

To assess sensitivity of the hypothetical inundation with respect to the bottom friction, we consider an additional scenario. As in the previous scenario, we assume that the initial deformation is equal to the vertical displacement computed by Okada's formulae, but now set the Manning roughness μ=0.03. The maps of computed flow depth for the two scenarios are compared in figure 65. Note that significant differences between the computed inundation zones occur inside the Los Angeles harbor (point 11) and near the Aquatic Center (point 10). The largest difference in the inundation extents is observed in flat areas, where the water flow can easily spread laterally and the bottom friction is important. In most of the flooded areas the difference in the simulated flow water depths is less than 0.2 m. The difference in inundation can also be partially explained by the slightly larger wave heights that are modeled in the case of μ=0.01—compare the water level plots for points 10 and 11 in figure 64. We emphasize that the degree of inundation along the northern edge of the displayed extent, near the Los Angeles River (fig. 65), can be a numerical artifact due to the solid-wall boundary condition imposed along the northern edge of the high-resolution grid.

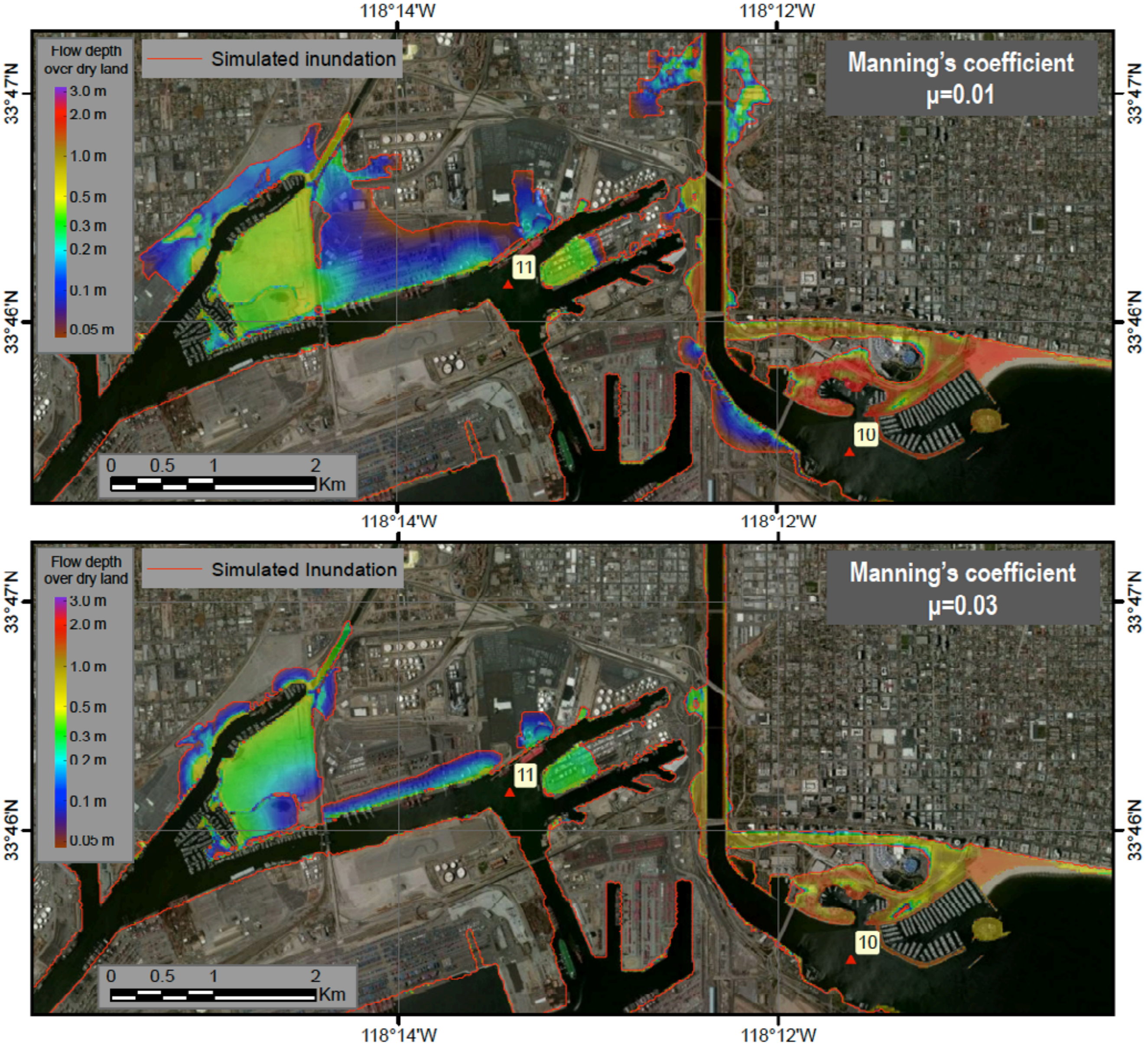

Figure 65. Maps showing modeled flow depths from the scenario tsunami in Los Angeles Harbor with different values of the Manning coefficient. Top: the flow depth above the dry land in the case of Manning's coefficient μ=0.01. Bottom: the potential flow depth in the case of μ=0.03. The coseismic deformation is assumed to be equal to the vertical sea-floor displacement. The most significant differences in the simulated inundation occur in the completely flat areas.

To analyze sensitivity of the hypothetical inundation to inclusion of the horizontal displacements into the sea-floor deformation, we consider another scenario. Here, the initial sea-floor displacement is computed with a contribution of the horizontal coseismic displacements, and the Manning roughness μ is set to 0.01. The differences in these parameters among all three considered scenarios are listed in table 13. The computed hypothetical inundation zones for the first and last considered scenarios are shown in figure 66. The difference in the maximum water level near the Aquatic Park and in the Inner Harbor can be as much as 0.25 and 0.15 meters, respectively, which is high enough to cause inundation in some flats regions. The time series of the water level dynamics at points 10 and 11 are shown in figure 64.

Table 13. Differences in assumptions under the three considered tsunami scenarios:

	Sea-floor deformation	Manning's coefficient
Scenario 1	Vertical displacement only	μ=0.01
Scenario 2	Vertical displacement only	μ=0.03
Scenario 3	Vertical and horizontal displacements	μ=0.01

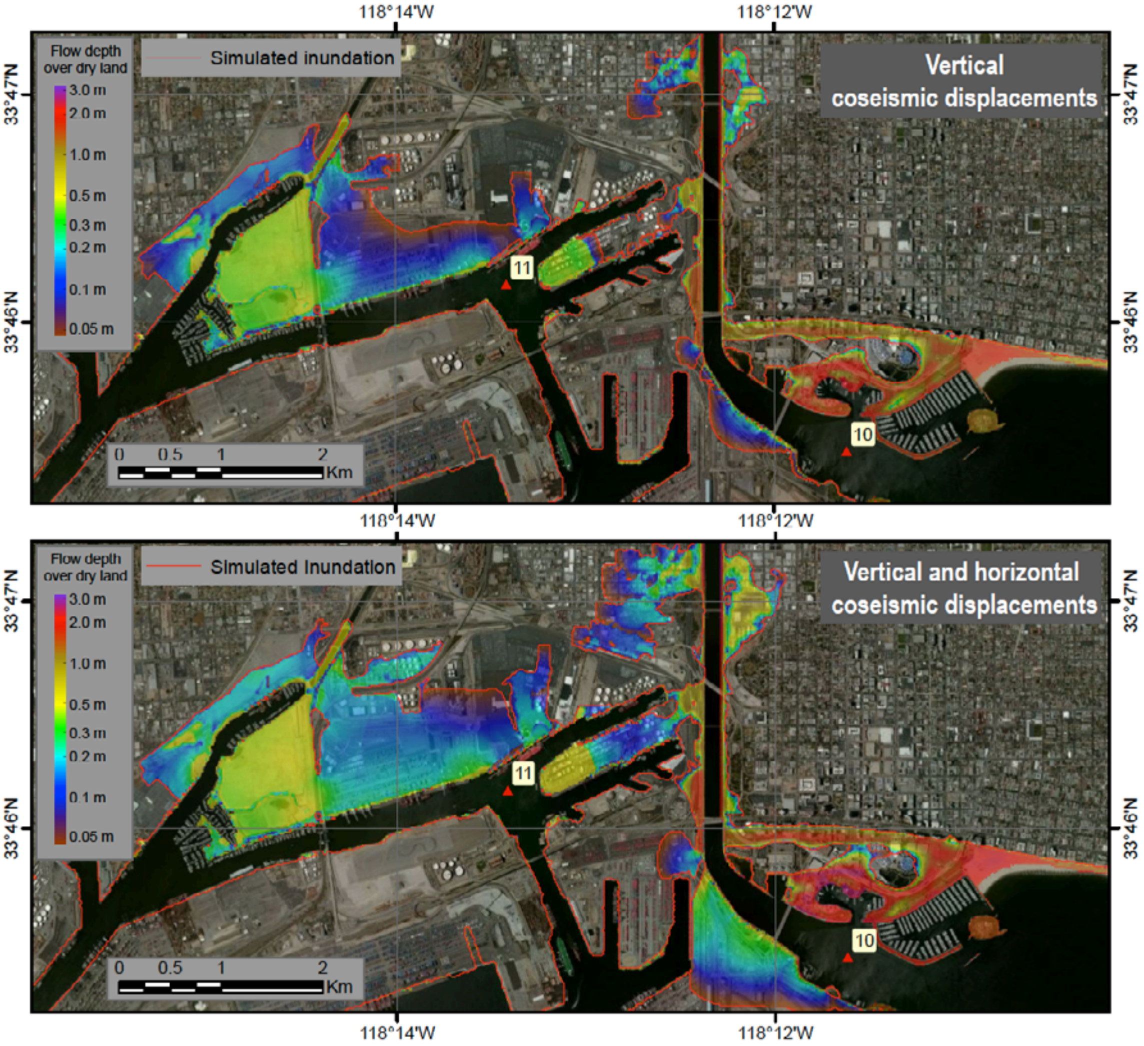

Figure 66. Maps showing inundation and flow depths in Los Angeles Harbor under two different scenarios. Top: the flow depth modeled under the assumption that the vertical coseismic deformation is equal to the vertical displacement of the seafloor during the earthquake. Bottom: the flow depth modeled under the assumption that the vertical coseismic deformation is a product of both the vertical and horizontal displacements of the seafloor during the earthquake. The Manning coefficient μ is assumed to be equal to 0.01 in both cases.

Sources of Errors and Uncertainties

The hydrodynamic model used to calculate tsunami propagation and runup is a nonlinear flux-formulated shallow water model (Nicolsky and others, 2011). It passed the validation and verification tests required for models used to simulate the tsunami dynamics (Synolakis and others, 2007; National Tsunami Hazard Mitigation Program, 2012). This model is currently employed to simulate the hypothetical tsunamis along the coast of Alaska and was successfully applied to model the 1964 tsunami propagation and runup. The model is being verified to simulate historic tsunamis along the California coast. The source mechanism remains the biggest unknown in the problem of tsunami modeling. Because the initial condition for the modeling is determined by the displacement of the ocean bottom, the largest source of errors is the earthquake model.

The horizontal resolution of the grid used for inundation modeling is about 12–13 m. This resolution is high enough to describe major relief features, but small topographic features, buildings, and other facilities cannot be accurately resolved. The San Pedro, Middle, and Long Beach breakwaters are resolved with one or two grid cells in the high-resolution DEM, while some smaller jetties might have some partial breaks in the DEM.

Summary

In this study we present the results of numerical modeling of earthquake-generated tsunamis for the Port of Los Angeles, California. The results of our modeling (figs. 62, 64–66) have been based on the best information available and are believed to be accurate; however, their preparation required many assumptions. Actual conditions during a tsunami event may vary from those considered, so the accuracy cannot be guaranteed. The limits of inundation shown should be used only as a guideline and require an expert interpretation. Actual areas inundated will depend on specifics of the earth deformations, on land construction, and on tide level, and they may differ from areas shown on the figures. The numerical results are not intended for land-use regulation or building-code development.

Acknowledgments

This project was supported in part by the Cooperative Institute for Alaska Research (CIFAR) with funds from the National Oceanic and Atmospheric Administration (NOAA) under cooperative agreement NA08OAR4320751 with the University of Alaska, and in part by the California Geological Survey under agreement 1011–023. Numerical calculations for this work were supported by a grant of High Performance Computing (HPC) resources from the Arctic Region Supercomputing Center (ARSC) at the University of Alaska Fairbanks as part of the U.S. Department of Defense High Performance Computing Modernization Program.

7. Port & Harbor Hydrodynamics

By Patrick Lynett and Sangyoung Son

Introduction and Background

In coastal locations where flooding and inundation are not a significant tsunami hazard for a particular event, the strong and erratic currents induced by the tsunami can still lead to major damage. Areas that are particularly exposed to tsunami current hazards are ports, harbors, and marinas. The 2011 Japan tsunami caused widespread damage to harbors along the California coastline; these effects were almost exclusively due to strong currents (Lynett and others, 2012). Also during the 2011 event, there was a remarkable occurrence at the Naval Harbor in Guam. Two nuclear submarines, tied side-by-side in series to the wharf, were pulled from their lines and floated briefly without control in the Harbor. The recorded tsunami amplitude (crest elevation) in this location was only 1 foot (0.3 m), and the hindcast modeled currents were 4 knots (2 m/s).

During the 2004 Indian Ocean tsunami, damage to harbors was noted in a series of papers by Okal and others (2006a,b,c). The most remarkable of these events occurred in the Port of Salalah, Oman. About 90 minutes after tsunami first arrival, strong currents near the farthest offshore unloading berth broke all of the mooring lines on a 285-m ship, the Maersk Mandraki, and pulled it away from the terminal and out of the Port. The vessel then drifted on the currents for hours, spinning numerous times, before beaching on a nearby sandbar. Once the vessel was pulled from its berth, tugs were quickly dispatched to the ship. However, because of the complex and rapidly varying nature of the flow—essentially a mess of large eddies and jets of current—the tugs were unable to control the motion of the Mandraki. At nearly the same time as the Mandraki parted its lines, the 292-m Maersk Virginia was approaching the Port entrance, and strong currents caused it to strike a breakwater. The Virginia experienced only minor damage due to this collision, and the Captain waited offshore of the entrance for 7 additional hours until he deemed the currents safe enough to enter the Port.

There were no direct measurements of the currents in the Port of Salalah, and we rely on numerical hindcasting of the event to provide flow speeds. Near the initial location of the Mandraki, numerically predicted currents are approximately 6 knots (3 m/s). For both the Salalah and Guam examples, the flow speeds would conventionally be thought of as not strong enough to pull a vessel from its lines; however, the highly sheared and rotational nature of the currents in these areas likely produced very irregular drag loading on the hull, including significant yaw, causing the vessel to act as a huge moment arm and leading to uneven loading of mooring lines. The goal of this modeling exercise is to perform highly detailed and resolved tsunami current simulations, such that the remarkable effects observed recently in harbors might be understood and evaluated for the SAFRR scenario.

Hydrodynamic Modeling Approach and Results

With incident tsunami information provided by basin-scale propagation models, high-resolution simulations with a high-order physics model have been done for select locations. Specifically, the dispersive, rotational, and turbulent flow model of Kim and Lynett (2011) is applied at San Diego Bay, Ports of Los Angeles (POLA) and Long Beach (POLB), and Ventura Harbor. For these three coastal locations, a uniform spatial resolution of 5 m is used, and the tsunami signal is super-imposed over the tidal signal, such that the complete hydrodynamic forcing is included. The tsunami signal is taken from a 2-arc-min resolution, open-ocean propagation simulation of the entire Pacific Ocean basin using the

COMCOT model (Liu and others, 1995), forced with the initial condition described in previous sections. The simulations presented in this section take the output from the propagation simulation at the 25-m offshore depth; at this depth, the tsunami height (maximum crest-to-trough distance) is 1.1 m at POLA/POLB, 2.2 m at Ventura, and 2.1 m at San Diego, with wave periods of the leading waves in the range of 20-30 minutes.

A weakly dispersive and rotational Boussinesq-type modeling approach is used for the simulations in this section. Recently, a number of nontraditional Boussinesq approaches have been developed, with the goal of including horizontal vorticity explicitly in the flow field. An attempt to include these dynamics under a breaking wave is found in Veeramony and Svendsen (2000), with further advances given in Musemeci and others (2005). A similar attempt, resulting in the model employed here, was made by Kim and others (2009), who included the viscous effects of a bottom shear, and the associated rotationality, directly in a Boussinesq-type derivation. Although this leads to a far more complex equation model, it includes the physics necessary to simulate boundary shear and the complete coupling of these effects with a nonlinear, dispersive wave field. This model can predict the friction-induced changes to the vertical profile of velocity under weakly unsteady flow, and it thereby can provide good estimates of internal kinematics. It is also able to translate the bottom-created horizontal vorticity into a vertical vorticity field. Most important to the harbor simulations provided here, results include highly localized current features, such as jets and whirlpools, which tend to exhibit the greatest flow speeds. Additionally, all of the numerical efforts here implement established aspects of Boussinesq-type modeling, developed by the lead author and other researchers. These aspects include wind wave breaking (Kennedy and others, 2000; Lynett, 2006) and accurate moving boundary schemes for shoreline motion (Lynett and others, 2002). Because Boussinesq-type models tend to be complicated sets of lengthy equations, usually requiring high-order numerical solution schemes, the computational cost of a solution is not insignificant. To lessen this burden, a parallel implementation based on message passing interface (MPI) has been used here (Sitanggang and Lynett, 2005), permitting the large-scale simulation (tens of square kilometers and tens of millions of grid points) in a reasonable duration of processing time.

Figures 67 and 68 show the predicted maximum sea-surface elevations and current speed, respectively, for Ventura Harbor. Flood elevations are between 2 and 3 m in the area, with water overtopping the dune in a couple of locations. Maximum currents through the Ventura Harbor channel exceed 14 knots (7.2 m/s), with widespread maximum speeds greater than 8 knots (4 m/s). Under these conditions it would be reasonable to expect widespread damage to floating infrastructure throughout the harbor.

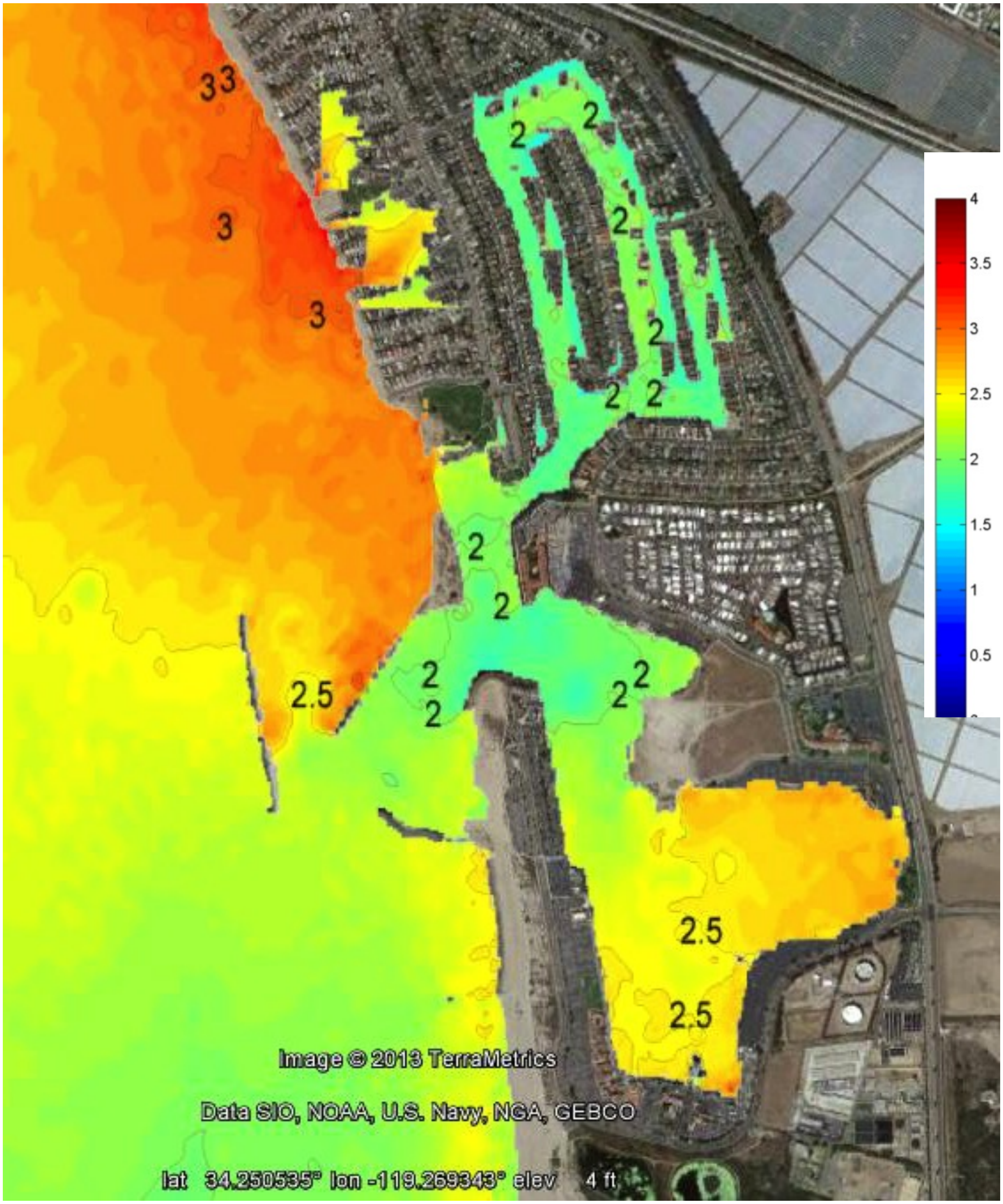

Figure 67. Map showing maximum predicted water surface elevation from the scenario tsunami, relative to mean high water datum, for Ventura harbor. Color scale in meters.

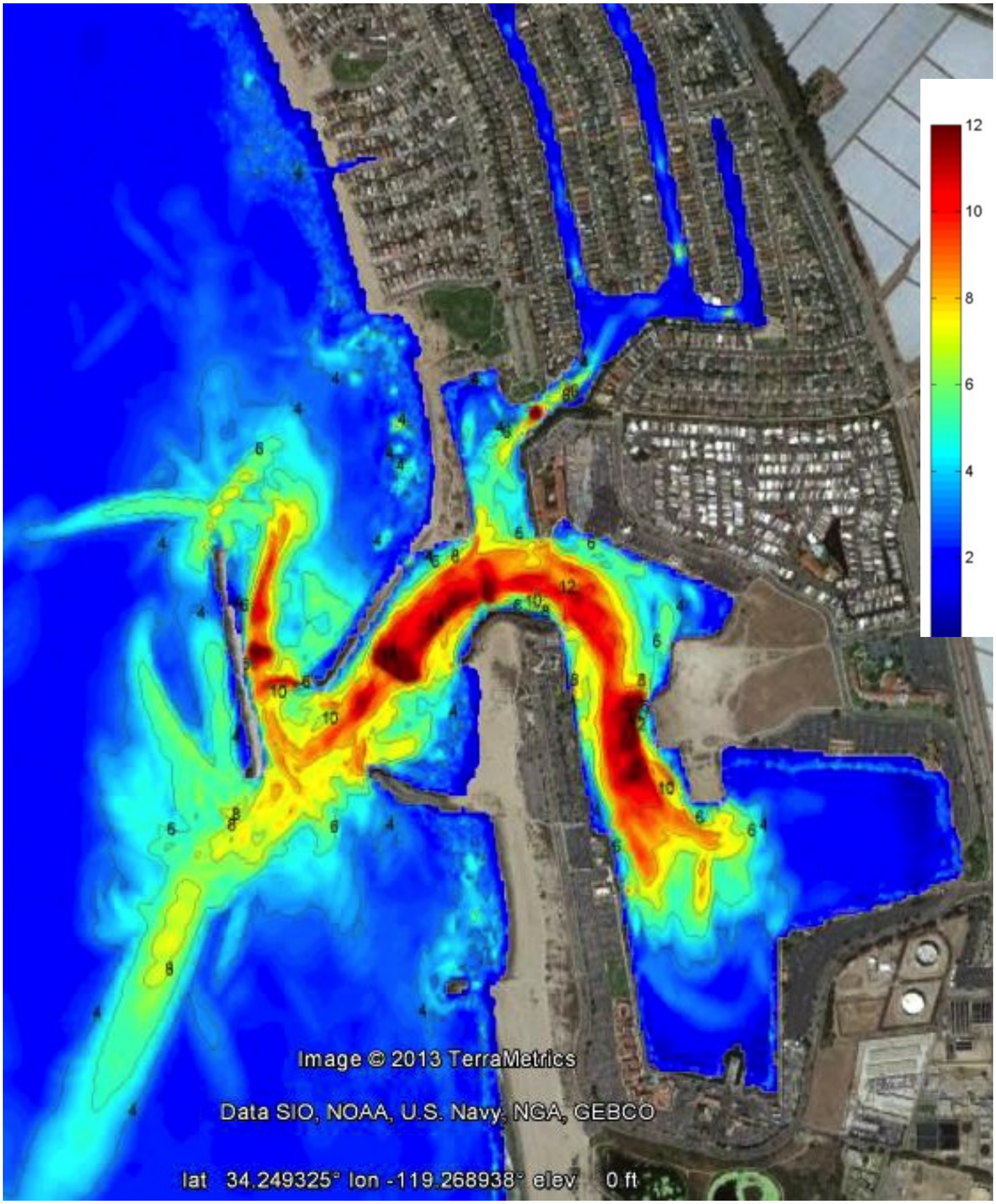

Figure 68. Map showing maximum predicted tsunami-induced currents (knots; 1 knot = 0.51 m/s) for Ventura Harbor. Color scale in knots.

The maximum predicted currents in San Diego Bay are given in figure 69. In general, the modeled current speeds are not great. The Shelter Island area appears to be the most at-risk location in the Bay, but strong currents might also affect Point Loma. Farther inside the Bay, near the primary naval piers, currents are weak, and vessel complications here have a low probability. Debris from Shelter Island could plausibly cause obstructions in the main channel and hinder traffic in and out of the Bay.

Figures 70 and 71 give maximum current speeds for the Port of Los Angeles (POLA) and the Port of Long Beach (POLB), respectively. Note that the numerical domain used here was continuous; the POLA and POLB were in fact simulated together because they are adjacent and contiguous. In the POLA, currents are strongest at Angels Gate, the Cabrillo Marina, the Boat Yard, and the old Navy Yard. Once the tsunami event is underway, navigation through the Gate would be very dangerous. In the Cabrillo Marina and Boat Yard, currents are likely strong enough to break apart floating docks, damage piles, and pull small vessels from their mooring lines. The strongest currents are found in the old Navy Yard; however there are no exposed floating assets in this immediate area. At the POLB, again strong currents are found at Queens Gate. Also in the POLB, strong and jet-like currents are predicted at the entrance to the main cargo container area (Pier J). Currents here may be strong enough to damage, and possible break, mooring lines.

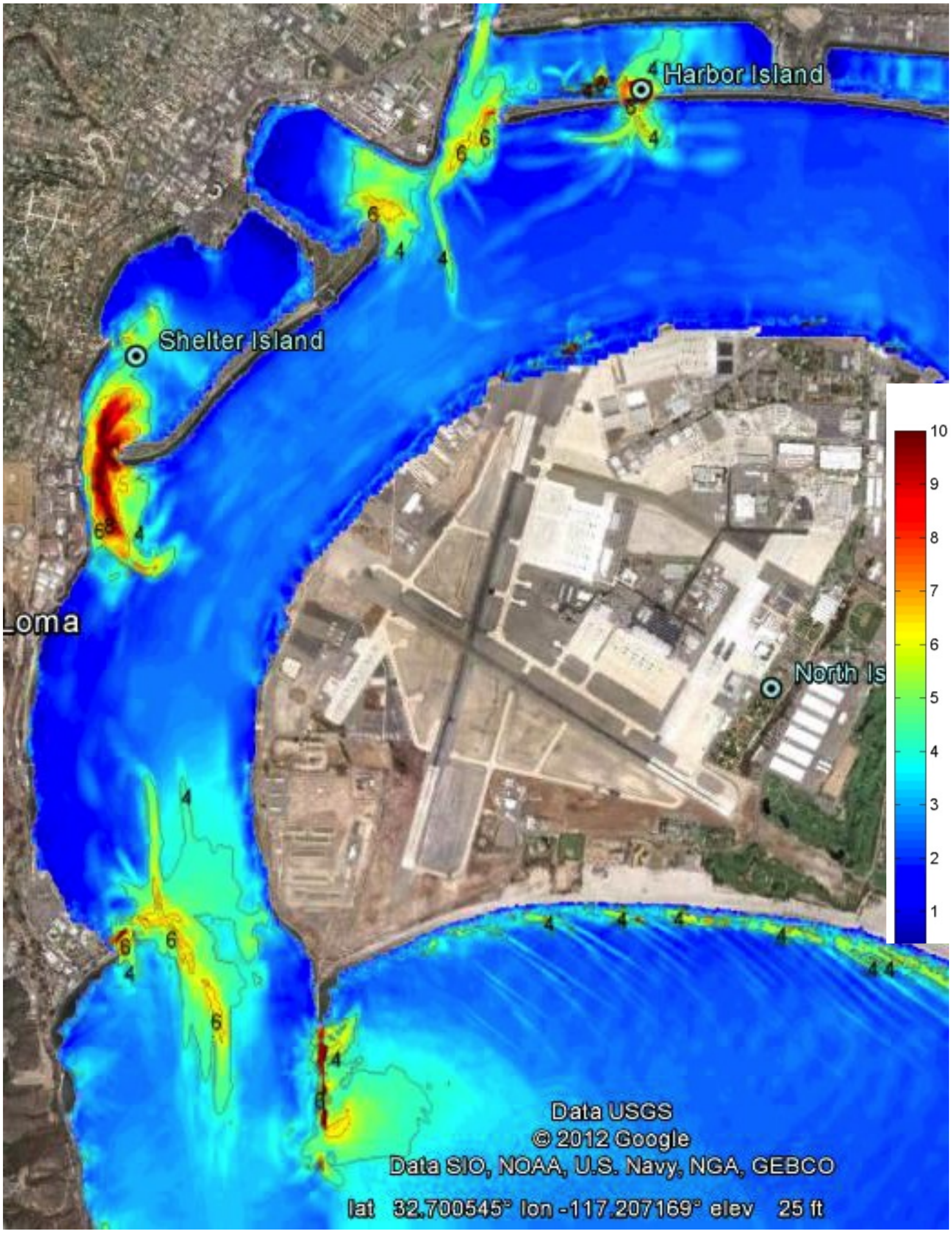

Figure 69. Map showing maximum predicted tsunami-induced currents (knots; 1 knot = 0.51 m/s) for San Diego Harbor. Color scale in knots.

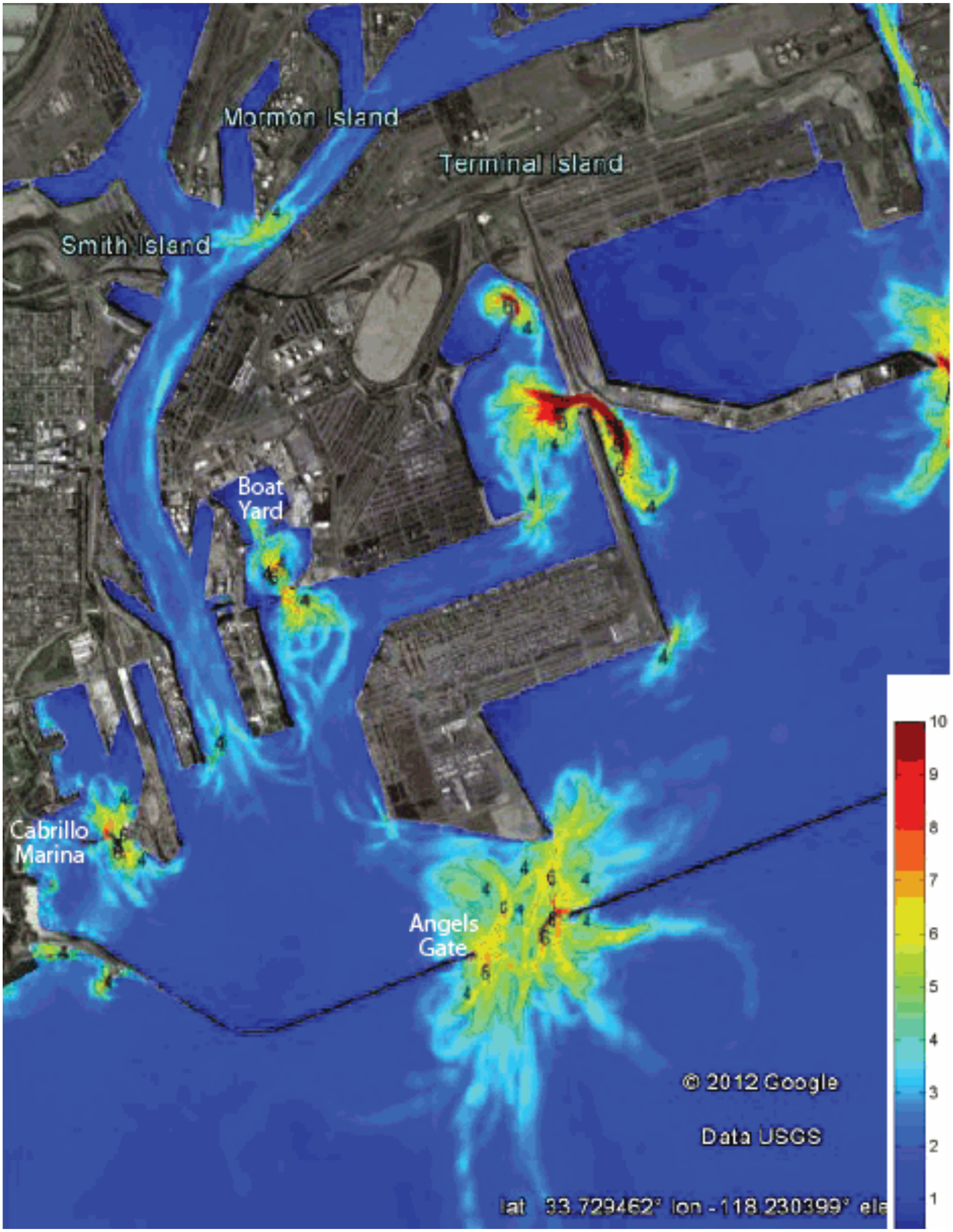

Figure 70. Map showing maximum predicted tsunami-induced currents (knots) for the Port of Los Angeles.

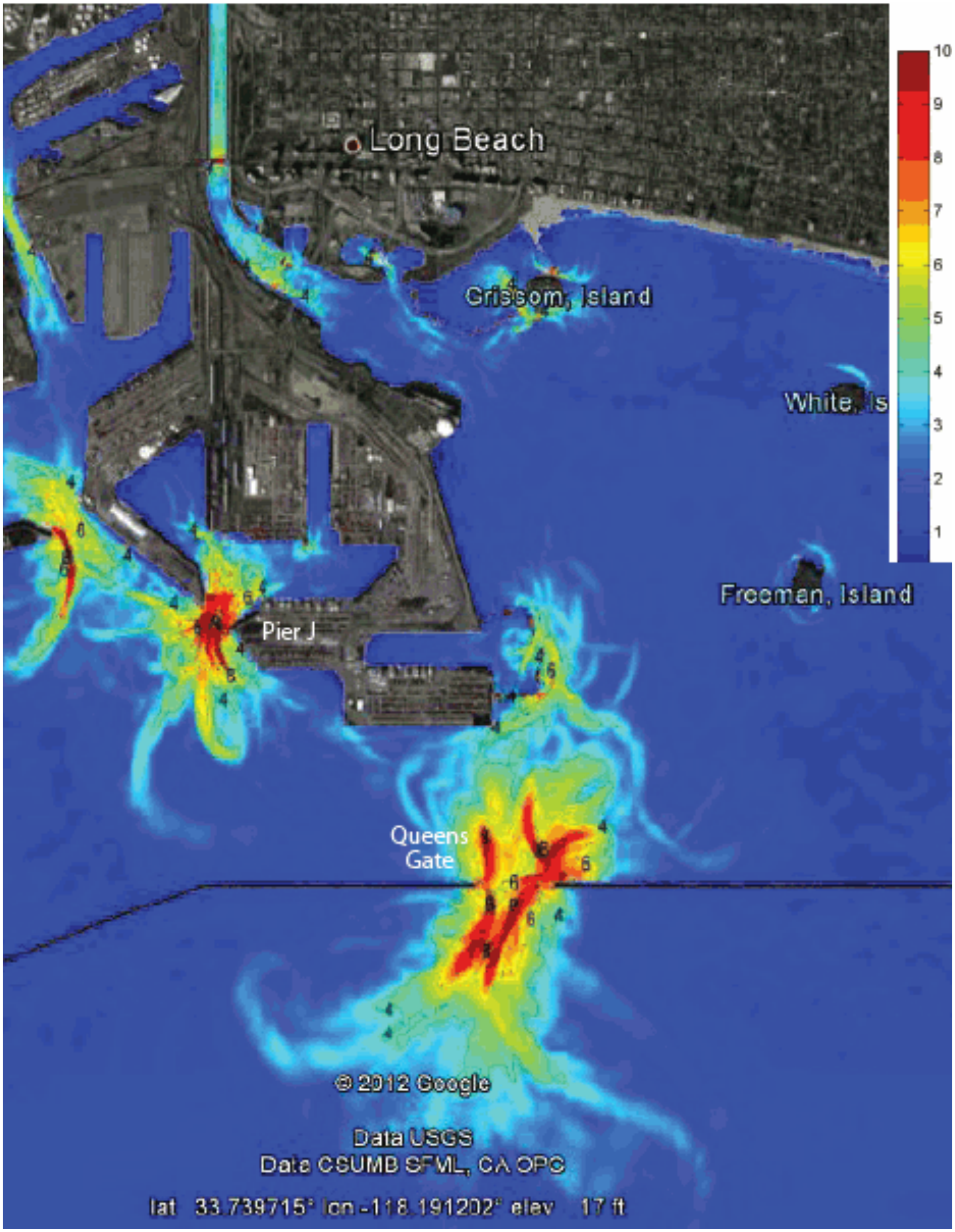

Figure 71. Map showing maximum predicted tsunami-induced currents (knots) for the Port of Long Beach.

Modeling of Tsunami-Induced Sediment Transport

Theoretical Approach

In this modeling we attempt to use a weakly dispersive Boussinesq model to study transport and morphological changes in the nearshore area (see, for example, Xiao and others, 2010). In the present study, three separate models, as given below, are coupled appropriately to create a complete sediment transport model system in the coastal area. The hydrodynamic foundation is the same as that used in the above section, and is given in condensed form as:

$$\frac{\partial H}{\partial t}+\frac{\partial HU}{\partial x}+\frac{\partial HV}{\partial y}+B_c=\frac{E-D}{1-p}$$

$$\frac{\partial HU}{\partial t}+\frac{\partial HU^2}{\partial x}+\frac{\partial HUV}{\partial y}+gH\frac{\partial \zeta}{\partial x}+HB_x+UB_c=-\frac{(E-D)U}{1-p}$$

$$\frac{\partial HV}{\partial t}+\frac{\partial HUV}{\partial x}+\frac{\partial HV^2}{\partial y}+gH\frac{\partial \zeta}{\partial y}+HB_y+VB_c=-\frac{(E-D)V}{1-p}$$

where $H=\zeta+h$ is total water depth, ζ is surface elevation, h is water depth, and U and V are the x and y components of velocity at −0.531h. B_c, B_x, B_y represent higher order terms adding dispersive and bed-frictional turbulent effects, which distinguish this Boussinesq system from a potential shallow-water set. Full descriptions for those terms can be found in Kim and others (2009) and Son and others (2011).

Note also that some source terms are added here to the "fixed-bed" Boussinesq model on the right hand side, among which E and D are sediment erosion and deposition fluxes, respectively, and p is bed porosity (Cao and others, 2004; Xiao and others, 2010). Sediment transport is modeled as:

$$\frac{\partial HC}{\partial t}+\frac{\partial HCU}{\partial x}+\frac{\partial HCV}{\partial y}=\frac{\partial}{\partial x}\left(K_xH\frac{\partial C}{\partial x}\right)+\frac{\partial}{\partial y}\left(K_yH\frac{\partial C}{\partial y}\right)+E-D$$

where C is the depth-averaged sediment concentration and K_x, K_y are the sediment diffusivities, assumed to be the same as the turbulent eddy viscosity (Rakha and others, 1997). Sediments entrained by the flow field are governed by the transport model above. This model is a typical form for scalar transport, but has additional source and sink terms on the right hand side, to account for the addition and removal of sediment to and from the water column through erosion and deposition, respectively. In this study erosion and deposition fluxes are calculated by empirical formulas.

The erosion flux can be obtained by (Cao and others, 2004):

$$E=\begin{cases}\varphi(\theta-\theta_c)(U^2+V^2)^{0.5}\,H^{-1}\,(d_{50})^{-0.2} & if\ \theta>\theta_c\\ 0 & else\end{cases}$$

whereas deposition flux can be calculated by

$$D=C_aw_0$$

In the above equations,

$\theta=\frac{U_*^2}{(\rho_s/\rho_w-1)gd_{50}}$; Shields parameter

θ_c = critical Shields parameter (=0.045 in this study)

$U_*=\sqrt{f}U$; friction velocity

$f=\frac{gn^2}{H^{1/3}}$; friction factor using Manning's formula

n= Manning's coefficient

ρ_s= density of sediment

ρ_w= density of water (1,000 kg/m^3 is used in this study)

d_{50} = median grain diameter

φ = empirical coefficient

$C_a = \square C$ near-bed concentration

$\square = \min[2.0, (1-p)/C]$

$\mathrm{w}_0 = \frac{4\times g\times d_{50}}{3\times(0.2)^{(\rho s/\rho w-1)}}$; fall velocity (see Ponce, 1989)

The morphological evolution of the seafloor is given by the simple conservation equation

$$\frac{\partial h}{\partial t} = \frac{(E-D)}{1-p}$$

which is, of course, controlled only by the erosion and deposition rates. The updated bathymetry predicted by this equation is then used in the hydrodynamic model; all of these equations are coupled and solved simultaneously.

In the hydrodynamic model, turbulent closure models for bed stress, bottom-induced turbulence, wave-breaking, and stochastic backscatter are included in the higher-order terms (B_c, B_x, B_y) of the equations. Although complete details of the individual components can be found directly in relevant references, some are briefly introduced here. For the calculation of bottom-induced turbulence, Smagorinsky's turbulent eddy viscosity model for horizontal eddy viscosity and Elder's (1959) model for vertical eddy viscosity are adopted (Kim and others, 2009). It is well recognized that turbulent energy transfer from subgrid scales to resolved scales can be significant in regions where high shear stresses are present. To yield a better representation of this 3D turbulent process in the 2HD model, the stochastic backscatter model proposed by Hinterberger and others (2007) is included in (B_x, B_y). Through the inclusion of the above-mentioned physics in the model, which have increasingly important effects in shallow regions, a more realistic and physically rigorous recreation of the sediment transport can be achieved.

Model Validation and Calibration

To validate the developed model, four typical tests have been attempted. First, one-dimensional dam-break flow over a movable bed is simulated by the model and compared with the laboratory data by Fraccarollo and Capart (2002). The experiment was performed in a channel with 2.5-m length, 0.1-m width and 0.25-m depth, which had 0.1 m initial water depth upstream while a dry condition was initially retained downstream. PVC particles of 3.5-mm diameter with 1,540-kg/m^3 density were used for the movable bed materials.

In the numerical simulation, the grid size (dx) is 0.005 m and time step (dt) is dynamically determined by a Courant number of 0.1. The sediment porosity (p) and settling velocity (w_0) are set to 0.3 and 0.18 m/s, respectively, based on Wu and Wang (2008). Manning's coefficient (n) is 0.025, and the empirical coefficient in the erosion flux equation (φ) is 0.003. Simulated results compared with measured data are shown in figure 72. Generally good agreement between calculation and measurement is found, while some discrepancies exist in surface elevations near the leading front and hydraulic jump locations.

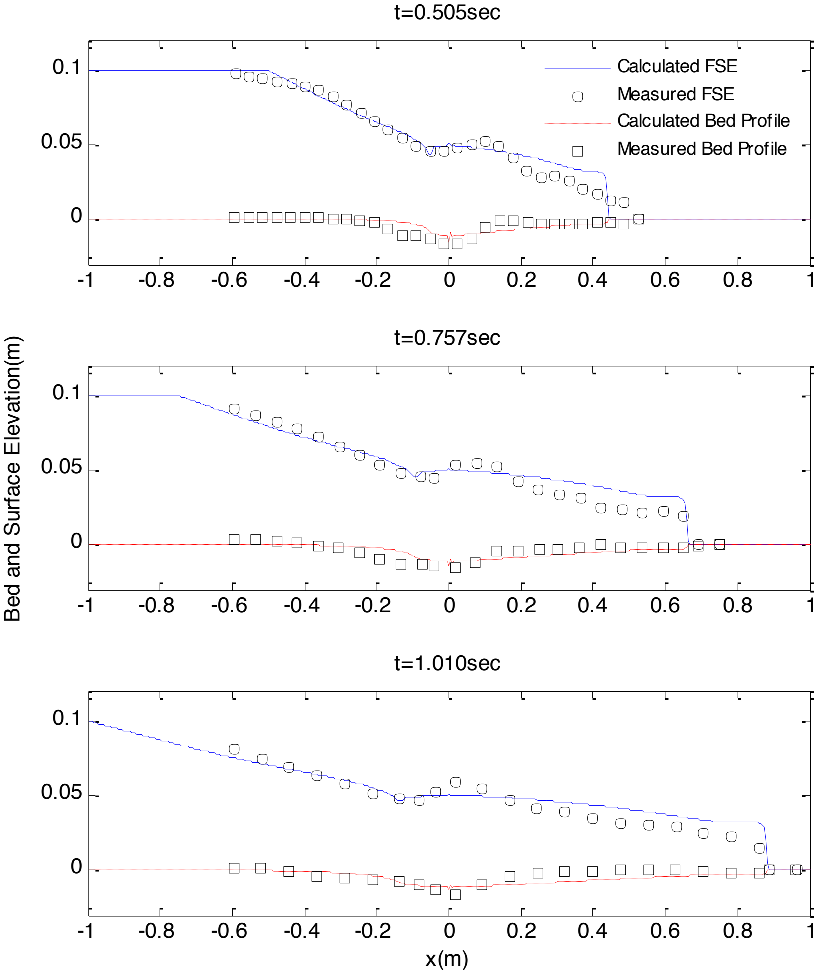

Figure 72. Graphs comparing measured and simulated dam-break flows over a movable bed at different elapse time after dam break. x=0: position of dam. Elevation = 0: initial bed surface elevation.

Recently, Kobayashi and Lawrence (2004) carried out laboratory experiments in a wave flume (length 30 m, width 2.4 m, and height 1.5 m) to study beach profile changes under breaking solitary waves, as shown in figure 73. A solitary wave of 0.216-m height was generated by wave paddle and propagated to the sloping beach composed of sand grains. The water depth beyond the base of the beach was 0.8 m. The beach has initial slope of 1:12 that is expected to be changed by the breaking solitary waves. The solitary wave was repeated eight times to consider the effects by multiple wave attacks. Bottom profiles after four and eight waves, as well as surface elevations at eight locations (G1 to G8) across the beach after four waves, were measured. The median grain diameter (d_{50}), fall velocity (w_0), specific gravity, and porosity (p) are 0.18 mm, 2.0 cm/s, 2.6, and 0.4, respectively.

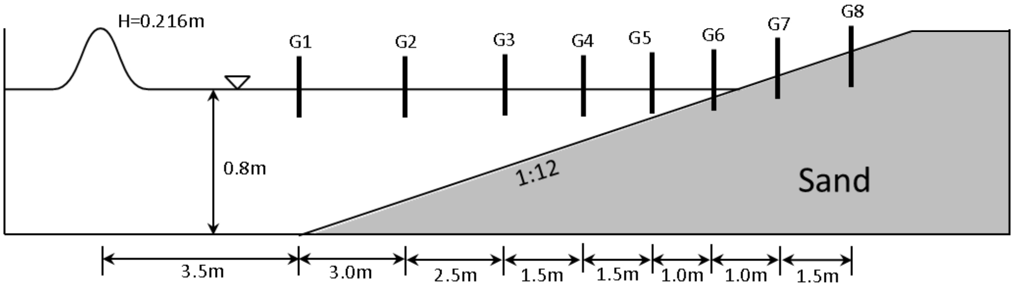

Figure 73. Diagrammatic cross section showing experimental setup for breaking solitary waves on a sloping sand beach.

To evaluate the accuracy and performance of the model, their experiment was recreated through numerical modeling using the same conditions as in the experimental setup. The simulation was performed using a uniform grid size of 0.1 m and varying time step with a Courant number of 0.4. For Manning's coefficient (n) and empirical parameter (φ), 0.025 and 7.5×10^{-6} are used, respectively. Additionally, to account for turbulent mixing and dissipation by wave breaking, the eddy-viscosity model proposed by Kennedy and others (2000) is adopted in the test.

Calculated beach profiles compared with the measured data are shown in figure 74. Fairly good agreement is found in both results after four and eight waves. Significant erosion at the foreshore is observed in both measured and computed results, which may be explained by the strong backwash current caused when the solitary wave rushes back down. The entrained sediments are deposited on the seaward side. In figure 75, calculated surface elevations agree well with measurements, although some errors are seen in gauges G6–G8 for wave runup and rundown. This discrepancy is largely due to the errors in the simulated shoreline (fig. 74), which affects the water depth.

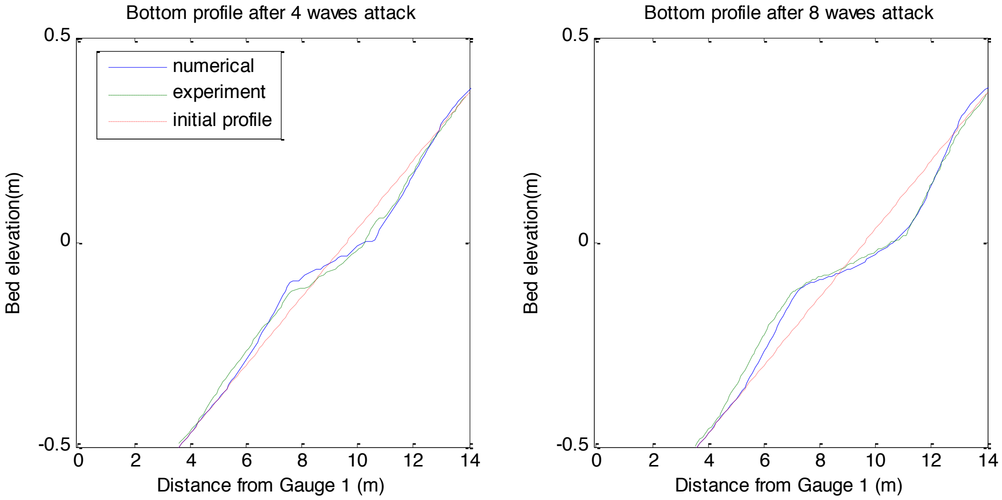

Figure 74. Graphs comparing measured and calculated beach profiles for Kobyashi test.

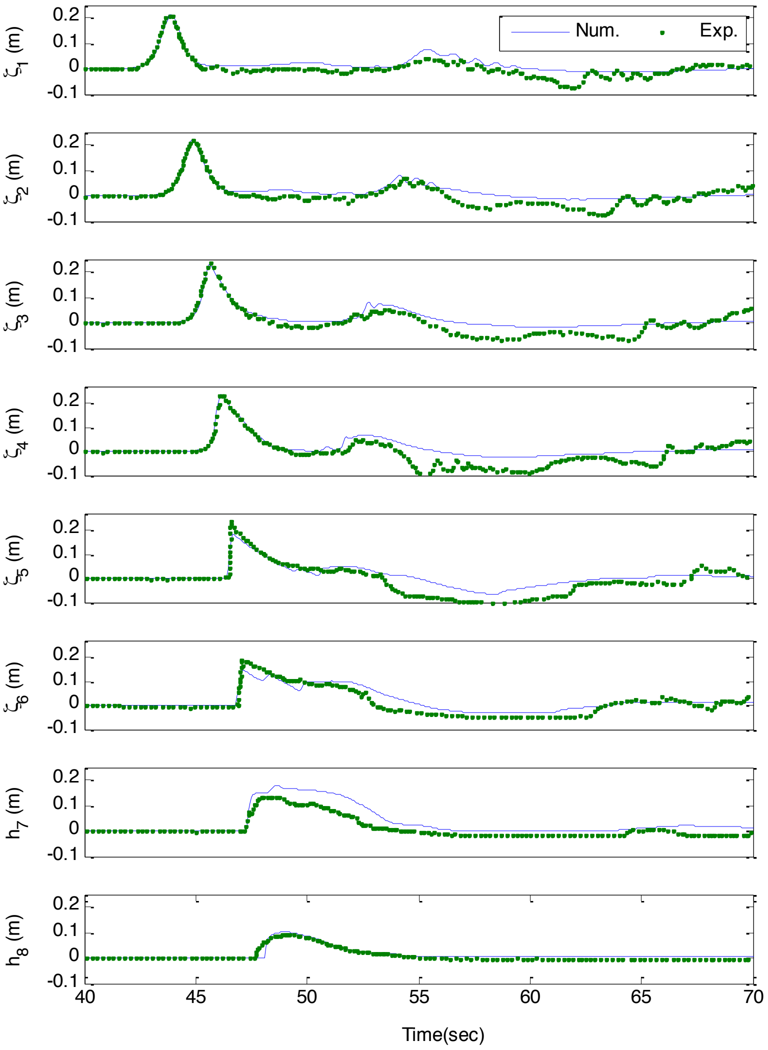

Figure 75. Graphs comparing experimental (Exp.) and numerical (Num.) simulated temporal free surface elevations at different locations (gauges G1 to G8) during the fifth wave in the simulated erosion of a beach profile.

Finally, the case of flow in a partially breached dam-break was used to test the present model. This test was conducted experimentally in Xiao and others (2010). Figure 76 depicts the experimental setup of the test, in which the middle of the channel has a moveable bed section composed of coal ash. The median diameter (d_{50}) of the coal ash was 0.135 mm and the density was 2,248 kg/m^3. Initial water depths were 0.4 m and 0.12 m for upstream and downstream, respectively. Strong jet-like flow through the 0.2-m-wide gap caused significant erosion, and cross-sectional profiles of the bottom were measured at cs1 (x = 2.5 m) and cs2 (x = 3.5 m) after 20 seconds.

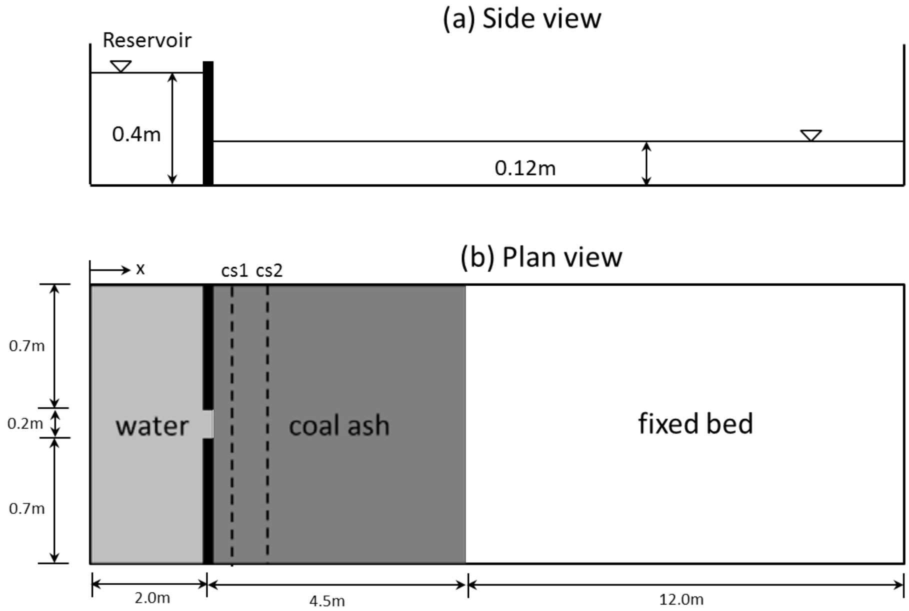

Figure 76. Diagrams showing side view (a) and plan view (b) of the experimental setup of a dam-break flow through a partial breach over a moveable bed. Cross-sectional profiles of the bottom were measured at locations cs1 and cs2.

The identical situation to this experimental test has been reproduced numerically with a grid resolution of 0.025 m. As in previous tests, our time step varies and is based on a Courant number of 0.3. Following Xiao and others (2010), Manning's coefficient (n) is set to 0.015 while the empirical parameter (φ) is tuned to 5.0×10^{-5} based on Kim and Lee (2011). Fall velocity can be approximated by an empirical formula (Ponce, 1989) because it is not given explicitly in the experimental description.

Figure 77 compares the bottom profiles in the simulated and measured data. Reasonable agreement is seen at both profiles cs1 and cs2, but the simulation overestimates the peak erosion depth at cs1. As pointed out by Hinterberger and others (2007), in depth-averaged 2D modeling, turbulence backscattering needs to be considered when strong horizontal shear exists (as near the breached gap in this test). Through it, turbulence energy transfer from unresolved subdepth scale to the resolved 2D flows can be explained. Figure 78 shows the same results as in figure 77 but with the backscatter model used. Prediction of maximum erosion depth at cs1 is much improved by including backscatter model.

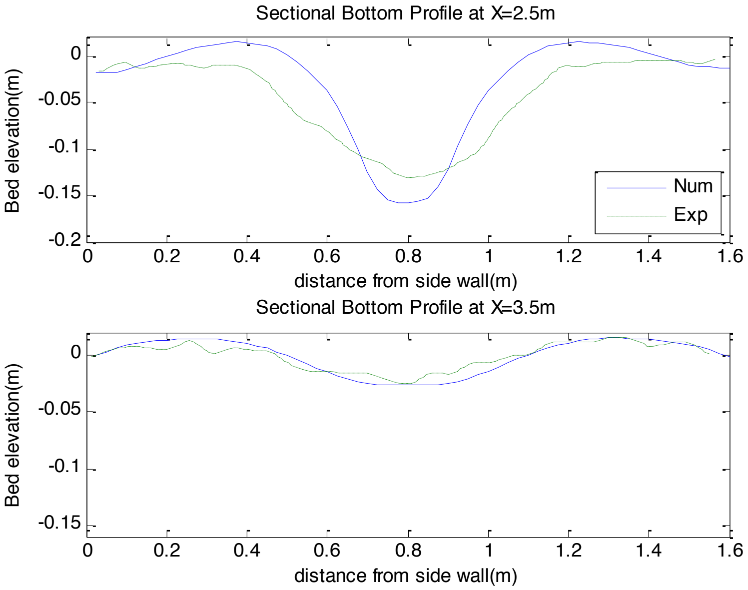

Figure 77. Graphs comparing measured (Exp) and calculated (Num) bottom profiles in the case of the partially breached dam-break test (Xiao and others, 2010).

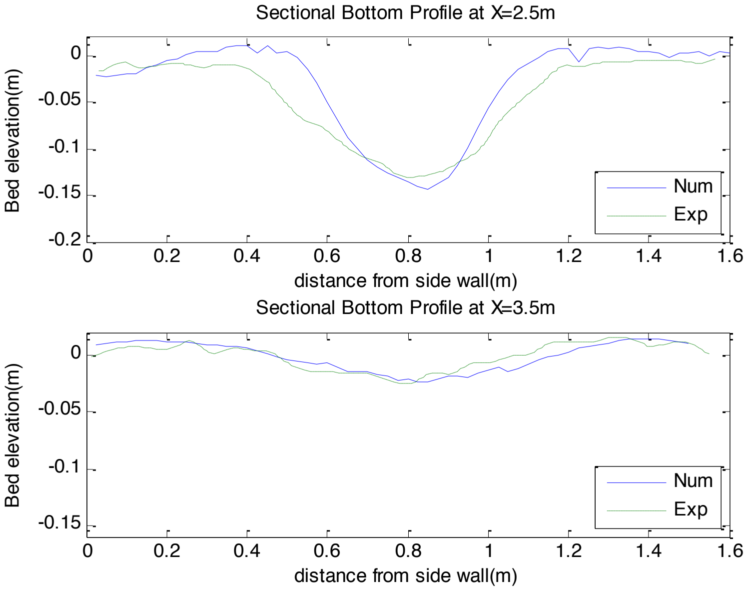

Figure 78. Graphs comparing measured (Exp) and calculated (Num) (with backscatter model) bottom profiles in the case of the partially breached dam-break test (Xiao and others, 2010).

Model Application to Santa Cruz Harbor, California

Some recent observations have shown that far-field tsunami events can lead to severe changes in bottom morphology, especially in the nearshore area (Lacy and others, 2012; Wilson and others, 2012). Because relatively small-amplitude tsunami waves (< 1–2 m) can create strong current fields near harbor basins (see, for example, Son and others, 2011; Lynett and others, 2012), tsunamis have great potential to mobilize bed sediments. Needless to say, therefore, it is important to estimate tsunami currents accurately in the nearshore area in evaluating morphological changes near the shoreline. Traditional approaches to estimate sediment transport by tsunami waves are based on the shallow-water equation model (for example, Li and others, 2012).

As a practical application of the present model to the coastal region, the 2011 Japan tsunami event is considered For precise estimations of current fields from far-field tsunami waves in the nearshore area, a multigrid and multiphysics model developed by Son and others (2011) was applied to 2011 Japan event. A total of five nested layers were employed, with different levels of resolution. The final layer has the smallest domain focusing only on the Santa Cruz Harbor area, with relatively fine grid size (10 m), and is solved by Boussinesq equations to account for higher order effects by dispersive and turbulent processes. On the other hand, the rest of the layers, which generally cover a larger domain with deeper ocean rather than the shallow coastal region, are solved by shallow-water equations. The parametric values used in the sediment model are the median sediment diameter $d_{50} = 0.15$mm, Manning's coefficient (n) = 0.025, and the empirical parameter (φ) = 5.0×10^{-5}, which is an acceptable value for coastal sedimentation (see, for example, Kim and Lee, 2011). The Courant number of the Boussinesq model is set to 0.4.

The simulation was performed for 14 hours of tsunami waves at the harbor to allow enough duration for the erosion and sedimentation processes. Resultant bathymetric change at the harbor entrance is shown in figure 79, compared with observed data. The overall pattern of sedimentation and erosion is quite well recreated by the numerical model.

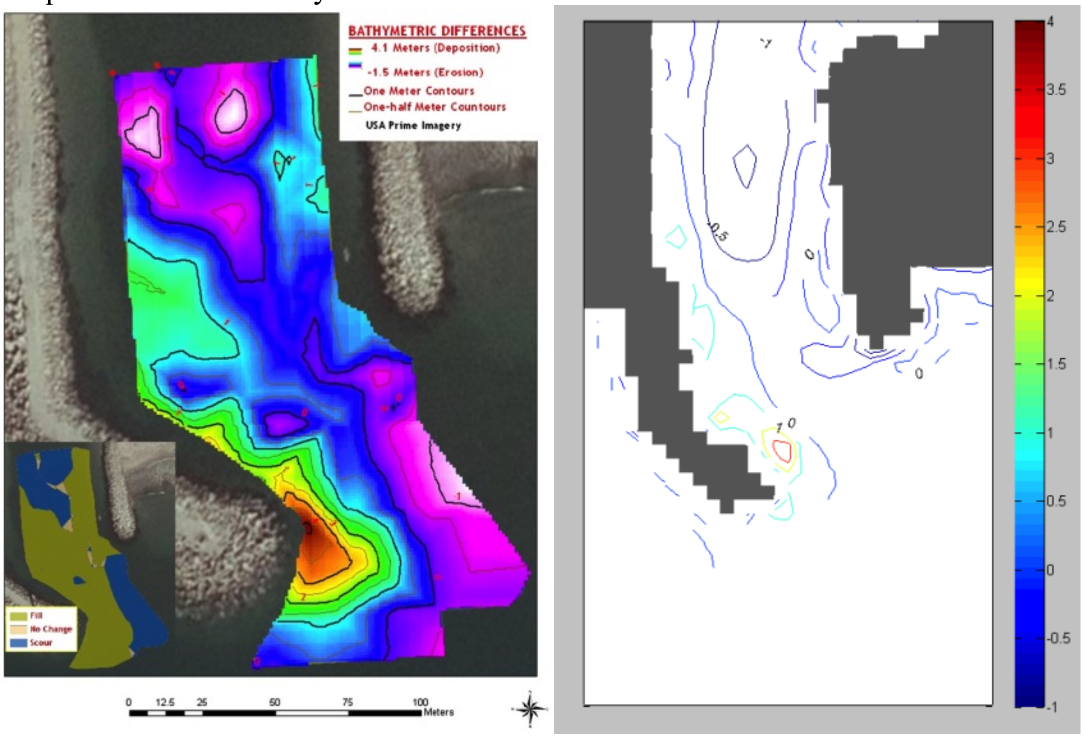

Figure 79. Changes in bottom bathymetry from tsunami-induced currents in Santa Cruz Harbor, California. Left: observed changes in the 2011 Japan tsunami event, excerpted from Wilson and others (2012). Right: computed bathymetric changes from the simulation. Color scale in meters (positive = deposition; negative = erosion).

Acknowledgments

The Science Application for Risk Reduction (SAFRR) Tsunami Modeling Working Group gratefully acknowledges the constructive and helpful comments of the following reviewers: Yong Wei (National Oceanic and Atmospheric Administration/Pacific Marine Environmental Laboratory), David Dykstra (Moffatt & Nichol), Ruth Harris (U.S. Geological Survey, USGS), and Jessica Lacy (USGS). The SAFRR tsunami project and the modeling effort described in this report would not have been possible without the expert coordination and management efforts of Stephanie Ross (USGS).

References

Ammon, C.J., Lay, T., Kanamori, H., and Cleveland, M., 2011, A rupture model of the 2011 off the Pacific coast of Tohoku earthquake: Earth Planets Space, v. 63, p. 693–696.

Andrews, D.J., 1976, Rupture velocity of plane strain shear cracks: Journal of Geophysical Research, v. 81, p. 5679–5687.

Andrews, D.J., 2004, Rupture models with dynamically determined breakdown displacement: Bulletin of the Seismological Society of America, v. 94, p. 769–775.

Baba, T., Hirata, K., and Kaneda, Y., 2004, Tsunami magnitudes determined from ocean-bottom pressure gauge data around Japan: Geophysical Research Letters, v. 31, doi:10.1029/2003GL019397.

Baba, T., Cummins, P.R., Thio, H.K., and Tsushima, H., 2009, Validation and joint inversion of teleseismic waveforms for earthquake source models using deep ocean bottom pressure records—a case study of the 2006 Kuril megathrust earthquake: Pure and Applied Geophysics, v. 166, p. 55–76.

Balay, S., Buschelman, K., Eijkhout, V., Gropp, W.D., Kaushik, D., Knepley, M.G., McInnes, L.C., Smith, B.F., and Zhang, H., 2004, PETSc Users Manual, Revision 2.1.5: Argonne National Laboratory Tech. Rep. ANL-95/11.

Barall, M., 2008, FaultMod Finite Element Code, available at http://scecdata.usc.edu/cvws/download/codedesc/Barall_FaultMod_Desc.pdf, 6 p.

Barall, M., 2009, A grid-doubling finite-element technique for calculating dynamic three-dimensional spontaneous rupture on an earthquake fault: Geophysical Journal International, v. 178, p. 845–859.

Barberopoulou, A., Borrero, J.C., Uslu, B., Kalligeris, N., Goltz, J.D., Wilson, R.I., and Synolakis, C.E., 2009, New maps of California to improve tsunami preparedness: Eos (American Geophysical Union Transactions), v. 90(16), p. 137–138.

Becker, J.J., Sandwell, D.T., Smith, W.H.F., Braud, J., Binder, B., Depner, J., Fabre, D., Factor, J., Ingalls, S., Kim, S.-H., Ladner, R., Marks, K., Nelson, S., Pharaoh, A., Trimmer, R., Von Rosenberg, J., Wallace, G., and Weatherall, P., 2009, Global bathymetry and elevation data at 30 arc seconds resolution; SRTM30_PLUS: Marine Geodesy, v. 32, p. 355–371.

Beroza, G.C., and Mikumo, T., 1996, Short slip duration in dynamic rupture in the presence of heterogeneous fault properties: Journal of Geophysical Research, v. 103, p. 489–511.

Bilek, S.L., and Lay, T., 2002, Tsunami earthquakes possibly widespread manifestations of frictional conditional stability: Geophysical Research Letters, v. 29, doi:10.1029/2002GL015215.

Blanpied, M.L., Tullis, T.E., and Weeks, J.D., 1998, Effects of slip, slip rate, and shear heating on the friction of granite: Journal of Geophysical Research, v. 103, p. 489–511.

Borrero, J.C., Bell, R., Csato, C., DeLange, W., Goring, D., Greer, D., Pickett, V., and Power, W.L., 2012, Observations, effects and real time assessment of the March 11, 2011 Tohoku-oki tsunami in New Zealand: Pure and Applied Geophysics, doi: 10.1007/s00024-00012-00492-00026.

Brune, J.N., 1996, Particle motions in a physical model of shallow angle thrust faulting: Proceedings of the Indian Academy of Sceinces (Earth Planetary Sciences), v. 105, p. L196–L206.

Bruns, T.R., von Huene, R., Culotta, R.C., Lewis, S.D., and Ladd, J.W., 1987, Geology and petroleum potential of the Shumagin margin, Alaska, in Scholl, D.W., Grantz, A., and Vedder, J.G., eds., Geology and Resource Potential of the Continental Margin of Western North America and Adjacent Ocean Basins: Circum-Pacific Council for Energy and Mineral Resources, Earth Science Series, v. 6, p. 157–189.

Burbridge, D., Cummins, P.R., Mleczko, R., and Thio, H.K., 2008, A probabilistic tsunami hazard assessment for western Australia: Pure and Applied Geophysics, v. 165, p. 2059–2088.

Burridge, R., and Halliday, G.S., 1971, Dynamic shear cracks with friction as models for shallow focus earthquakes: Geophysical Journal of the Royal Astronomical Society, v. 25, p. 261–283.

Cao, Z., Pender, G., Wallis, S., and Carling, P., 2004, Computational dam-break hydraulics over erodible sediment bed: Journal of Hydraulic Engineering, v. 130, p. 689–703.

Chester, F.M., and Higgs, N.G., 1992, Multimechanism friction constitutive model for ultrafine quartz gouge and hypocentral conditions: Journal of Geophysical Research, v. 97, p. 1859–1870.

Cummins, P.R., and Kaneda, Y., 2000, Possible splay fault slip during the 1946 Nankai earthquake: Geophysical Research Letters, v. 27, no. 17, p. 2725–2728.

Dalguer, L.A., and Day, S.M., 2007, Staggered-grid split-node method for spontaneous rupture simulation: Journal of Geophysical Research, v. 112, doi:10.1029/2006JB004467.

DeDontney, N., and Rice, J.R., 2012, Tsunami wave analysis and possibility of splay fault rupture during the 2004 Indian Ocean earthquake: Pure and Applied Geophysics, v. 169, p. 1707–1735.

Dengler, L., and Uslu, B., 2011, Effects of harbor modification on Crescent City, California's tsunami vulnerability: Pure and Applied Geophysics, v. 168, p. 1175–1185.

Dieterich, J.H., 1978, Time-dependent friction and the mechanics of stick-slip: Pure and Applied Geophysics, v. 116, p. 790–806.

Dieterich, J.H., 1979, Modeling of rock friction. Part 1. Experimental results and constitutive equations: Journal of Geophysical Research, v. 84, p. 2161_2168.

Dieterich, J.H., 1992, Earthquake nucleation on faults with rate- and state-dependent strength: Tectonophysics, v. 211, p. 115–134.

Duan, B., and Day, S., 2008, Inelastic strain distribution and seismic radiation from rupture of a fault kink: Journal of Geophysical Research, v. 113, doi:10.1029/2008JB005847.

Duan, B., and Oglesby, D.D., 2006, Heterogeneous fault stresses from previous earthquakes and the effect on dynamics of parallel strike-slip faults: Journal of Geophysical Research, doi:10.1029/2008JB005847.

Elder, J.W., 1959, The dispersion of marked fluid in turbulent shear flow: Journal of Fluid Mechanics, v. 5, p. 544–560.

Fraccarollo, L., and Capart, H., 2002, Riemann wave description of erosional dam-break flows: Journal of Fluid Mechanics, v. 461, p. 183–228.

Freymueller, J.T., and Beavan, J., 1999, Absence of strain accumulation in the western Shumagin segment of the Alaska subduction zone: Geophysical Research Letters, v. 26, p. 3233–3236.

Freymueller, J.T., Woodard, H., Cohen, S.C., Cross, R., Elliot, J., Larsen, C.F., Hreinsodóttir, S., and Zweck, C., 2008, Active deformation processes in Alaska, based on 15 years of GPS measurements, in Freymueller, J.T., Haeussler, P.J., Wesson, R.L., and Ekström, G., eds., Active tectonics and seismic potential of Alaska: Washington, D. C., American Geophysical Union, p. 1–42.

Fujii, Y., and Satake, K., 2006, Source of the July 2006 West Java tsunami estimated from tide gauge records: Geophysical Research Letters, v. 33, doi:10.1029/2006GL028049.

Geist, E.L., 1999, Local tsunamis and earthquake source parameters: Advances in Geophysics, v. 39, p. 117–209.

Geist, E.L., 2002, Complex earthquake rupture and local tsunamis: Journal of Geophysical Research, v. 107, doi:10.1029/2000JB000139.

Geist, E.L., and Bilek, S.L., 2001, Effect of depth-dependent shear modulus on tsunami generation along subduction zones: Geophysical Research Letters, v. 28, no. 7, p. 1315–1318.

Geist, E.L., and Dmowska, R., 1999, Local tsunamis and distributed slip at the source: Pure and Applied Geophysics, v. 154, p. 485–512.

Guatteri, M., Mai, P.M., Beroza, G.C., and Boatwright, J., 2003, Strong ground-motion prediction from stochastic-dynamic source models: Bulletin of the Seismological Society of America, v. 93, p. 301–313.

Guatteri, M., and Spudich, P., 2000, What can strong-motion data tell us about slip-weakening fault-friction laws?: Bulletin of the Seismological Society of America, v. 90, p. 98–116.

Harris, R.A., and Day, S., 1993, Dynamics of fault interaction; parallel strike-slip faults: Journal of Geophysical Research, v. 98, p. 4461–4472.

Harris, R.A., and 21 others, 2009, The SCEC/USGS dynamic earthquake rupture code verification exercise: Seismological Research Letters, v. 80, p. 119–126.

Harris, R.A., and 13 others, 2011, Verifying a computational method for predicting extreme ground motion: Seismological Research Letters, v. 82, p. 638–644.

Hayes, G.P., Wald, D.J., and Johnson, R.L., 2012, Slab 1.0; a three-dimensional model of global subduction zone geometries: Journal of Geophysical Research, v. 117, doi:10.1029/2011JB008524.

Hinterberger, C., Fröhlich, J., and Rodi, W., 2007, Three-dimensional and depth-averaged large eddy simulations of some shallow water flows: Journal of Hydraulic Engineering, v. 133, p. 857–872.

Horrillo, J., Knight, W., and Kowalik, Z., 2008, Kuril Islands tsunami of November 2006, 2. Impact at Crescent City by local enhancement: Journal of Geophysical Research, v. 113, doi:10.1029/2007JC004404.

Hyndman, R.D., Yamano, M., and Oleskevich, D.A., 1997, The seismogenic zone of subduction thrust faults: The Island Arc, v. 6, p. 244–260.

Ichinose, G., Somerville, P., Thio, H.K., Graves, R., and O'Connell, D., 2007, Rupture process of the 1964 Prince William Sound, Alaska, earthquake from the combined inversion of seismic, tsunami, and geodetic data: Journal of Geophysical Research, v. 112, doi:10.1029/2006JB004728.

Ida, Y., 1972, Cohesive force across the tip of a longitudinal-shear crack and Griffith's specific surface energy: Journal of Geophysical Research, v. 77, p. 3796–3805.

Johnson, J.M., and Satake, K., 1994, Rupture extent of the 1938 Alaskan earthquake as inferred from tsunami waveforms: Geophysical Research Letters, v. 21, p. 733–736.

Kanamori, H., 1972, Mechanism of tsunami earthquakes: Physics of the Earth and Planetary Interiors, v. 6, p. 346–359.

Kennedy, A.B., Chen, Q., Kirby, J.T., and Dalrymple, R.A., 2000, Boussinesq modeling of wave transformation, breaking and runup, I. one dimension: Journal of Waterway, Port, Coastal, and Ocean Engineering, v. 126, p. 39–47.

Kim, D.-H., and Lynett, P.J., 2011, Turbulent mixing and passive scalar transport in shallow flows: Physics of Fluids, v. 23, doi:10.1063/1061.3531716.

Kim, D.-H., and Lynett, P.J., 2011, Turbulent mixing and passive scalar transport in shallow flows: Physics of Fluids, v. 23, doi:10.1063/1061.3531716.

Kim, D.-H., Lynett, P., and Socolofsky, S., 2009, A depth-integrated model for weakly dispersive, turbulent, and rotational fluid flows: Ocean Modeling, v. 27, p. 198–214.

Kirby, S., Scholl, D., von Huene, R., and Wells, R., 2013, Alaska earthquake source for the SAFRR tsunami scenario, chap. B, in Ross, S.L., and Jones, L.M., eds.,The SAFRR (Science Application for

Risk Reduction) Tsunami Scenario: U.S. Geological Survey Open-File Report 2013–1170, 46 p., http://pubs.usgs.gov/of/2013/1170/b/.

Kobayashi, M., and Lawrence, A., 2004, Cross-shore sediment transport under breaking solitary waves: Journal of Geophysical Research, v. 109, doi:10.1029/2003JC002084.

Kowalik, Z., Horrillo, J., Knight, W., and Logan, T., 2008, Kuril Islands tsunami of November 2006, 1. Impact at Crescent City by distant scattering: Journal of Geophysical Research, v. 113, doi: 10.1029/2007JC004402.

Kozdon, J.E., and Dunham, E.M., in press [? see comments at top of references], Rupture to the trench; dynamic rupture simulations of the 11 March 2011 Tohoku earthquake: Bulletin of the Seismological Society of America.

Lacy, J., Rubin, D., and Buscombe, D., 2012, Currents, drag, and sediment transport induced by a tsunami: Journal of Geophysical Research, v. 117, doi:10.1029/2012JC007954.

Li, L., Qiu, Q., and Huang, Z., 2012, Numerical modeling of the morphological change in Lhok Nga, west Banda Aceh, during the 2004 Indian Ocena tsunami; understanding tsunami deposits using a forward modeling method: Natural Hazards, v. 64, p. 1549–1574.

Linker, M.F., and Dieterich, J.H., 1992, Effects of variable normal stress on rock friction; observations and constitutive equations: Journal of Geophysical Research, v. 97, p. 4923–4940.

Liu, P.L.-F., Cho, Y.S., Yoon, S.B., and Seo, S.N., 1995, Numerical simulations of the 1960 Chilean tsunami propagation and inundation at Hilo, Hawaii, in Tsuchiya, Y., and Shuto, N., eds., Tsunami—progress in prediction, disaster prevention and warning: Kluwer Academic Publishers, p. 99–115.

Lynett, P., 2006, Wave breaking velocity effects in depth-integrated models: Coastal Engineering, v. 53, p. 325–333.

Lynett, P.J., Wu, T.-R., and Liu, P.L.-F., 2002, Modeling wave runup with depth-integrated equations: Coastal Engineering, v. 46, p. 89–107.

Lynett, P.J., Borrero, J.C., Weiss, R., Son, S., Greer, D., and Renteria, W., 2012, Observations and modeling of tsunami-induced currents in ports and harbors: Earth and Planetary Science Letters, v. 327–328, p. 68–74.

Musumeci, R.E., Svendsen, I.A., and Veeramony, J., 2005, The flow in the surf zone; a fully nonlinear Boussinesq-type of approach: Coastal Engineering, v. 52, p. 565–598.

National Tsunami Hazard Mitigation Program (NTHMP), 2009, Guidelines and best practices for tsunami inundation modeling for evacuation planning: U.S. Department of Commerce, National Oceanic and Atmospheric Administration, 7 p.

National Tsunami Hazard Mitigation Program (NTHMP), 2010, Guidelines and best practices for tsunami inundation modeling for evacuation planning: National Oceanic and Atmospheric Administration, NTHMP Mapping & Modeling Subcommittee, 8 p.

National Tsunami Hazard Mitigation Program (NTHMP), 2012, Proceedings and results of the 2011 NTHMP Model Benchmarking Workshop: U.S. Department of Commerce, National Oceanic and Atmospheric Administration, 436 p.

Nicolsky, D.J., 2012, Alaska tsunami model, in Proceedings and results of the 2011 NTHMP Model Benchmarking Workshop: Boulder, Colorado, U.S. Department of Commerce/National Oceanic and Atmospheric Administration Special Report, p. 55-87.

Nicolsky, D.J., Suleimani, E.N., and Hansen, R.A., 2011, Validation and verification of a numerical model for tsunami propagation and runup: Pure and Applied Geophysics, v. 168, p. 1199–1222.

Nielsen, S.B., 1998, Free surface effects on the propagation of dynamic rupture: Geophysical Research Letters, v. 25, p. 125–128.

Oglesby, D.D., and Archuleta, R.J., 2000, Dynamics of dip-slip faulting; explorations in two dimensions: Journal of Geophysical Research, v. 105, p. 13643–13653.

Oglesby, D.D., and Archuleta, R.J., 2003, The three-dimensional dynamics of a nonplanar thrust fault: Bulletin of the Seismological Society of America, v. 93, p. 2222–2235.

Oglesby, D.D., Archuleta, R.J., and Nielsen, S.B., 1998, Earthquakes on dipping faults; the effects of broken symmetry: Science, v. 280, p. 1055–1059.

Oglesby, D.D., Archuleta, R.J., and Nielsen, S.B., 2000, The three-dimensional dynamics of dipping faults: Bulletin of the Seismological Society of America, v. 90, p. 616–628.

Okada, Y., 1985, Surface deformation due to shear and tensile faults in a half-space: Bulletin of the Seismological Society of America, v. 75, p. 1135–1154.

Okal, E.A., Fritz, H.M., Raad, P.E., Synolakis, C.E., Al-Shijbi, Y., and Al-Saifi, M., 2006a, Oman field survey after the December 2004 Indian Ocean tsunami: Earthquake Spectra, v. 22, p. S203–S218.

Okal, E.A., Fritz, H.M., Raveloson, R., Joelson, G., Pancoskova, P., and Rambolamanana, G., 2006b, Madagascar field survey after the December 2004 Indian Ocean tsunami: Earthquake Spectra, v. 22, p. S263–S283.

Okal, E.A., Sladen, A., and Fritz, H.M., 2006c, Mauritius and Réunion Islands, field survey after the December 2004 Indian Ocean tsunami: Earthquake Spectra, v. 22, p. S241–S261.

Olsen, K.B., Madariaga, R., and Archuleta, R.J., 1997, Three-dimensional dynamic simulation of the 1992 Landers earthquake: Science, v. 278, p. 834–838.

Olsen, K.B., Day, S.M., Dalguer, L.A., Mayhew, J., Cui, Y., Zhu, J., Cruz-Atienza, V.M., Roten, D., Maechling, P., Jordan, T.H., Okaya, D., and Chourasia, A., 2009, ShakeOut-D; Ground motion estimates using an ensemble of large earthquakes on the southern San Andreas fault with spontaneous rupture propagation: Geophysical Research Letters, v. 36, doi:10.1029/2008GL036832.

Peyrat, S., Olsen, K., and Madariaga, R., 2001, Dynamic modeling of the 1992 Landers earthquake: Journal of Geophysical Research, v. 106, p. 26467–26482.

Ponce, V.M., 1989, Engineering hydrology, principles and practices: Prentice Hall, 640 p.

Press, W.H., Teukolsky, S.A., Vetterling, W.T., and Flannery, B.P., 2007, Numerical recipes—the art of scientific computing (3d ed.): Cambridge, Cambridge University Press, 1,235 p.

Rakha, K., Deigaard, R., and Broker, I., 1997, A phase-resolving cross shore sediment transport model for beach profile evolution: Coastal Engineering, v. 31, p. 231–261.

Ruina, A.L., 1980, Friction laws and instabilities; a quasistatic analysis of some dry friction behavior: Providence, R.I., Brown University, Ph.D. dissertation, 99 p.

Ruina, A.L., 1983, Slip instability and state variable friction laws: Journal of Geophysical Research, v. 88, p. 10359–10370.

Ryan, H.F., von Huene, R., Scholl, D.W., and Kirby, S.H., 2012, Tsunami hazards to U.S. coasts from giant earthquakes in Alaska: Eos (American Geophysical Union Transactions), v. 93, p. 185–186.

Santini, S., Dragoni, M., and Spada, G., 2003, Asperity distribution of the 1964 Great Alaska earthquake and its relation to subsequent seismicity in the region: Tectonophysics, v. 367, p. 219–233.

Satake, K., 1995, Linear and nonlinear computations of the 1992 Nicaragua earthquake tsunami: Pure and Applied Geophysics, v. 144, p. 455–470.

Satake, K., 2002, Tsunamis, in Lee, W.H.K., Kanamori, H., Jennings, P.C., and Kisslinger, C., eds., International handbook of earthquake and engineering seismology, Part A: San Diego, Academic Press, p. 437–451.

Satake, K., 2007, Tsunamis, in Kanamori, H., and Schubert, G., eds., Treatise on geophysics, Volume 4—Earthquake seismology: Elsevier, p. 483–511.

Scholz, C.H., 1998, Earthquakes and friction laws: Nature, v. 391, p. 37–42.

Shuto, N., 1991, Numerical simulation of tsunamis—its present and near future: Natural Hazards, v. 4, p. 171–191.

Sitanggang, K.I., and Lynett, P., 2005, Parallel computation of highly nonlinear Boussinesq equation model through domain decomposition: International Journal for Numerical Methods in Fluids, v. 49, no. 57–74.

Son, S., Lynett, P., and Kim, D.-H., 2011, Nested and multi-physics modeling of tsunami evolution from generation to inundation: Ocean Modeling, v. 38, p. 96–113.

Synolakis, C.E., Bernard, E.N., Titov, V.V., Kanoglu, U., and González, F.I., 2007, Standards, criteria, and procedures for NOAA evaluation of tsunami numerical models: National Oceanic and Atmospheric Administration, Pacific Marine Environmental Laboratory Technical Memorandum OAR PMEL-135, 55 p.

Tanioka, Y., and Satake, K., 1996, Tsunami generation by horizontal displacement of ocean bottom: Geophysical Research Letters, v. 23, p. 861–865.

Thio, H.K., Somerville, P., and Ichinose, G., 2007, Probabilistic analysis of strong ground motion and tsunami hazards in southeast Asia: Journal of Earthquake and Tsunami, v. 1, doi:10.1142/S1793431107000080.

Titov, V.V., and Synolakis, C.E., 1995, Modeling of breaking and nonbreaking long wave evolution and runup using VTSC-2: Journal of Waterway, Port, Coastal, and Ocean Engineering, v. 121, p. 308–316.

Titov, V.V., and Synolakis, C.E., 1996, Numerical modeling of 3-D long wave runup using VTCS-3, in Yeh, H., Liu, P.L.F., and Synolakis, C.E., eds., Long wave runup models: Singapore, World Scientific Publishing Co., p. 242–248.

Titov, V.V., and Synolakis, C.E., 1998, Numerical modeling of tidal wave runup: Journal of Waterway, Port, Coastal, and Ocean Engineering, v. 124, p. 157–171.

Titov, V.V., Moore, C.W., Greenslade, D.J.M., Pattiaratchi, C., Badal, R., Synolakis, C.E., and Kanoglu, U., 2011, A new tool for inundation modeling; community modeling interface for tsunamis (ComMIT): Pure and Applied Geophysics, v. 168, p. 2121–2131.

Veeramony, J., and Svendsen, I.A., 2000, The flow in surf-zone waves: Coastal Engineering, v. 39, p. 93–122.

Wang, R., Lorenzo-Martin, F., and Roth, F., 2003, Computation of deformation induced by earthquakes in a multi-layered elastic crust--FORTRAN programs EDGRN/EDCMP: Computers & Geosciences, v. 29, p. 195–207.

Wang, R., Lorenzo-Martin, F., and Roth, F., 2006, Erratum to "Computation of deformation induced by earthquakes in a multi-layered elastic crust--FORTRAN programs EDGRN/EDCMP": Computers & Geosciences, v. 32, p. 1817.

Wells, R.E., Blakely, R.J., Sugiyama, Y., Scholl, D.W., and Dinterman, P.A., 2003, Basin-centered asperities in great subduction zone earthquakes—a link between slip, subsidence, and subduction erosion?: Journal of Geophysical Research, v. 108, no. B10, 2507, doi:10.1029/2002JB002072.

Wells, R.E., Blakely, R.J., Scholl, D.W., and Ryan, H.F., 2011, Seismicity, topography, and free-air gravity of the Aleutian-Alaska subduction zone: American Geophysical Union, Fall Meeting, Abstract T21B-2322.

Wendt, J., Oglesby, D.D., and Geist, E.L., 2009, Tsunamis and splay fault dynamics: Geophysical Research Letters, v. 36, doi:10.1029/2009GL038295.

Wilson, R.I., Barberopoulou, A., Miller, K.M., Goltz, J.D., and Synolakis, C.E., 2008, New maximum tsunami inundation maps for use by local emergency planners in the State of California, USA [abs.]:

Eos (American Geophysical Union Transactions), v. 89(53), Fall Meeting Supplement, p. OS43D–1343.

Wilson, R., Davenport, C., and Jaffe, B., 2012, Sediment scour and deposition within harbors in California (USA), caused by the March 11, 2011 Tohoku-oki tsunami: Sedimentary Geology, v. 282, doi:10.1016/j.sedgeo.2012.1006.1001.

Wu, W., and Wang, S., 2008, One-dimensional explicit finite-volume model for sediment transport with transient flows over movable beds: Journal of Hydraulic Research, v. 46, p. 87–98.

Xiao, J., Lin, B., Falconer, R., and Wang, G., 2010, Modeling dam-break flows over mobile beds using a 2D coupled approach: Advances in Water Resources, v. 33, p. 171–183.

Appendix A—SAFRR Tsunami Inundation Maps for Select Areas of California's Coast

The Science Application for Risk Reduction (SAFRR) tsunami scenario would cause inundation of dry land along California's coast. The following maps provide examples of inundation for select areas of the coastline. These maps identify residential, business, and maritime areas and assets that could become flooded during a large tsunami event generated in the Pacific offshore the Alaska Peninsula. A GoogleEarth KML file provided on the U.S. Geological Survey and California Geological Survey SAFRR Web sites shows all areas mapped in California where inundation could occur from this scenario. The CGS SAFRR tsunami scenario web site provides access to the inundation maps and other information related to the scenario. This web site is found at http://www.conservation.ca.gov/cgs/geologic_hazards/Tsunami/Pages/SAFRR.aspx

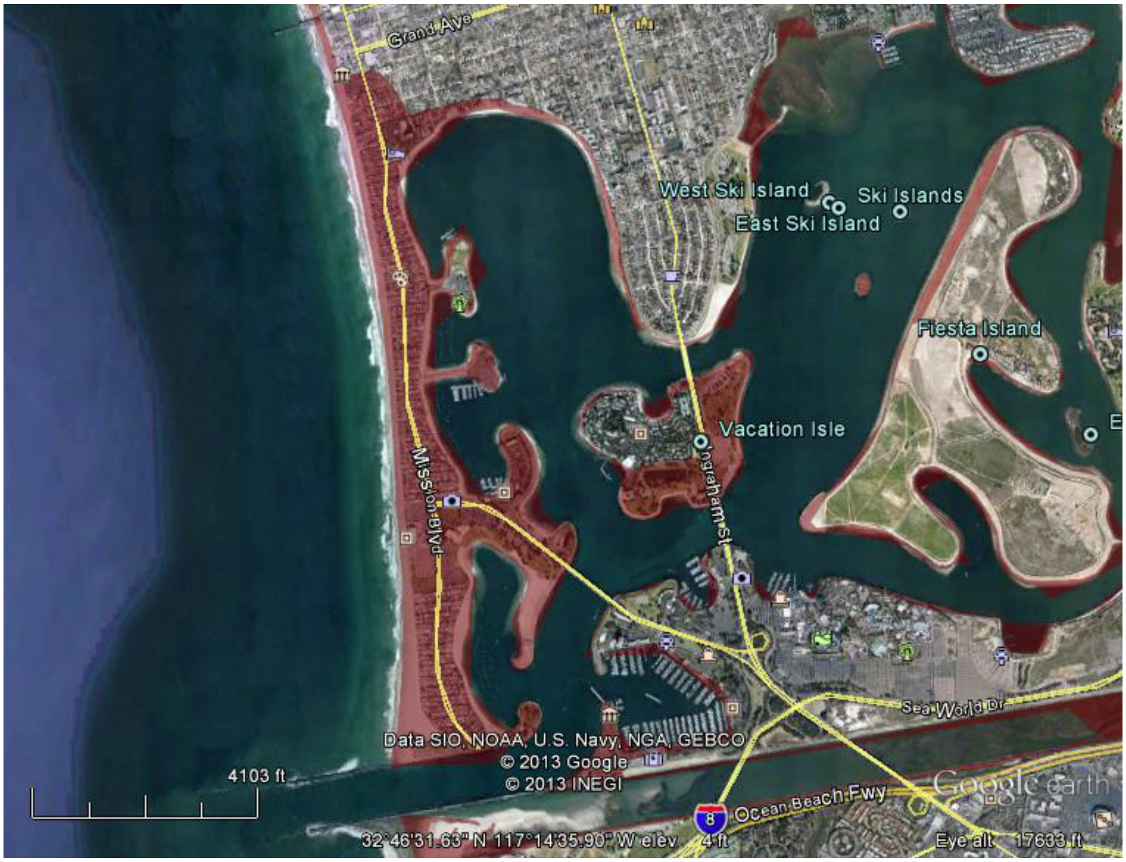

Figure A1 San Diego County – Ocean Beach: Peninsula is overtopped.

Figure A2 San Diego County – Del Mar: Several blocks and fairgrounds flooded.

Figure A3 Orange County – Newport Beach: Complete and partial flooding of islands and near overtopping of Balboa Peninsula

Figure A4 Orange County – Huntington Beach: Flooding overtops some levees and floods areas inland.

Figure A5 Orange County – Huntington Beach (Sunset Beach): Flooding isolates and nearly overtops all parts of the community.

Figure A6 Orange County – Seal Beach: Flooding occurs behind beach-front areas.


Los Angeles County – Naples area: Significant flooding occurs in this area.

Figure A7 Los Angeles County – Naples area: Significant flooding occurs in this area.

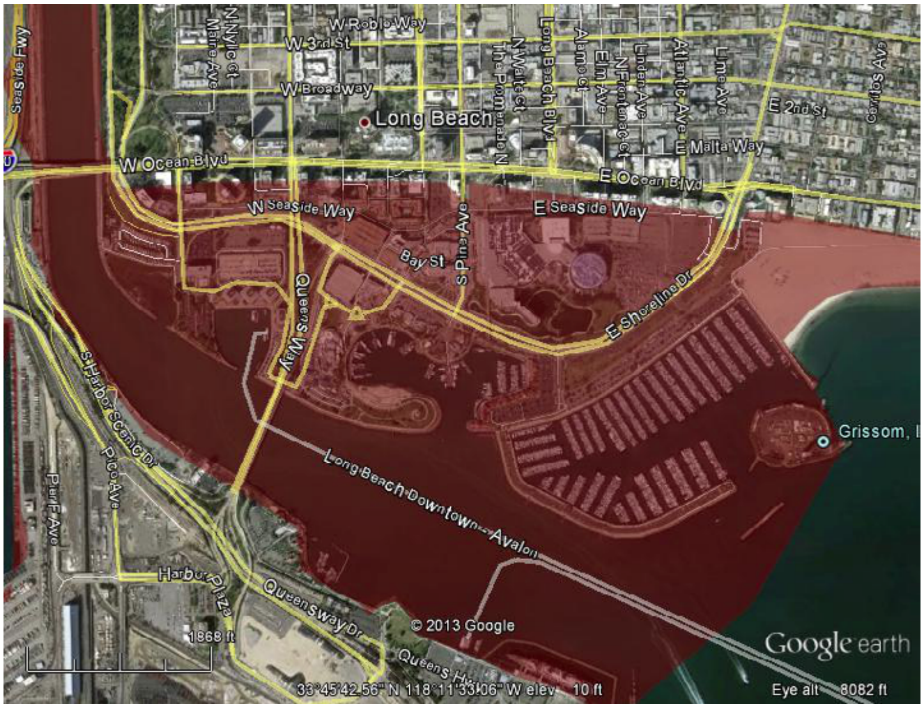

Figure A8 Los Angeles County – Long Beach: Flooding of downtown area occurs where many

Figure A9 Ventura County: Ventura and harbor: Several blocks and islands are inundated.

Figure A10 Santa Barbara County – Carpinteria: Several blocks are inundated.

Figure A11 San Luis Obispo County – Pismo Beach dunes and portions of the city are inundated.

Figure A12 San Luis Obispo County – Portions of Avila Beach are flooded by a tsunami over 5m in height.

Figure A13 San Luis Obispo County – Morro Bay: The Embarcadero is inundated.

Figure A14 San Luis Obispo County – Cayucos: Several blocks of the town are inundated.

Figure A15 Monterey County – Monterey: Flooding in the downtown and waterfront areas occurs.

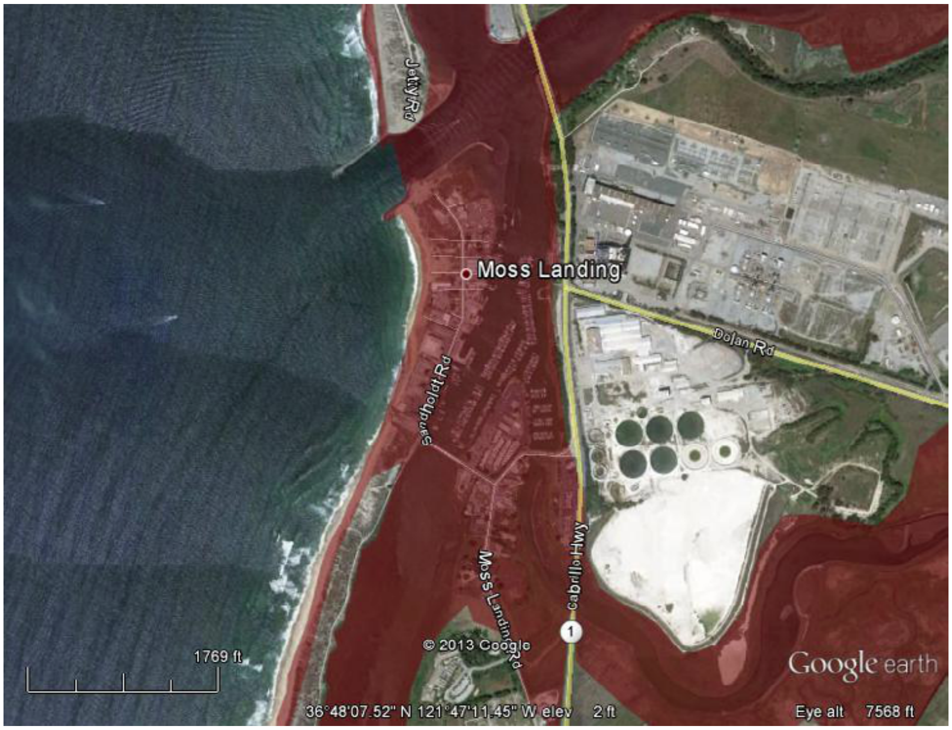

Figure A16 Monterey County – Moss Landing peninsula gets overtopped and inundated.

Figure A17 Santa Cruz County – Santa Cruz: Flooding of area around Beach and Boardwalk and other inland areas.

Figure A18 San Mateo County – Princeton/Half Moon Bay: Flooding of all of Princeton and Half Moon Bay waterfront occurs.

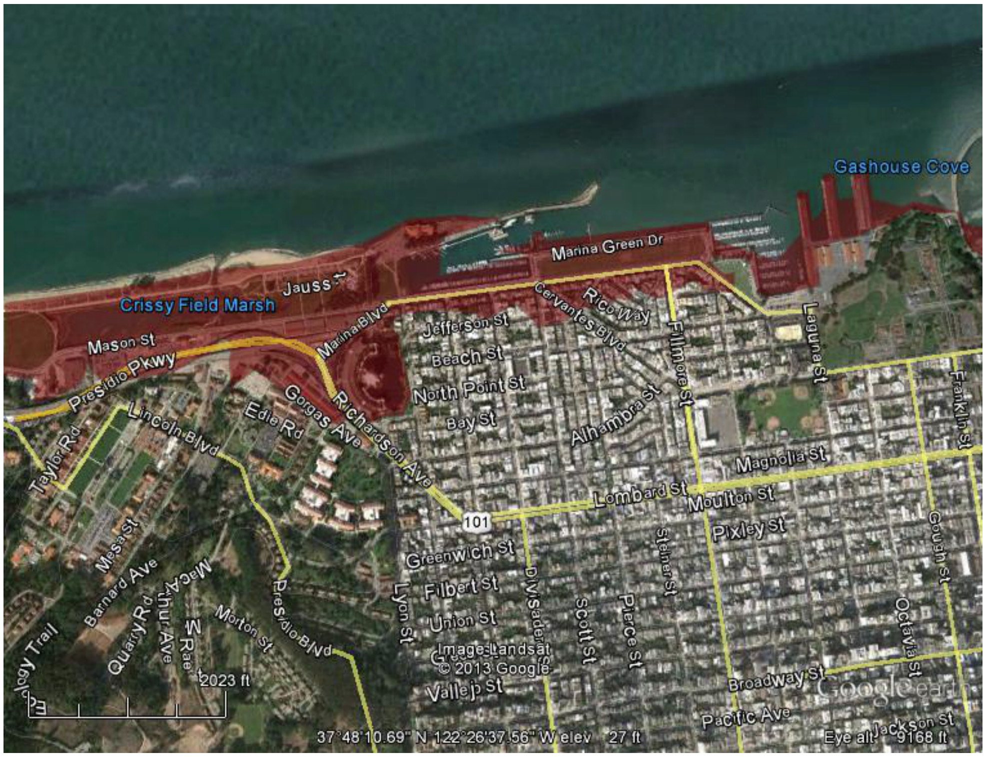

Figure A19 San Francisco: Flooding in parts of Marina District.

Figure A20 Alameda County – Oakland: Large portions of Bay Farm Island and Oakland Airport are flooded.

Figure A21 Contra Costa County – Areas around Port of Richmond are inundated.

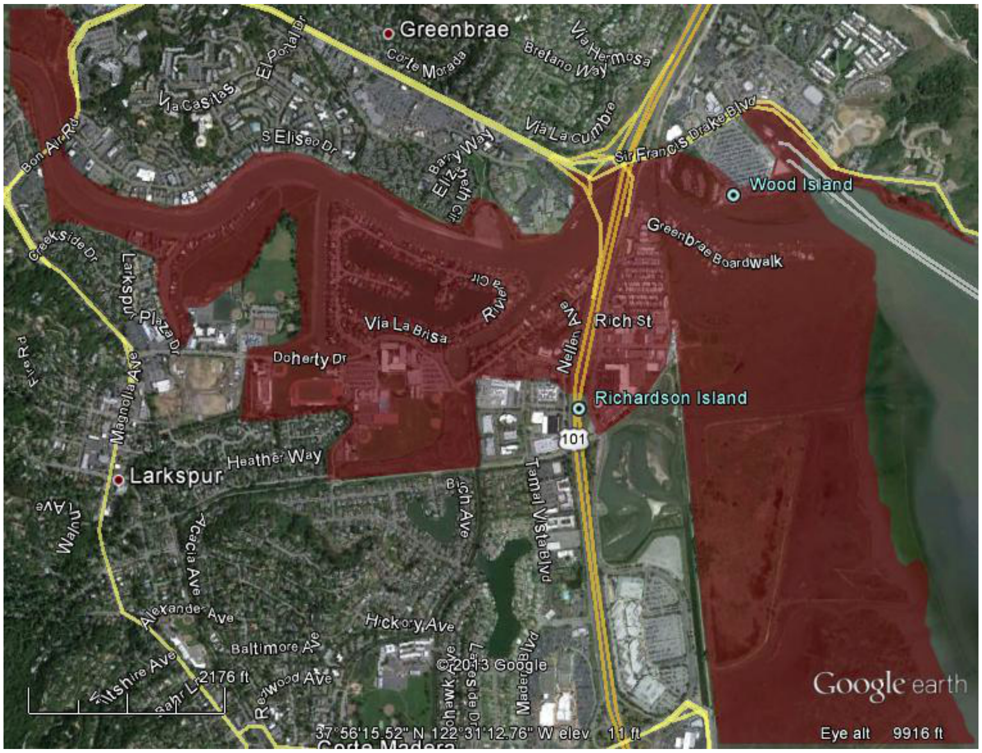

Figure A22 Marin County – Areas around Richardson Bay are inundated.

Figure A23 Marin County – Belvedere and Tiburon: A large number of low-lying homes are flooded.

Figure A24 Marin County – Stinson Beach: A large number of homes on the peninsula are flooded.

Figure A25 Sonoma County – The Bodega Bay peninsula campground gets overtopped.

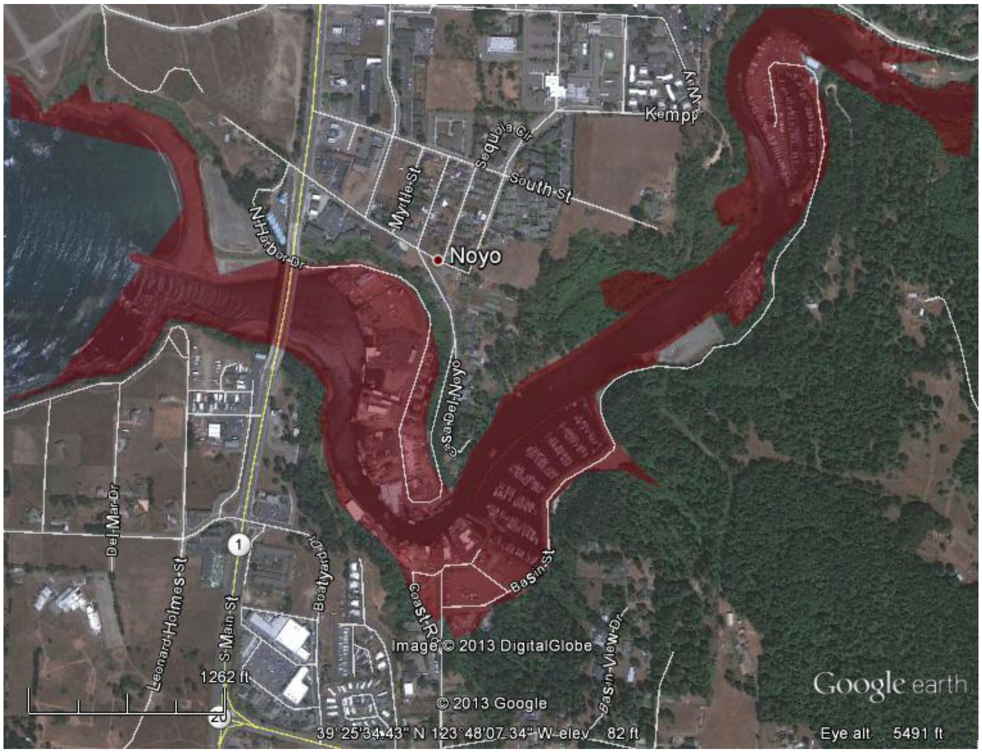

Figure A26 Mendocino County – Low-lying areas within Noyo River harbor gets inundated.

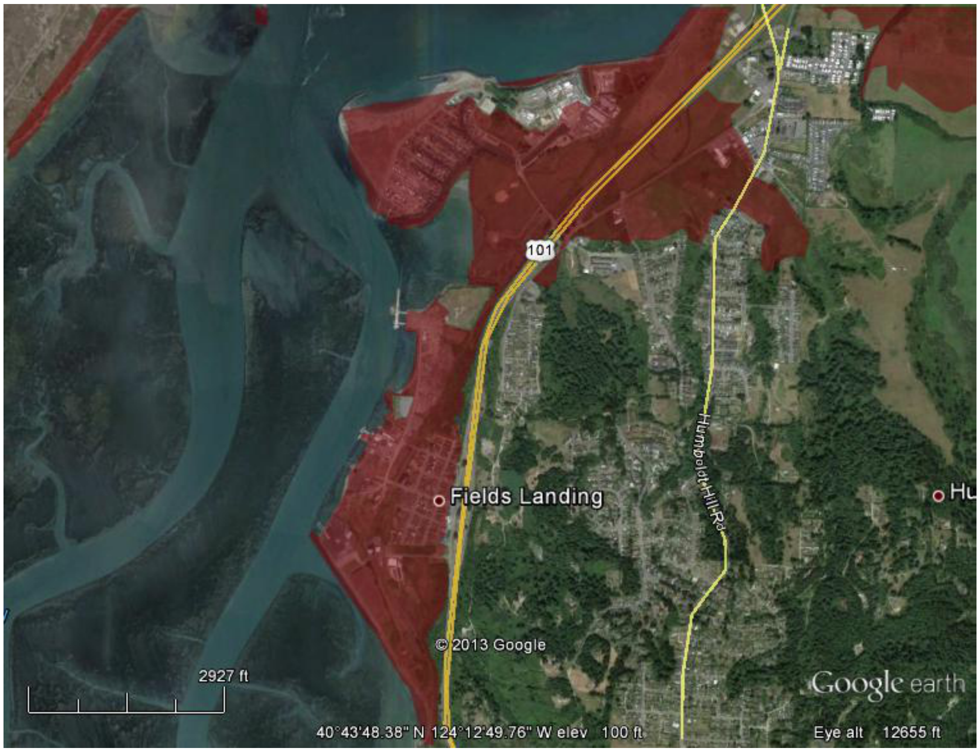

Figure A27 Humboldt County – Significant portions of Fields Landing and King Salmon get inundated.

Figure A28 Del Norte County – All of the waterfront area in Crescent City gets inundated.